COMPUTER MODELLING OF LIQUID CRYSTAL DISPLAYS

By

Huifang DENG

University College London

Department of Electronic and Electrical Engineering

A thesis submitted in conformity with the requirements of University College London for the degree of Doctor of Philosophy

1999-04-19 — 2000-02-14

TO MY MOTHER AND FATHER

Without their direct and indirect support and encouragement, it would be very hard to imagine that I could have finished this project and completed this thesis in time.

I am indebted to them very much. Therefore, this thesis is dedicated to them.

Acknowledgements

I wish to express my sincere gratitude to many people who have contributed to this research project.

First, I would like to thank my supervisors Dr Anibal Fernandez and Dr Sally Day for having offered me their invaluable time to listen to my problems, to discuss the solutions, to suggest the different ways to tackle them, and in general, to guide me through the whole research process step by step with exceptional patience when going over some coding details/logic with me and when correcting the English of my papers and theses, and the extraordinary tolerance towards my expressing outspokenly and candidly different opinions on different problems, as well as great helpfulness when helping me prepare each presentation by offering their distinctive suggestions.

Second, I wish to extend my thanks to Professor Brian Davies who participated in our regular group meeting, listened to my problem, and offered his valuable opinions and suggestions with great interest.

Third, my thanks also go to Dr Fabrizio Di Pasquale for answering my questions when I initially came cross the constant voltage modelling program.

My great debts are owed to following people at Philips Research Laboratories (Redhill): Andy Pearson, who arranged everything very well for me to visit their laboratories twice and helped me carry out the measurements with joy and ease; Dr Alan Knapp, who spared his valuable time to discuss some issues and make my mind clear of some specific points; John Hughes, who helped set up the signal generator; Andrew Guest for exchanging some information about the capacitance; and others who offered their generous assistance.

Finally, the financial support for this project from EPSRC and Philips (Redhill) are greatly appreciated.

Abstract

This thesis describes research work in modelling 2-dimensional twisted nematic liquid crystal display devices. There are three salient aspects of this work:

The first and more extensive is the development, implementation and testing of a new formulation for the dynamic modelling of these devices using a constant-charge assumption, which more accurately represents the case of thin-film-transistor (TFT)-driven devices.

Based on a dynamic tensor formulation (to preserve the nematic symmetry) and a single elastic constant approximation, the mode is developed to simulate the TFT driven device switching by allowing the voltages to be connected to the pixel electrodes for only a line time duration (typically 15μs ~ 30μs) and then letting them float for the rest of the half frame time while the charge remains constant. The director and electric potential distributions are dynamically calculated using a combination of finite differences and finite element methods under given electrode configurations and boundary conditions. The capacitance matrix is determined using a perturbation technique, and this further allows the voltages on the pixel electrodes to be found during the drifting time. This method can predict the dynamic behaviour of such a device more accurately than earlier models using a direct (fixed voltage) driving scheme and can include the effect of external storage capacitors. The programs developed in this project include as a special case the direct driving situation, produce as results the dynamic responses of various physics properties such as pixel voltages, capacitances of all electrodes, tilt angles and transmittance of the cell etc., and can also reproduce flicker behaviour due to the DC bias. There is good agreement between predicted results and experimental observations.

The second part of the work involves the theoretical derivation of a dynamic tensorial formulation for the liquid crystal behaviour, using three elastic constants. This derivation will be implemented outside this work and the resulting programs will give an even better modelling capability.

In the third part, in order to have a better interpretation of viewing angle characteristic of the studied cells, the extended 2×2 Jones matrix approach has been further generalised to include *arbitrary* incident (polar and azimuthal) angles.

Contents

PART II. Numerical Modelling

List of Figures

List of Tables

1. Introduction

Thin Film Transistor (TFT) driven Active Matrix Liquid Crystal Displays (AMLCDs) technology as shown in Figure 1 has successfully created a big market for notebooks, portable computers with large size displays of 14 to 20 inches [1], projection light valves and miniature displays. The improvements in viewing characteristics, low power consumption and light weight have been considerable [1]. AMLCDs are even penetrating into the desktop monitor market and poised to compete with Cathode Ray Tubes (CRTs) [2]. Among the various liquid crystal operating modes, the Twisted Nematic (TN) is most commonly used in the TFT driven LCDs. This is because the TN mode has a low threshold voltage, relatively good optical performance, and TN LC materials with very high resistivity and high photostability are commercially available.

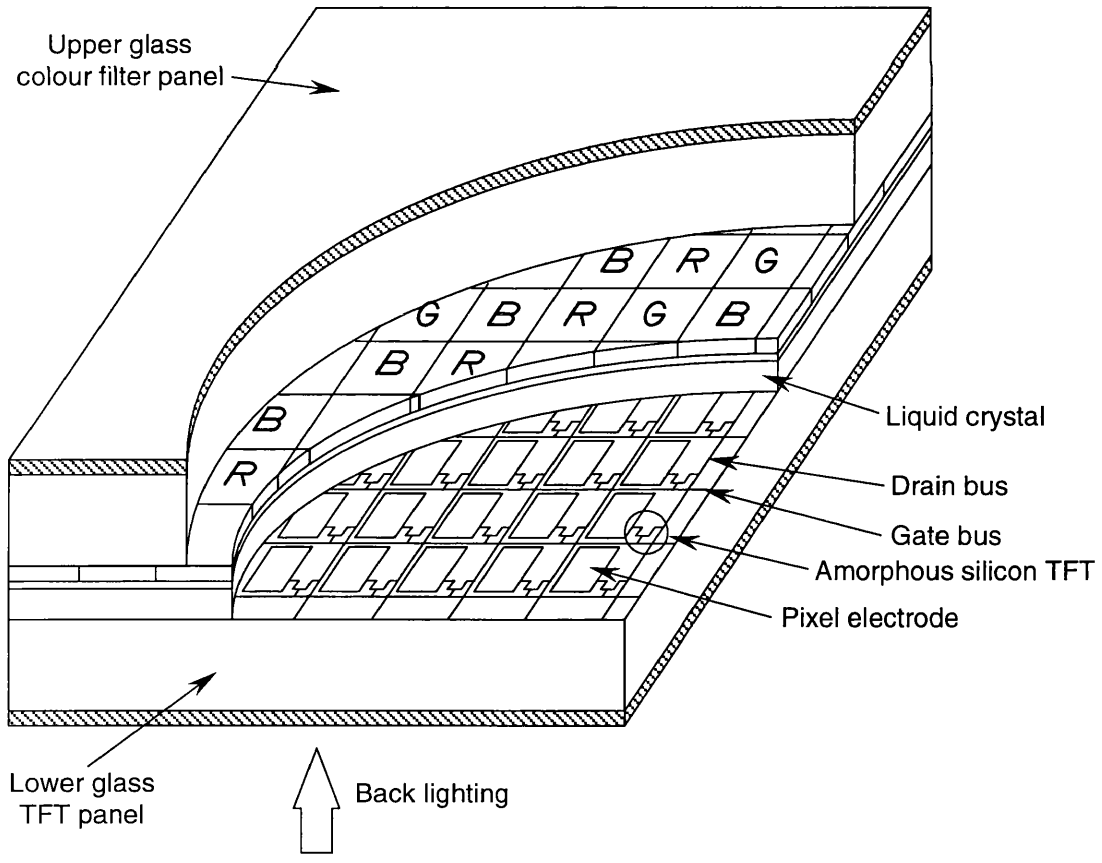

Figure 1 A cross-sectional view of an active matrix TFT LCD

In order to understand the experimentally observed dynamic behaviour of such systems, especially their electro-optical properties, and hence improve these properties, one must have a detailed knowledge of director and potential field profiles, static or dynamic. In order to obtain this detailed knowledge, computer modelling (CM) has been used [3-30] to numerically solve either Oseen-Frank free energy equation [31],[32] for static problems or Leslie-Erickson equations [33],[34] or the nematic symmetry-preserved tensorial formulation [15], which govern the spatial or temporal-spatial distributions of director and potential fields.

As displays' resolution becomes higher, 3D or at least 2D modelling is needed. New efforts to improve the viewing angle such as In-Plane Switching (IPS) are at least 2D structures, so 1D is no longer enough to simulate performance. Furthermore, the computer model that simulates the direct driving using the constant voltage condition [4-9], [13-21], [23] is no longer suitable for accurately simulating the situation where the driving is realised by Thin Film Transistors (TFTs) and the electrode-induced edge effects cannot be ignored. Therefore, at least, a 2-dimensional computer model is needed.

1.1. Objectives and motivation

As we already know, in the case of direct driving the voltage that is applied to the pixel electrode maintains a constant value during the whole frame time (disregarding polarity) as shown in Figure 2. However, in the case of TFT driving, as shown in Figure 3, the voltage that is applied to the LC pixel electrode is controlled by the gate pulse which acts as a switch, as shown in Figure 4, and is typically of a duration from 15μs to 30μs. That means the source voltage is only applied to the pixel electrode for this very short switch-on time. During this period of line time, the charges are deposited on the pixel electrode and the external storage capacitor C_{ext} which is employed to help keep the voltage constant.

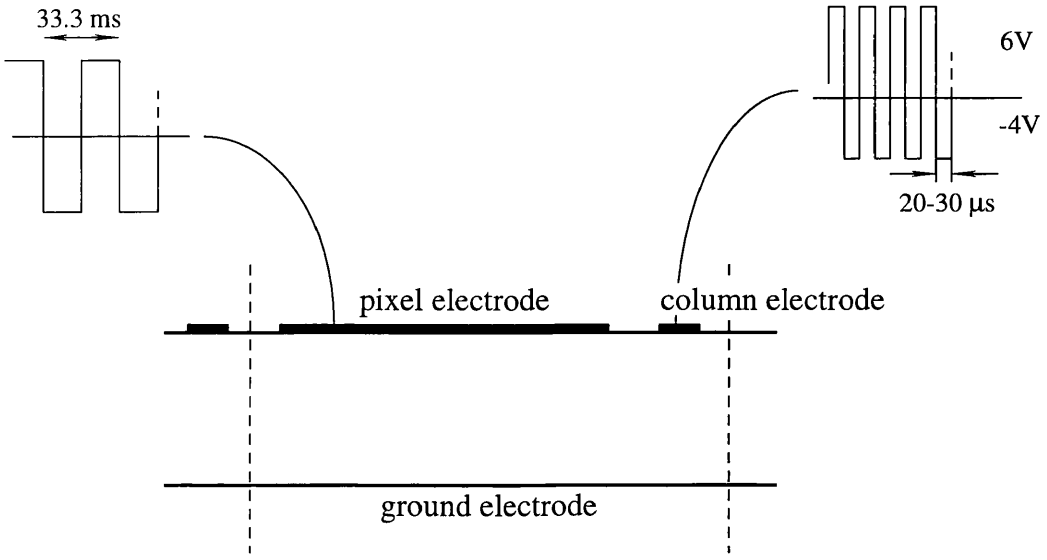

Figure 2 A constant voltage driving model

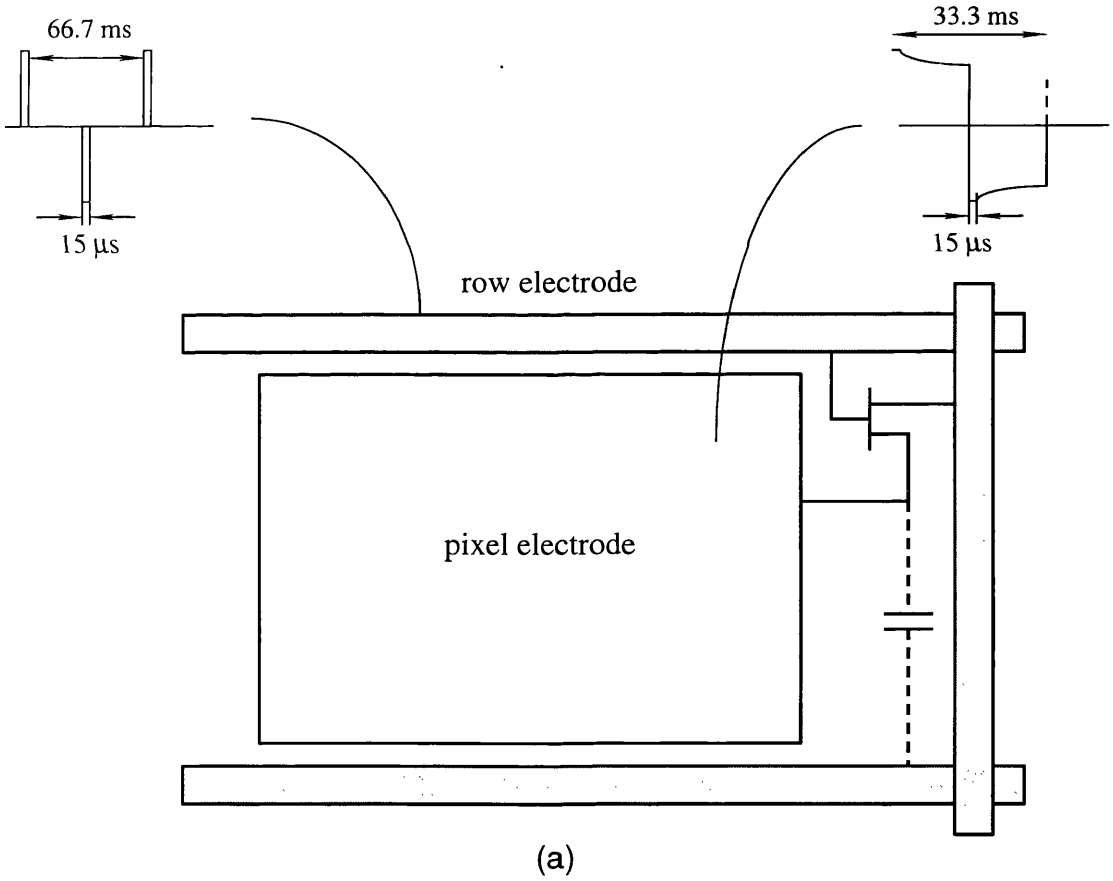

(a)

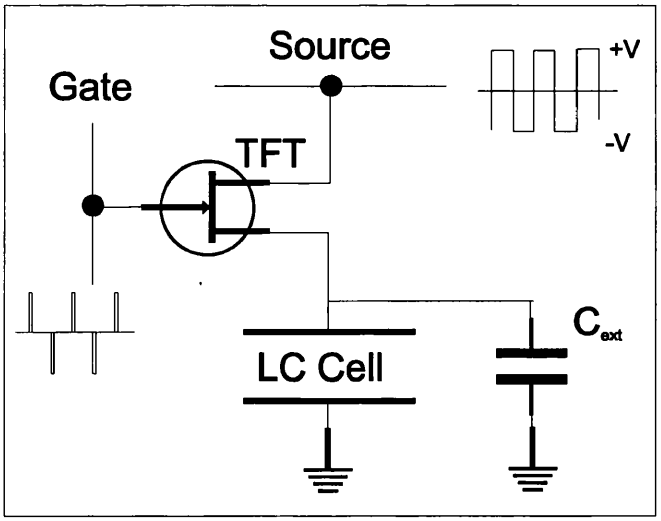

(b)

Figure 3 (a) A single TFT driving unit and (b) its equivalent circuit

After this time, the voltage is withdrawn by switching off the TFT device and the total charges on the pixel electrode and the external capacitor remain constant (although re-distribution between them takes place at each time step) as no conductivity within the LC cell is considered (in fact, the conductivity can be very low [35],[36]) and an infinite off-resistance between source and drain is assumed (actually, the off-resistance between source and the drain of the TFT device can be a very high [37]).

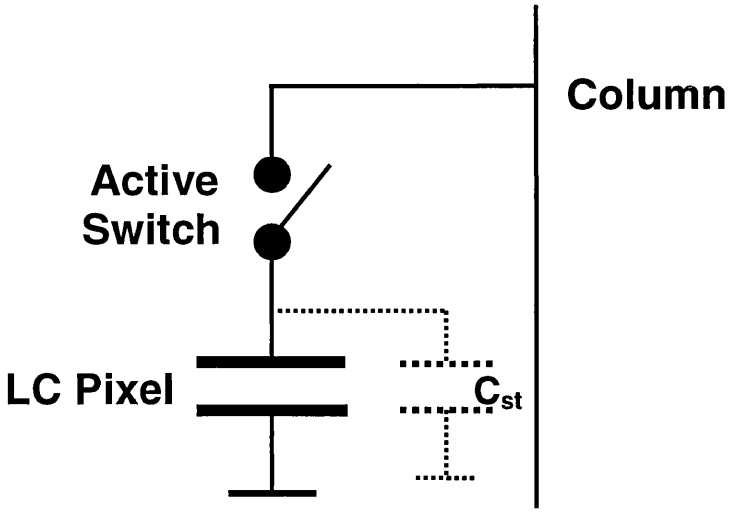

Figure 4 A TFT device acting like an active switch

The pixel voltage is left drifting for the rest of frame time. The drifting voltage is then determined by the charges $\boldsymbol{Q}$ and the LC cell capacitance matrix $\boldsymbol{C}$.

In order to calculate the charges Q and generalised capacitance matrix C, one needs to know not only the potential spatial distribution but also director profiles as the latter determines the permittivity at a given time. In accurately calculating the charges and the mutual capacitance between, say, bus electrodes and pixel electrodes, special care must be taken of the electrode-induced edge effects.

Therefore, from the above discussion it becomes clear that the TFT driven device cannot be simply described by the previous *constant voltage model* (CVM). In addition, the electrode edge effects and external capacitance must be taken into account. That means that the a one-dimensional model developed for the TFT driven situation [24-26] is not adequate either as it is only valid for a region far away from the edge of the electrodes and it cannot include external storage capacitance. Therefore, at least , a 2-dimensional model [28] is required. Because the total charges remain constant during the whole floating time, this model is referred to as *constant charge model* (CCM) in order to differentiate CVM as discussed above.

1.2. Achievements

The achievements in this project consist mainly of 3 salient aspects:

(i) The first and most extensive is the development, implementation and testing of a new formulation for the dynamic modelling of LC devices using the constant-charge assumption, which can represent more accurately the behaviour of TFT-driven devices.

This new 2-dimensional model can predict the dynamic behaviour (such as voltage drifting, director distribution, self- and mutual capacitances, charges, and transmittance) of LCD cells more accurately and therefore it is more realistic than previous CVM and all existing one-dimensional CCMs. This is because it simulates the actual TFT driving situation; and it takes the physical sizes of electrode into account, therefore it enables us to calculate dynamically the self-capacitance of pixel electrodes, the mutual capacitance between pixel and bus electrodes, and the charges deposited in the electrodes. This in turn enables us to predict the pixel floating voltages and to calculate the director and potential distributions across the whole cell more accurately and realistically.

Furthermore, the current model offers the following additional functionality:

- ♠ It allows us to include an external storage capacitor, commonly used in this type of devices to help keep the voltage constant and examine its effects;
- ♠ It treats the constant voltage model as a special case;
- ♠ It can handle two domains, each having different settings of pretilt and twist angles;
- ♠ Boundary conditions implemented include a Neumann boundary condition along with the free boundary, Dirichlet, and periodic;
- ♠ The bus voltage can be of asymmetric form, say, from +6v to –4v; and
- ♠ The levels of pixel voltages can be changed at any time during the running of the program.

(ii) In order to overcome the limitation of a single elastic constant formulation of the dynamics, a three elastic constant tensorial dynamic equation that governs the evolution of director field has also been derived. This derivation is implemented outside this work and the resulting programs give an even better modelling capability.

(iii) Finally, in order to examine the optical properties of LCDs, a complete theoretical formulation for the calculation of the transmittance *at arbitrary incident angles* is developed by releasing the constraint to the azimuthal angle $\varphi_k=0$ as imposed in Lien's extended 2×2 Jones matrix method [38-43], and letting it take any value. This formulation gives us the power to have the calculated transmittance of crossed polarizers and single- and two-domain systems against arbitrary φ_k and ϑ_k, and to examine viewing angle characteristics (contrast ratio), an important aspect in liquid crystal display design and development [44]. A good agreement has been found between theoretical results and experimental data for a TN system in IPS mode.

1.3. Outline of the thesis

The whole thesis can be divided into three parts:

PART I. Physics of LCDs;

PART II. Numerical modelling;

PART III. Optical properties of twisted nematic LCDs.

The first part consists of two chapters: In Chapter 2, a brief review of properties and applications of LC materials and LCD devices is given as well as description of driving schemes and display mechanism. Chapter 3 contains the theoretical formulation of LC physics. Particularly, a complete derivation of the three-elastic constant tensorial dynamic equation is given that describes the evolution of the director which is an extension to the commonly used single elastic constant expression [19]. The steady state model is briefly discussed there as well.

The second part comprises Chapters 4, 5, and 6.

In Chapter 4, numerical methodologies used for solving static and dynamic equations, i.e., for finding out director field and potential field distribution are discussed. Those include the finite element method and variational principles for calculating the potential, and finite difference for spatial discretization of director and Crank-Nicolson central difference for temporal discretization of director.

Chapter 5 gives a brief description of the constant voltage model.

Chapter 6 constitutes the central part of the thesis where the constant charge model is addressed in detail. The main coverage includes:

1) theoretical description and computational procedures of the perturbation technique for calculation of capacitance matrix;
2) the formalism of calculation of the charges deposited on the pixel and bus electrodes;
3) results on different LCD systems with different electrode configurations;
4) a comparison between measurements and the numerical modelling;
5) a study of flicker;
6) a study of numerical accuracy such as the effects of the different discretization step lengths on the calculation results of physics properties of LCDs.

Chapter 7 alone constitutes Part III where a complete derivation of restriction-free extended 2×2 Jones matrix theory is given that enables us to study the transmittance at arbitrary incident angles. Transmittance polar diagrams for some typical LCD configurations are given and the contrast of bright against dark states are discussed and presented. A comparison is made between theoretical prediction and the

experimental data from Philips for a TN system in IPS mode. A good agreement has been found and the full details are given in a published paper, which is appended to this thesis.

Finally, Chapter 8 contains the conclusions to this work.

2. Liquid crystal displays

The most commonly seen LCD devices are the flat panel displays. According to the display technology, they can be classified as 3 groups: The first one includes watches, calculators and instruments etc, which are associated with the twisted nematic LCD technology; the second one is represented by laptop computers and instruments etc, which are associated with supertwisted nematic; and the third one contains video applications and laptop computers, associated with active matrix. There are a number of references addressing the LCDs [45-49] and LCD technology [1],[2],[45].

2.1. Liquid crystal materials

Liquid-crystal materials [49-52] are broadly divided into lyotropic and thermotropic types. Lyotropics are solutions that exhibit a phase transition with concentration change and temperature. Thermotropic materials are not solutions, and their phase transitions are determined by temperature. Lyotropics are of importance in biology and related fields such as soap industries but of no value in current display technology.

All matter has traditionally been considered as existing in one of three states or phases: the solid, liquid or gaseous. In certain temperature ranges, however, some organic compounds possess an intermediate phase, called the mesomorphic state [53] in which solid and liquid characteristics exist together, i.e., they exhibit crystalline properties and at the same time have the fluidity associated with liquids. Their molecules lie in a loosely ordered crystalline arrangement but still retain a freedom of motion. The shape of molecules tends to be a long thin shape. Such organic compounds were studied by a number of scientists [54] but almost three quarters of a century elapsed before serious efforts were expended to use their properties in technological applications.

The average orientation of LC molecules is described by a unitary vector called *director* **n**, while the orientational order determines anisotropic properties such as birefringence of LC materials. Anisotropy in refractive indices Δn and permittivity $\Delta\varepsilon$ means that switching with **E**-field leads to change in optical properties. So liquid crystals are anisotropic in certain physical properties.

2.2. Liquid-crystal mesophases

Ordinary liquids generally possess some short-range order on a molecular scale but lack any macroscopic or long-range order. This is described as the *isotropic phase.* At sufficiently high temperature, any liquid crystal material will become isotropic (see Figure 5). The transition temperature to the isotropic state is called the *clearing temperature because* of drastic reduction in light scattering in the bulk material at this point.

Below the clearing temperature, various degrees of ordering in the fluid produce the liquid-crystal phases also known as *ordered fluids.* This regular crystal periodicity is lost in the fluid phase. However, orientational order and diffuse structures are consistent with fluidity.

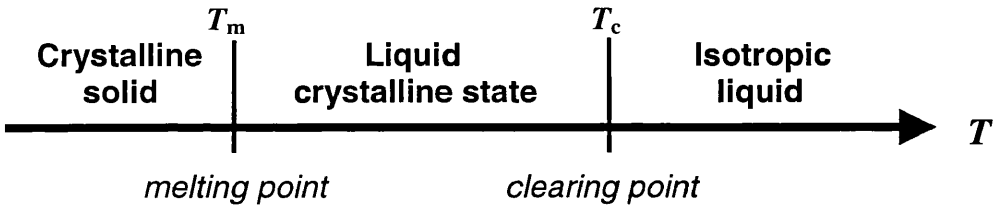

Figure 5 Phases of matter by temperature

The liquid-crystal mesophases were first identified by their interesting birefringent textures observed with the polarizing microscope. There are a number of different structures (phases) in liquid crystal state. One of them is called *nematic (Greek,* thread) phase which looks like the threadlike structures. A variant of the nematic phase is described as *cholesteric* phase, simply because the first materials demonstrating this property were cholesterol derivatives, and because it contains *chiral* molecules, it is also called chiral nematic (N^*). The term *smectic* (Greek, soap) phase is associated with the soaplike character of the early materials. It can be further classified into smectic-A (S_A), smectic-C (S_C), and chiral S_C (S_C^*) etc. according to its diffuse positional order in addition to orientational order. Further study of liquid crystal state continues to reveal unexpected behaviour, such as chiral S_A (S_A^*) and *discotic* phases whose device applications are not yet obvious. Because this thesis only deals with the nematic liquid crystal, a brief discussion of its properties is given below. Discussions for all other types are not covered here and can be found in references [48], [50], and [51] etc..

- **Nematic phase**

The molecules whose appearance of the texture assumes threadlike in a polarising microscope arrange parallel or nearly parallel to one another. They are free to move in all directions and can rotate about their long axes. Like pencils in a box they can roll around and slide back and forth, but generally point in the same direction.

The nematic liquid-crystal (NLC) phase is the simplest of the liquid-crystal structures. Orientational order exists in the presence of translational disorder. The structure of a uniaxial nematic is sketched in Figure 6, where typical liquid-crystal rod-like molecules are indicated, with dimensions on the order of 2nm [48]. The orientation axis is labelled by a unit vector **n**, known as the nematic *director*. The NLC is not polar, and + **n** is physically the same as -**n**.

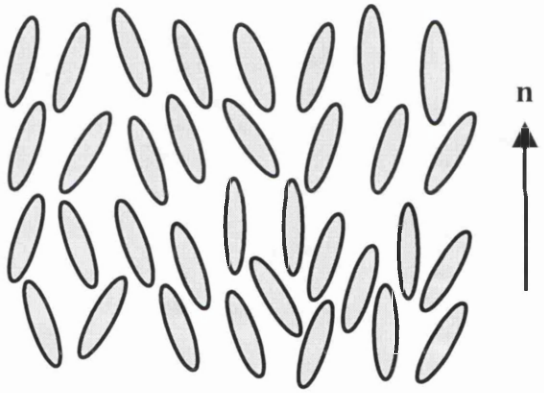

Figure 6 Nematic liquid-crystal phase

The molecular orientational order gives rise to anisotropic properties such as birefringence, and dielectric anisotropy – arguably the same thing just a different frequency, but it is important for display operation. The nematic molecules undergo translational and rotational motions such that the orientational order is a statistical property subject to local fluctuations. The corresponding refractive fluctuations scatter light and limit the transmission of bulk nematics. However, the short optical path in LCDs and the orientation by alignment layers make light scattering insignificant.

The degree of NLC order is quantified by an orientational order-parameter S,

$$S = \frac{1}{2}\left(3\langle \cos^2 \theta \rangle - 1\right) \qquad (1)$$

where θ is the fluctuation in polar angle relative to **n**, and $\langle\cos^2\theta\rangle$ is a molecular average. For complete order, θ = 0, implying $S = 1$; in the totally random case, $\langle\cos^2\theta\rangle = 1/3$, giving $S = 0$ for the isotropic liquid. Typically S may approach 0.8, well below the clearing point, and decreases to approximately 0.4 near the discontinuous phase transition to the isotropic state.

Nematic liquids are commonly used in devices using LCDs. Their two features: (1) response to the applied electric fields and (2) ability to rotate the plane of vibration of polarised light (birefringence and its effects on polarised light) are employed in LCDs.

2.3. Liquid-crystal properties

2.3.1. Elasticity

The minimum free energy of the NLC state corresponds to uniform orientation throughout the entire volume, analogous to the perfect single-crystal state in a solid. Elastic response to shearing forces is not possible in a fluid. Distortions in nematic orientation are opposed by forces much weaker than solid-state elasticity. The light-scattering behaviour and low energy requirements of LCDs are related to the weak elasticity.

The NLC thermodynamic free energy can be expanded in spatial derivatives of **n**, where the coefficients in this expansion are identified with elasticity. Symmetry restrictions eliminate first-order terms and reduce the number of bulk curvature, (second-order) elastic constants to three independent terms [31], [32], [50]:

$$F_d = 1/2\left[K_{11}(\nabla \bullet \mathbf{n})^2 + K_{22}(\mathbf{n} \bullet \nabla \times \mathbf{n})^2 + K_{33}(\mathbf{n} \times \nabla \times \mathbf{n})^2\right] \quad (2)$$

The coefficients K_{11}, K_{22}, and K_{33} are known as the Frank elastic constants and correspond to splay, twist, and bend deformations, respectively, as shown in. Figure 7. Higher order terms in the free-energy expansion are associated with higher order elastic coefficients, which are of academic interest only. In LCD NLCs at room temperature, K is on the order of 10 pN. Generally, $5 \leq K_{11} \leq 20$ pN, $K_{22}/K_{11} \approx 0.5$, and $0.5 < K_{33}/K_{11} < 3.0$[49]. The elasticity weakens with declining order related to increasing temperature such that $K \propto S^2$.

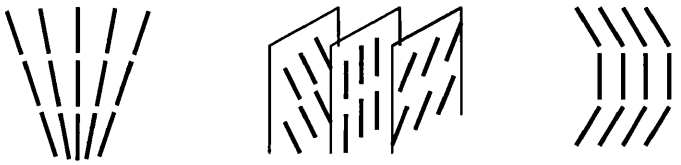

Figure 7 The three distinct curvature strains of a liquid crystal: splay, twist, and bend, described by three elastic constants: K_{11}, K_{22}, and K_{33}

2.3.2. Viscosity

The viscous behaviour of liquid crystals is anisotropic; moreover, flow and orientation are coupled. A flow process induces a favoured director orientation, and conversely a field-induced reorientation of the director induces a flow effect. A detailed analysis of the NLC involves five independent viscous coefficients [33],[34],[48]. The behaviour is usually approximated by a single rotational viscous coefficient (γ).

$$\text{Viscous torque} = \gamma \frac{\partial \theta}{\partial t} \tag{3}$$

The flow and rotation viscous interaction can be taken into account by a modified rotation viscosity (γ^*) [55],[56]. At room temperature the LCD NLC flows with a viscosity about an order of magnitude greater than that of water or 0.10 Pa•s

The viscosity rises exponentially with decreasing temperature [48], imposing a corresponding increase in LCD response time. High viscosity at low temperature limits the range of video-rate LCDs to near-room-temperature operation. At a given temperature the viscosity is determined by molecular structure, and great effort has been made to synthesize low-viscosity NLCs for video-rate LCDs.

2.3.3. Dielectric anisotropy and birefringence

The NLC dielectric response is anisotropic, with uniaxial symmetry. The dielectric constants perpendicular and parallel to **n** are labelled $\varepsilon_\perp$, and $\varepsilon_\parallel$, respectively. The dielectric anisotropy $\Delta\varepsilon$, which may be positive or negative, increases with order parameter S and is written

$$\Delta\varepsilon = \varepsilon_\parallel - \varepsilon_\perp \tag{4}$$

The dielectric constants decrease with increasing frequency, as some components of the induced dipole moment are related to molecular motion. At room temperature, in the audio-frequency range, typical LCD NLC relative permittivities and anisotropies are on the order of 5 [48] ($-10 \leq \Delta\varepsilon \leq 50$ in general [49]). At optical frequency the dielectric response determines the refractive indices $n_\perp$ (or n_o-ordinary) and $n_\parallel$ (or n_e-extraordinary) perpendicular and parallel, respectively, to the director or optic axis. The birefringence (Δn) increases with order parameter S,

$$\Delta n = n_\parallel - n_\perp \tag{5}$$

For LCD NLC materials the refractive index is approximately $n_\perp = 1.5$, and the birefringence Δn is on the order of $0.03 \sim 0.3$ [49].

2.3.4. Applied field effects

An applied electric field contributes an additional term (F_E) to the liquid crystal free-energy density,

$$F_E = -1/2\,\varepsilon_0 \Delta\varepsilon (\mathbf{E} \bullet \mathbf{n})^2 \tag{6}$$

which favours alignment along the electric field ($\mathbf{E}$) direction for positive dielectric anisotropy $+\Delta\varepsilon$ and orthogonal to $\mathbf{E}$ for $-\Delta\varepsilon$. Physically, the induced dipole moment reacts with the applied field to produce a torque, which therefore varies as E^2 . The torque and resulting director alignment are independent of $\mathbf{E}$ polarity. The orientational effect of an electric field is the basis for most LCDs.

2.4. Display mechanisms

2.4.1. Display requirements

There are many LC effects that might be used in display devices, but the options are restricted by the display requirements. Adequate visual contrast may be as low as 2:1 or approach 100:1, depending on the application. Brightness and optical efficiency are needed in addition to contrast, particularly in outdoor or other bright environments. The viewing angular range, or off-axis viewing angle, is important in direct-view LCDs. Basic black-and-white operation is valued where colour is provided by filters. A strongly non-linear response, or sharp electro-optic characteristic, is critical in passive-matrix addressing. Tolerance to manufacturing fluctuations is a cost consideration. Power dissipation limits the display size and

applications. Adequate response time is essential in video applications. Colour and gray-level ranges are critical in TV-type applications. Stability and long lifetime are indispensable. Flicker and edge effects should be eliminated.

2.4.2. Display mechanisms

Temporal variation of the driving voltage $V(t)$ leads to the change of director configuration $\mathbf{n}(\varphi,\mathbf{r};t)$ (here φ denotes potential) which determines permittivity $\bar{\bar{\varepsilon}}(\mathbf{n},t)$. As a function of the permittivity, the cell capacitance $C(\bar{\bar{\varepsilon}},t)$ changes with time. The change in the cell capacitance will have two different consequences depending on the driving schemes according to relation $CV=Q$:

If the driving is direct, i.e., the voltage V is constant (see Figure 8), then the charge will be varying with time;

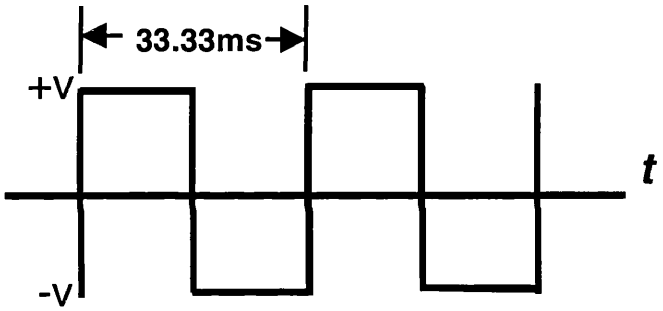

Figure 8 Constant voltage driving

If the driving is TFT controlled, i.e., the charge Q is constant, then the voltage V should be drifting as shown in the Figure 9 below.

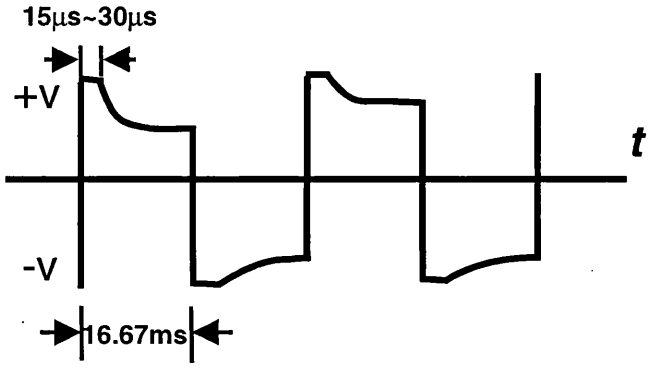

Figure 9 Voltage floating in TFT driving

This predicted behaviour is verified by the 2-dimensional constant charge model that is developed by the author and to be described in this thesis.

3. Theory

There are two theories on the physics of liquid crystals. One is called molecular field theory, the other is called curvature elasticity theory.

3.1. Molecular field theory of liquid crystals

The molecular field theory is based on *macroscopic* thermodynamics and *microscopic* statistical physics.

3.1.1. Laudau theory

The theory which is based on the macroscopic thermodynamics is called Landau theory [Landau (1937 [57]), Landau and Lifshitz (1958)[58]]. It aims to examine the relation between Gibbs free energy density and order parameter tensor and establishes an equation of state, hence, predicts the transition temperature T_c, above which the isotropic phase is stable and below which the nematic phase is stable.

3.1.2. Maier-Saupe theory

The theory that is based on the microscopic statistical model is called the theory of Maier and Saupe (1958,1959,1960)[59-61]. This theory tries to explain the phase transition in a nematic liquid crystal from a statistical perspective, and makes the following assumptions:

an attractive, orientation-dependent van der Waals interaction between molecules,

the configuration of the centres of mass is not affected by the orientational-dependent interaction,

the mean field approximation.

The experimental measurements of the order parameter in p-azoxyanisole (PAA) by McColl and Shih (1972a,b)[62],[63] also indicate that short-range repulsive forces are important, and van der Waals interaction can not explain the observed values of T_c. Therefore, Maier-Saupe theory is best viewed as a semi-phenomenological model.

3.1.3. Onsager theory

By considering a collection of orientable particles interacting pairwise through some potential $V(\mathbf{r}_1, \Omega_1; \mathbf{r}_2, \Omega_2)$ which depends on both position ($\mathbf{r}_1$, $\mathbf{r}_2$) and orientation (Ω_1, Ω_2), Onsager (1949 [64] showed how the Mayer cluster theory (1958) [65] may be used to give an expansion for the equation of state of this system, therefore to calculate the phase transition temperature. The solutions are qualitatively similar to those of the Maier-Saupe equation, but the principal remaining difference is that the Maier-Saupe theory is commonly applied to liquids only slightly compressible, whereas the Onsager expansion is most appropriately applied to dilute suspensions of particles for which the change in free energy with density is relatively small. Therefore the Onsager theory predicts large changes in density at the transition, as is appropriate to such systems.

3.2. Curvature elasticity theory – continuum elastic theory

Our aim is to use the computer to model the behaviour of the director field and the potential field in a liquid crystal materials,

3.2.1. Curvature strains

In a given microscopic region of a liquid crystal, there is a definite preferred axis along which the molecules orient themselves. Even in equilibrium the direction of this axis can vary from place to place, and it can be forced to vary by the action of external forces and boundary conditions. The deformation of relative orientations away from the equilibrium position is referred to as *curvature strain* and the restoring forces which attempt to oppose these deformation is referred to as *curvature stress* or *torques*. Normally, in liquid crystals, these changes in molecular orientation vary slowly in space relative to the molecular distance scale. Therefore the response of the liquid crystal can be treated within the framework of continuum elastic theory as originated by Zocher (1933) [66], Oseen(1933) [31], and Frank (1958) [32].

Due to sufficiently small curvature strains occurring in the liquid crystals, the Hooke's law applies, i.e., the stresses are proportional to the strains. In other words, free energy density is a quadratic function of the curvature strains.

Consider a uniaxial liquid crystal and let n(**r**) be a unit vector giving the direction of the preferred orientation at the point **r**, i.e., so-called *director*, and being parallel to the *z* axis, then six components of curvature at this point can be defined as

splay: $s_1 = \partial n_x/\partial x, \quad s_2 = \partial n_y/\partial y$

twist: $t_1 = -\partial n_y/\partial x, \quad t_2 = \partial n_x/\partial y$ (7)

bend: $b_1 = \partial n_x/\partial z, \quad b_2 = \partial n_y/\partial z$

The meaning of those three types of elastic deformations are shown in the Figure 10

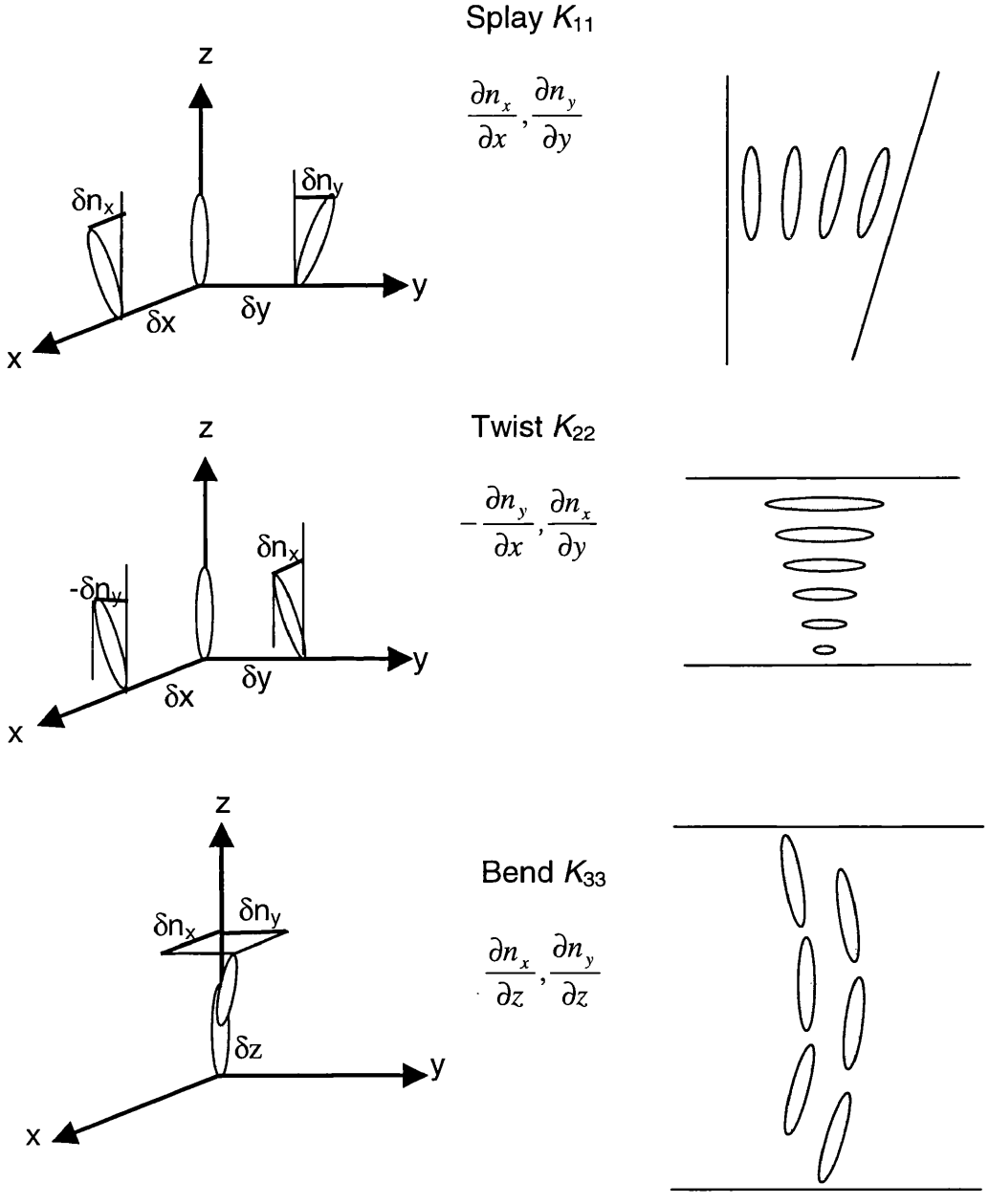

Figure 10 Splay, twist, and bend - meanings of their definitions

3.2.2. Free energy

(i) General expression

Oseen [31] assumed that energy in the liquid crystal can be written as the sum of pairwise interactions of molecules. This pair interaction depends on the relative orientations of the two molecules. This is similar to the approach in which Cauthy first considered the elastic theory of solids, whereas Frank [32] based the theory of curvature elastic energy on the symmetry properties of the liquid crystal alone.

As the Gibbs free energy density f_d is a function of director $\mathbf{n}(\mathbf{r})$, i.e., $f_d = f_d[\mathbf{n}(\mathbf{r})]$, functional expansion with respect to $\mathbf{n}(\mathbf{r})$ can be performed on f:

$$f_d = f_d^0(\mathbf{n}^0) + \nabla f_d \bullet (\mathbf{n}-\mathbf{n}^0) + \frac{1}{2}\nabla\nabla f_d : (\mathbf{n}-\mathbf{n}^0)(\mathbf{n}-\mathbf{n}^0) + \cdots$$

$$= f_d^0[\mathbf{n}^0(\mathbf{r}^0)] + \nabla f_d \bullet [\mathbf{n}(\mathbf{r})-\mathbf{n}^0(\mathbf{r}^0)] + \frac{1}{2}\nabla\{\nabla f_d \bullet [\mathbf{n}(\mathbf{r})-\mathbf{n}^0(\mathbf{r}^0)]\} \bullet [\mathbf{n}(\mathbf{r})-\mathbf{n}^0(\mathbf{r}^0)] \quad (8)$$

where $\mathbf{n}^0(\mathbf{r}^0)$ denotes a deformation-free configuration of the director field distribution; f_d^0 is the corresponding energy density or background energy density that does not interest us; and $\nabla f = \left(\frac{\partial}{\partial n_x}, \frac{\partial}{\partial n_y}, \frac{\partial}{\partial n_z}\right) f\Big|_{\mathbf{n}=\mathbf{n}^0}$ where ∇ only acts on f.

Now expand $\mathbf{n}(\mathbf{r})$ around $\mathbf{r}^0$ to the first order and keep in mind that $n_z(\mathbf{r})=1$ (uniaxial symmetry around z):

$$\mathbf{n}(\mathbf{r}) = \mathbf{n}^0(\mathbf{r}^0) + (\nabla_r \mathbf{n}) \bullet (\mathbf{r}-\mathbf{r}^0) = \mathbf{n}^0(\mathbf{r}^0) + (\nabla_r \mathbf{n}) \bullet \delta\mathbf{r} \quad (9)$$

Inserting Eq. (9) to Eq. (8) and making use of Eq. (7), Gibbs free energy density f of a liquid crystal, relative to its free energy density $f_d^0(\mathbf{n}^0)$ in the state of uniform orientation (which is not necessarily the equilibrium conformation), can be expressed in term of the six curvature strains as defined in Eq. (7)

$$f_d = \sum_{i=1}^{6} K_i a_i + \frac{1}{2}\sum_{i,j=1}^{6} K_{ij} a_i a_j \quad (10)$$

where K_i and K_{ij} $(=K_{ji})$ are the expansion coefficients, i.e., curvature elastic constant and $a_1 = s_1, a_2 = t_2, a_3 = b_1, a_4 = -t_1, a_5 = s_2, a_6 = b_2$

Because the energy density f_d is invariant under rotation about z due to the uniaxiality of the liquid crystal, there are only two independent moduli K_i, and five independent K_{ij}. Consequently, the expression (10) for the free energy density now reduces to (Frank, 1958)[32]

$$\begin{aligned} f_d = {} & K_1(s_1 + s_2) + K_2(t_1 + t_2) + \tfrac{1}{2}K_{11}(s_1 + s_2)^2 \\ & + \tfrac{1}{2}K_{22}(t_1 + t_2)^2 + \tfrac{1}{2}K_{33}(b_1^2 + b_2^2) \\ & + K_{12}(s_1 + s_2)(t_1 + t_2) \\ & - (K_{22} + K_{24})(s_1 s_2 + t_1 t_2) \end{aligned} \tag{11}$$

Here $(s_1 s_2 + t_1 t_2) = \dfrac{\partial}{\partial x}\left(n_x \dfrac{\partial n_y}{\partial y}\right) - \dfrac{\partial}{\partial y}\left(n_x \dfrac{\partial n_y}{\partial x}\right)$ appearing in the last term above only contributes surface energies (Ericken, 1962) [67] and can be dropped if only the properties of the bulk liquid crystal are considered. Eq. (11) gives the most general dependence of the free energy on the curvature strains in a uniaxial liquid crystal.

(ii) Special form for nematic phase

Because the nematic liquid crystal lacks polarity, i.e., the head-tail symmetry (**n** equivalent to –**n**), that requires that K_1=K_{12}=0; and enantiomorphy, i.e., the mirror symmetry , that means K_2=K_{12}=0. As a result, the elastic free energy density takes the following simple form:

$$f_d = \tfrac{1}{2}\left[K_{11}(s_1 + s)^2 + K_{22}(t_1 + t_2)^2 + K_{33}(b_1^2 + b_2^2)\right] \tag{12}$$

Using Eq. (7), and after some algebraic manipulation [31],[32],[51],[52],[68],[69] the above expression can be rewritten to be:

$$f_d = \frac{1}{2}\left[K_{11}(\nabla \bullet \mathbf{n})^2 + K_{22}(\mathbf{n} \bullet \nabla \times \mathbf{n})^2 + K_{33}(\mathbf{n} \times \nabla \times \mathbf{n})^2\right] \tag{13}$$

(iii) Contribution due to an external field

So far only the free energy due to elastic deformation is considered. The presence of an applied electric field results in an additional term to the free energy density (13)

$$f_e = -\varepsilon_0\left[\Delta\varepsilon(\mathbf{n} \bullet \mathbf{E})^2 + \varepsilon_\perp(\mathbf{E} \bullet \mathbf{E})\right] \tag{14}$$

where ε_0 is the vacuum permittivity; $\Delta\varepsilon=\varepsilon_{\parallel}-\varepsilon_{\perp}$, is a measurement of dielectric anisotropy, as $\varepsilon_{\parallel}$ and $\varepsilon_{\perp}$ are, respectively, the permittivities parallel and perpendicular to the director vector **n**; **E** is the applied electric field vector.

(iv) Total energy

The total free energy is the volume integral of the sum of deformation-related energy density (13) and the electric field-induced energy density (14):

$$F = F_d + F_e = \frac{1}{2}\int_v \{K_{11}(\nabla \bullet \mathbf{n})^2 + K_{22}(\mathbf{n} \bullet \nabla \times \mathbf{n})^2 + K_{33}(\mathbf{n} \times \nabla \times \mathbf{n})^2 - \varepsilon_0[\Delta\varepsilon(\mathbf{n} \bullet \mathbf{E})^2 + \varepsilon_{\perp}(\mathbf{E} \bullet \mathbf{E})]\}dV \quad (15)$$

This is so-called Oseen-Frank free-energy equation. It is a static model and also it is the starting point of static analysis of liquid crystal properties.

3.3. Energy approach – steady state

The model which is based on the above free energy expression (15) is called steady state model or static model because it does not depend on the time and minimisation of the total energy gives rise to an equilibrium state of liquid crystal. From this equilibrium state, director and potential fields can be found by numerically solving this equation. With the detailed knowledge of director orientation and the potential distribution, the defect structure of the liquid crystal can be revealed, the optical properties can be predicted, and charge and capacitance can be examined.

3.4. Dynamic model

The limitation to the static model lies in that it cannot yield any dynamic information about the evolution of the system with time. Therefore dynamic behaviour of liquid crystal displays, e.g., switch response time, pre-stable-state transit behaviour of optical properties cannot be explored. Those motivations require establishing a dynamic model.

3.4.1. Single elastic constant formulation

A single elastic constant dynamic equation of change for the director for nematic liquid crystals is given by Kilian and Hess [15].

$$\sum_{\nu=1}^{3} n_\nu \left[\gamma \frac{\partial}{\partial t}\left(n_\nu n_\mu\right) - K\nabla^2\left(n_\nu n_\mu\right) - \varepsilon_0 \Delta\varepsilon E_\nu E_\mu \right] = 0 \qquad (16)$$

where γ is the rotational viscosity and $\nabla^2=\partial_\alpha\partial_\alpha$ is the Laplacian operator. This is a tensorial expression. A vectorial expression can also be written:

$$\gamma \frac{\partial n_\mu}{\partial t} - K\nabla^2 n_\mu - \varepsilon_0 \Delta\varepsilon \sum_{\nu=1}^{3} n_\nu E_\nu E_\mu = 0 \qquad (17)$$

In practice, only expression (16), rather than expression (17), is useful for the numerical calculation because the former maintains the nematic symmetry (i.e., head-tail symmetry) whereas the latter does not when conducting the spatial discretization. This aspect can be seen from the form of constituent of Eq. (16) as well – it takes the form of *nn*.

3.4.2. Three elastic constant formulation

The above single elastic constant dynamic equation for the director (16) is simple to implement. It is an approximation to the real situation where three elastic constants are involved. In what follows, it is going to show that single elastic constant equation (16) is special case of three-elastic constant formulation under the condition of $K_{11} \equiv K_{22} \equiv K_{33}$. Therefore it cannot describe the supertwisted nematic LCD or other interesting cases where the ratios of K_{33}/K_{11} and K_{22}/K_{11} are far from 1. Even in the normal case of nematic LCD the values of the elastic constant can be, for example, $K_{11}=13.2\times10^{-12}$N, $K_{22}=6.5\times10^{-12}$N, $K_{33}=18.3\times10^{-12}$N. Therefore it is quite necessary to have a three-elastic constant dynamic model to analyse accurately the LCDs. In this section, a complete effort is dedicated to derive a three-elastic constant dynamic model for the director evolution in tensorial form.

(i) The limitation of single constant tensorial equation

A single elastic constant tensorial equation (16) for the director field $\{n_\nu\}$ evolution in time is derived by Kilian and Hess [15], [70]. It is based on the coupled non-linear relaxation equations for the alignment tensor [51], [52], [68], [71-78], which are

obtained within the framework of irreversible thermodynamics [70], [73], [74], [79], [80] by starting from a generalized Fokker-Planck equation [74], [81] in order to acquire a unified treatment of non-equilibrium phenomena in the isotropic and the nematic phase. For the sake of simplicity, let us drop the summation sign and assume that the repeated indices is to be understood as a summation unless otherwise stated. The equation (16) can be rewritten as

$$n_\mu\left[\gamma\frac{\partial}{\partial t}(n_\mu n_\nu)-K\nabla^2(n_\mu n_\nu)-\varepsilon_0\Delta\varepsilon E_\mu E_\nu\right]=0 \tag{18}$$

Here K is the Frank elastic constant; $\nabla^2=\partial_\alpha\partial_\alpha$ is the Laplacian operator $n_{\mu(\nu)}$ are the Cartesian components of the directors n, describing the average orientation of a molecule, confined to $n_\mu n_\mu=1$ and $E_{\mu(\nu)}$ are the components of the applied electric field **E**, $\mu,\nu=(1,2,3)$ or, (x, y, z); γ is Leslie's coefficient, i.e., the rotational viscosity; ε_0 is the vacuum permittivity; $\Delta\varepsilon=\varepsilon_\parallel-\varepsilon_\perp$, a measurement of the dielectric anisotropy, as $\varepsilon_\parallel$ and $\varepsilon_\perp$ are, respectively, the permittivities parallel and perpendicular to **n**.

For simplicity of numerical calculations, the assumption $K_{11}=K_{22}=K_{33}=K$ has been made. However, this is not actually true in real materials. One finds various elastic coefficient ratios[68], [82], [83]. For example, MBBA at 23° reveals $K_{33}/K_{11}=1.4$ and $K_{33}/K_{22}=2.2$ [82] and p-azoxyanisole or methyloxyazooxybenzene (PAA) at 120° has $K_{33}/K_{11}=1.9$ and $K_{33}/K_{22}=3.0$ [83] etc.. As it will be shown later, the single elastic constant turns out to be K_{22} when $K_{11}=K_{22}=K_{33}$. In order to take all elastic constants into account, one should start from Oseen-Frank static formulation [31], [32], [50] for free-energy density, which consists of the elastic interaction of the LC molecules and the applied field

$$F_g=\tfrac{1}{2}K_{11}(\nabla\bullet\boldsymbol{n})^2+\tfrac{1}{2}K_{22}(\boldsymbol{n}\bullet\nabla\times\boldsymbol{n})^2+\tfrac{1}{2}K_{33}(\boldsymbol{n}\times\nabla\times\boldsymbol{n})^2$$
$$+(2\pi/\xi)K_{22}(\mathbf{n}\bullet\nabla\times\mathbf{n})-\underbrace{\tfrac{1}{2}\varepsilon_0\left[\Delta\varepsilon(\mathbf{n}\bullet\mathbf{E})^2+\varepsilon_\perp(\mathbf{E}\bullet\mathbf{E})\right]}_{=\frac{1}{2}\mathbf{D}\bullet\mathbf{E}=\frac{1}{2}\varepsilon_0\mathbf{E}\bullet\bar{\bar{\varepsilon}}\bullet\mathbf{E}} \tag{19}$$

with

$$\varepsilon_{\alpha\beta}=\varepsilon_\perp\delta_{\alpha\beta}+\Delta\varepsilon n_\alpha n_\beta,\ \alpha,\beta=x,\ y,\ z \text{ or } 1,2,3 \tag{20}$$

Here K_{11}, K_{22}, K_{33} are Frank's three elastic constants which are, respectively, associated with the splay, twist, and bend deformations [50]; ξ is the cholesteric pitch

($\xi=\infty$ for nematic LC); $\bar{\bar{\varepsilon}}$ is a dielectric tensor whose components are of form (20); and the rest of quantities have the same meanings as given following Eq. (18).

(ii) The spatial discretisation of three constant static formulation does not conserve the head-tail symmetry of director field

Although the above equation contains all information about elastic deformations, it turns out that a straight forward discretisation of the spatial derivations in (19) leads to a loss of the head-tail-symmetry, which means that **n** is no longer physically equivalent to –**n** [15],[24]. For example, let us examine the following term that stems from the finite difference discretisation of first term on the right-hand side of the expression (19): $\partial_x n_x(i,j,k) = [n_x(i+1,j,k) - n_x(i-1,j,k)]/(2\delta x)$. When the sign of either term on the right-hand side is reversed, it is found that the left-hand side will no longer be equal to the right-hand side. In order to obtain an equation that describes the director field evolution and distribution, not only containing all three elastic constants, but also preserving head-tail symmetry, one should seek a different form of the expression for the free-energy.

(iii) Tensor representation of strain energy

(a) Second-rank tensor order parameter

First of all, for the characterization of the orientational order, two aspects have to be taken into account: the local preferred direction **n**(**r**) and the amount of ordering, i.e., the distribution of the long molecular axes around **n**. In order to construct an order parameter suppose one can define a unit vector $\hat{a}(\mathbf{r})$, describing the orientation of the long axis of a molecule at the site **r**. In that case, one should imagine the molecules to be rod-like entities. Now, consider the thermal average of various tensors, that are composed of $\hat{a}$, over a small but macroscopic volume around the point **r**. As the average $<\hat{a}\bullet\hat{a}>$ is a constant by definition, it is clear that a scalar order parameter (tensor order parameter of *rank zero*) is out of the question. Next, one might try a vector order parameter $<\boldsymbol{a}>$ (tensor order parameter of *rank one*), analogous to the magnetization in a ferromagnet. However, a non-zero value of $<\boldsymbol{a}>$ would violate the equivalence of **n** and –**n** as shown in Refs.[13], [15], [16]. Accordingly, in order to

avoid contradictions, one has to use the concept of director very carefully. For a proper description one must turn to the next possibility, i.e., a *second-rank* tensor, which is associated with the optical anisotropy (birefringence) of a liquid and it is the most relevant type of alignment for a liquid crystal [50-52], [68], [70]

(b) Construction of macroscopic tensor order parameter [69]

All liquid crystalline states are characterised by an orientational order of the molecules. In fact, this is the only aspect in which the nematic and isotropic phase differ. As discussed above, the orientational order must be described by a tensor of the second rank. Now a macroscopic approach is presented to construct the second-rank order parameter independent of any assumption regarding the interactions of the constituent molecules. A tensor order parameter can be obtained in the following way. Imagine that application of some field $\boldsymbol{X}$ results in a response $\boldsymbol{Y}$ of the system given by

$$Y_\alpha = T_{\alpha\beta} X_\beta \tag{21}$$

where $T_{\alpha\beta}$, is a symmetric tensor, i.e., $T_{\alpha\beta}=T_{\beta\alpha}$, and X_α and Y_α denote the components of $\boldsymbol{X}$ and $\boldsymbol{Y}$, respectively, in a given co-ordinate system. As an example $\boldsymbol{X}$ and $\overline{\overline{\boldsymbol{T}}}$ may represent respectively the external magnetic field $\boldsymbol{B}$ and the susceptibility tensor χ; then $\mu_0^{-1} Y$ is the magnetization $\boldsymbol{M}$, where μ_0 denotes the permeability of the vacuum. Clearly $\overline{\overline{\boldsymbol{T}}}$ is diagonal in a properly chosen co-ordinate system, i.e.,

$$\overline{\overline{\boldsymbol{T}}} = \begin{bmatrix} T_1 & 0 & 0 \\ 0 & T_2 & 0 \\ 0 & 0 & T_3 \end{bmatrix} \tag{22}$$

The tensor order parameter is obtained by extracting the *anisotropic* part of $\overline{\overline{\boldsymbol{T}}}$. This can be accomplished by putting $\sum_{i=1}^{3} T_i = T$ and then expressing the elements T_1, T_2, and T_3 as

$$\begin{aligned} T_1 &= (1/3)\, T(1-S_1+S_2) \\ T_2 &= (1/3)\, T(1-S_1-S_2) \\ T_3 &= (1/3)\, T(1+2S_1) \end{aligned} \tag{23}$$

According to Eq. (23) the diagonalized version of the tensor $\overline{\overline{\boldsymbol{T}}}$ can be constructed as

$$T_{\alpha\beta} = T\left(\tfrac{1}{3}\delta_{\alpha\beta} + Q_{\alpha\beta}\right) \tag{24}$$

Where a tensor $\overline{\overline{Q}}$ with element $Q_{\alpha\beta}$ is defined and called *tensor order parameter*, $\delta_{\alpha\beta}$ is the Kronecker δ symbol which equals 1 if $\alpha=\beta$ and 0 otherwise. The diagonal representation of the tensor order parameter is given by

$$\overline{\overline{Q}} = \begin{bmatrix} -\frac{1}{3}(S_1 - S_2) & 0 & 0 \\ 0 & -\frac{1}{3}(S_1 + S_2) & 0 \\ 0 & 0 & \frac{2}{3}S_1 \end{bmatrix} \tag{25}$$

The tensor $\overline{\overline{Q}}$ is called the tensor order parameter because of the appearance of the two-order parameter S_1 and S_2. Obviously, it is traceless, i.e., $\sum_{\alpha=1}^{3} Q_{\alpha\alpha} = 0$. As expected, when $S_1=S_2=0$, all elements of the tensor order parameter $\overline{\overline{Q}}$ become zero, this exactly corresponds to an isotropic state of a liquid crystal – the anisotropy should not exist! For the anisotropic liquid with uniaxial symmetry, only one order parameter is required in order to describe its state. That is $S_1 \neq 0$ and $S_2=0$ if the unique axis is conventionally chosen along the basis vector e_3, i.e., z-axis. In this case,

$$\overline{\overline{Q}} = \begin{bmatrix} -\frac{1}{3}S_1 & 0 & 0 \\ 0 & -\frac{1}{3}S_1 & 0 \\ 0 & 0 & \frac{2}{3}S_1 \end{bmatrix} \tag{26}$$

Changing the uniaxial symmetry into a biaxial can be achieved by including the second independent order parameter S_2 as shown in Eq. (25).

(c) The general expression for the tensor order parameter

The general expression for the tensor order parameter is obtained by an arbitrary rotation of the co-ordinate system. The starting point is a Cartesian co-ordinate system with basis vectors $\bar{e}_\alpha$ giving rise to a diagonal representation of the tensor order parameter. The elements of this representation are $\overline{Q}_{\alpha\beta}$, already given by Eq. (25) [to avoid notational confusion, a single bar is added to each element of $\overline{\overline{Q}}$ in Eq. (25) with basis vectors $\bar{e}_\alpha$, and elements $Q_{\alpha\beta}$ *without* bar denote the to-be-derived general tensor order parameter $\boldsymbol{Q}$]. Next an arbitrary rotation is carried out leading to a co-ordinate system with basis vector e_α. Now the elements $Q_{\alpha\beta}$ of the tensor $\overline{\overline{Q}}$, with respect to the new co-ordinate system, are given by

$$Q_{\alpha\beta} = \sum_{\gamma,\delta=1}^{3} \overline{R}_{\alpha\gamma} \overline{Q}_{\gamma\delta} \overline{R}_{\delta\beta} \tag{27}$$

Using $\overline{R}_{\alpha\beta} = \boldsymbol{e}_\alpha \bullet \bar{\boldsymbol{e}}_\beta$ and Eq. (25), it follows directly that

$$Q_{\alpha\beta} = -\tfrac{1}{3}(S_1 - S_2)(\boldsymbol{e}_\alpha \bullet \bar{\boldsymbol{e}}_1)(\boldsymbol{e}_\beta \bullet \bar{\boldsymbol{e}}_1) - \tfrac{1}{3}(S_1 + S_2)(\boldsymbol{e}_\alpha \bullet \bar{\boldsymbol{e}}_2)(\boldsymbol{e}_\beta \bullet \bar{\boldsymbol{e}}_2) + \tfrac{2}{3} S_1 (\boldsymbol{e}_\alpha \bullet \bar{\boldsymbol{e}}_3)(\boldsymbol{e}_\beta \bullet \bar{\boldsymbol{e}}_3) \tag{28}$$

This is the general expression of the tensor order parameter for a biaxial medium. It is symmetric and traceless. A considerable simplification of this expression is obtained if the restriction is made to *nematics* with *uniaxial* symmetry. In this case, the direction of the unique axis, which is given by the director **n**, coincides with one of the basis vectors belonging to the Cartesian co-ordinate system in which $\overline{\overline{\boldsymbol{Q}}}$ is diagonal. Conventionally, one chooses that $\mathbf{n} = \bar{\boldsymbol{e}}_3$ or $\mathbf{n} = -\bar{\boldsymbol{e}}_3$, i.e., S_2=0. Thus, Eq. (28) reduces to

$$\begin{aligned} Q_{\alpha\beta} &= -\tfrac{1}{3} S_1 (\boldsymbol{e}_\alpha \bullet \bar{\boldsymbol{e}}_\gamma)(\boldsymbol{e}_\beta \bullet \bar{\boldsymbol{e}}_\gamma) + S_1 (\boldsymbol{e}_\alpha \bullet \mathbf{n})(\boldsymbol{e}_\beta \bullet \mathbf{n}) \\ &= S_1 \left(n_\alpha n_\beta - \frac{1}{3} \delta_{\alpha\beta} \right) \end{aligned} \tag{29}$$

Here expressions of $(\boldsymbol{e}_\alpha \bullet \bar{\boldsymbol{e}}_\gamma)(\boldsymbol{e}_\beta \bullet \bar{\boldsymbol{e}}_\gamma) = \overline{R}_{\alpha\gamma} \overline{R}^{-1}_{\gamma\beta} = \delta_{\alpha\beta}$ and $(\boldsymbol{e}_\alpha \bullet \mathbf{n}) = n_\alpha$ are used.

(d) Tensor representation of strain energy

Because the tensor order parameter (29) contains a component ($n_\alpha n_\beta$) of a dyad **nn**, inverting the sign of **n** to –**n** leaves it invariant, i.e., head-tail symmetry of the director **n** is preserved. Therefore, it can be used as a good independent variable to expand the free-energy (19) for a uniaxial nematic or cholesteric system. [52], [68], [72], [84-86]. By disregarding the coupling effect with the flow field and surface term by which the static equilibrium configurations surrounded by boundaries of pre-determined orientation are not affected, and including *one* third order term in $\boldsymbol{Q}$ that removes the degeneracy between K_{11} and K_{33}, i.e., differentiates between K_{11} and K_{33} [84] the expanded expression for the static strain energy for uniaxial alignment in terms of $\boldsymbol{Q}$ in the second order is given by [16], [84], [85]

$$\begin{aligned} F_g = &\left(-\frac{K_{11}}{12} + \frac{K_{22}}{4} + \frac{K_{33}}{12} \right) Q_{\alpha\beta,\gamma} Q_{\alpha\beta,\gamma} + \left(\frac{K_{11} - K_{22}}{2} \right) Q_{\alpha\beta,\beta} Q_{\alpha\gamma,\gamma} \\ &+ \left(\frac{K_{33} - K_{11}}{4} \right) Q_{\alpha\beta} Q_{\gamma\lambda,\alpha} Q_{\gamma\lambda,\beta} - \left(\frac{2\pi}{\xi} \right) K_{22} e_{\alpha\beta\gamma} Q_{\alpha\lambda} Q_{\beta\lambda,\gamma} \end{aligned}$$

$$-\frac{1}{2}\varepsilon_0\bar{\varepsilon}E_\alpha E_\alpha - \frac{1}{2}\varepsilon_0\Delta\varepsilon E_\alpha E_\beta Q_{\alpha\beta} \tag{30}$$

Here $\bar{\varepsilon} = \dfrac{2\varepsilon_\perp + \varepsilon_{//}}{3}$, the average of the diagonal elements of dielectric tensor $\bar{\bar{\varepsilon}}$ that describes a uniaxial symmetry; the electric field energy has been split into two parts, one is related to the electric field only, independent of the liquid crystal molecular orientation, and the other is directly proportional to the tensor order parameter $\boldsymbol{Q}$, which contains all information about the anisotropy of liquid crystal system. The subscript after a comma in $Q_{\alpha\beta,\gamma}$ represents differentiation with respect to the corresponding rectangular co-ordinate, i.e., $Q_{\alpha\beta,\gamma} = \partial_\gamma Q_{\alpha\beta,} = \nabla_\gamma Q_{\alpha\beta}$. e_{ijk} is the Levi-Civita symbol. It is a perfect antisymmetric tensor, which gives 0 if two or more subscripts are equal, 1 if they are in the order 123, 231, or 312, and –1 otherwise.

(iv) Derivation of tensorial expression for director dynamics with three elastic coefficients

(a) Euler-Lagrange Equation in term of director field {n}

The expression (19) for static specific free-energy F_g is the sum of elastic deformation energy and applied field energy. In fact, it is called Gibbs free-energy density [77], [86]. It is a functional of director field $\{n_\alpha\}$ and its spatial derivatives $\{\partial_\beta n_\alpha = n_{\alpha,\beta}\}$ as well as derivatives of potential field $\{\partial_\alpha V\}$, whereas **n** field and V field are functions of spatial position **r** and time t in general (dynamic). Only if the system stays on a stationary state, are they independent of time t (static). On this state, we have

$$\delta\mathcal{F}_g = 0, \qquad \mathcal{F}_g = \int F_g dv, \qquad F_g = F_s - F_e \tag{31}$$

Where $\mathcal{F}_g$ is the Gibbs free-energy and F_g is its density given by Eq. (19); F_s and F_e represent the strain field related part and the external field related part respectively.

Performing variation of F_g with respect to $\{n_\nu\}$ and its spatial derivatives $\{\partial_\lambda n_\nu\}$ as well as the spatial derivatives of $\{\partial_\lambda V\}$, and then carrying out the integration by parts, give rise to the Euler-Lagrange equations for potential field $\{\phi\}$ and director field $\{\mathbf{n}\}$

$$\partial_\alpha\left(\varepsilon_0\varepsilon_{\alpha\beta}\partial_\beta\phi\right) = 0 \tag{32}$$

$$\frac{\partial F_g}{\partial n_\nu} - \partial_\alpha \frac{\partial F_g}{\partial n_{\nu,\alpha}} = 0 \tag{33}$$

Where $\partial_\alpha = \nabla_\beta$ denotes differentiation with respect to the corresponding rectangular co-ordinate and $n_{\nu,\alpha}\ \partial_\alpha n_\nu = \nabla_\alpha n_\nu$.

Eqs. (32) and (33) provide four scalar partial differential equations. In principle, they can be solved for the unknown functions: ϕ, n_x, n_y, n_z. This leads to a static solution. It is preferable however, to look for a dynamic solution for which the static solution is a particular case. Consequently, we have to introduce a dynamic term in Eq. (33). Considering only the rotational viscosity γ_1 and neglecting flow effects, we have

$$\gamma_1 \frac{\partial}{\partial t} n_\nu + \frac{\partial F_g}{\partial n_\nu} - \partial_\lambda \frac{\partial F_g}{\partial n_{\nu,\lambda}} = 0 \tag{34}$$

However, if we directly insert equation (19) in the above expression, what we will get is a vectorial equation for **n**, that will break head-tail symmetry of director when carrying out the spatial discretisation [15], [16], [24]. In order to avoid this, we are bound to use the tensorial expression (30) for F_g, the Frank free energy, that will conserve the nematic symmetry.

(b) Euler-Lagrange Equation in terms of tensor order parameter *Q*

Since the Frank free energy (30) is now a functional of $\boldsymbol{Q}$, the second-rank tensor order parameter (a function of **n**), by following a procedure similar to the above, we perform the variations of F_g with respect to $\{Q_{\alpha\beta}\}$ and its spatial derivatives of $\{Q_{\alpha\beta,\lambda}\}$ first, then do the derivatives $\{Q_{\alpha\beta}\}$ and $\{Q_{\alpha\beta,\lambda}\}$ with respect to $\{n_\nu\}$ – a function of **r**, and finally carrying out integration by parts, we get

$$\gamma_1 n_\mu \frac{\partial}{\partial t} Q_{\mu\nu} + \left[\frac{\partial F_g}{\partial Q_{\alpha\beta}} - \partial_\lambda \frac{\partial F_g}{\partial Q_{\alpha\beta,\lambda}} \right] \frac{\partial Q_{\alpha\beta}}{\partial n_\nu} =$$

$$\gamma_1 n_\mu \frac{\partial}{\partial t} Q_{\mu\nu} + \left[\frac{\partial F_g}{\partial Q_{\alpha\beta}} - \partial_\lambda \frac{\partial F_g}{\partial Q_{\alpha\beta,\lambda}} \right] \left[n_\alpha \delta_{\beta\nu} + n_\beta \delta_{\alpha\nu} \right] = 0 \tag{35}$$

Here $n_\mu \frac{\partial}{\partial t} Q_{\mu\nu} = n_\mu \left(n_\mu \partial_t n_\nu + n_\nu \partial_t n_\mu \right) = \left(\underbrace{n_\mu n_\mu}_{=1} \right) \partial_t n_\nu + \frac{1}{2} n_\nu \partial_t \left(\underbrace{n_\mu n_\mu}_{=1} \right) = \frac{\partial}{\partial t} n_\nu$ has been used.

(c) Derivation of tensorial expression for director dynamics with three elastic coefficients

Now we are in position to derive the tensorial expression for director dynamics containing three elastic coefficients. Inserting Eq. (30) in the above differential equation and for simplicity, assuming perfect ordering, i.e., S_1=1 without loss of generality, after careful, and tedious algebraic manipulation, we finally arrive at the required tensorial equation that contains three constants and preserves the head-tail symmetry as follows:

$$n_\mu\Big\{\gamma_1\frac{\partial}{\partial t}\underbrace{(n_\mu n_\nu)}_{A}-K_{22}\underbrace{\partial_\alpha\partial_\alpha(n_\mu n_\nu)}_{B}-(K_{11}-K_{22})\underbrace{[\partial_\nu\partial_\lambda(n_\mu n_\lambda)+\partial_\mu\partial_\lambda(n_\nu n_\lambda)]}_{C}$$

$$-(K_{33}-K_{11})\underbrace{[(n_\lambda n_\beta)\partial_\beta\partial_\lambda(n_\mu n_\nu)+\partial_\lambda(n_\lambda n_\beta)\partial_\beta(n_\mu n_\nu)-\tfrac{1}{2}\partial_\mu(n_\lambda n_\beta)\partial_\nu(n_\lambda n_\beta)]}_{D}$$

$$+2q_0K_{22}\underbrace{[e_{\alpha\mu\lambda}\partial_\lambda(n_\alpha n_\nu)+e_{\alpha\nu\lambda}\partial_\lambda(n_\alpha n_\mu)]}_{E}-\varepsilon_0\Delta\varepsilon\underbrace{E_\mu E_\nu}_{F}\Big\}=0 \qquad (36)$$

Here q_0 =($2\pi/\xi$). Obviously, if K_{11}=K_{22}=K_{33}=K, then the above expression immediately reduce to the single-constant approximation (18) apart from the cholesteric term. Also, because director n appears in the above expression in the form of the pair ($n_\mu n_\nu$) everywhere, the spatial discretization would not destroy the nematic symmetry as discussed later on.

(v) Expansion of the tensorial equation

In order to carry out the numerical calculation we have to expand all repeated subscripts. Due to the complication of the equation (36), we shall do it term by term. They will be named $A_{\mu\nu}$, $B_{\mu\nu}$, $C_{\mu\nu}$, $D_{\mu\nu}$, $E_{\mu\nu}$, $F_{\mu\nu}$ to avoid writing extremely long expressions.

The first term is simple, as shown before:

$$n_\mu A_{\mu\nu}=\frac{\partial n_\nu}{\partial t} \qquad (37)$$

The second term:

$$
\begin{aligned}
n_\mu B_{\mu\nu} = {} & n_x\left[\frac{\partial^2}{\partial x^2}(n_x n_\nu)+\frac{\partial^2}{\partial y^2}(n_x n_\nu)+\frac{\partial^2}{\partial z^2}(n_x n_\nu)\right] \\
& + n_y\left[\frac{\partial^2}{\partial x^2}(n_y n_\nu)+\frac{\partial^2}{\partial y^2}(n_y n_\nu)+\frac{\partial^2}{\partial z^2}(n_y n_\nu)\right] \\
& + n_z\left[\frac{\partial^2}{\partial x^2}(n_z n_\nu)+\frac{\partial^2}{\partial y^2}(n_z n_\nu)+\frac{\partial^2}{\partial z^2}(n_z n_\nu)\right]
\end{aligned} \tag{38}
$$

The third term:

$$
\begin{aligned}
n_\mu C_{\mu\nu} = {} & n_x\left[\partial_\nu\partial_x(n_x n_x)+\partial_\nu\partial_y(n_x n_y)+\partial_\nu\partial_z(n_x n_z)\right] \\
& + n_y\left[\partial_\nu\partial_x(n_y n_x)+\partial_\nu\partial_y(n_y n_y)+\partial_\nu\partial_z(n_y n_z)\right] \\
& + n_z\left[\partial_\nu\partial_x(n_z n_x)+\partial_\nu\partial_y(n_z n_y)+\partial_\nu\partial_z(n_z n_z)\right]
\end{aligned} \tag{39}
$$

The fourth term which is the most complicated:

$$
\begin{aligned}
n_\mu D_{\mu\nu} = {} & n_x n_x n_x\partial_x\partial_x(n_x n_\nu)+n_x n_y n_y\partial_y\partial_y(n_x n_\nu)+n_x n_z n_z\partial_z\partial_z(n_x n_\nu) \\
& + n_y n_x n_x\partial_x\partial_x(n_y n_\nu)+n_y n_y n_y\partial_y\partial_y(n_y n_\nu)+n_y n_z n_z\partial_z\partial_z(n_y n_\nu) \\
& + n_z n_x n_x\partial_x\partial_x(n_z n_\nu)+n_z n_y n_y\partial_y\partial_y(n_z n_\nu)+n_z n_z n_z\partial_z\partial_z(n_z n_\nu) \\
& + 2n_x n_x n_y\partial_x\partial_y(n_x n_\nu)+2n_x n_x n_z\partial_x\partial_z(n_x n_\nu)+2n_x n_y n_z\partial_y\partial_z(n_x n_\nu) \\
& + 2n_y n_x n_y\partial_x\partial_y(n_y n_\nu)+2n_y n_x n_z\partial_x\partial_z(n_y n_\nu)+2n_y n_y n_z\partial_y\partial_z(n_y n_\nu) \\
& + 2n_z n_x n_y\partial_x\partial_y(n_z n_\nu)+2n_z n_x n_z\partial_x\partial_z(n_z n_\nu)+2n_z n_y n_z\partial_y\partial_z(n_z n_\nu) \\
& + n_x\partial_x(n_x n_x)\partial_x(n_x n_\nu)+n_x\partial_y(n_y n_x)\partial_x(n_x n_\nu)+n_x\partial_z(n_z n_x)\partial_x(n_x n_\nu) \\
& + n_x\partial_x(n_x n_y)\partial_y(n_x n_\nu)+n_x\partial_y(n_y n_y)\partial_y(n_x n_\nu)+n_x\partial_z(n_z n_y)\partial_y(n_x n_\nu) \\
& + n_x\partial_x(n_x n_z)\partial_z(n_x n_\nu)+n_x\partial_y(n_y n_z)\partial_z(n_x n_\nu)+n_x\partial_z(n_z n_z)\partial_z(n_x n_\nu) \\
& + n_y\partial_x(n_x n_x)\partial_x(n_y n_\nu)+n_y\partial_y(n_y n_x)\partial_x(n_y n_\nu)+n_y\partial_z(n_z n_x)\partial_x(n_y n_\nu) \\
& + n_y\partial_x(n_x n_y)\partial_y(n_y n_\nu)+n_y\partial_y(n_y n_y)\partial_y(n_y n_\nu)+n_y\partial_z(n_z n_y)\partial_y(n_y n_\nu) \\
& + n_y\partial_x(n_x n_z)\partial_z(n_y n_\nu)+n_y\partial_y(n_y n_z)\partial_z(n_y n_\nu)+n_y\partial_z(n_z n_z)\partial_z(n_y n_\nu) \\
& + n_z\partial_x(n_x n_x)\partial_x(n_z n_\nu)+n_z\partial_y(n_y n_x)\partial_x(n_z n_\nu)+n_z\partial_z(n_z n_x)\partial_x(n_z n_\nu) \\
& + n_z\partial_x(n_x n_y)\partial_y(n_z n_\nu)+n_z\partial_y(n_y n_y)\partial_y(n_z n_\nu)+n_z\partial_z(n_z n_y)\partial_y(n_z n_\nu) \\
& + n_z\partial_x(n_x n_z)\partial_z(n_z n_\nu)+n_z\partial_y(n_y n_z)\partial_z(n_z n_\nu)+n_z\partial_z(n_z n_z)\partial_z(n_z n_\nu)
\end{aligned}
$$

$$
\begin{aligned}
&-\tfrac{1}{2}n_x\partial_x(n_xn_x)\partial_\nu(n_xn_x)-\tfrac{1}{2}n_x\partial_x(n_yn_y)\partial_\nu(n_yn_y)-\tfrac{1}{2}n_x\partial_x(n_zn_z)\partial_\nu(n_zn_z)\\
&-\tfrac{1}{2}n_y\partial_y(n_xn_x)\partial_\nu(n_xn_x)-\tfrac{1}{2}n_y\partial_y(n_yn_y)\partial_\nu(n_yn_y)-\tfrac{1}{2}n_y\partial_y(n_zn_z)\partial_\nu(n_zn_z)\\
&-\tfrac{1}{2}n_z\partial_z(n_xn_x)\partial_\nu(n_xn_x)-\tfrac{1}{2}n_z\partial_z(n_yn_y)\partial_\nu(n_yn_y)-\tfrac{1}{2}n_z\partial_z(n_zn_z)\partial_\nu(n_zn_z)\\
&-n_x\partial_x(n_xn_y)\partial_\nu(n_xn_y)-n_x\partial_x(n_yn_z)\partial_\nu(n_yn_z)-n_x\partial_x(n_xn_z)\partial_\nu(n_xn_z)\\
&-n_y\partial_y(n_xn_y)\partial_\nu(n_xn_y)-n_y\partial_y(n_yn_z)\partial_\nu(n_yn_z)-n_y\partial_y(n_xn_z)\partial_\nu(n_xn_z)\\
&-n_z\partial_z(n_xn_y)\partial_\nu(n_xn_y)-n_z\partial_z(n_yn_z)\partial_\nu(n_yn_z)-n_z\partial_z(n_xn_z)\partial_\nu(n_xn_z)
\end{aligned}
\tag{40}
$$

The fifth term:

$$
\begin{aligned}
n_\mu E_{\mu\nu} &= n_x\partial_y(n_zn_\nu)-n_x\partial_z(n_yn_\nu)+n_y\partial_z(n_xn_\nu)-n_y\partial_z(n_zn_\nu)+n_z\partial_x(n_yn_\nu)-n_z\partial_y(n_xn_\nu)\\
&+\delta_{\nu x}\left[n_x\partial_y(n_zn_x)-n_x\partial_z(n_yn_x)+n_y\partial_y(n_zn_y)-n_y\partial_z(n_yn_y)+n_z\partial_y(n_zn_z)-n_z\partial_z(n_yn_z)_y\right]\\
&+\delta_{\nu y}\left[n_x\partial_z(n_xn_x)-n_x\partial_x(n_zn_x)+n_y\partial_z(n_xn_y)-n_y\partial_x(n_zn_y)+n_z\partial_z(n_xn_z)-n_z\partial_x(n_zn_z)\right]\\
&+\delta_{\nu z}\left[n_x\partial_x(n_yn_x)-n_x\partial(n_xn_x)+n_y\partial_x(n_yn_y)-n_y\partial_y(n_xn_y)+n_z\partial_x(n_yn_z)-n_z\partial_y(n_xn_z)\right]
\end{aligned}
\tag{41}
$$

The sixth term that involves interaction between external field **E** and the director field {**n**}

$$
n_\mu F_{\mu\nu} = n_xE_xE_\nu + n_yE_yE_\nu + n_zE_zE_\nu \tag{42}
$$

So far, a detailed derivation of three-elastic-constant dynamic equation (36) for the director has been completed and it has been shown that the single-elastic-constant expression (16) is a special case of it when $K_{11}\equiv K_{22}\equiv K_{33}$ as declared earlier. Because we are working with tensor representation, it is easy to verify that, either Eq. (16) or Eq. (36) retains the head-tail symmetry of the director **n**. In the following section, some numerical methods that are used for computer modelling are addressed.

4. Numerical calculation

Due to highly non-linear nature of Eq. (36), it is impossible to obtain an analytical solution for the director field and the potential distribution within the LC pixel under an external voltage. Therefore, numerical calculation becomes inevitable.

4.1. Computer simulation and finite element method

There is an increasing interest in numerical methods for engineering-related problems because it is not possible to obtain analytical solutions mathematically for many problems. An analytical solution is a mathematical expression that gives the values of the desired unknown quantity at any time-space point in the problem domain. However, analytical solutions can be obtained only for certain simple cases. For many mathematical physics problems involving complex material properties and boundary conditions, engineers have to resort to numerical methods that provide approximate, but physically acceptable solutions. In most of the numerical methods, the solutions yield approximate values of unknown quantities being found only at a discrete number of points in the domain. The process of selecting only a certain number of discrete points in the domain is called *discretization*. One of the ways to discretize a domain is to divide it into an equivalent system of smaller domains or units. The assemblage of such units then represents the original domain. Instead of solving the problem for the entire domain in one operation, the solutions are formulated for each constituent unit and combined to obtain the solution for the original domain. This approach is known as *going from part to the whole*. Although the analysis procedure is thereby considerably simplified, the amount of data to be handled depends on the number of subdivisions, and it is a formidable task to handle the volume of data manually. Consequently, Such a task must be handed to ever increasingly powerful computers to complete.

The finite element methods [87-89] are essentially a product of the computer age. It has developed simultaneously with the increasing use of high-performance computers and with the growing emphasis on numerical methods for engineering analysis. Although the approach shares many of the features common to the previous numerical approximations, it possesses certain characteristics that take advantage of the special facilities offered by high-speed computers. In particular, the method can be

systematically programmed to accommodate such complicated and difficult problems as inhomogeneous anisotropic materials, and complicated geometries and boundary conditions. It is difficult to accommodate these complexities in the methods mentioned above.

The finite element method was originally developed for structural analysis, the general nature of the theory on which it is based has also made possible its successful application for solutions of problems on other fields of engineering, such as heat flow, fluid dynamics as well as electromagnetics, etc.. As a result of this broad applicability and the systematic generality of the associated computer codes, the method has gained wide acceptance by researchers and designers.

4.2. Computer modelling

Due to dramatic increase in the capacities of CPU and the RAM, even now a home PC or a Laptop can have a > 500 MHz processor and 128 MB or higher RAM. That means a PC or a Laptop now can be used to carry out the same job as a traditional Unix based workstation does. Whereas the PC is much cheaper than a workstation. The hard disk capacity of a PC is no longer a problem. It can reach over 10 GB. Therefore, it is quite attractive now to use computer to do numerical calculations which demand large memory, fast speed and huge amount of data storage. In terms of LCD modelling, the advantages of using computer simulation have been pointed out before. In fact, computer modelling has become a very important tool for physicists, chemists, and engineers.

4.3. Numerical methods

Many numerical methods have been developed for use with fast computers. Different methods are devised for different mathematical physics and engineering problems. For a *deterministic* problem appearing in the classic Newtonian mechanics, the Molecular Dynamic (MD) approach has been used in order to monitor the movement of each particle comprising the system that obeys the Newtonian law of motion. The sum of each particle's behaviour contributes to the macroscopic physical properties of a system. For *probabilistic* problem such as in statistical mechanics, Monte Carlo (MC) method is employed to sample certain microscopic states of a particle or a system that obeys laws of statistical mechanics. An average over the large sampling gives the macroscopic properties of a system.

For the well-established macroscopic thermodynamic or fluid dynamics, every unknown physical quantity in the equation sets is global, but with restriction to the boundary conditions and initial conditions. In this case, the Finite Elements (FE) method is usually applied by subdividing a domain into units.

4.3.1. Spatial difference schemes

There are several schemes for approximating numerically the first and second derivatives and each provides a different order of accuracy. Commonly seen schemes of approximations are as follows:

(i) Forward difference for 1st derivatives, order of error: $O(\Delta x, \Delta y)$

$$\begin{cases} \left.\dfrac{\partial n}{\partial x}\right|_{l,m} \approx \dfrac{n_{l+1,m} - n_{l,m}}{\Delta x} \\ \left.\dfrac{\partial n}{\partial y}\right|_{l,m} \approx \dfrac{n_{l,m+1} - n_{l,m}}{\Delta y} \end{cases} \tag{43}$$

(ii) Backward difference for 1st derivatives, order of error: $O(\Delta x, \Delta y)$

$$\begin{cases} \left.\dfrac{\partial n}{\partial x}\right|_{l,m} \approx \dfrac{n_{l,m} - n_{l-1,m}}{\Delta x} \\ \left.\dfrac{\partial n}{\partial y}\right|_{l,m} \approx \dfrac{n_{l,m} - n_{l,m-1}}{\Delta y} \end{cases} \tag{44}$$

(iii) Central difference for 1st derivatives, order of error: $O(\Delta x^2, \Delta y^2)$

$$\begin{cases} \left.\dfrac{\partial n}{\partial x}\right|_{l,m} \approx \dfrac{n_{l+1,m} - n_{l-1,m}}{2\Delta x} \\ \left.\dfrac{\partial n}{\partial y}\right|_{l,m} \approx \dfrac{n_{l,m+1} - n_{l,m-1}}{2\Delta y} \end{cases} \tag{45}$$

(iv) Central difference for 2nd derivatives, order of error: $O(\Delta x^2, \Delta y^2)$

$$\begin{cases} \left.\dfrac{\partial^2 n}{\partial x^2}\right|_{l,m} \approx \dfrac{n_{l+1,m} - 2n_{l,m} + n_{l-1,m}}{\Delta x^2} \\ \left.\dfrac{\partial^2 n}{\partial y^2}\right|_{l,m} \approx \dfrac{n_{l,m+1} - 2n_{l,m} + n_{l,m-1}}{\Delta y^2} \end{cases} \tag{46}$$

The *central difference* which gives higher order of accuracy than *forward* or *backward* scheme is exploited for the discretisation of the first and second derivatives of director field $\{\mathbf{n}\}$ with respect to space positions $\mathbf{r}$. For determination of the potential field distribution, *finite element* method is employed along with variational technique.

4.3.2. The θ-method and time-stepping

(i) θ-method

θ-method [90],[91] is a very simple method designed for time-stepping or initial-value problems. It is the most widely used algorithm for the numerical solution of first order systems of equations. In fact, it is the basis for many numerical methods for solving non-linear first order problems [91]. Its mathematical formulation takes the following form:

$$\left.\frac{\partial n_\mu}{\partial t}\right|_{t+\theta\Delta t} = \frac{n_\mu(t+\Delta t) - n_\mu(t)}{\Delta t}$$

$$n_\mu(t+\theta\Delta t) = \theta n_\mu(t+\Delta t) + (1-\theta) n_\mu(t) \begin{cases} (a)\ n_\mu\left(t+\tfrac{1}{2}\Delta t\right) = \left[n_\mu(t+\Delta t) + n_\mu(t)\right]/2 \\ \qquad\qquad \text{for } \theta = \tfrac{1}{2} \Rightarrow \text{Crank - Nicolson} \\ (b)\ n_\mu(t) = n_\mu(\mathrm{t}) \text{ for } \theta = 0 \Rightarrow \text{Forward(Euler)} \\ (c)\ n_\mu(t+\Delta t) = n_\mu(\mathrm{t}+\Delta \mathrm{t}) \text{ for } \theta = 1 \Rightarrow \text{Backward} \end{cases} \tag{47}$$

where θ is a constant with range of $0 \le \theta \le 1$. From the above expression it can be seen that θ=0 corresponds to forward time difference with an error which is $O(\Delta t)$, θ=1/2 gives the Crank-Nicolson centred time difference [92] with the order of accuracy $O(\Delta t^2)$ and unconditional stability, while θ=1 is simply a backward time difference whose accuracy is same as forward difference. It has been shown that if θ≥0.5, θ-method provides unconditional stability [90-93].

If the differential equation has an oscillatory solution, e.g., in the case of damping less than critical, this method will give an oscillatory solution also [90-93].

Based on the consideration of higher accuracy and ensured stability without oscillatory situation involved in this work, the Crank-Nicolson method (i.e., choosing $\theta = 0.5$) is used to perform time stepping.

(ii) Crank-Nicolson central difference for 1st derivative, $O(\Delta t^2)$

$$\begin{cases} \left.\dfrac{\partial n}{\partial t}\right|_{t+\frac{1}{2}\Delta t} = \dfrac{n(t+\Delta t)-n(t)}{\Delta t} \\ n(t \pm \tfrac{1}{2}\Delta t) = \dfrac{n(t \pm \Delta t)+n(t)}{2} \end{cases} \tag{48}$$

Note that the Crank-Nicolson scheme essentially is a special case of general central difference when an intermediate point is considered as a value-taking point and in consequence, it gives a second order of accuracy. However, the most important advantage of Crank-Nicolson over the general central difference lies in that it can guarantee the numerical stability [90-93]. Because of this, it is used in this work to discretise the first derivative of director **n** with respect to time t

4.3.3. Variational principle

Some physics problems can be stated directly in the form of a variational principle. One example here is the minimization of the total potential, i.e., the electric field energy in the Oseen-Frank free energy expression (19) to determine a potential field that gives an equilibrium state of the LC system. In general, the variational principle involves determination of a function which makes a certain integral formulation (or functional) *stationary*. By using trial function or finite element method, one can make functional stationary with respect to variations in the unknown parameters.

(i) Natural variational procedure

Let a functional Π be of the following integral form:

$$\Pi(\phi) = \int_{\Omega} F\left(\phi, \frac{\partial \phi}{\partial x}, \cdots\right) d\Omega + \int_{\Gamma} G\left(\phi, \frac{\partial \phi}{\partial x}, \cdots\right) d\Gamma \tag{49}$$

where F and G are functions of trial function $\phi(x,\ldots)$ and its derivatives, and Γ is the curve bounding the closed region Ω. Now let us attempt to make Π stationary with respect to variations in ϕ among the admissible set of functions satisfying general boundary conditions as set below:

$$B_1(\phi) = 0 \quad \text{on } \Gamma_1 \tag{50}$$

$$B_2(\phi) = 0 \quad \text{on } \Gamma_2 \tag{51}$$

Where $\Gamma_1+\Gamma_2=\Gamma$. For a small admissible variation from ϕ to $\phi+\delta\phi$, the corresponding first variation in Π can be defined as

$$\delta\Pi = \int_{\Omega}\left[\frac{\partial F}{\partial \phi}\delta\phi + \frac{\partial F}{\partial(\partial\phi/\partial x)}\delta\left(\frac{\partial \phi}{\partial x}\right)\cdots\right]d\Omega$$

$$+\int_{\Gamma}\left[\frac{\partial G}{\partial \phi}\delta\phi + \frac{\partial G}{\partial(\partial\phi/\partial x)}\delta\left(\frac{\partial \phi}{\partial x}\right)\cdots\right]d\Gamma \tag{52}$$

and the stationarity of Π at ϕ then requires that [86]:

$$\delta\Pi = 0 \tag{53}$$

If, by suitable manipulation, Eq. (52) can be written

$$\delta\Pi = \int_{\Omega} A(\phi)\delta\phi\, d\Omega \tag{54}$$

since $\delta\phi$ is arbitrary, then the stationarity requirement of Eq. (53) shows that

$$A(\phi) = 0 \quad \text{in } \Omega \tag{55}$$

The above process is called *natural variational principle* or *procedure*. Its aim is to derive the differential equation (55) for ϕ under the boundary conditions of Eqs (50) and (51) that makes the functional $\Pi(\phi)$ of Eq. (49) stationary with respect to variations in ϕ among the set of functions satisfying the boundary conditions. Eq. (55) is termed the Euler equation corresponding to the variational principle which requires the stationary of Π. If the analytical solution cannot be obtained, then trial function or finite element method needs to be used to determine ϕ over the whole domain by numerically solving a sets of algebraic equations for the discretised $\{\phi_i\}$. It can be shown that for any variational principle of this form, a corresponding Euler equation can be established [88].

(ii) Application to Electric field energy

The expression (14) for the electric field energy can be rewritten as a well-known form that can be found in any textbook of electromagnetics:

$$F_e = -\frac{1}{2}\int_{\Omega} \mathbf{E} \bullet \mathbf{D} d\Omega \tag{56}$$

here **D** is called electric displacement vector and is related to the electric field vector **E** by

$$\mathbf{D} = \varepsilon_0 \bar{\bar{\varepsilon}} \bullet \mathbf{E} \tag{57}$$

where $\bar{\bar{\varepsilon}}$ is a 3×3 relative dielectric tensor as defined in Eq. (20). In its explicit form for a uniaxial nematic LC, the full components are given by

$$\bar{\bar{\varepsilon}} = \begin{bmatrix} \varepsilon_\perp + \Delta\varepsilon n_x n_x & \Delta\varepsilon n_x n_y & \Delta\varepsilon n_x n_z \\ \Delta\varepsilon n_y n_x & \varepsilon_\perp + \Delta\varepsilon n_y n_y & \Delta\varepsilon n_y n_z \\ \Delta\varepsilon n_z n_x & \Delta\varepsilon n_z n_y & \varepsilon_\perp + \Delta\varepsilon n_z n_z \end{bmatrix} \tag{58}$$

Obviously, it is symmetric.

Using Eq.(57), Eq. (56) then becomes:

$$F_e = -\frac{1}{2}\varepsilon_0 \int_{\Omega} \mathbf{E} \bullet \bar{\bar{\varepsilon}} \bullet \mathbf{E} d\Omega \tag{59}$$

Due to

$$\mathbf{E} = -\nabla\varphi \tag{60}$$

Eq. (59) finally takes the form:

$$F_e = -\frac{1}{2}\varepsilon_0 \int_{\Omega} \nabla\varphi \bullet \bar{\bar{\varepsilon}} \bullet \nabla\varphi d\Omega \tag{61}$$

Note that only first derivatives of φ with respect to space coordinates in the above expression are involved. Now, following the procedure discussed above and applying the variational technique to both sides of the above equation with respect to φ give

$$\delta F_e = -\frac{1}{2}\varepsilon_0 \int_{\Omega} \left[\nabla(\delta\varphi) \bullet \bar{\bar{\varepsilon}} \bullet \nabla\varphi + \nabla\varphi \bullet \bar{\bar{\varepsilon}} \bullet \nabla(\delta\varphi)\right] d\Omega = -\varepsilon_0 \int_{\Omega} \nabla(\delta\varphi) \bullet \bar{\bar{\varepsilon}} \bullet \nabla\varphi d\Omega \tag{62}$$

Here the nature of the symmetry of the dielectric tensor $\bar{\bar{\varepsilon}}$ has been used.

Carrying out the integral of the above equation by parts to separate δφ:

$$\delta F_E = -\varepsilon_0 \underbrace{\oint_S \delta\varphi d\mathbf{S} \bullet \overline{\overline{\varepsilon}} \bullet \nabla\varphi}_{\equiv 0} + \varepsilon_0 \int_\Omega \nabla \bullet \left(\overline{\overline{\varepsilon}} \bullet \nabla\varphi\right) \delta\varphi d\Omega = \varepsilon_0 \int_\Omega \nabla \bullet \left(\overline{\overline{\varepsilon}} \bullet \nabla\varphi\right) \delta\varphi d\Omega = 0 \quad (63)$$

The first term is equal to zero because the value of $\delta\varphi$ on the surface **S** is zero by the definition of the variational (surface restraint).

Due to the arbitrariness of $\delta\varphi$, from Eqs. (54) and (55), the above expression means that

$$\nabla \bullet \left(\overline{\overline{\varepsilon}} \bullet \nabla\varphi\right) = 0 \quad (64)$$

or

$$L\varphi = 0 \quad (65)$$

That is the Laplace or Poisson equation for a static electric potential without external charge source in form of tensor. Here L denotes $\nabla \bullet \overline{\overline{\varepsilon}} \bullet \nabla$.

The solution for φ found from Eq. (64) ensures the minimisation of the total potential energy F_E, i.e., makes it stationary. It is, however, worthwhile to point out that Eq. (64) contains second derivatives with respect to space, therefore it is not convenient to discretise it directly to find φ, unless the shape function is chosen of second order (quadratic), which certainly will make things a little bit more complicated. What we want here is to use a linear expression to make calculation easier.

4.3.4. Finite Elements

For many classic mathematical physics problems, such as heat conduction, particle transport/diffusion etc., physicists have established a system of ordinary or partial differential equations that are valid in a certain region (or domain), under continuum approximation, and certain types of boundary and initial conditions. In most of these cases, however, there are no analytical solutions that can be obtained. Therefore it is necessary to recast the problem in pure algebraic form, involving only basic arithmetic operations by discretising the continuum problem through which the infinite set of numbers representing the unknown function or functions is replaced by a finite number of unknown parameters. One of the simplest discretization scheme is the *finite different process* which can be regarded as a subclass of finite element methods. Various trial function approximations fall under the general classification of finite element methods. The essential idea of the finite element process lies in that if

the sub-domains are of a relatively simple shape and if the definition of the trial functions over these sub-domains can be made in a repeatable manner, then it is possible to deal in this fashion with assembled regions of complex shapes quite readily. Particularly, if the trial functions are to be defined in a piece-wise manner, it is advantageous to assign to them a narrow "base" and make their value zero everywhere except in the element in question and in the sub-domains immediately adjacent to this element. This will give sparse matrices in the final approximation equations, resulting in yet another advantage of the finite element process.

(i) Construction of mesh

In order for the numerical calculation to be performed, a physical area (domain) of a pixel in study with dimension of $L_x \times L_y \times L_z$ must be subdivided into a number of small cells by dividing L_x into a number of divisions $N_{\Delta x}$ in the x-direction, L_y into $N_{\Delta y}$, and L_z into $N_{\Delta z}$. The total number of cells is the product of $N_{\Delta x} \times N_{\Delta y} \times N_{\Delta z}$. A vertex of a cell is called a node or in physics term a lattice point. The total independent number of nodes for a given pixel is given by $(N_{\Delta x}+1)\times(N_{\Delta y}+1)\times(N_{\Delta z}+1)$. The node is numbered serially by a single index integer, say, i, rather than assigned a set of integer indices like (i,j,k) in order to use finite element technique. Each node has a unique integer number (index) to be referred to and also has a unique x-y-z co-ordinates. Director and potential fields are calculated by referring to the node as a requirement of discretisation. In the case of 2D model where x axis denotes pixel width, z denotes the height (cell gap), and y is the depth, assuming extended to infinity so that we do not have to consider. The dividing interval Δx is not necessarily required being equal to Δz, depending on the problem in study although Δx being equal to Δz gives an ideal aspect ratio, therefore, more accurate numerical approximation, but not necessarily the most efficient algorithm. In the case of liquid crystal displays, normally, a pixel width L_x is in the range from 30 μm to 90 μm while the height L_z goes only from 4 μm to 5 μm. L_x is much greater than L_z. However the light propagates and the voltage are applied across z, therefore we have to pay close attention to variation across z. Hence, in this work, Δx is in the most cases chosen to be in the order of six times Δz unless stated otherwise. The issue of the influences of different aspect ratios on the computational results is addressed and discussed in the Section 6.16. Figure 11 shows a sample mesh of a pixel whose dimension is L_x=30 μm and L_z=5 μm. The choice of

discretisation intervals are 1.5μm in x and 0.25μm in z respectively (which gives a aspect ratio of 6). The number of divisions $N_{\Delta x}$=20 and $N_{\Delta z}$=20, which makes 20×20=400 cells, or 800 triangle elements, and 441(=21×21) nodes. Two shortest thick horizontal solid lines at the top of the mesh represent the two bus electrodes, the line at the top centre represents the pixel electrode, and the long line at the bottom is the ground electrode. The pixel area is divided into appropriate blocks (boxes) according to the boundary conditions. The co-ordinates of each box's boundary lines are given as well as numbers of divisions $N_{\Delta x_i}^{b_i}$ $N_{\Delta z_i}^{b_i}$ of each box in x and in z. In the sample mesh shown in Figure 11, the pixel is divided into 7 boxes, co-ordinates of each box and division numbers are shown in the Table 1.

box	*1*	*2*	*3*	*4*	*5*	*6*	*7*
(x_1,x_2)	(-15,-12)	(-12,-9)	(-9,-6)	(-6,6)	(6,9)	(9,12)	(12,15)
$N_{\Delta x}^{b}$	2	2	2	8	2	2	2
(z_1,z_2)	(-2.5 , 2.5)						
$N_{\Delta z}^{b}$	20						

Table 1 Parameters used in generating sample mesh as shown in Figure 11

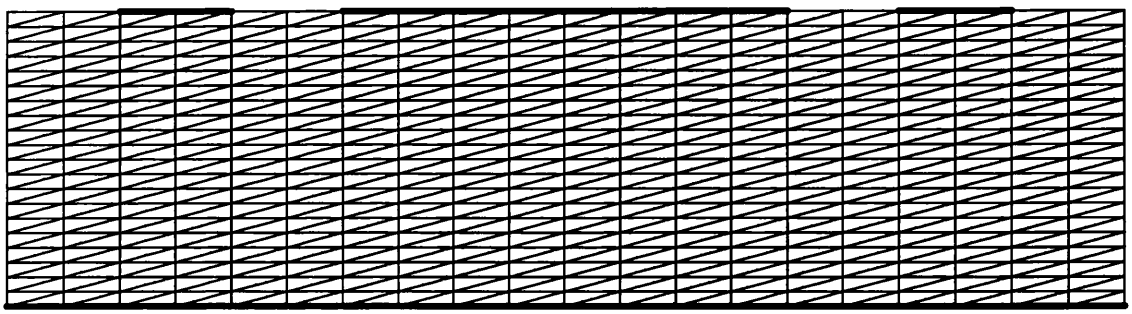

Figure 11 A sample mesh of a pixel with two bus electrodes, one pixel electrode and a ground electrode

(ii) Triangular elements

The elements used in the finite element method can have any shape so far as they constitute a tesselation of the problem domain. In this respect, the most common shapes are triangular and quadrilateral. Triangular elements are a popular choice for

the analysis of problem involving two space dimensions because of the ease with which arbitrarily shaped domains may be closely approximated by an assembly of triangles plus the characteristic that a sufficient number of nodes may be generated at all time to construct a family of complete polynomials [88],[89]. Therefore in this work, the triangle element is used. The triangle element is obtained by dividing each rectangular cell into two triangles as shown in the Figure 11. The triangle element is numbered serially. Three vertices (nodes) of each triangular element are numbered locally. The node number (i.e., an integer index) to which each vertex corresponds is identified and stored. The co-ordinates of each vertex is given by its corresponding nodal co-ordinates. In this way, the position of each triangular element is solely determined by its three vertices' co-ordinates, hence three corresponding nodal co-ordinates. The nearest neighbours elements to each given node are found by the mesh generator program and stored as an output which is used as an input to the main program.

(iii) Construction of shape function

(a) Triangular element family and Pascal triangle

The following forms of triangular elements constitute a family. They are (1) linear [Figure 12(a)], (2) quadratic [Figure 12(b)], and (3) cubic [Figure 12(c)] which

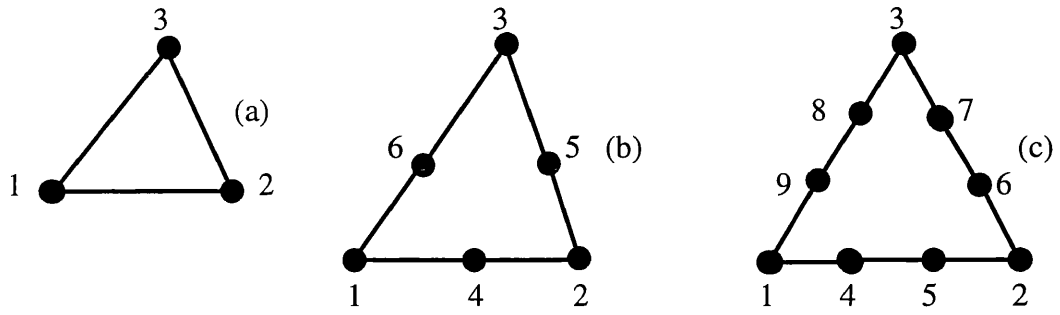

Figure 12 Triangular element family: (a) linear, (b) quadratic, and (c) cubic

correspond, respectively, to first order, second order, and third order polynomials expansions as shown in Pascal triangle (see Figure 13). Among them, only linear element interests us. Therefore in what follows, the focus will only be put on the first order polynomial.

Consider a series of triangles generated on a pattern indicated in Figure 12. The number of nodes in each member of the family is now such that a complete

polynomial expansion, of the order needed for inter-element compatibility, is ensured. This follows by comparison with the Pascal triangle of Figure 13 in which the number of nodes exactly match the number of polynomial terms required. This particular feature puts the triangle family in a special, privileged position.

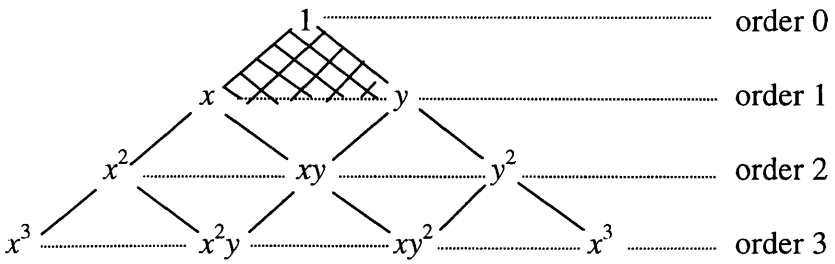

Figure 13 The Pascal triangle (Linear expansion shaded – 3 terms)

However, once again, a direct generation of shape functions will be preferred – and indeed will be shown to be particular easy.

Before proceeding further it is convenient to define a special set of normalised coordinates for a triangle.

(b) Area coordinates

Whilst Cartesian directions parallel to the sides of a rectangle were a natural choice for that shape, in the triangle these are not convenient.

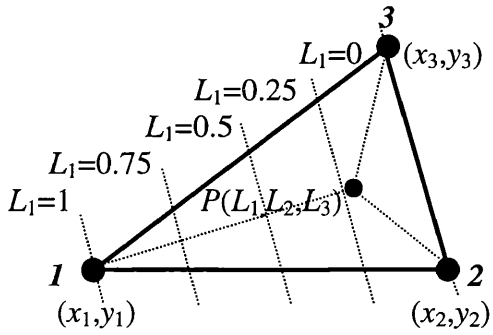

Figure 14 Area co-ordinates

A convenient set of co-ordinates, L_1, L_2, and L_3 for a triangle 1,2,3 (Figure 14), can be defined by the following linear relation between these and the Cartesian system:

$$\begin{aligned} x &= L_1 x_1 + L_2 x_2 + L_3 x_3 = L_i x_i \\ y &= L_1 y_1 + L_2 y_2 + L_3 y_3 = L_i y_i \\ 1 &= L_1 + L_2 + L_3 \end{aligned} \tag{66}$$

Notice that among L_1, L_2, and L_3, only two of them are independent according to the third equation, and to every set L_1, L_2, L_3, corresponds a unique set of Cartesian co-ordinates. At point 1, x must be equal to x_1, and y must be equal to y_2, this requires $L_1=1$ and $L_2 \equiv L_3 \equiv 0$, etc.. A linear relation between the new and cartesian coordinates implies that contours of L_1 are equally placed straight lines parallel to side 2-3 on which $L_1=0$, etc. as shown in Figure 14.

It is easy to see that there exists an equivalent definition of the coordinate L_1, L_2, L_3 of a point P by ratios of the areas of the triangles $\Delta P23$, $\Delta P13$, and $\Delta P12$ to that of the total triangle $\Delta 123$:

$$L_1 = \frac{\text{area } \Delta P23}{\text{area } \Delta 123}, \quad L_2 = \frac{\text{area } \Delta P13}{\text{area } \Delta 123}, \quad L_3 = \frac{\text{area } \Delta P12}{\text{area } \Delta 123} \tag{67}$$

That is why they are named *area co-ordinates.*

Solving Eq. (66) for x and y gives

$$\begin{aligned} L_1 &= \frac{a_1 + b_1 x + c_1 y}{2d} \\ L_2 &= \frac{a_2 + b_2 x + c_2 y}{2d} \quad \text{or} \quad L_i = \frac{a_i + b_i x + c_i y}{2d} \\ L_3 &= \frac{a_3 + b_3 x + c_3 y}{2d} \end{aligned} \tag{68}$$

in which

$$d = \frac{1}{2}\det\begin{vmatrix} 1 & x_1 & y_1 \\ 1 & x_2 & y_2 \\ 1 & x_3 & y_3 \end{vmatrix} = area\ \Delta 123 \tag{69}$$

and

$$\begin{aligned} a_{1[2,3]} &= x_{2[3,1]} y_{3[1,2]} - x_{3[1,2]} y_{2[3,1]} \\ b_{1[2,3]} &= y_{2[3,1]} - y_{3[1,2]} \\ c_{1[2,3]} &= x_{3[1,2]} - x_{2[3,1]} \end{aligned} \tag{70}$$

with cyclic rotation of indices 1,2, and 3 shown in the square brackets.

(c) Shape functions

In the case of linear triangular element, the shape functions are simply the area coordinates:

$$N_1(x,y) = L_1 \quad N_2(x,y) = L_2 \quad N_3(x,y) = L_3 \tag{71}$$

This is obvious as each individually gives unity at one node, zero at others, i.e.,

$$N_i(P_j) = L_i(P_j) = \delta_{ij}, i, j = 1,2,3 \tag{72}$$

and varies linearly everywhere. Here $P_j=(x_j,y_j)$.

it should be emphasised that for every triangle the formulation of the above shape functions (71) apply – that is the essence in the finite elements methods.

4.3.5. Calculation of the potential

(i) Derivation of A-matrix – calculation of potential

According to the earlier discussion, if the variational technique is directly applied to the potential energy equation (61) which only contains first space derivatives of φ, it will end up with a Poisson equation for the potential φ which involves the second space derivatives of φ and demands a quadratic expression for the shape functions. Obviously, that is not convenient. What is wanted here is to take advantage of the simplicity of the linear or first order expansion of shape functions as discussed before. Therefore it is quite worthwhile to seek a different approach to the problem.

By dividing the whole domain into triangle elements the total electric energy (61) can be approximated by

$$F_E = -\frac{1}{2}\varepsilon_0 \sum_{\Delta} \int_{\Delta} \nabla\varphi^{\Delta} \bullet \bar{\bar{\varepsilon}}^{\Delta} \bullet \nabla\varphi^{\Delta} d\Delta \tag{73}$$

here Δ denotes the triangle element over which the sum is made and integral is done. Now because φ(*x,y*) is defined at an arbitrary point within the triangle, it is necessary to expand it in terms of the shape functions (71):

$$\varphi^{\Delta}(x, y) = \sum_{i=1}^{3} \phi_i^{\Delta} N_i^{\Delta} = \sum_{i=1}^{3} \phi_i^{\Delta} \left(\frac{a_i + b_i x + c_i y}{2d^{\Delta}} \right), \qquad x, y \in \Delta \tag{74}$$

here the expansion coefficient ϕ_i^{Δ} is solely defined on each node. Application of ∇ to φ^{Δ} gives (note that the expressions (70) for the coefficients $a_i, b_i,$ and c_i are of the identical form for every triangle)

$$\nabla\varphi(x,y)=\frac{1}{2d}\sum_{i=1}^{3}\phi_i\left[b_i,c_i,0\right] \tag{75}$$

For convenience the superscript Δ is dropped. Putting expression (75) back to Eq. (73) and using Eq. (58), we have

$$F_E =$$

$$-\frac{\varepsilon_0}{8}\sum_{\Delta}\frac{1}{d^2}\sum_{i=1}^{3}\sum_{j=1}^{3}\phi_i\phi_j\int_{\Delta}\left[b_i\ c_i\ 0\right]\begin{bmatrix}\varepsilon_\perp+\Delta\varepsilon n_x n_x & \Delta\varepsilon n_x n_y & \Delta\varepsilon n_x n_z\\ \Delta\varepsilon n_y n_x & \varepsilon_\perp+\Delta\varepsilon n_y n_y & \Delta\varepsilon n_y n_z\\ \Delta\varepsilon n_z n_x & \Delta\varepsilon n_z n_y & \varepsilon_\perp+\Delta\varepsilon n_z n_z\end{bmatrix}\begin{bmatrix}b_j\\ c_j\\ 0\end{bmatrix}d\Delta$$

$$=-\frac{\varepsilon_0}{8}\sum_{\Delta}\frac{1}{d^2}\sum_{i=1}^{3}\sum_{j=1}^{3}\phi_i\phi_j\int_{\Delta}\left[\left(b_ib_j+c_ic_j\right)\varepsilon_\perp+b_ib_j\Delta\varepsilon n_x^2+2b_ic_j\Delta\varepsilon n_x n_y+c_ic_j\Delta\varepsilon n_y^2\right]d\Delta \tag{76}$$

here the nature of the symmetry: $\sum_{i=1}^{3}\sum_{j=1}^{3}\phi_i\phi_j b_i c_j=\sum_{i=1}^{3}\sum_{j=1}^{3}\phi_i\phi_j b_j c_i$ has been used. The integral of the first term in the square brackets in Eq. (76) simply gives rise to the area of the triangle element *d*.

Based on the same consideration, the director components n_x, and n_y that are defined at any point within the triangle element may be expanded in the shape functions:

$$n_{x[y]}=\sum_{m=1}^{3}n_{x[y]}^{m}N_m(x,y)=\sum_{m=1}^{3}n_{x[y]}^{m}\frac{a_m+b_m x+c_m y}{2d} \tag{77}$$

Like ϕ_i, the expanding coefficients $n_{x[y]}^{m}$ is only defined on the node *m* and is the entity to be found.

$$F_E=-\frac{\varepsilon_0}{8}\sum_{\Delta}\frac{1}{d^2}\sum_{i=1}^{3}\sum_{j=1}^{3}\phi_i\phi_j\left\{\left(b_ib_j+c_ic_j\right)\varepsilon_\perp d+\Delta\varepsilon\sum_{m=1}^{3}\sum_{l=1}^{3}\left[\left(b_ib_jn_x^m n_x^l\right.\right.\right.$$

$$\left.\left.\left.+2b_ic_jn_x^m n_y^l+c_ic_jn_y^m n_y^l\right)\int_{\Delta}N_mN_l d\Delta\right]\right\} \tag{78}$$

The integral involving the shape functions overlapping (quadratic) in the above expression can be performed as follows:

$$\int_{\Delta}N_mN_l d\Delta=2d\int_0^1\int_0^{1-\xi_1}\xi_1\xi_2 d\xi_1 d\xi_2=\underbrace{\frac{(1+\delta_{ml})}{12}}_{K_{ml}}d=d\begin{Bmatrix}1/6,\ \text{if } m=l\\ 1/12,\text{if } m\neq l\end{Bmatrix}\equiv K_{ml}d \tag{79}$$

Inserting Eq. (79) to Eq. (78) gives

$$F_E = -\frac{\varepsilon_0}{8}\sum_{\Delta}\frac{1}{d}\sum_{i=1}^{3}\sum_{j=1}^{3}\phi_i\phi_j\left[\left(b_ib_j + c_ic_j\right)\varepsilon_\perp + \Delta\varepsilon\sum_{m=1}^{3}\sum_{l=1}^{3}\frac{1+\delta_{ml}}{12}\left(b_ib_jn_x^mn_x^l\right.\right.$$
$$\left.\left. + 2b_ic_jn_x^mn_y^l + c_ic_jn_y^mn_y^l\right)\right] \tag{80}$$

The formulation for the electric field energy (61) has been transformed into an algebraic formulation (80) after application of finite element method. Now it is the time to apply the variational technique to the above equation to obtain another algebraic equation for the potential ϕ_i that minimises the above total energy. For each triangle element Δ, ϕ_i^{Δ} (i=1,2,3) now are the independent variables, the variational technique can be applied to each triangle element, i.e., locally:

$$\frac{\delta F_E}{\delta\phi_k} = -\frac{\varepsilon_0}{8}\sum_{\Delta}\frac{1}{d}\sum_{i=1}^{3}\sum_{j=1}^{3}\left(\delta_{ki}\phi_j + \phi_i\delta_{kj}\right)\left[\left(b_ib_j + c_ic_j\right)\varepsilon_\perp + \Delta\varepsilon\sum_{m=1}^{3}\sum_{l=1}^{3}\frac{1+\delta_{ml}}{12}\left(b_ib_jn_x^mn_x^l\right.\right.$$
$$\left.\left. + 2b_ic_jn_x^mn_y^l + c_ic_jn_y^mn_y^l\right)\right] = 0, \quad k = 1,2,3 \tag{81}$$

Re-organising the above expression and keeping in mind that all $\delta\phi_k$ (k=1,2,3) are independent, then we have

$$\sum_{\Delta}\frac{1}{d}\sum_{i=1}^{3}\left\{\varepsilon_\perp\left(b_ib_j + c_ic_j\right) + \Delta\varepsilon\sum_{m=1}^{3}\sum_{l=1}^{3}\frac{1+\delta_{ml}}{12}\left[b_ib_jn_x^mn_x^l\right.\right.$$
$$\left.\left. + \left(b_ic_j + b_jc_i\right)n_x^mn_y^l + c_ic_jn_y^mn_y^l\right]\right\}\phi_i = 0, \quad j = 1,2,3 \tag{82}$$

or in form of matrix in subspace, i.e., triangle element Δ, the above expression can be condensed as

$$\sum_{\Delta}\frac{1}{d^{\Delta}}\boldsymbol{A}^{\Delta}\boldsymbol{\varphi}^{\Delta} = 0 \tag{83}$$

where

$$\left(\boldsymbol{A}^{\Delta}\right)_{ij} = \varepsilon_\perp\left(b_ib_j + c_ic_j\right) + \Delta\varepsilon\sum_{m=1}^{3}\sum_{l=1}^{3}\frac{1+\delta_{ml}}{12}\left[b_ib_jn_x^mn_x^l + \left(b_ic_j + b_jc_i\right)n_x^mn_y^l + c_ic_jn_y^mn_y^l\right]$$
$$= b_ib_j\left(\varepsilon_\perp + \Delta\varepsilon\underbrace{\sum_{m=1}^{3}\sum_{l=1}^{3}K_{ml}n_x^mn_x^l}_{P}\right) + \left(b_ic_j + b_jc_i\right)\Delta\varepsilon\underbrace{\sum_{m=1}^{3}\sum_{l=1}^{3}K_{ml}n_x^mn_y^l}_{R}$$
$$+ c_ic_j\left(\varepsilon_\perp + \Delta\varepsilon\underbrace{\sum_{m=1}^{3}\sum_{l=1}^{3}K_{ml}n_y^mn_y^l}_{Q}\right)$$

$$= b_i b_j \left(\varepsilon_\perp + \Delta\varepsilon P^\Delta\right) + \left(b_i c_j + b_j c_i\right)\Delta\varepsilon R^\Delta + c_i c_j \left(\varepsilon_\perp + \Delta\varepsilon Q^\Delta\right) \qquad (84)$$

That is what we have been looking for - the element of coefficient matrix for potential function ϕ for each triangle element and obviously it is symmetric about the nodal pair (i, j).

Adding up the contributions from all triangle elements, Eq. (83) can be further rewritten in a form of the assembled global matrix as follows:

$$\boldsymbol{A}\Phi = 0 \qquad (85)$$

Here $\boldsymbol{A}$ is the assembled matrix of $N_p \times N_p$ order for the whole mesh from the expression (84) for each triangle element; $\boldsymbol{\Phi}$ is global vector of size of N_p for the potentials on each node, N_p is the total number of the nodes of the whole domain.

Now we have finished the construction of the $\boldsymbol{A}$ matrix which determines the potentials $\boldsymbol{\Phi}$ on each node.

Summary, discussion, and comments

Directly starting from equation (61) for the total electric energy that involves only first spatial derivatives, by using Rayleigh Ritz method with FE shape functions, the original complicated problem has been transformed into an easy-to-handle algebraic problem [see Eq. (80)]. The application of the variational technique to Eq. (80) in the subspace further transformed the problem into a matrix one [see Eqs. (83) and (85)] that the nodal potentials satisfy and we are looking for. The advantage of this approach is that only linear shape functions are needed.

(ii) Sparsity of A matrix

The assembled coefficient matrix $\boldsymbol{A}$ in Eq. (85) is of dimensions $N_p \times N_p$ (e.g., 441×441=194,481 as shown in the sample mesh Figure 11). However because only contributions from nearest neighbours form the matrix $\boldsymbol{A}$ and in a regular mesh, any given node has at most 6 neighbours, there will be no more than 7 coefficients in each row of $\boldsymbol{A}$, irrespective of the order.

Most elements of $\boldsymbol{A}$ will be zero and the sparsity of the matrix increases with the order of all $N_p \times N_p$ possible elements, only the nonzero values are calculated and stored.

(iii) Boundary conditions and rank reduction of A matrix and Φ vector

We can consider three-different types of boundary conditions: Dirichlet (fixed values at boundary), periodic, and Neumann (zero normal derivative) conditions. All those conditions will reduce the number of unknowns ϕ_i (i=1,2,…,N_p).

(a) Dirichlet condition

Here Dirichlet condition is represented by the bus, pixel, and ground electrodes as the values of potential ϕ on each node along the electrodes is assigned or fixed. That means the number of unknowns of ϕ will be reduced and hence the rank of the coefficient matrix $\boldsymbol{A}$.

(b) Periodic condition

A periodic boundary condition means $\phi_{left\_boundary}=\phi_{right\_boundary}$. This is a commonly used boundary condition in the LC structure. Imposition of this condition will also reduce the size of both $\boldsymbol{A}$ and $\boldsymbol{\Phi}$.

(c) Neumann condition

This condition imposes $\partial_\mu \phi = 0$. It is applied to impose continuity of normal **E** field at dielectric interfaces and to simulate a region of unchanging directors far from the centre of the cell.

(d) Reformulation of eigenvalue problem

After using all the above boundary conditions, the number of unknowns ϕ will reduce, say, from N_p to N'_p, hence the size of assembled $\boldsymbol{A}$ will become $N'_p \times N'_p$. The eigenvalue problem (85) now becomes a normal linear equation system

$$\boldsymbol{A'\varphi' = B} \tag{86}$$

Here $\boldsymbol{A'}$ denotes the rank-reduced $N'_p \times N'_p$ matrix, $\boldsymbol{\varphi'}$ represents the actual unknown vector (potential values) of size of N'_p, and $\boldsymbol{B}$ consists of elements originated from the reorganisation of the eigenvalue equation (85) when the Dirichlet condition is applied.

Once the reduced matrix equation has been solved, the vector of potential values ϕ can be expanded, reinstating the values determined by boundary conditions.

(iv) Solution for the potential

(a) Solution of the matrix problem

The sparse system of N'_p of linear equations in N'_p unknowns ϕ_i is solved by Gaussian elimination using the Harwell Subroutine **MA48**, which consists of three main subroutines: **MA48AD** for choosing a good pivot order, **MA48BD** for factorising matrix A' with the already calculated pivot order, and **MA48CD** for solving the system of equations using the factorised matrix.

(b) LU decomposition – factorization of matrix A'

Factorisation (also called LU decomposition) means to decompose the matrix A' into two triangular matrices: Lower triangular matrix L and upper triangular matrix U as follows:

$$A' = LU \tag{87}$$

After this crucial step, the solution of each ϕ component is easily be done by forward and backward substitutions.

4.3.6. Calculation of director

Given that the potential field $\{\phi\}$ has been found in the above Section, the next step is to find the director profile from the dynamic tensorial equation (36). To this end, first the discretisation of spatial derivatives should be done and then temporal discretisation to find a self-consistent director profile at a given time t from the profile at previous time t-Δt by iteration.

(i) Spatial discretisation

Due to the complicated combinations of second derivatives in the expanded expressions (38-41) for the three-elastic constant tensorial dynamic equation (36), special care must be taken when dealing with spatial discretisation. First, the finite difference scheme described above (46) is used to discretise diagonal terms of second derivatives, e.g.,

$$\begin{aligned}\partial_\alpha\partial_\alpha\left(n_\mu(i,j,k)n_\nu(i,j,k)\right) = &\left[n_\mu(i+1,j,k)n_\nu(i+1,j,k)+n_\mu(i-1,j,k)n_\nu(i-1,j,k)\right.\\ &\left.-2n_\mu(i,j,k)n_\nu(i,j,k)\right]/(\delta x^2)\\ &+\left[n_\mu(i,j+1,k)n_\nu(i,j+1,k)+n_\mu(i,j-1,k)n_\nu(i,j-1,k)\right.\\ &\left.-2n_\mu(i,j,k)n_\nu(i,j,k)\right]/(\delta y^2)\\ &+\left[n_\mu(i,j,k+1)n_\nu(i,j,k+1)+n_\mu(i,j,k-1)n_\nu(i,j,k-1)\right.\\ &\left.-2n_\mu(i,j,k)n_\nu(i,j,k)\right]/(\delta z^2)\end{aligned} \tag{88}$$

For mixed derivatives terms, for example, with respect to x and y, the central difference scheme is used.

$$\begin{aligned}\partial_x\partial_y\left(n_\mu(i,j,k)n_\nu(i,j,k)\right) = &\left[n_\mu(i+1,j+1,k)n_\nu(i+1,j+1,k)-n_\mu(i-1,j+1,k)n_\nu(i-1,j+1,k)\right.\\ &\left.+n_\mu(i-1,j-1,k)n_\nu(i-1,j-1,k)-n_\mu(i+1,j-1,k)n_\nu(i+1,j-1,k)\right]/(4\delta x\delta y)\end{aligned} \tag{89}$$

From expressions (88) and (89) it can be clearly seen that at any observation point, say, point i, if the director **n** at point $i\pm1$ changes its sign to **–n**, the expressions remain invariant, i.e., anti-parallel neighbours are treated like parallel ones, i.e.,

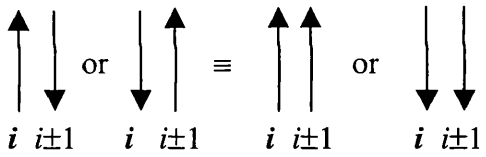

Figure 15 Parallel and anti-parallel neighbors are treated the same

For cubic terms, for example, $n_x(i,j,k)n_x(i,j,k)n_x(i,j,k)$, the following replacement: $\Rightarrow$ $n_x(i,j,k)[1\text{-}n_y(i,j,k)n_y(i,j,k) - n_z(i,j,k)n_z(i,j,k)]$ is done to make the expression linear in n_x and also to enforce the unitary character of **n**.

(ii) Temporal discretization

Since forward and backward differences often bring about the instability of the numerical calculation [90-93], the Crank-Nicolson scheme [92] is used instead. This is essentially a central difference method and offers higher order of accuracy while effectively maintaining the convergence of iteration procedure [90-93].

After spatial discretization, tensor equation (36) for $n_{x(y,z)}$ can be expressed in general as

$$\gamma \frac{\partial n_{x[y,z]}(t)}{\partial t} = F_{x[y,z]}\left[n_x(t), n_y(t), n_z(t); \{\phi\}\right] \tag{90}$$

Here the subscripts y and z in the square brackets in the sub-indices denote similar expressions or functions that correspond to components y and z. $F_{x[y,z]}$ are the functions of $n_x(t)$, $n_y(t)$, and $n_z(t)$ and potential field $\{\phi\}$.

Applying the Crank-Nicolson central difference formula (48) to the left-hand side of the Eq. (90) gives

$$\gamma \frac{n_{x[y,z]}\left(t+\frac{1}{2}\Delta t\right) - n_{x[y,z]}\left(t-\frac{1}{2}\Delta t\right)}{\Delta t} = F_{x[y,z]}\left[n_x(t), n_y(t), n_z(t); \{\phi\}\right] \tag{91}$$

Because $t+\frac{1}{2}\Delta t$ is not located at a mesh point, the following replacement: $t \rightarrow t+\frac{1}{2}\Delta t$ needs to be done on *both* sides of the above equation. We then have

$$\gamma \frac{n_{x[y,z]}(t+\Delta t) - n_{x[y,z]}(t)}{\Delta t} = F_{x[y,z]}\left[n_x\left(t+\tfrac{1}{2}\Delta t\right), n_y\left(t+\tfrac{1}{2}\Delta t\right), n_z\left(t+\tfrac{1}{2}\Delta t\right); \{\phi\}\right] \tag{92}$$

Based on the same reason as above, applying Crank-Nicolson formula (48)

$$n\left(t+\tfrac{1}{2}\Delta t\right) = \frac{n(t+\Delta t)+n(t)}{2} \tag{93}$$

again to the right-hand side of equation (92) gives

$$n_{x[y,z]}(t+\Delta t) = n_{x[y,z]} + \frac{\Delta t}{\gamma} F_{x[x,y]}\left[n_x(t), n_y(t), n_z(t); n_x(t+\Delta t), n_y(t+\Delta t), n_z(t+\Delta t); \{\phi\}\right] \tag{94}$$

(iii) Calculation of director

Eq. (94) is a system of highly non-linear and coupled equations for the unkowns: $n_x(t+\Delta t)$, $n_y(t+\Delta t)$ and $n_z(t+\Delta t)$ in terms of the knowns values: $n_x(t)$, $n_y(t)$, $n_z(t)$ and $\{\phi\}$. A numerical iteration procedure must be adopted in order to obtain solutions to $n_x(t+\Delta t)$, $n_y(t+\Delta t)$,and $n_z(t+\Delta t)$. To do so, one has to make some kind of "guess" at the start of iterations for a given time step by using some tentative values, for example, the values of $n_x(0)$, $n_y(0)$, and $n_z(0)$, to replace $n_x(\Delta t)$, $n_y(\Delta t)$,and $n_z(\Delta t)$ appearing in function $F_{x[y,z]}$ on the right-hand side of Eq. (94) for the first time step. Once the values of $n_x(\Delta t)$, $n_y(\Delta t)$,and $n_z(\Delta t)$ are obtained after the first iteration, they are immediately inserted back in the function $F_{x[y,z]}$ for the second iteration to be carried on. After the second iteration is done, a comparison between the values from

the first iteration and those from just obtained, is made to check if the convergence tolerance has been reached. If not, this kind of iterative process continues until the final solution for $n_x(\Delta t)$, $n_y(\Delta t)$, and $n_z(\Delta t)$ satisfies the prescribed tolerance. Keeping in mind that once $n_{x[y,z]}(t+\Delta t)$ is obtained from $n_{x[y,z]}(t)$, the normalisation of $n_{x[y,z]}(t+\Delta t)$ by the modulus of $n(t+\Delta t)$, i.e.,

$$\frac{n_{x[y,z]}(t+\Delta t)}{\|\boldsymbol{n}(t+\Delta t)\|} \Rightarrow n_{x[y,z]}(t+\Delta t) \tag{95}$$

is immediately done (in fact, after each iteration), so that the newly obtained director $n(t+\Delta t)$ satisfies $\|\boldsymbol{n}(t+\Delta t)\| = 1$ after each iteration for each time step.

In general, to calculate the values of $n_x(t+k\Delta t)$, $n_y(t+k\Delta t)$, and $n_z(t+k\Delta t)$ at time $t+k\Delta t$, the values of $n_x(t+(k-1)\Delta t)$, $n_y(t+(k-1)\Delta t)$ and $n_z(t+(k-1)\Delta t)$ obtained from previous time step, i.e., at $(k-1)$th time step must be used as new guess values for the items: $n_x(t+k\Delta t)$, $n_y(t+k\Delta t)$ and $n_z(t+k\Delta t)$ appearing in the function $F_{x[y,z]}$.

4.3.7. A comparison between FE method and FD method

It is useful to compare the finite element (FE) method and finite difference (FD) methods. The advantages of FE method are

The application to problem with irregular geometry and different size of element in different regions of the domain is no more difficult than for regular geometry and meshes;

Once a computer code has been written for a particular order of trial function, only very minor change to the code are needed in order to change the order of trial function. Conversely, however, in order to change the accuracy of a FD code, major modifications are usually required;

Procedures involving successive mesh refinements are more easily incorporated into FE schemes.

Other considerations, however, may favour FD methods. For example:

It is generally much easier to write a FD rather than a FE computer code.

Error analysis is much easier to perform for FD methods.

5. Constant voltage model

The earlier constant voltage model developed in this group consists of two versions: a steady-state model with three elastic constants [11], [12], [14]] and a single elastic constant dynamic model [14], [17], [19]]. In this work, the ability of the time-domain model has been extended to study the dynamic behaviour of the capacitance and total charges of pixel and bus electrodes, and charge distributions along the pixel and bus electrodes. For completeness, a brief overview of the constant charge model is given below.

5.1. Steady state model

Steady state modelling mainly involves minimising the Oseen-Frank total free energy (19) to find the potential and director profiles.

To solve Eq. (19) under the fixed boundary conditions and applied voltage in two dimensions, it is crucial to look for the correct combination of electric field and director distributions throughout the device that makes the free energy stationary.

5.1.1. Optimisation

As the problem is highly non-linear, the procedure followed is iterative and is divided into two parts: the first consists of the solution for the potential $\{\varphi_i\}$, given a known director profile following the procedure discussed earlier, i.e., minimise the total electrical field energy using finite element method and variational technique giving linear algebraic system of equation for the potential values on each node, and the second is the solution for director field distribution $\{n_i\}$ when the distribution of φ is known. By alternating between the solution of a variational form for φ with given n and a numerical optimisation procedure for **n** with given φ, the iterative procedure converges to the sought consistent solution and the unitary condition: $|\boldsymbol{n}|^2 = 1$ is imposed throughout. To be specific, the free energy F_g is expressed in terms of φ and two angles θ and ψ which describe director **n** ($\cos\psi\cos\theta$, $\cos\psi\sin\theta$, $\sin\psi$). The cross-section of the LC cell is discretised using first order triangular finite elements. In this way, the problem now becomes solving systems of equations which are linear in φ

and minimising the total free-energy with respect to the angles θ and ψ. Our FE code takes maximum advantage of the sparsity of the matrix.

Boundary conditions for **n** are derived by assuming strong anchoring to the bounding surfaces by prescribing some pre-tilt and twist angles on the surface planes of the liquid crystal layer.

5.1.2. Iterative procedure

The iterative procedure is described as follows:

(1) Set up boundary conditions for directors and the potential, and initial state

(2) Calculate the potential field $\{\varphi\}$ with fixed director field $\{n\}$, i.e., solve linear systems of equations for φ using FE method and variational technique

(3) Calculate the directors $\{\mathbf{n}\}$ with fixed potential $\{\varphi\}$ which is obtained after step (2), by minimizing total energy with respect θ and ψ to find a set of θ_{min} and ψ_{min}, hence $\mathbf{n}_{min}$.

(4) Check if the solutions of $\{\mathbf{n}\}$ and $\{\varphi\}$ meet the required tolerance. If no, go back to step (2), the process will not cease until a set of self-consistent and convergent solutions are found. If yes execute next step (5)

(5) Output results.

5.1.3. flowchart

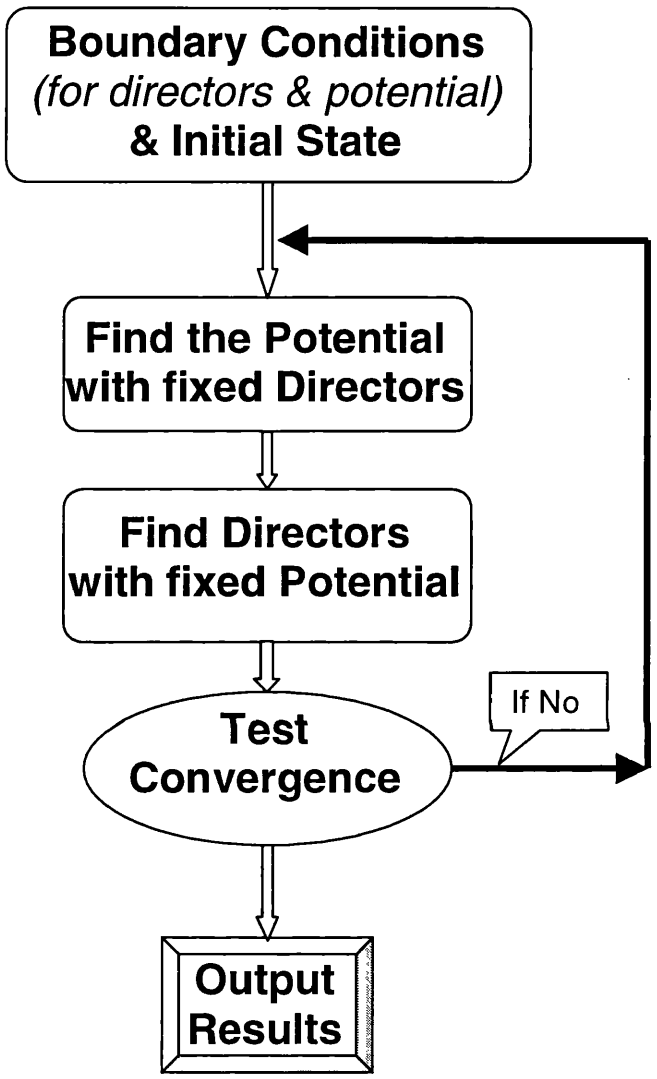

Figure 16 A flowchart for steady-state iteration

5.2. Dynamic model

Time domain modelling of liquid crystal display devices requires use of a dynamic model. In this section, a discussion is given of the methodology adopted in the dynamic computer modelling developed in our modelling group [14], [17], [19] as well as some modelling results.

5.2.1. The mathematical formulation

The mathematical description of the dynamic model for single elastic constant is given by the tensorial expression (16). Its main features include:

(1) Compared with static equation (19), director and potential fields are not only given as spatial distributions, but also evolve with time;

(2) The tensor description preserves the head-tail symmetry of the director fields, i.e., $-\boldsymbol{n}$ is equivalent to $\boldsymbol{n}$.

However, due to the feature (1), solution to equation (16) is much more computing demanding and complicated than in the steady state case.

5.2.2. The methodology for the numerical solution

The numerical methods that are used to solve Eq. (16) for director and potential field distributions are given in 4.3.5 and 4.3.6. In order to obtain the consistent director and potential field distributions, an iterative procedure is followed. Before starting the iterations, the boundary and initial conditions need to be specified and the sparse pattern needs to be identified.

(i) Determination of sparse pattern

As discussed before, although the size of the eigen-matrix A in Eq. (85) is very large ($N_p \times N_p$, N_p is the total number of the nodes of the cell), it is not a dense matrix, rather, it is symmetric and highly sparse because a huge number of its elements are zero due to the first-order triangular local approximation. A subroutine is designed to determine the position of each nonzero element and prepare the storage space. These elements will then be identified by a single index. Their row and column locations are stored in one-dimensional arrays and can be retrieved later by the single index in order to take advantage of the FE technique.

(ii) Initial conditions

In order to start the time stepping procedure, the initial values of potential and director field on each node must be set up. Therefore, the potential is set varying linearly in the z direction from the values applied to the pixel electrodes. The initial director filed distribution is determined by the pre-tilt and twist angles. By assuming the pre-tilt

angle (usually 2°~ 4°) is the same everywhere, the twist angle is allowed to vary linearly in the z direction from a fixed value, say, 45° at the bottom layer to another fixed value, say, -45° at the top layer.

(iii) Boundary conditions

Boundary conditions for potential and directors involved in this work consist of Dirichlet conditions (first-type), free and periodical boundary conditions as well as Neumann conditions (second-type).

(a) Dirichlet conditions

First, as far as the constant voltage model is concerned, the voltages are directly applied to electrodes with fixed values at all times. This constitutes the first type, i.e., Dirichlet boundary conditions. Under these conditions, the values of potential on all electrode nodes are known. Those nodes are identified and stored first of all by the Subroutine **BOUNDID**. Although the potential values on those nodes are given beforehand, because the applied pixel and bus voltages change polarities periodically, so a Subroutine called **VOLTSET** is designed to assign the voltage data with correct polarities and amplitudes to the corresponding electrode node during the time stepping process.

Second, because the pretilt and twist angles of director are fixed at the top and bottom layers, the value of director on each node at the top and bottom layers is known and does not change with time. Those nodes are identified and stored from the beginning by Subroutine **BOUNDID** too. The values of directors on those nodes are stored as well by the same Subroutine. Therefore, all those nodes on those two boundary layers (marked by × in Figure 17) are excluded from time-stepping of director n_v and hence there is no need to calculate the derivatives of n_v and φ with respect to x or y on those nodes.

(b) Periodical boundary condition

Normally a LC display device consists of hundreds and thousands of pixels. All such pixels and their electrode configurations are identical and periodically aligned in a repeated pattern. The model pixel is one of them, cut from this periodic alignment pattern. Therefore the nodes on the left-hand side boundary can be regarded as

identical to those on the right-hand side boundary. That means the values of potential and director on left-hand side boundary nodes take the same values as on the right-hand side boundary nodes. Those nodes are identified from the beginning and stored for reference later by Subroutine **BOUNDID**.

In treating normal derivatives of director **n** and potential φ at node, say, l on the left-hand side in Figure 17, for first derivative the central difference (45) can be used and for second derivative, the finite difference (46) can be used because of the left- and right-hand periodicity, i.e., $\varphi(l)=\varphi(l+N_{\Delta x})$ and $\mathbf{n}(l)=\mathbf{n}(l+N_{\Delta x})$. That is to say the node number l-1 in the difference formulas (45) and (46), which does not actually exist in the mesh, can be simply replaced by the node number $l+N_{\Delta x}$-1 on the right-hand side as shown in Figure 17.

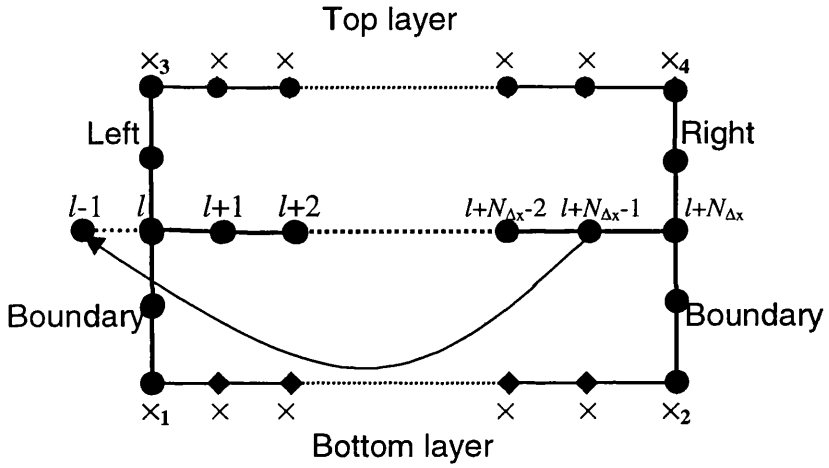

Figure 17 A schematic figure for boundary nodes

In treating tangential derivatives the central and finite differences can be directly applied for director **n** and the central difference is for potential φ (note that there is no second derivatives of φ involved in question).

Note that in both cases, 4 vertices marked by bold $\times_i$ (i=1,2,3,4) do not need to be considered as there the values of **n** are already known as mentioned above. Only derivatives of φ for the vertex $\times_3$ need to be calculated with care as $\varphi(\times_4)=\varphi(\times_3)$ and the ground electrode is assumed to covers all nodes on the bottom layer. However, if $\times_3$ is covered by an electrode node, it does not have to be considered either.

(c) Free boundary condition

Free boundary condition means that the nodes on left-hand and right-hand side boundaries are treated in the same way as any other internal node, and the values of director **n** and potential φ are determined by Eqs. (36) and (86) too. However in dealing with the spatial derivatives of φ and **n** on those nodes as shown in Figure 17, special care must be taken because now there does not exist any periodicity that can be used to implement the central and finite differences as discussed above. Because all nodes at the top layer and bottom layer boundaries are excluded from the calculation of the director **n** in the time-stepping (the values are already known), there is no need to calculate the derivatives of **n** with respect to x or y on those nodes. Only the derivatives of φ for vertices $\times_3$ and $\times_4$ are needed to be calculated with care if they are not covered by electrode nodes.

First, let us deal with the first derivatives of potential φ and director **n** with respect x. For a node, say, l, on the left-hand side boundary, the forward difference discretisation is used and for a node on the right-hand side boundary, say, $l+N_{\Delta x}$, the backward difference formula is used. Note that in neither case can the central difference formula be employed!

Second, for the derivatives of **n** with respect to y on any other node on the left-hand and right-hand side boundaries, the central and finite difference formula can be directly applied without any problem and for φ on nodes $\times_3$ and $\times_4$, backward differences can be used.

Third, for the second derivative of **n** with respect to x, the following difference formula can be derived:

$$\left.\frac{\partial^2 n}{\partial x^2}\right|_l = \frac{n(l+2)-2n(l+1)+n(l)}{(\Delta x)^2} \tag{96}$$

for node on the left-hand side (see Figure 17) and

$$\left.\frac{\partial^2 n}{\partial x^2}\right|_{l+N_{\Delta x}} = \frac{n(l+N_{\Delta x})-2n(l+N_{\Delta x}-1)+n(l+N_{\Delta x}-2)}{(\Delta x)^2} \tag{97}$$

for node on the right-hand side.

(d) Neumann boundary condition

If a LCD cell consists of several regions, each containing different dielectric material, then some physical properties should be still continuous on the interface when crossing from one medium to another. Computationally that means $n(l+1)=n(l)$ or $n(l+N_{\Delta x})=n(l+N_{\Delta x}-1)$ on the adjacent two nodes on the boundaries, which stems from its definition: $\partial_{\mu} n=0$. This is the so-called Neumann condition, or second type of boundary condition. All those nodes are also identified and stored by the Subroutine **BOUNDID**. All arguments in the Subsection (c) apply to this section but with a replacement by the condition of $n(l+1)=n(l)$ or $n(l+N_{\Delta x})=n(l+N_{\Delta x}-1)$. Therefore, in this case, equations (96) and (97) become:

$$\left.\frac{\partial^2 n}{\partial x^2}\right|_l = \frac{n(l+2)-n(l+1)}{(\Delta x)^2} = \frac{n(l+2)-n(l)}{(\Delta x)^2} \tag{98}$$

for any node on the left-hand side boundary and

$$\left.\frac{\partial^2 n}{\partial x^2}\right|_{l+N_{\Delta x}-1} = \frac{n(l+N_{\Delta x}-2)-n(l+N_{\Delta x})}{(\Delta x)^2} = \frac{n(l+N_{\Delta x}-2)-n(l+N_{\Delta x}-1)}{(\Delta x)^2} \tag{99}$$

and all forward and backward differences, i.e., the first derivatives vanish on the relevant boundary nodes as required by Neumann condition.

(iv) Reduction of the size of matrix A

According to the above discussion on all boundary conditions, it has been clear that the values of potential and director on all those boundary nodes are fixed or related to each other, therefore the actual number of unknowns can be reduced from the original N_p to N_p', hence the rank of the matrix A. The original $N_p \times N_p$ eigenvalue problem (85) now becomes a problem of solving a lower ranked $N_p' \times N_p'$ linear algebraic system (86). In this way, the workload for the computer is reduced and hence the CPU time.

The procedure is implemented by the Subroutine **BOUNDV**.

(v) Computer program structure

In what follows, the underlined bold phrases in the brackets denote the relevant subroutines.

(1) Reading in input data (**READING**)

(2) Set boundary and initial conditions for directors and the potential, for example, let applied voltage $\varphi(z=d_1;t)=V_1$, $\varphi(z=d_2;t)=V_2$, $\varphi(d_1<z<d_2;t=0)$=*(variation linearly in z from* V_1 to V_2*)*; and director field $n(z=d_1;t)$=*(pre-tilt,*$twist_1$*)* and $n(z=d_2,;t)$=*(pre-tilt,*$twist_2$*)*, $n(d_1<z<d_2$ *; t=0)=(pre-tilt, twist angle linear variation in z from* $twist_1$ *to* $twist_2$*)* (**INIVAL**, **BOUNDID**)

(3) Determine sparsity pattern (**SPARS**)

(4) Start the time stepping process

(5) Calculate potential field $\{\varphi\}$ with fixed directors distribution using the procedure described in 4.3.5 (**MATV**, **BOUNDV**, **MA48AD**,**MA48BD**,**MA48CD**,**NEWV**)

(6) Calculate director field $\{\mathbf{n}\}$ with fixed potential obtained in (5) using the procedure given in 4.3.6 (**TIMENXNYNZ**)

(7) Check to see if the fields: $\{\mathbf{n}\}$ and $\{\varphi\}$ are convergent to the given tolerance. If yes, go to next procedure (8). If no, go back to (5) to repeat until a self-consistent solution is found for $\{\mathbf{n}\}$ and $\{\varphi\}$(**NORMNXYZ**)

(8) Snapshot request. If a snapshot is needed then go to process (9) to output the intermediary results, if not, then do next time step, i.e., repeat the processes (5) to (7).

(9) Output intermediary/final results. If it is not the final time step, then do next time step, i.e., go back to repeat (5) to (8) until the final time step is reached and finally result is stored.

Figure 18 shows the complete flowchart of this procedure:

(vi) Flowchart

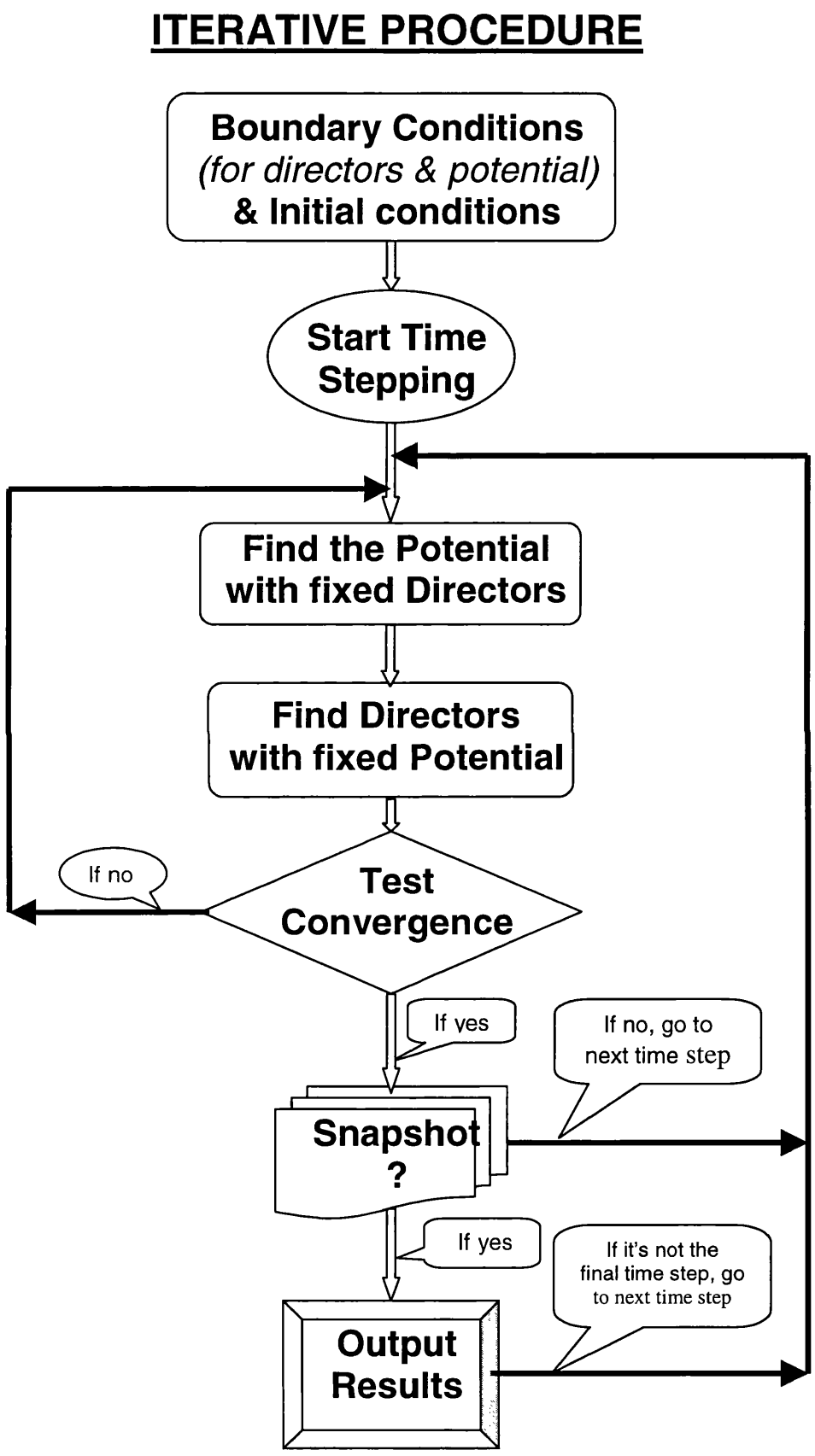

Figure 18 A flowchart for solution of the dynamic model

5.2.3. Results and discussions

Some simulation results for a typical LCD cell are shown and discussed in this section. The cell parameters and geometry and other parameters used in the modelling are given in Table 2 below.

Pixel voltage[v]	Bus voltage[v]	LC cell gap[μm]	K [pN]	$\varepsilon_\perp$	$\Delta\varepsilon$	γ [Pa•s]	θ-method θ	n_o(LC)
[+4, -4]	[+6, -4]	5	13.0	3.1	5.2	0.123	0.5	1.4794
Pre-tilt angle(θ)	Twist angle(φ) (bottom)	Twist angle(φ) (top)	Time step(Δt) length[μs]		Pixel voltage period[s]		Bus voltage period[μs]	n_e(LC)
4°	45°	-45°	5		1/30		60	1.5763
Geometry of the LCD cell and mesh resolution								λ[nm]
$[x_1, x_2]$ [μm]	$[y_1, y_2]$ [μm]	Pixel electrode	Bus electrode		Δx	Δz	Pixel & bus separation	
[-45, 45]	[-2.5, 2.5]	48μm	6μm		1.5	0.25	6μm	589.0

Table 2 Parameters used in the modelling.

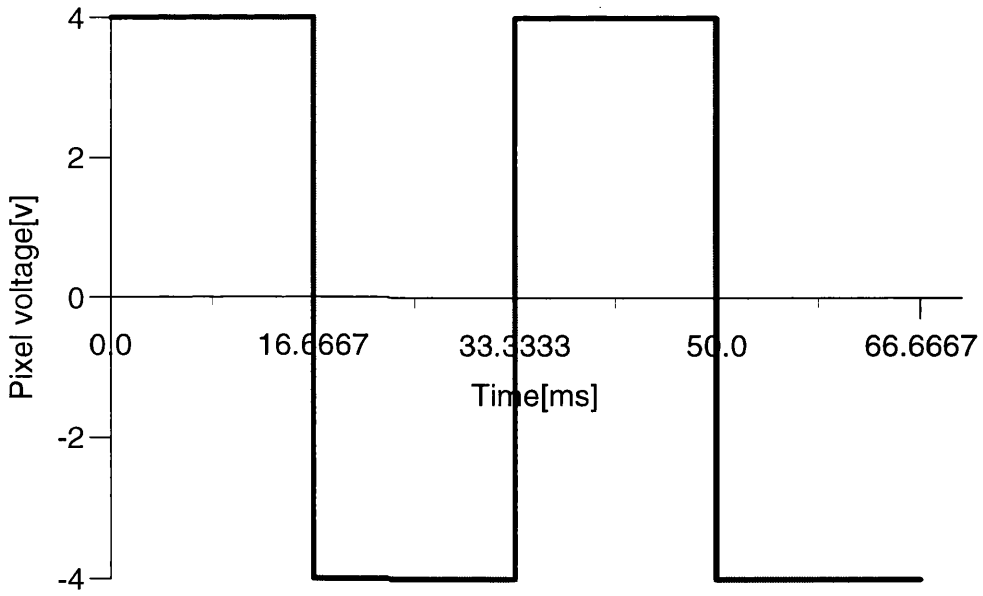

Figure 19 Pixel voltage waveform used in modelling for the LCD cell as specified in Table 2

A schematic diagram of the cell can be seen superposed to the potential and director results in Figure 21.

Pixel and bus voltage waveforms are shown in Figure 19 and Figure 20. Note that bus voltage pattern is not symmetric and chosen to vary from $+6V$ to $-4V$ as usually happens in real display device.

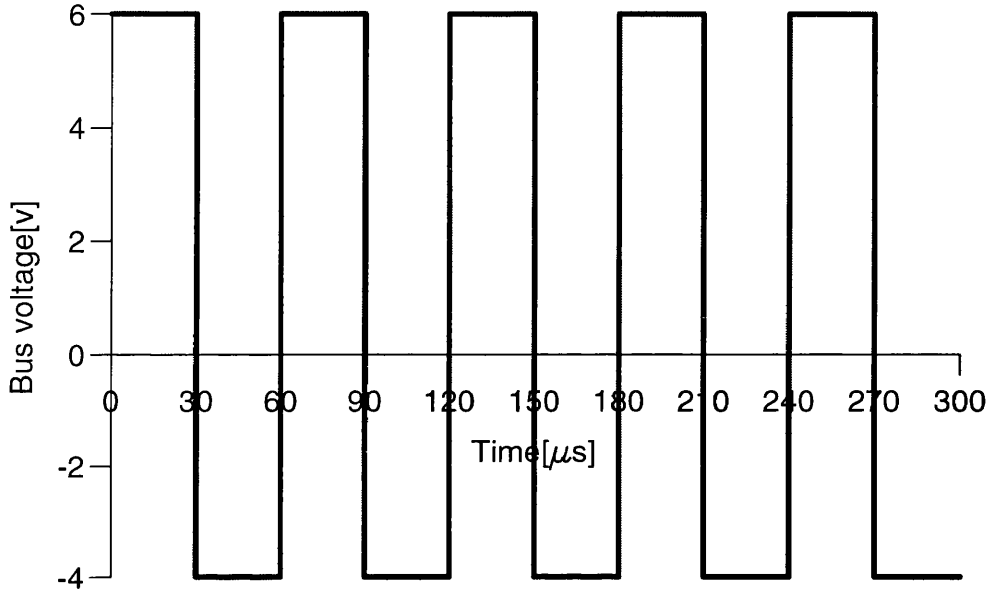

Figure 20 Bus voltage used in modelling for the LCD cell as specified in Table 2

(i) Evolution of director and potential fields

In order to study the evolution of potential and director fields with time and examine the formation of defects, 4 snapshots have been taken which correspond, respectively, to the particular time points: t=8.33ms, 16.66ms, 33.32ms, and 66.64ms. Respective director and potential field spatial distributions are given in Figure 21 (a)-(d).

It can be seen from those figures that with the time progressing, the system evolves from a partially switched state to the fully switched state with the tilt angle of the director increased from initial 4° to nearly vertical under the electrodes. The existence of the bus electrodes causes the distortion of the potential field and the discontinuity (disclination) of the director orientation under the edges of the pixel electrode and the gaps between bus electrodes and the pixel electrode, and the structure of distortion does not appear symmetrically over the left-hand gap/edge and right-hand gap/edge. After two time frames, the system approaches stable state, the potential tends to assume a symmetric distribution, while the director [Figure 21 (d)] does not. As a

result, the defect is permanently left under the right-hand side edge of the pixel electrode. This is clearly depicted in the curve of the transmittance versus position as shown in the Figure 22 (a)-(d) below.

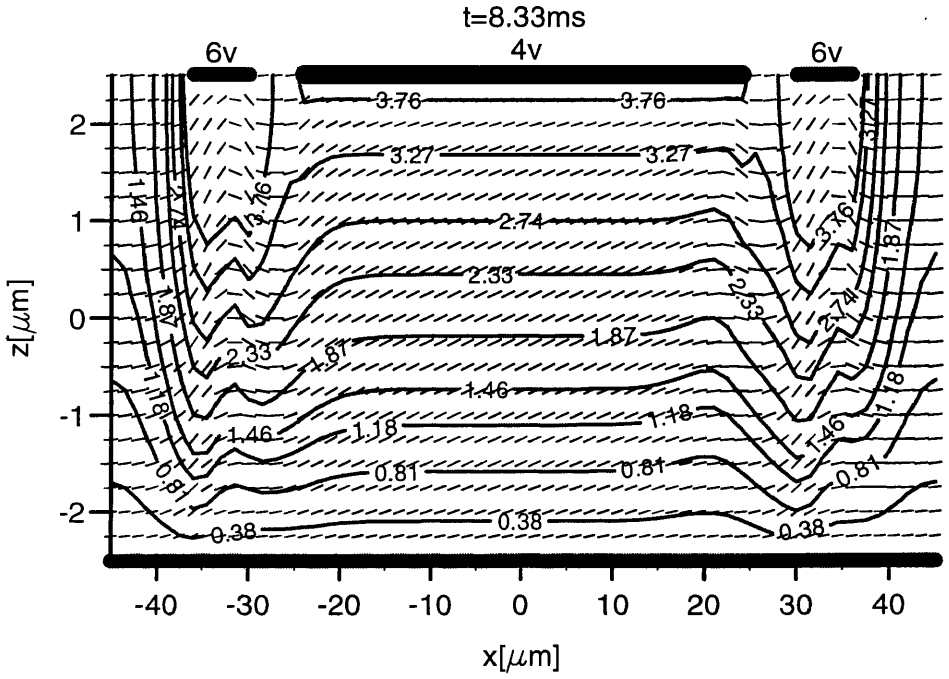

(a)

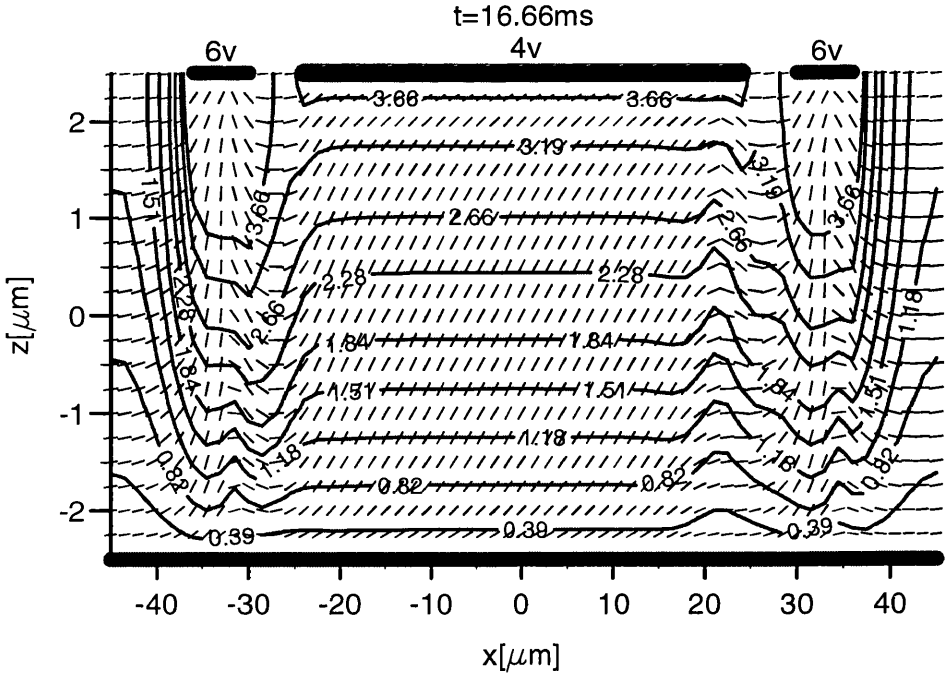

(b)

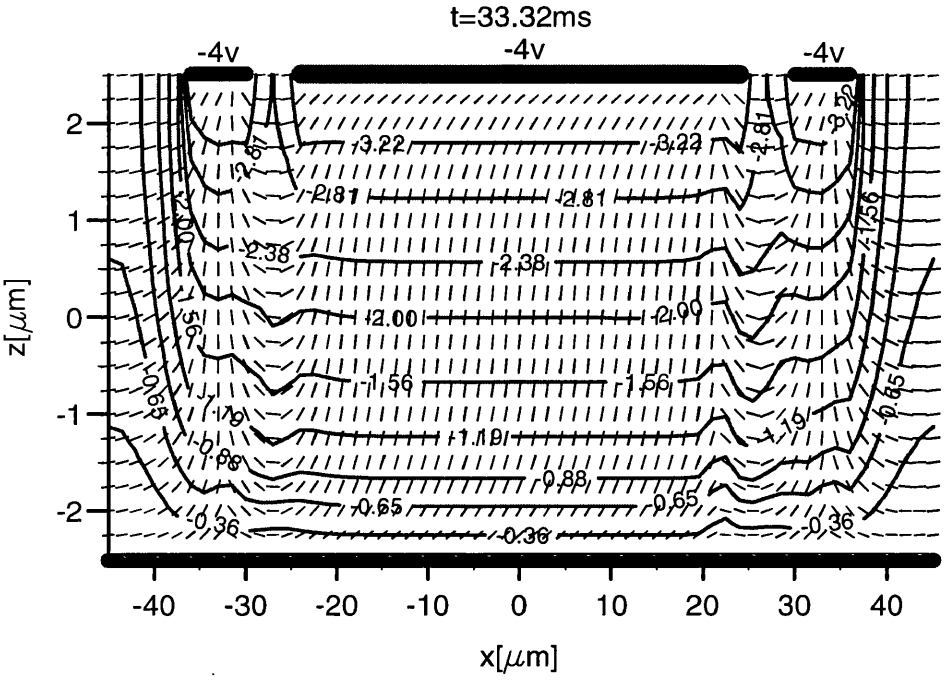

(c)

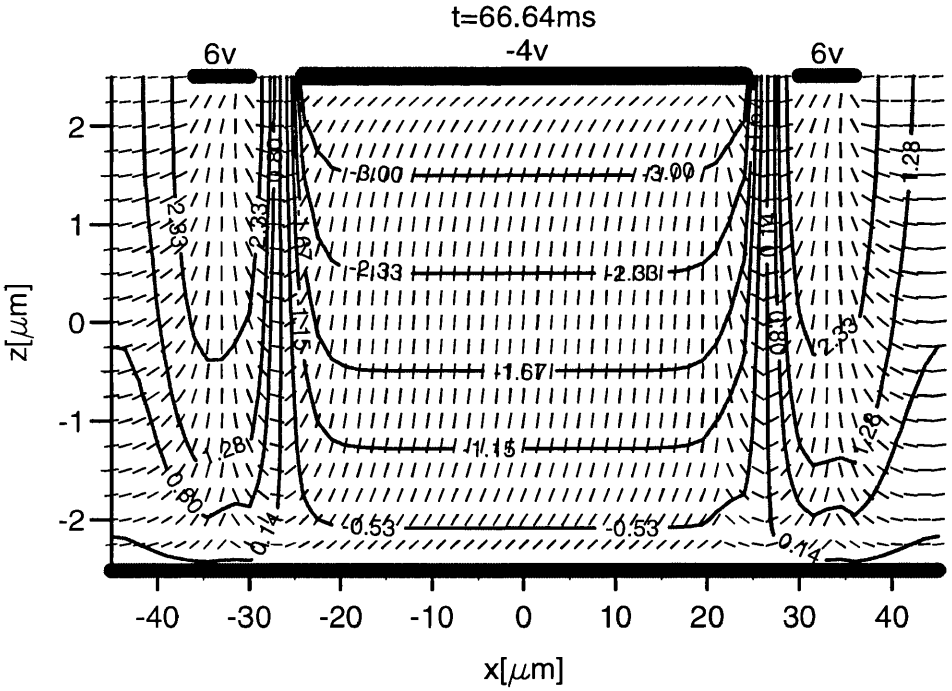

(d)

Figure 21 Evolution of potential and director fields. Snapshot at *t*=8.33ms (a), 16.66ms (b), 33.32ms (c), and 66.64ms (d)

(ii) Evolution of transmittance spatial profile

The next set of figures shows the effect of the distortion resulting from the bus electrodes on transmittance and hence verifies the asymmetric structure of the director and potential field profiles. When the system is switched on for only quarter of frame time, the transmittance that passes through the pixel electrode is large in magnitude, i.e., system assumes a nearly bright state due to small degree of the tilt of the directors, while under the bus electrodes, system looks dark due to nearly vertical tilt of the directors as shown in the Figure 22(a). The structure of curve also clearly reveals the complexity of the disturbance from the bus electrodes. It is this disturbance or distortion under the edges of the pixel electrode that reduces the usable area of the pixel. As time passes, the earlier complex pattern of the distortion becomes simpler and the transmittance becomes smaller in magnitude because the tilt angle of the director becomes bigger. After switched on for two-frame time, the areas under the pixel electrode and the bus electrodes look dark because the system has become fully switched – the tilt angle of the director now has been nearly vertical to the pixel electrode and the bus electrodes. That means little light passes through because with this large tilt, the twist has become irrelevant and hence has little effect in guiding the light. In contrast, the pixel edges and the gaps look bright because of the existence of the discontinued directors, i.e., disclination which are not vertically tilted and therefore allow the light to pass through by the guidance of the twist. This reduces the designed range of the pixel from 48μm (–24μm to 24μm) to a usable range about 43μm (-23μm to 20μm) as shown in the Figure 22 (d). Furthermore, the asymmetric shape of the transmittance curve along x is visible due to discontinuity of directors under the edges of the pixel and the gaps. This kind of discontinuity means the abrupt changes in the orientations, i.e., tilt and the twist angles of the directors. Different orientations exert different influence on the propagation of the incident light.

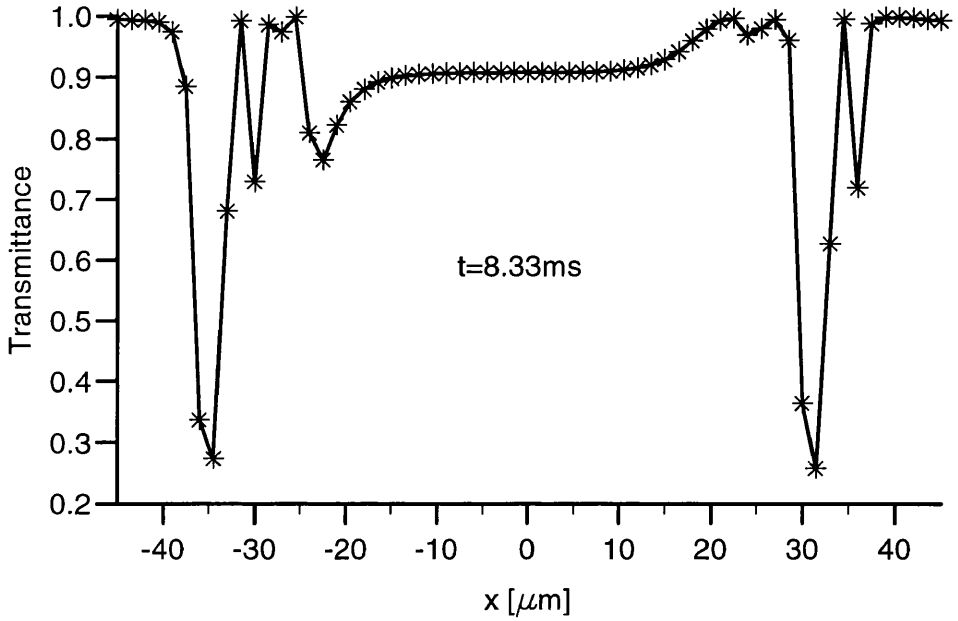
Transmittance
1.0
0.9
0.8
0.7
0.6
0.5
0.4
0.3
0.2
t=8.33ms
-40
-30
-20
-10
0
10
20
30
40
x [μm]

(a)

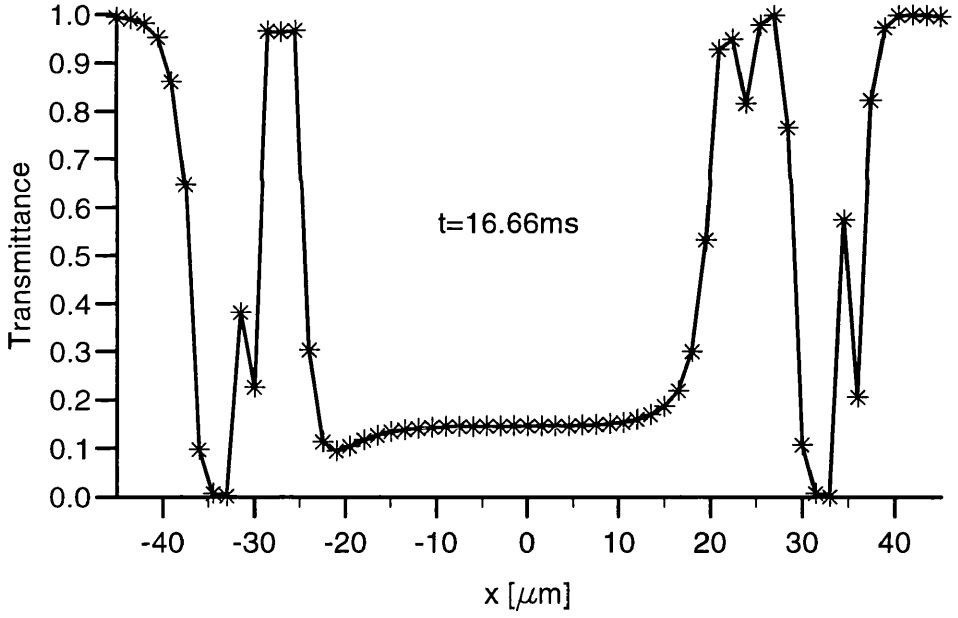
Transmittance
1.0
0.9
0.8
0.7
0.6
0.5
0.4
0.3
0.2
0.1
0.0
t=16.66ms
-40
-30
-20
-10
0
10
20
30
40
x [μm]

(b)

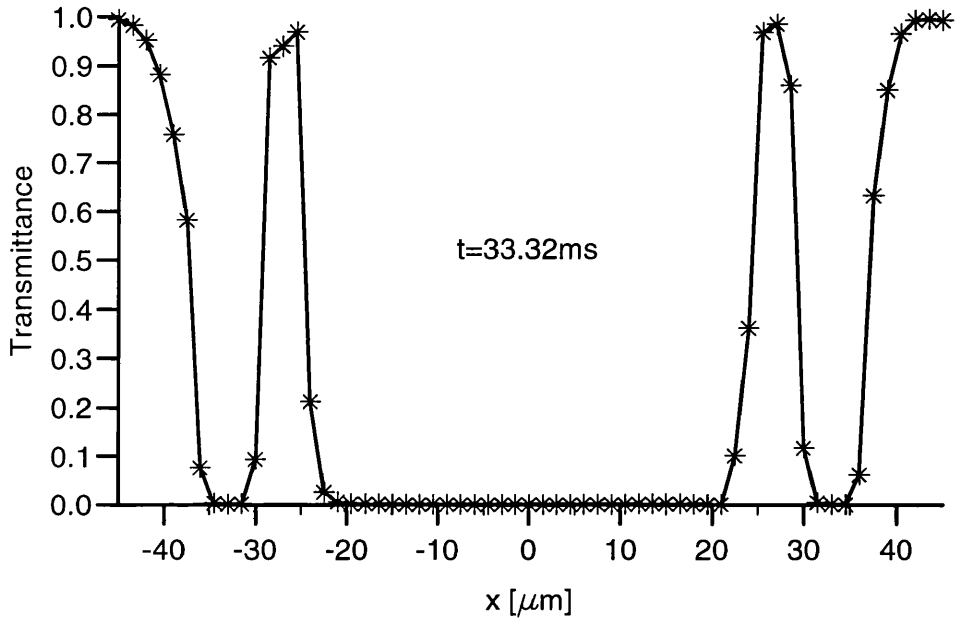

(c)

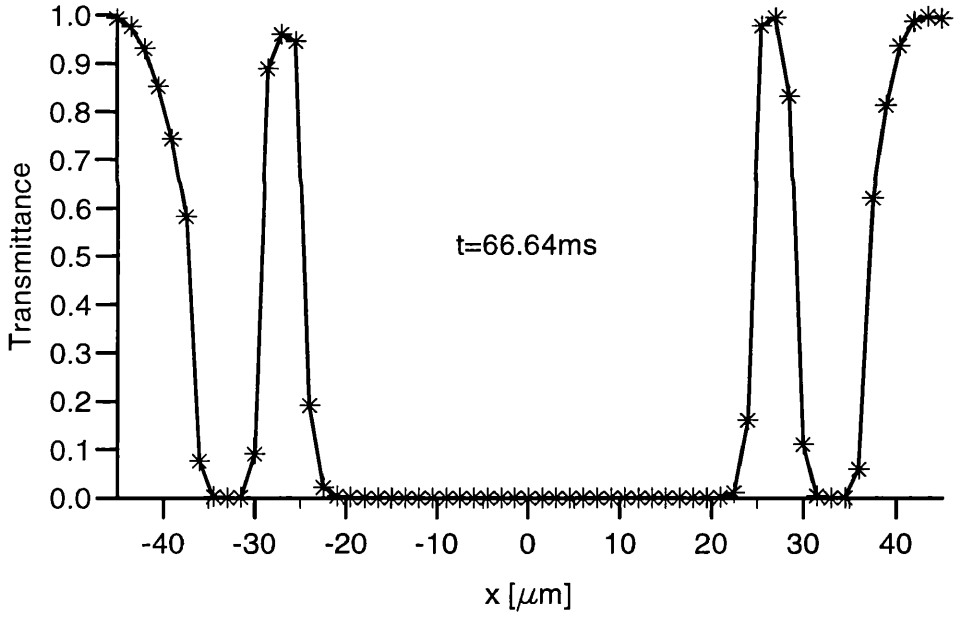

(d)

Figure 22 Time evolution of spatial profiles of normal transmittance. 4 snapshots corresponding to Figure 21 (a)-(d)

(iii) Dynamic behaviour of tilt angle

In order to help understand the process of the system switching , the variation in tilt angle of a director with time is studied and plotted as below. The director is picked from position (0,0), i.e., in the middle of the cell (mid-plane) as a representative point

because all other points centred there, under the pixel electrode, should behave in a similar way in terms of tilting. It can be seen that the tilt angle increases with the time from initial 4° to the limit 85° during the time span of three quarters of a frame time (25ms). After that it keeps this limit, indicating the system has been fully switched as verified by the average transmittance dynamic curve (Figure 24) and the capacitance dynamic curve (Figure 25).

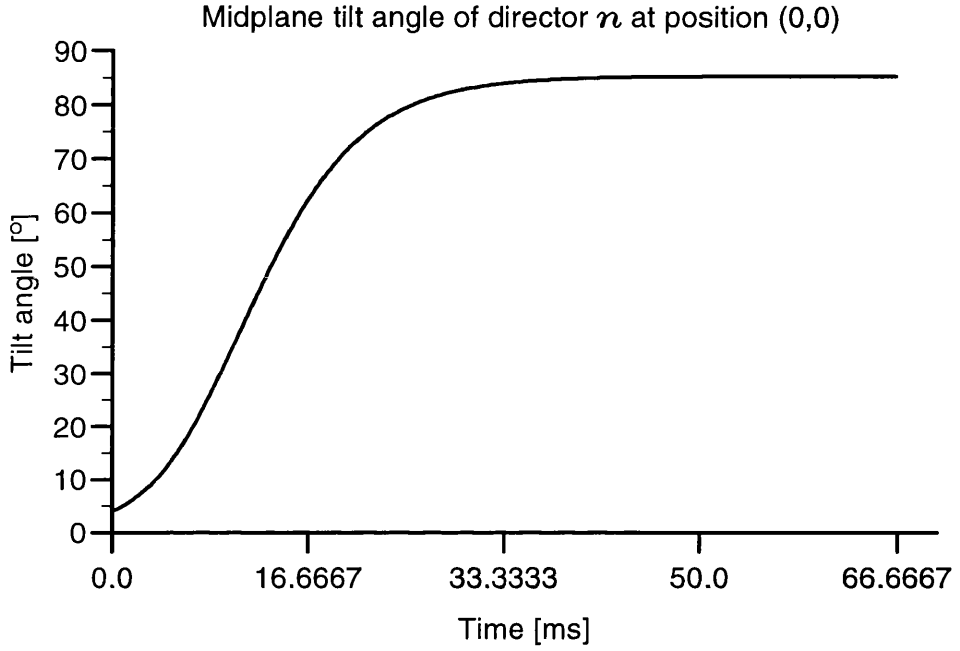

Figure 23 Dynamic behaviour of the tilt angle of a director at the specified space point of (0,0) under the pixel (in the middle of the LCD cell)

(iv) Dynamic behaviour of average transmittance

Figure 24 below shows the dynamic behaviour of the normal incident transmittance averaged over the undistorted range from -23μm to 20μm along x under the pixel electrode. It can be see that after about three quarters of a frame time (25ms), the system become fully switched. The state goes from bright (the highest transmittance) to near dark (the lowest transmittance). The process of the change in the states corresponds to that of the change in tilt angle of director as shown in the Figure 23

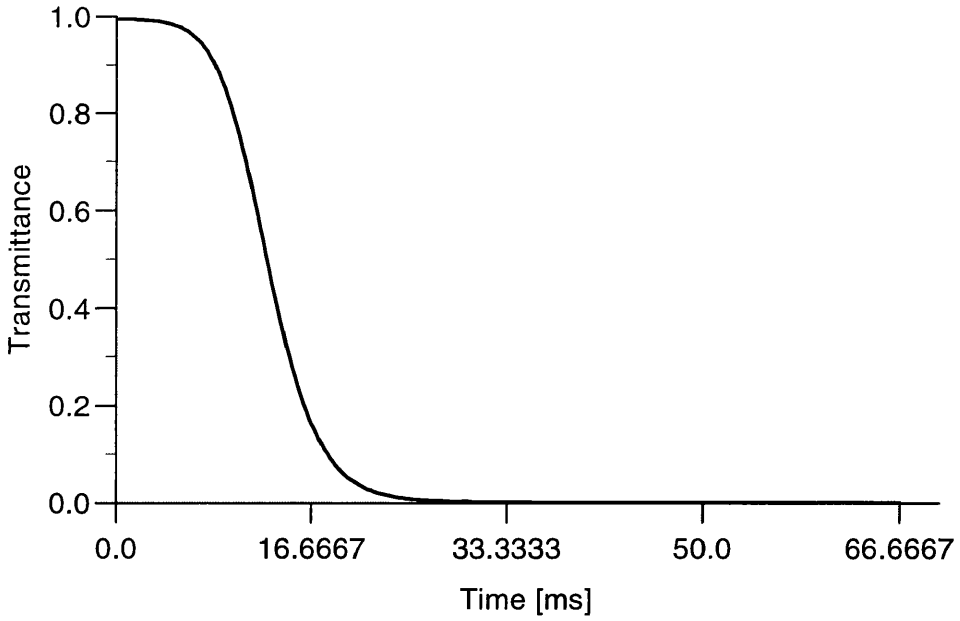

Figure 24 Average normal-incident transmittance versus time

(v) Dynamic behaviour of pixel capacitance

Figure 25 shows the dynamic behaviour of the pixel self-capacitance. Because the LCD cell can be regarded as a capacitor, its capacitance can be calculated in the way explained in the following Chapter in details. This calculation has been introduced here because the fixed voltage (direct driven) model as explained before has been realised as a special case of the constant charge model which has as a necessary step the dynamic calculation of all capacitances. Since the capacitance is proportional to the permittivity $\overline{\overline{\varepsilon}}$, while $\overline{\overline{\varepsilon}}$ is proportional to the anisotropy $\Delta\varepsilon$ which increases with order parameter S, the greater the tilt angle of the director, the more anisotropic the system and hence, bigger the value of the order parameter S [Eq. (1)], so the capacitance is expected to increase with time until when the director **n** becomes fully switched, i.e., vertically tilted. This is also supported by the dynamic behaviour of the tilt angle as shown in the Figure 23. Again, after about 25ms (three-quarters of a frame time), the capacitance approaches a constant value.

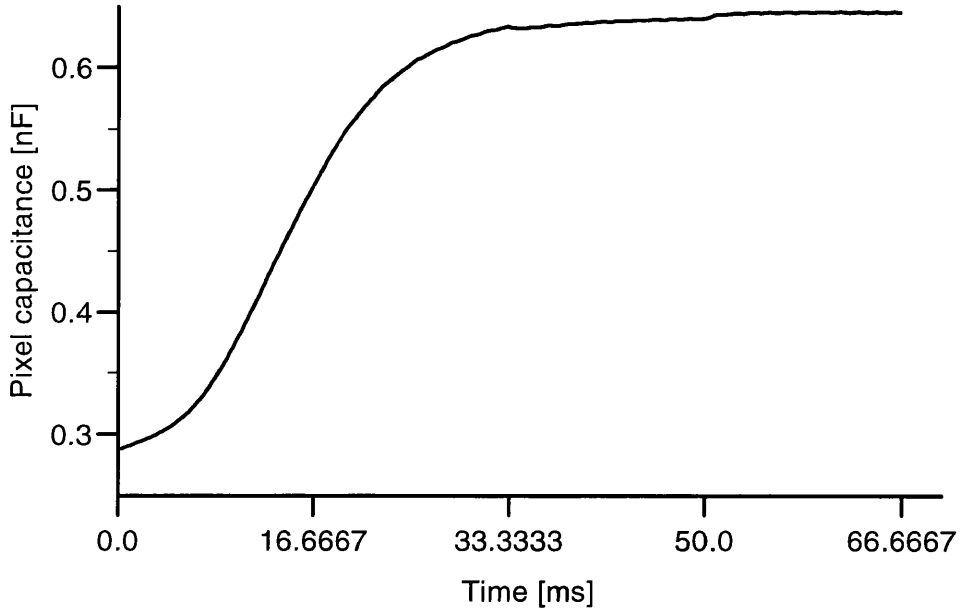

Figure 25 Pixel self-capacitance versus time

(vi) Dynamic behaviour of pixel and bus charges

Figure 26 shows the dynamic behaviour of the charges that deposit in the pixel and bus electrodes when the external fields are applied. The way of calculating those charges is addressed in the following Chapter. According to $CV=Q$, under the constant voltage condition (except the polarity), an increase in the capacitance with time brings about the corresponding increase in the charges. This is clearly shown in the Figure. The charge both in the pixel and bus electrodes increase in magnitude with time until they reach constant levels respectively – a saturated point at which the capacitance becomes a constant – the system arrives at the stable state on which the director becomes fully switched and the potential exhibits a stable distribution. Again, the time when this occurs is at about one frame time in this case. Note that the quick fluctuation of the charge in the pixel electrode around the average value is solely due to the rapid change in the polarity of the bus voltage. Because the sign of the bus voltage is alternating rapidly so are the charges in the bus electrodes, this results in a corresponding change in the electrical field distribution near and under the edges of the pixel electrode. Therefore, this change is eventually embedded into the average total charge of the pixel electrode. As is shown later, if the polarity of the bus voltage is fixed, this oscillating behaviour superposed onto the pixel charge will disappear.

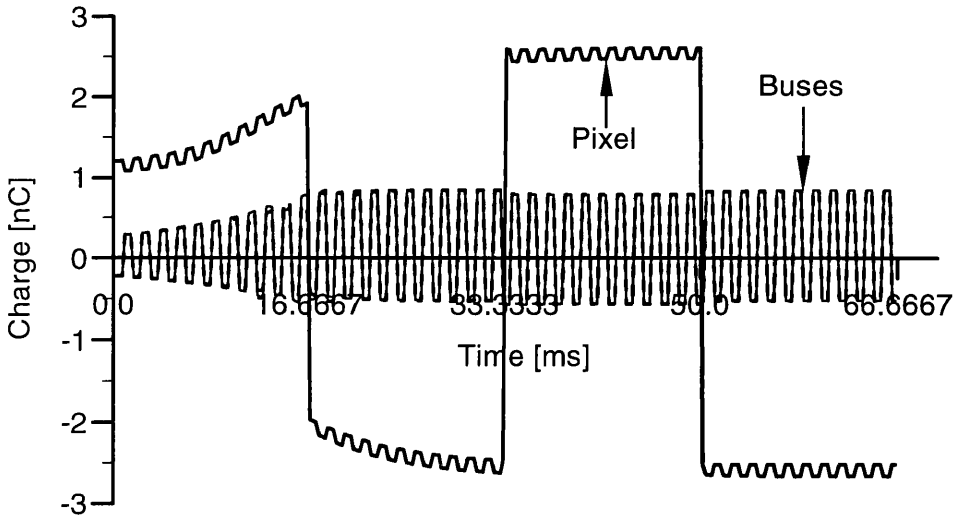

Figure 26 The dynamic behaviour of charges in pixel and bus electrodes

As we can see from the above results, if the voltage is constant, then the charge will vary, therefore, it is expected (and shown in the following Chapter) that if the charge is constant, then the voltage will be varying.

6. Constant charge model

In the case of the fixed voltage mode, as discussed in the previous chapter, the pixel voltage is known (i.e., given beforehand) at all times. What was done was to calculate the director and potential temporal-spatial distributions under this given voltage condition and then from this, to obtain information about the formation and evolution of the defects and optical properties such as viewing angle characteristics and transmittance of the system. In the case of TFT-driven devices, the source voltage is applied (connected) to the pixel electrode for only a line duration t_c of about 15μs ~ 30μs, a very small fraction of the half frame time.

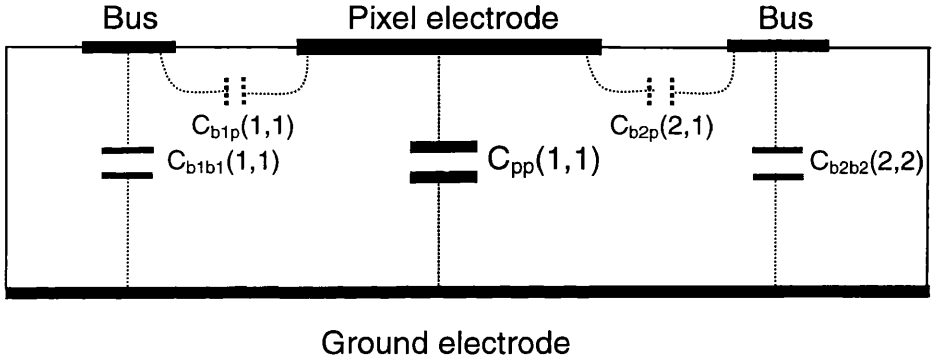

Figure 27 A schematic diagram of equivalent circuit of a LCD cell

After this time t_c the pixel voltage becomes unknown (floating) for the rest of half-frame time although the charge Q deposited in the pixel cell electrode during the connection t_c remains constant. To be able to calculate how directors and potential distributions vary in time, it is necessary to calculate first the temporal variation of the pixel voltages. This is done at the end of each time step in our method of calculation. First, in order to obtain the floating voltage V for next time step, the knowledge of capacitance matrix of the cell $\boldsymbol{C}$ is needed. Second, this capacitance $\boldsymbol{C}$ depends on the dielectric property of the materials of the LCD cell or director field profile. Third, the mentioned director profile in turn is pre-determined by the floating pixel voltage while the latter is not yet known and is exactly what is being found! This gives rise to another set of iterations embedded in the time stepping process. The capacitance matrix is calculated using a perturbation method and the process will be explained using as an example the LCD cell with one pixel and two bus electrodes and its equivalent circuit shown the Figure 27.

6.1. Prediction of floating voltage

Of the many possible combinations of pixel and bus electrodes, only 3 will be analysed here. The first and the simplest has only one pixel electrode (and no buses) corresponding, for example, to a test cell. The second has one pixel electrode and 2 buses as shown in Figure 27. The last consists of 2 pixels and 1 bus as in the region between 2 adjacent cells in a display. For all the above configurations the storage capacitor(s) C_{ext} connected in parallel to the pixel(s) can be included as shown in Figure 3.

6.1.1. Theoretical formulation (I) - without external storage capacitor

(i) Notation

Let us define some notation first.

$C_{pp}(i,j)$ – pixel capacitance matrix. If $i \neq j$, it denotes mutual capacitance between pixel electrode i and pixel electrode j, if $i=j$, it denotes pixel electrode self capacitance, $i,j = 1,2,\ldots n_p$, n_p, the number of pixel electrodes in the cell;

$C_{bb}(i,j)$ - bus capacitance matrix. Likewise, if $i \neq j$, it denotes mutual capacitance between bus electrode i and bus electrode j, if $i=j$, it denotes bus electrode self capacitance, $i,j = 0,1,2,\ldots n_b$, n_b, the number of bus electrodes; If no bus, i.e., $i, j=0$, this matrix does not exist.

$C_{pb}(i,j)$ – pixel-bus mutual capacitance matrix between *pixel* electrode i and *bus* electrode j. $i=1,2,\ldots n_p$, $j=0,1,2,\ldots n_b$. If no bus, i.e., $j=0$, this matrix does not exist.

$C_{bp}(i,j)$ – bus-pixel mutual capacitance matrix between *bus* electrode i and *pixel* electrode j. $i=0,1,2,\ldots n_b$, $j=1,2,\ldots n_p$. If no bus, i.e., $i=0$, this matrix does not exist.

$V_p(i)$ – floating voltage to be found for pixel electrode i ($i=1,2,\ldots n_p$).

$V_b(i)$ – voltage that is applied to the bus electrode i ($i=1,2,\ldots n_b$) and is known.

$Q_p(i)$ – charge that is deposited in pixel electrode i ($i=1,2,\ldots n_p$) at the time $t = k\frac{T_p}{2} + t_c$ (here $k=0,1,2,\ldots$, T_p is the full frame time), *immediately* before the electrode de-links to the source. It is assumed not varying with the time until the source voltage changes polarity.

$Q_b(i)$ – charge that is deposited in bus electrode i (i=1,2,...n_b) and is known.

Not that both indices i and j appearing above are local or subspace (pixels or buses)-referred, i.e., they are defined in the spaces ($n_p \times n_p$) or ($n_b \times n_b$) or ($n_p \times n_b$)

$C(i,j)$, $V(i)$, and $Q(i)$ - global or integrated capacitance, voltage and charge matrices defined with respect to the whole *space* consisting of n_p+n_b. Therefore the indices i,j now take the values of 1,2,...n_p,n_p+1,...n_p+n_b, in a way that the number of bus electrodes n_b is appended to the number of the pixel electrodes n_p.

(ii) General formulation

Assuming that there are n_p pixel and n_b bus electrodes in the LCD cell in question, then the problem concerning how to find the floating voltages that will be applied to the pixel electrodes n_p turns to solve the matrix equation

$$\boldsymbol{C}(t)\boldsymbol{V}(t)=\boldsymbol{Q}(t) \tag{100}$$

or

$$\begin{bmatrix} C(1,1) & C(1,2) & C(1,3) & \cdot \\ C(2,1) & C(2,2) & C(2,3) & \cdot \\ C(3,1) & C(3,2) & C(3,3) & \cdot \\ \cdot & \cdot & \cdot & \cdot \end{bmatrix} \begin{bmatrix} V(1) \\ V(2) \\ V(3) \\ \cdot \end{bmatrix} = \begin{bmatrix} Q(1) \\ Q(2) \\ Q(3) \\ \cdot \end{bmatrix} \tag{101}$$

Here the array indices i and j in $C(i,j)$ are defined in the whole space $(n_p+n_b)\times(n_p+n_b)$ and are arranged such that the indices for the buses follow the indices for the pixels, i.e., i,j=1,2,...n_p,n_p+1,n_p+2,...n_p+n_b. Since (1) all voltages applied to the bus electrodes are known, (2) the charges deposited in the latter can be calculated, and (3) the charges in pixel electrodes are known also when the pixel electrodes become disconnected to the data line, then the floating voltage that will appear in the pixel electrodes can be calculated as long as all self- and mutual capacitances are given. However a quick and intuitive examination of expression (101) reveals that the capacitance matrix $\boldsymbol{C}$ can be partitioned or decomposed into blocks that are defined in the relevant subspaces according to the known data and unknowns. The benefit from doing so is that only relevant elements of the $\boldsymbol{C}$ matrix are needed to be calculated in order to obtain the complete information about the floating voltages. That means computing time will be saved as calculating the elements of $\boldsymbol{C}$ is a very expensive task. Following this, equation (101) can be rewritten as

$$\begin{bmatrix} \boldsymbol{C}_{pp} & \boldsymbol{C}_{pb} \\ \boldsymbol{C}_{bp} & \boldsymbol{C}_{bb} \end{bmatrix} \begin{bmatrix} \boldsymbol{V}_p \\ \boldsymbol{V}_b \end{bmatrix} = \begin{bmatrix} \boldsymbol{Q}_p \\ \boldsymbol{Q}_b \end{bmatrix} \tag{102a}$$

or

$$\begin{bmatrix} C_{pp}(1,1) & C_{pp}(1,2) & \cdot & C_{pb}(1,1) & C_{pb}(1,2) & \cdot \\ C_{pp}(2,1) & C_{pp}(2,2) & \cdot & C_{pb}(2,1) & C_{pb}(2,2) & \cdot \\ \cdot & \cdot & \cdot & \cdot & \cdot & \cdot \\ C_{bp}(1,1) & C_{bp}(1,2) & \cdot & C_{bb}(1,1) & C_{bb}(1,2) & \cdot \\ C_{bp}(2,1) & C_{bp}(2,2) & \cdot & C_{bb}(2,1) & C_{bb}(2,2) & \cdot \\ \cdot & \cdot & \cdot & \cdot & \cdot & \cdot \end{bmatrix} \begin{bmatrix} V_p(1) \\ V_p(2) \\ \cdot \\ V_b(1) \\ V_b(2) \\ \cdot \end{bmatrix} = \begin{bmatrix} Q_p(1) \\ Q_p(2) \\ \cdot \\ Q_b(1) \\ Q_b(2) \\ \cdot \end{bmatrix} \tag{102b}$$

Here, as mentioned before, all block matrices in the above expression are confined to their respective subspaces [($n_p \times n_p$), ($n_b \times n_b$), ($n_p \times n_b$)]. Expanding the above matrix gives rise to:

$$\boldsymbol{C}_{pp}\boldsymbol{V}_p + \boldsymbol{C}_{pb}\boldsymbol{V}_b = \boldsymbol{Q}_p \tag{103}$$

$$\boldsymbol{C}_{bp}\boldsymbol{V}_p + \boldsymbol{C}_{bb}\boldsymbol{V}_b = \boldsymbol{Q}_b \tag{104}$$

Clearly, both the above equations lead to the solution for the $\boldsymbol{V}_p$. However, equation (103) is chosen for this purpose because of two reasons: (a) it is directly related to the constant charge condition through $\boldsymbol{Q}_p$ and (b) due to small physical dimension of bus electrodes, there are inevitably some numerical errors occurring in calculating $\boldsymbol{C}_{bb}$ and $\boldsymbol{Q}_b$ if Eq. (104) were used.

From Eq. (103), we have

$$\boldsymbol{V}_p = \boldsymbol{C}_{pp}^{-1}\left(\boldsymbol{Q}_p - \boldsymbol{C}_{pb}\boldsymbol{V}_b\right) \tag{105}$$

or

$$\begin{bmatrix} V_p(1) \\ V_p(2) \\ \cdot \\ \cdot \end{bmatrix} = \begin{bmatrix} C_{pp}(1,1) & C_{pp}(1,2) & \cdot & \cdot \\ C_{pp}(2,1) & C_{pp}(2,2) & \cdot & \cdot \\ \cdot & \cdot & \cdot & \cdot \\ \cdot & \cdot & \cdot & \cdot \end{bmatrix}^{-1} \begin{bmatrix} Q_p(1) - C_{pb}(1,1)V_b(1) - C_{pb}(1,2)V_b(2) - \cdots \\ Q_p(2) - C_{pb}(2,1)V_b(1) - C_{pb}(2,2)V_b(2) - \cdots \\ \cdot \\ \cdot \end{bmatrix} \tag{106}$$

here $\boldsymbol{C}_{pp}^{-1}$ denotes the inverse of the matrix $\boldsymbol{C}_{pp}$. It can be seen that the existence of bus voltages and mutual capacitance between pixel and bus gives rise to a correction or

superposition to the situation where there does not exist any bus. Therefore, the behaviour of the bus voltage will be reflected in the pattern of the floating voltage of the pixel as will be seen below.

(iii) One pixel and no buses

This simplest electrode geometry normally appears in a test cell. In this case, the formula for V_p from the above Eq. (106) takes the simplest form:

$$V_p(1) = \frac{Q_p(1)}{C_{pp}(1,1)} \tag{107}$$

(iv) One pixel and two buses

This is the most commonly seen electrode configuration. According to Eq. (106), the expression for the floating pixel voltage takes the form of

$$V_p(1) = \frac{1}{C_{pp}(1,1)}\left[Q_p(1) - C_{pb}(1,1)V_b(1) - C_{pb}(1,2)V_b(2)\right] \tag{108}$$

Note that indices i and j in the $C_{pb}(i,j)$ are local. The first index i labels pixel electrode (i=1 in this case) and the second index j labels bus electrode (j=1,2 in this case). It can be seen that in order to get the floating voltage V_p for the pixel, not only the pixel self-capacitance is needed, but the mutual capacitances C_{pb} between pixel and the two bus electrodes need to be calculated as well.

(v) Two pixels and one bus

This model is a simplified electrode configuration where the physical dimension of each pixel electrode in a periodic arrangement is too big to be convenient for a complete computer modelling. By keeping only part of each pixel electrode and one

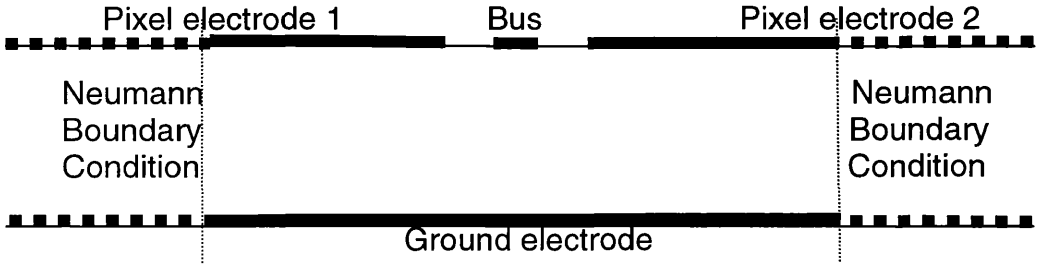

Figure 28 A simplified model for the geometry with very large pixel electrode periodically aligned

complete bus electrode between two pixel electrodes and using a Neumann boundary condition, the modelling by computer is then feasible with the geometry as shown in Figure 28.

In this case, the explicit expression for pixel voltages according to Eq. (106) is given by

$$V_p(1)=\frac{C_{pp}(2,2)\left[Q_p(1)-C_{pb}(1,1)V_b(1)\right]-C_{pp}(1,2)\left[Q_p(2)-C_{pb}(2,1)V_b(1)\right]}{C_{pp}(1,1)C_{pp}(2,2)-C_{pp}(1,2)C_{pp}(2,1)} \tag{109}$$

$$V_p(2)=\frac{-C_{pp}(2,1)\left[Q_p(1)-C_{pb}(1,1)V_b(1)\right]+C_{pp}(1,1)\left[Q_p(2)-C_{pb}(2,1)V_b(1)\right]}{C_{pp}(1,1)C_{pp}(2,2)-C_{pp}(1,2)C_{pp}(2,1)} \tag{110}$$

6.1.2. Theoretical formulation (II) - with external storage capacitors

In real TFT LCD devices, an external storage capacitor $C_{ext}(i)$ is usually connected to each pixel i to help keep the pixel voltage constant. This $C_{ext}(i)$ can be regarded as in parallel to the pixel capacitor $C_{pp}(i,i)$ as shown in Figure 3. As a result, the charge is redistributed between the pixel self-capacitance $C_{pp}(i,i)$ and the storage capacitor $C_{ext}(i)$ at each time step while the total charge $Q_{total}(i)$ remains constant, i.e.,

$$Q_{total}(i)=Q_p(i)\big|_t+Q_{ext}(i)\big|_t \equiv Q_0(i)\big|_{t=k\frac{T_p}{2}+t_c,k=0,1,2,\ldots}=Constant(i) \tag{111}$$

Where $Q_p(i)$ can be calculated from the potential distribution, and hence, the charge density on the nodes of the pixel electrode i; $Q_{ext}(i)$ is given by

$$Q_{ext}(i)=C_{ext}(i)V_p(i) \tag{112}$$

Here $C_{ext}(i)$ is a given time-independent quantity, V_p is supposed to be known before the previous time step was finished; and $Q_0(i)$ is the total charge at the time step immediately before the floating process starts and it should be maintained constant for the rest of the half-frame time (typically 8.3333ms less 20μs). It is obtained through the formula

$$Q_0(i)\big|_{t=k\frac{T_p}{2}+t_c}=Q_p(i)\big|_{t=k\frac{T_p}{2}+t_c}+C_{ext}(i)V_p(i)\big|_{t=k\frac{T_p}{2}+t_c} \tag{113}$$

Contrary to the case without external capacitors as discussed in the previous section, the expression (111) tells us that the charge in each pixel electrode is no longer

constant. Instead, it changes with time so as to reflect the re-distribution of the total constant charge Q between C_{pp} and C_{ext}.

Because each storage capacitor C_{ext} is in parallel to the LC pixel equivalent capacitance C_{pp}, the total capacitance for the pixel i is the sum of them:

$$C_{total}(i,i)=C_{pp}(i,i)+C_{ext}(i) \tag{114}$$

By simply doing the following replacements: $C_{pp}(i,i)+C_{ext}(i)=C_{total}(i,i)\rightarrow C_{pp}(i,i)$ and $Q_{total}(i)\rightarrow Q_p(i)$ whenever there are the terms $C_{pp}(i,i)$ and $Q_p(i)$ appearing in all expressions in above section 6.1.1, all formulas there are valid here.

6.2. Calculation of charges Q

6.2.1. Formula for calculating the Q

It has been clear from the above formulations that in order to predict the floating voltage V_p of the pixel electrode, the knowledge of the charges Q_p and Q_b in the pixel and bus electrodes are necessary. Because both the pixel voltage V_p and the capacitance matrix C are unknown, it is not possible to simply apply the formula $CV=Q$ to find the charges Q. However, we can calculate the charges on the electrodes by integrating the surface (line) charge densities obtained by examining the potential distribution in the LC cell. Thus, the total charge on an electrode is given by

$$Q=\int_0^l \sigma(x)dx \tag{115}$$

Where the integration is done along the electrode cross section which is assumed aligned along the x direction and of length l and σ is the line charge density on the electrode. This is determined by the normal component (pointing towards LC cell, i.e., along the direction of the unit vector $\hat{\mathbf{s}}$, i.e., $-\hat{\mathbf{z}}$ in Figure 29) of the electrical displacement vector $\mathbf{D}$ on the electrode layer, i.e.,

$$\sigma=\mathbf{D}\bullet\hat{\mathbf{s}}=-\mathbf{D}\bullet\hat{\mathbf{z}}=-D_z \tag{116}$$

while $\mathbf{D}$ is defined by

$$\mathbf{D}=-\bar{\bar{\varepsilon}}\bullet\nabla\phi \tag{117}$$

Here ϕ is the potential and $\bar{\bar{\varepsilon}}$ is the dielectric tensor which is given by (58). It is straightforward to find

$$\sigma = -D_z = \left(\varepsilon_{zx} \underbrace{\frac{\partial \phi}{\partial x}}_{=0} + \varepsilon_{zz} \frac{\partial \phi}{\partial z} \right) = (\varepsilon_\perp + \Delta\varepsilon n_z n_z) \frac{\partial \phi}{\partial z} \tag{118}$$

The condition $\partial\phi/\partial x=0$ is used here because the values of the potential along the electrode direction (i.e., x) are all the same according to the boundary condition.

Inserting expression (118) to the Eq. (115) yields

$$Q = \int_0^l (\varepsilon_\perp + \Delta\varepsilon n_z n_z) \frac{\partial \phi}{\partial z} dx \tag{119}$$

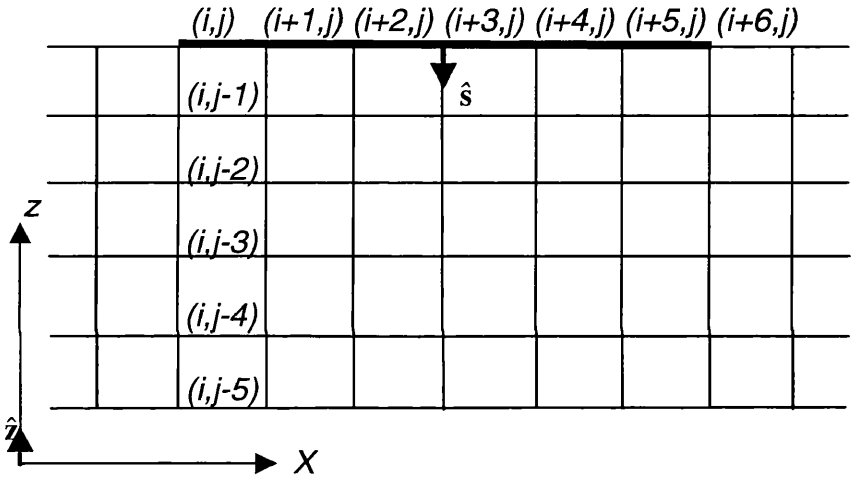

Figure 29 A schematic mesh for calculating the charge on the electrode

Now, by discretising the integral along the electrode nodes as shown in Figure 29 one has

$$Q = \sum_{i=1}^{k_q-1} \left[\frac{\overbrace{(\varepsilon_\perp + \Delta\varepsilon n_z n_z)_{i,j} \left(\frac{\partial \phi}{\partial z} \right)_{i,j}}^{\sigma_i} + \overbrace{(\varepsilon_\perp + \Delta\varepsilon n_z n_z)_{i+1,j} \left(\frac{\partial \phi}{\partial z} \right)_{i+1,j}}^{\sigma_{i+1}}}{2} \right] \Delta x_i$$

$$\equiv \sum_{i=1}^{k_q-1} \underbrace{\left[\frac{\sigma_i + \sigma_{i+1}}{2} \right]}_{\rho_i} \Delta x_i \equiv \sum_{i=1}^{k_q-1} \underbrace{\rho_i \Delta x_i}_{q_i} \equiv \sum_{i=1}^{k_q-1} q_i \tag{120}$$

Here, k_q is the number of nodes on the electrode and k_q-1 is the number of segments; ρ_i denotes the line charge density on the electrode *segment i* which is the arithmetic average of the densities σ on node i and i+1, i.e., $\rho_i=(\sigma_i+\sigma_{i+1})/2$; q_i is the corresponding charge which is simply the density ρ_i times the length of the segment Δx_i. Note that the index j is fixed and confined to the electrode layer only.

The accuracy of the charge calculation can be affected by the following factors:

The quality of the original data ϕ and **n**;

The magnitude of spatial steps Δx and Δz when discretising $\partial\phi/\partial z$;

The way of discretising the derivative $(\partial\phi/\partial z)_{i,j}$ and its accuracy;

The ways of treating the end nodes of the electrode and handling the edge field.

Now let us address some of the above issues:

6.2.2. Formula for calculating $(\partial\phi/\partial z)_{i,j}$

First, let us show how we could derive a general expression for the calculation of $\partial\phi/\partial z)_{i,j}$ and then discuss several typical cases.

(i) General formulation

In order to find the most accurate expression for the numerical calculation of $(\partial\phi/\partial z)_{i,j}$, let us consider the following sequences of Taylor series expansions of potential ϕ around node (i,j) (referring to the Figure 29):

$$\begin{aligned}
\phi_{i,j-1} &= \phi_{i,j} - \left(\frac{\partial\phi}{\partial z}\right)_{i,j}\Delta z + \frac{1}{2!}\left(\frac{\partial^2\phi}{\partial z^2}\right)_{i,j}\Delta z^2 - \frac{1}{3!}\left(\frac{\partial^3\phi}{\partial z^3}\right)_{i,j}\Delta z^3 + \cdots \\
\phi_{i,j-2} &= \phi_{i,j} - \left(\frac{\partial\phi}{\partial z}\right)_{i,j}(2\Delta z) + \frac{1}{2!}\left(\frac{\partial^2\phi}{\partial z^2}\right)_{i,j}(2\Delta z)^2 - \frac{1}{3!}\left(\frac{\partial^3\phi}{\partial z^3}\right)_{i,j}(2\Delta z)^3 + \cdots \\
\phi_{i,j-3} &= \phi_{i,j} - \left(\frac{\partial\phi}{\partial z}\right)_{i,j}(3\Delta z) + \frac{1}{2!}\left(\frac{\partial^2\phi}{\partial z^2}\right)_{i,j}(3\Delta z)^2 - \frac{1}{3!}\left(\frac{\partial^3\phi}{\partial z^3}\right)_{i,j}(3\Delta z)^3 + \cdots \qquad (121) \\
&\cdots \\
\phi_{i,j-n} &= \phi_{i,j} - \left(\frac{\partial\phi}{\partial z}\right)_{i,j}(n\Delta z) + \frac{1}{2!}\left(\frac{\partial^2\phi}{\partial z^2}\right)_{i,j}(n\Delta z)^2 - \frac{1}{3!}\left(\frac{\partial^3\phi}{\partial z^3}\right)_{i,j}(n\Delta z)^3
\end{aligned}$$

Because $\phi_{i,j}$ and $\phi_{i,j-1}$, $\phi_{i,j-2}$, $\phi_{i,j-3}$,..., $\phi_{i,j-n}$ are all known, the above system can be cast into a compact matrix form:

$$\begin{bmatrix} 1 & 1 & 1 & \cdot \\ 2 & 2^2 & 2^3 & \cdot \\ \cdot & \cdot & \cdot & \cdot \\ n & n^2 & n^3 & \cdot \end{bmatrix} \begin{bmatrix} (-\Delta z)(\partial\phi/\partial z)_{i,j} \\ (-\Delta z)^2(1/2!)(\partial^2\phi/\partial z^2)_{i,j} \\ \cdot \\ (-\Delta z)^n(1/n!)(\partial^n\phi/\partial z^n)_{i,j} \end{bmatrix} = \begin{bmatrix} \phi_{i,j-1} - \phi_{i,j} \\ \phi_{i,j-2} - \phi_{i,j} \\ \cdot \\ \phi_{i,j-n} - \phi_{i,j} \end{bmatrix} \tag{122}$$

Note that the matrix can be written as the product of a diagonal matrix and one of the Vandermonde type [94] and the inverse can be calculated analytically. From this, we can write the general form for the first derivative $(\partial\phi/\partial z)_{i,j}$:

$$\left(\frac{\partial\phi}{\partial z}\right)_{i,j} = \frac{1}{\Delta z}\sum_{k=1}^{n-1}(-1)^k \frac{(n-1)!}{(n-1-k)!\,k!}\frac{(\phi_{i,j-k} - \phi_{i,j})}{k} + O\left[(\Delta z)^{n-1}\right] \tag{123}$$

Here, n is the number of nodes that the discretised approximation takes from the base point j along $-z$ direction (i.e., from the electrode position downwards, see Figure 29). Notice that the order of error in the above expression is of $O(\Delta z^{n-1})$.

(ii) Specific cases

The general expression (123) for $(\partial\phi/\partial z)_{i,j}$ enables us to write down easily the explicit expressions for the following specific situations.

(a) n=2

For n=2, expression (123) gives the first-order approximation:

$$\left(\frac{\partial\phi}{\partial z}\right)_{i,j} = \frac{\phi_{i,j} - \phi_{i,j-1}}{\Delta z} + O(\Delta z) \tag{124}$$

which is the backward difference.

(b) n=3

This 3-point expansion gives rise to the second-order approximation:

$$\left(\frac{\partial\phi}{\partial z}\right)_{i,j} = \frac{1}{2\Delta z}\left(3\phi_{i,j} - 4\phi_{i,j-1} + \phi_{i,j-2}\right) + O\left[(\Delta z)^2\right] \tag{125}$$

(c) n=4

The 4-point formula corresponds to the third-order approximation:

$$\left(\frac{\partial\phi}{\partial z}\right)_{i,j} = \frac{1}{6\Delta z}\left(11\phi_{i,j} - 18\phi_{i,j-1} + 9\phi_{i,j-2} - 2\phi_{i,j-3}\right) + O\left[(\Delta z)^3\right] \qquad (126)$$

(d) n=5

For n=5, a 4th-order expression can be obtained:

$$\left(\frac{\partial\phi}{\partial z}\right)_{i,j} = \frac{1}{12\Delta z}\left(49\phi_{i,j} - 48\phi_{i,j-1} + 12\phi_{i,j-2} - 16\phi_{i,j-3} + 3\phi_{i,j-4}\right) + O\left[(\Delta z)^4\right] \qquad (127)$$

(e) n=6

For n=6, one has 5th-order expression:

$$\left(\frac{\partial\phi}{\partial z}\right)_{i,j} = \frac{1}{60\Delta z}\left(137\phi_{i,j} - 300\phi_{i,j-1} + 300\phi_{i,j-2} - 200\phi_{i,j-3} + 75\phi_{i,j-4} - 12\phi_{i,j-5}\right) + O\left[(\Delta z)^5\right] \qquad (128)$$

and so on.

Normally if Δz is very small, the 4th-order approximation could be considered appropriate. In principle, the charge density can be calculated for each electrode node by using the formulas (120) and (123). However due to existence of the numerical error in calculating derivatives $(\partial\phi/\partial z)_{i,j}$ caused by the field singularity around the ending nodes, special treatment must be conducted as discussed in the following section.

6.2.3. A more accurate calculation of the charge densities at the electrode edges

From the expression (120) it follows that the charge density σ_i on the electrode node i is directly proportional to the derivative $(\partial\phi/\partial z)_{i,j}$, i.e.,

$$\sigma_i = \left(\varepsilon_\perp + \Delta\varepsilon n_z n_z\right)_{i,j}\left(\frac{\partial\phi}{\partial z}\right)_{i,j} \propto \left(\frac{\partial\phi}{\partial z}\right)_{i,j} \qquad (129)$$

However, if we consider a thin electrode, the normal electric field (and the charge density) will have a singularity at the sharp edge of the form $x^{-1/2}$ where x is the distance from the edge. This is clear from the modelled potential distribution, where the isolines become very close near the electrode edges (see Figure 21). Hence if we use directly the formula (123) to calculate $(\partial\phi/\partial z)_{i,j}$ at the ending node i=1 or k_q (see

Figure 30) it will result in a significant numerical error and also in a very large value of σ_1 or σ_{k_q}, and since $\rho_1=(\sigma_1+\sigma_2)/2$ and $\rho_{k_q-1}=(\sigma_{k_q-1}+\sigma_{k_q})/2$, these, in turn, will weigh heavily in the total charge: $Q=\sum_{i=1}^{k_q-1}\rho_i\Delta x_i$, making the contributions from the central nodes insignificant. Therefore, the *discretised* charge density σ_1 and σ_{k_q} at

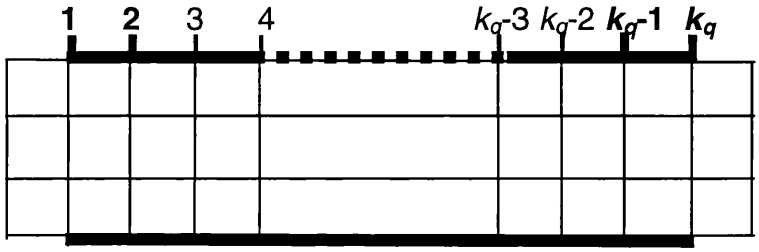

Figure 30 A schematic diagram for addressing end nodes effects

ending nodes i and k_q must be handled in a special way so that the average densities $\rho_1[=(\sigma_1+\sigma_2)/2]$ over segment 1 and $\rho_{k_q-1}[=(\sigma_{k_q-1}+\sigma_{k_q})/2]$ over segment k_q-1 are replaced by values considering the singularity at the edge. In what follows 4 different cases are addressed in detail.

(i) Case 1 and Case 2 – charge density distribution over segment 1

Let's consider first cases shown in Figure 31 where $\rho(x)$ is of form $\pm 1/\sqrt{x}$ (x: distance from the edge). When $x=\Delta x$, the density is required being equal to the density at node 2, i.e., σ_2; while for x large, the density should approach an asymptotic constant which is effectively equal to the value in the middle of the electrode. Putting all above arguments together, the density function being sought should take the following form:

$$\rho(x)=\left\{\begin{matrix}\pm\infty, x\to 0\\ \sigma_2, x=\Delta x_1\\ \sigma_{L_e/2}, x \text{ large}\end{matrix}\right\}=B\pm\frac{A}{\sqrt{x}} \tag{130}$$

Here L_e is the length of the electrode, the coefficient B is simply equal to $\sigma_{L_e/2}$

$$B=\sigma_{L_e/2} \tag{131}$$

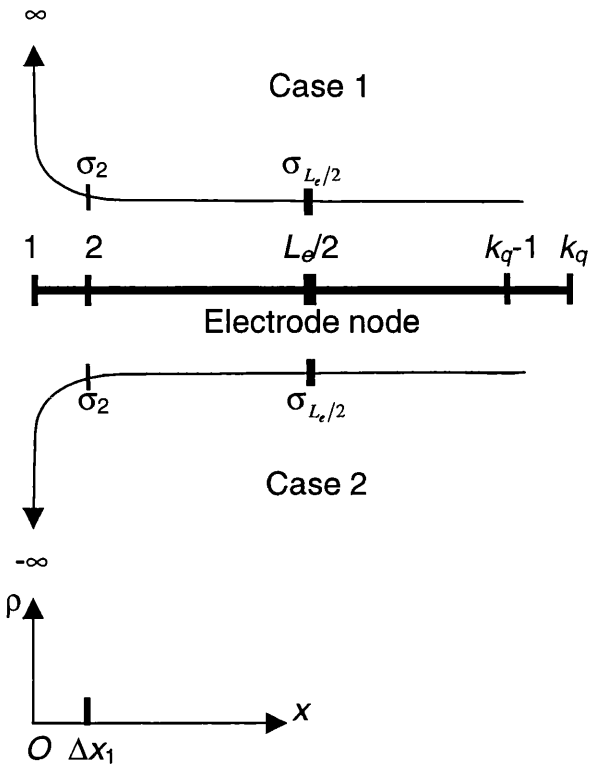

Figure 31 Charge density behaviour like $\pm 1/\sqrt{x}$ at the ending node of the electrode: $\rho(x)\to\infty$ (Case 1) or $\rho(x)\to-\infty$ (Case 2) when $x\to 0$, i.e., at node 1

and A can be easily found to be

$$A = \pm\sqrt{\Delta x_1}\left(\sigma_2 - \sigma_{L_e/2}\right) \tag{132}$$

by the restriction: $\sigma_2 = \sigma_{L_e/2} \pm A/\sqrt{\Delta x_1}$. Inserting expressions (131) and (132) for B and A into (130) gives the charge density function over segment 1:

$$\rho(x) = \sigma_{L_e/2} + \frac{\sqrt{\Delta x_1}\left(\sigma_2 - \sigma_{L_e/2}\right)}{\sqrt{x}} \tag{133}$$

The charge over the segment 1 therefore is the integral of $\rho(x)$ over 0 to Δx_1:

$$q_1 = \int_0^{\Delta x_1} \rho(x)dx = \int_0^{\Delta x_1}\left[\sigma_{L_e/2} + \frac{\sqrt{\Delta x_1}\left(\sigma_2 - \sigma_{L_e/2}\right)}{\sqrt{x}}\right]dx = \left(2\sigma_2 - \sigma_{L_e/2}\right)\Delta x_1 \tag{134}$$

It can be seen now from Eq. (134) that the charge q_1 over the segment 1 is no longer simply equal to $\Delta x_1(\sigma_1+\sigma_2)/2$ which is dominated by an always-big and erroneous σ_1; rather, it is only dependent on σ_2 and the asymptotic constant value $\sigma_{L_e/2}$. In the

hypothetical case of $\sigma_2 \approx \sigma_{L_e/2}$, we have $q_1 \approx \sigma_2 \Delta x_1$. However, because σ_2 is the density at the nearest node to the end node 1, normally its value is comparably big, $> \sigma_{L_e/2}$ but $<< \sigma_1$ in absolute value. So it dominates the q_1. This is the correction to the end node 1.

(ii) Case 3 and Case 4 – charge density distribution over segment k_q-1

By a similar argument having led to expression (130), the charge density ρ_{k_q-1} over segment k_q-1 should take the following form (see Figure 32)

$$\rho(x) = \left\{ \begin{array}{l} \pm\infty, x \to 0 \\ \sigma_{k_q-1}, x = -\Delta x_{k_q-1} \\ \sigma_{L_e/2}, x \to -\infty \end{array} \right\} = B' \pm \frac{A'}{\sqrt{-x}} \tag{135}$$

Here the constant B' is identical to the above B given by Eq. (131) and the constant A' can be determined by a similar way to be

$$A' = \pm\sqrt{\Delta x_{k_q-1}}\left(\sigma_{k_q-1} - \sigma_{L_e/2}\right) \tag{136}$$

Inserting the above expression into Eq. (135), the charge density function over segment k_q-1 is given by

$$\rho(x) = \sigma_{L_e/2} + \frac{\sqrt{\Delta x_{k_q-1}}\left(\sigma_{k_q-1} - \sigma_{L_e/2}\right)}{\sqrt{-x}} \tag{137}$$

The charge therefore can be calculated as

$$q_{k_q-1} = \int_{-\Delta x_{k_q-1}}^{0} \rho(x)dx = \int_{-\Delta x_{k_q-1}}^{0} \left[\sigma_{L_e/2} + \frac{\sqrt{\Delta x_{k_q-1}}\left(\sigma_{k_q-1} - \sigma_{L_e/2}\right)}{\sqrt{-x}} \right] dx = \left(2\sigma_{k_q-1} - \sigma_{L_e/2}\right)\Delta x_{k_q-1} \tag{138}$$

Similarly, it can be seen now from Eq. (138) that the charge q_{k_q-1} over the segment k_q-1 is no longer simply of form $\Delta x_{k_q-1}\left(\sigma_{k_q-1} + \sigma_{k_q}\right)/2$ which is dominated by the σ_{k_q} (although σ_{k_q-1} is relatively big, it is well less σ_{k_q} in magnitude). It only depends on σ_{k_q-1} and the asymptotic constant value $\sigma_{L_e/2}$ while σ_{k_q-1} is the dominant term ($> \sigma_{L_e/2}$ in magnitude). This is the correction to the end node k_q-1.

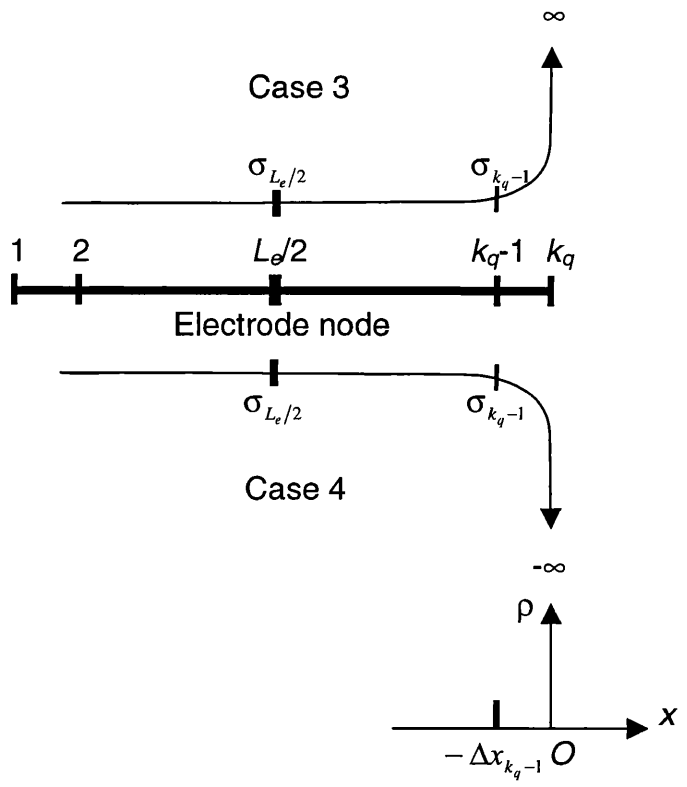

Figure 32 Charge density behaviour like $\pm 1/\sqrt{-x}$ at the ending node of the electrode: $\rho(x) \rightarrow \infty$ (Case 3) or $\rho(x) \rightarrow -\infty$ (Case 4) when $x \rightarrow 0$, i.e., at node k_q

(iii) Combinations of the above cases

There are 4 possible combinations of the charge density profiles on the electrode from

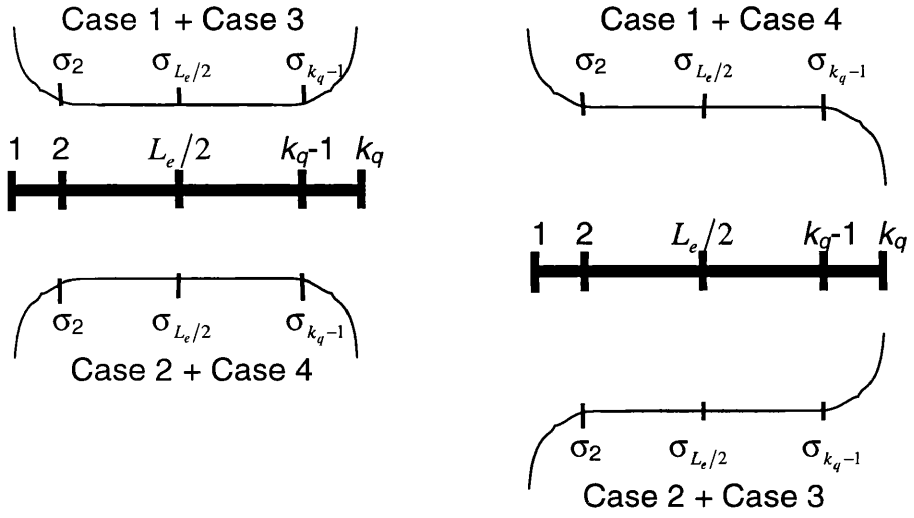

Figure 33 4 possible profiles of charge density on electrode from the combination of 4 individual cases

the above discussed 4 individual cases (see Figure 33). These will occur for different combinations of voltage polarities of the adjacent electrodes. The first one is case 1 + case 3, the second one is case 2 + case 4, the third is from the combination of case 1 with case 4, the last one consists of case 2 and case 3. However in any combination, the sum of the charge q_1 from segment 1 and charge q_{k_q-1} from segment k_q-1 keeps the same form if the length of the segment is the same, i.e., $\Delta x_1 = \Delta x_{k_q-1} \equiv \Delta x$:

$$q_1 + q_{k_q-1} = 2\Delta x\left(\sigma_2 + \sigma_{k_q-1} - \sigma_{L_e/2}\right) \tag{139}$$

(iv) Determination of $\sigma_{L_e/2}$

The value of the charge $\sigma_{L_e/2}$ used in the expressions for the calculation of the charge at the edge, can be taken as the charge at the centre of the electrode, where the charge is almost constant. In practice, the value used is

$$\sigma_{L_e/2} = \sigma_{[k_q/2]+1} \quad \left(k_q = odd\ number\right) \tag{140}$$

if the electrode has been discretised into an odd number of nodes or

$$\sigma_{L_e/2} = \left(\sigma_{[k_q/2]} + \sigma_{[k_q/2]+1}\right)/2 \quad \left(k_q = even\ number\right) \tag{141}$$

for an even number of nodes. Here $[k_q/2]$ means taking the integer part of $k_q/2$.

(v) Examples

According to the above arguments, it follows that as long as the potential and director profiles are known, the total charge Q and the profile of the segment charge q_i (i=1,2,3,...,k_q-1) can be calculated by Eqs. (120), (123), (134) and (138). Figure 34 shows the charge segment (spatial) distributions along the pixel electrode of 32 segments (33 nodes) before (dash line + octagons) and after (solid line + asterisks) ending-node corrections, when pixel (floating) voltage is equal to V_p=3.6v and bus voltage V_b=-4.0v at time t=5ms. The cell geometry and the electrode configuration are the same as those described in Section 5.2.3 but under constant charge restriction here.

The charge q on the segment 32 due to the correction to the density on the right-hand-side ending node 33 is reduced by 9.23% as evidenced in this figure. Figure 35 shows the corresponding charge profiles within each segment of the bus electrode 1 (left, under the segment number 1, 2, 3, and 4) and electrode 2 (right, under the segment

number 7, 8, 9, and 10) at the same time and under the same the pixel voltage and bus voltage as for Figure 34. As pointed out before, due to small physical dimension of the bus electrode and hence the significant edge errors in the calculation of the charge Q_b, the corrections are much more appreciable than those for the pixel electrode. For

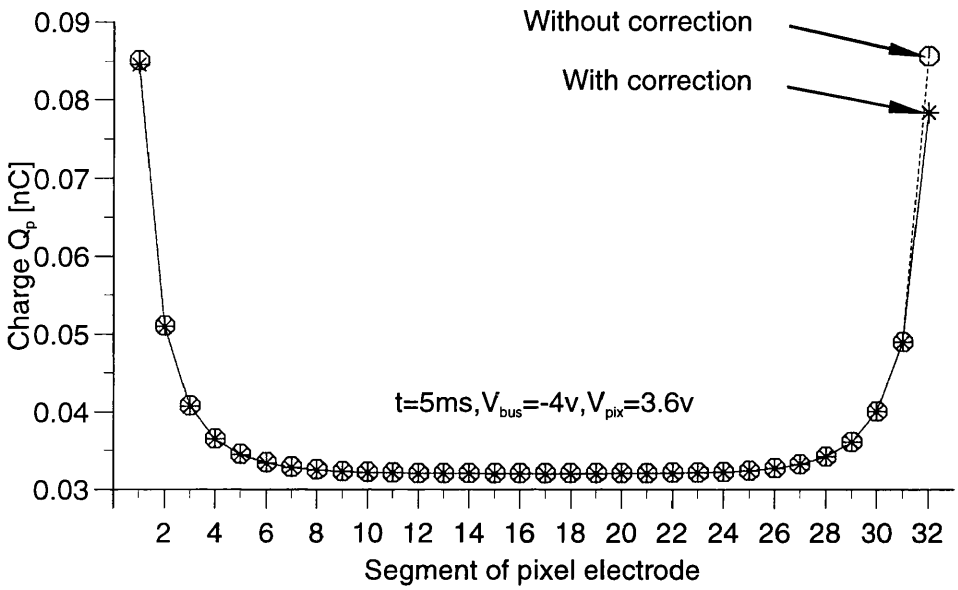

Figure 34 Charge spatial profile along the electrode consisting of 32 segments (33 nodes) with (solid line + asterisks) and without (dash line + octagons) ending node density corrections considered.

the bus electrode 1, the correction to the charge on the segment 1 (left-hand side ending node) is 24.28%, while on the right-hand side segment 4, the correction reaches as high as 26.3%, while for the bus electrode 2, the corrections are even more dramatic with 28% on the left-hand side segment 7 and 26.4% on the right-hand side segment 10. This revelation justifies for our preferential choice of Eq. (103) rather than the Eq. (104) to calculate the floating pixel voltage V_p as with this choice the calculation of the charge for any bus electrode Q_b can be avoided which has been proved error-prone.

It is also clear from the figure that even with the edge correction, the coarse discretisation of the bus electrode produces a rather crude representation of the charge distribution there. However, due to the small relative size of the bus compared with the pixel electrode, a finer discretisation would result in a prohibitively high number

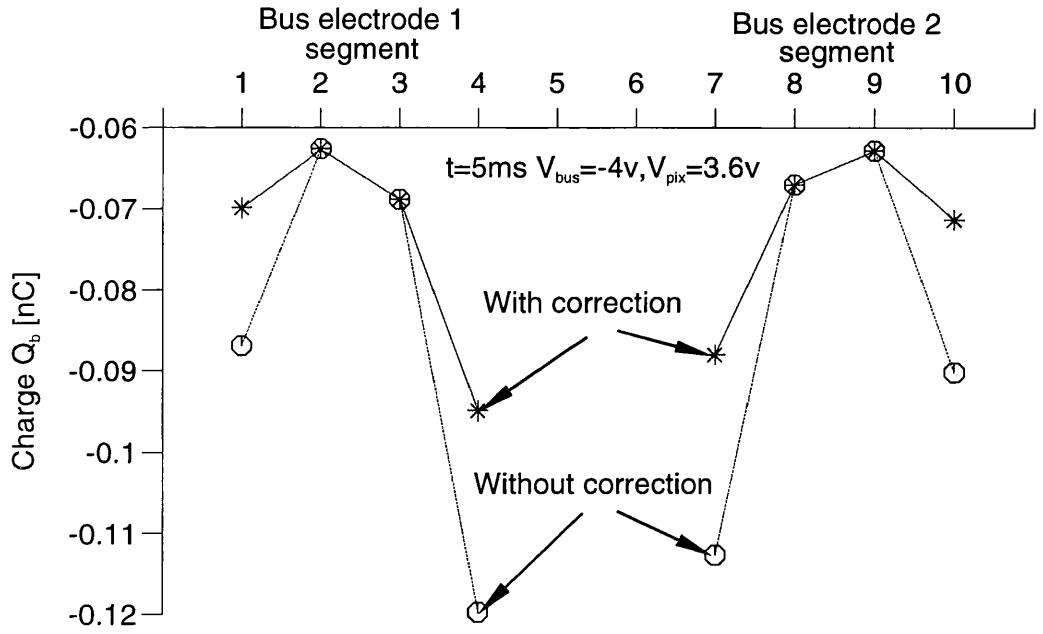

Figure 35 Corresponding spatial distributions of the charges along the bus electrode 1 (left, under segment number 1, 2, 3, and 4) and the bus electrode 2 (right, under segment number 7, 8, 9, and 10), both consisting of 4 segments (5 nodes) with (solid line + asterisks) and without (dash line + octagons) ending node density corrections.

of mesh nodes and hence, computing time. The effect of this less accurate calculation requires further investigation and possibly, the development of a variable mesh approach.

6.3. Calculation of the *C*-matrix

In the above section 6.2, it has been shown how the charge can be calculated directly from director and potential distributions. Now there is only one more step left towards the solution of the floating pixel voltage according to the expression (105) or (106), obtained in section 6.1.1. That is, to calculate the capacitance matrix $\boldsymbol{C}$. Generally, this $\boldsymbol{C}$-matrix consists of pixel self- or mutual (if more than one pixel) capacitances, bus self- and mutual (if more than one bus) capacitances, and bus-pixel mutual capacitances.

A way of calculating the capacitance matrix from the potential and director distributions using a perturbative approach is described next. Unlike all earlier one-dimensional models [25-27] which cannot take the actual sizes of pixel and bus electrodes into account, the method presented here not only enables us, from the

director and potential information, to calculate the pixel self-and mutual capacitances C_{pp}, but also the bus-pixel mutual capacitances C_{pb}.

6.3.1. Perturbation method

In the case of LCD cell, because the permittivity is a function of director and the director is time-dependent, the capacitance of the cell as a function of permittivity varies with time. That is different from an ordinary capacitor whose capacitance is a fixed constant. So, if we want to calculate the capacitance of the LC cell at a particular time (and voltage), we can fix (freeze) the director profile of the LC cell at that time. In doing so, the LC cell can be regarded as a standard capacitor whose dielectric configuration now is identical to that of the LC cell at that time and then the linear property between voltage V and charge Q for the standard capacitor can be employed for the LC cell. Based on this, the calculation of LC capacitance can be done by using the perturbation technique as described in details below.

(i) Theory

In the case of no bus electrode, the matrix formulation (100) now reduces to a scalar expression as already given in Eq. (107)

$$C(t)V(t)=Q(t) \tag{142}$$

where C, V, and Q are all scalars. We can see that at *any fixed time* the relationship between V and Q in the equivalent capacitor (frozen directors) is linear. In other words, the ratio of Q to V gives a constant value of C

$$C=\frac{Q}{V} \tag{143}$$

because if the voltage V increases by δV, then the charge Q will accordingly increase by δQ. That is, if we want to evaluate the capacitance C at this fixed time which corresponds to a *particular* (fixed) dielectric (director) distribution, we can use (142) in the form of

$$C=\frac{\delta Q}{\delta V} \tag{144}$$

Note that in the case of more than one electrode involved, the matrix expression (100) should replace the scalar form (142) and the above arguments still hold true. In this case, the elements of matrix $\boldsymbol{C}$ can be found with appropriate choices for different δV and for the same *fixed* director distribution. Advancing from one time step to another

gives another set of values of C. In what follows, a verification is given that the calculated procedure indeed satisfies the expected linear behaviour.

(ii) Verification of the theory by the modelling results

This section shows modelling results for a simple electrode configuration, in order to illustrate the procedure described above. The details of the geometry of the cell are the

Fixed director configuration						
After correction					Before correction	
Volt.	Charge	Capac	Capac	Capac	Charge	Capac
V[v]	Q[nC]	C[nF] $=\frac{Q}{V}$	C[nF]= $\frac{\delta Q}{\delta V}=\frac{\delta Q}{10V}$	C[nF]= $\frac{\delta Q}{\delta V}=\frac{\delta Q}{2V}$	Q[nC]	C[nF]= $\frac{\delta Q}{\delta V}=\frac{\delta Q}{10V}$
0.0	0.00000		0.28459	0.28459	0.00000	0.28647
1.0	0.28459	0.28459	0.28459	0.28459	0.28647	0.28647
1.5	0.42689	0.28459	0.28460	0.28460	0.42971	0.28647
2.0	0.56919	0.28459	0.28460	0.28460	0.57294	0.28648
2.5	0.71148	0.28459	0.28460	0.28460	0.71618	0.28648
3.0	0.85378	0.28459	0.28460	0.28461	0.85941	0.28648
4.0	1.13837	0.28459	0.28461	0.28462	1.14589	0.28649
5.0	1.42296	0.28459	0.28462	0.28463	1.43236	0.28650
10.0	2.84593	0.28459	0.28471	0.28475	2.86472	0.28660
15.0	4.27248	0.28483	0.28483	0.28483	4.30116	0.28674
20.0	5.70044	0.28502	0.28502	0.28502	5.73948	0.28696
50.0	14.3908	0.28782	0.28762	0.28755	14.5806	0.29140

Table 3 Calculated pixel charges Q and capacitances C in two cases: (1) with-charge-correction and (2) without-charge-correction under given applied voltages V for LC device as specified in Table 2 but without any bus electrodes used, showing C indeed keeps a constant no matter which way to calculate it and how big the perturbation amount δV is. This verifies the correctness of the theoretical predictions by Eqs. (143) and (144). Also shown in this table is the difference between case (1) and (2).

same as those in Table 2 (page 65). The calculations are done for two cases: (1) with charge corrected in the way discussed in section 6.2.3 and (2) without charge corrected. 11 values of voltages are tested for a fixed director profile. The charges Q are calculated using the method described in 6.2 and the capacitances C are calculated in 2 different ways: (1) directly (i.e., $C=Q/V$), and (2) by applying perturbation formula (144) (i.e., $C=\delta Q/\delta V$) for $\delta V=10V$ and $\delta V=2V$ respectively. All calculations are carried out under a single fixed director configuration as required which is equivalent to fixing all physical characters of a capacitor with voltage values varying only. The calculated results are given in Table 3 and Q-V curves are plotted in Figure 36. From them the following observations can be obtained: (1) as expected, the linear relationship between Q (δQ) and V (δV) is observed in the calculated results; (2) that the capacitances C obtained by perturbation technique as listed in columns 4 and 5 are

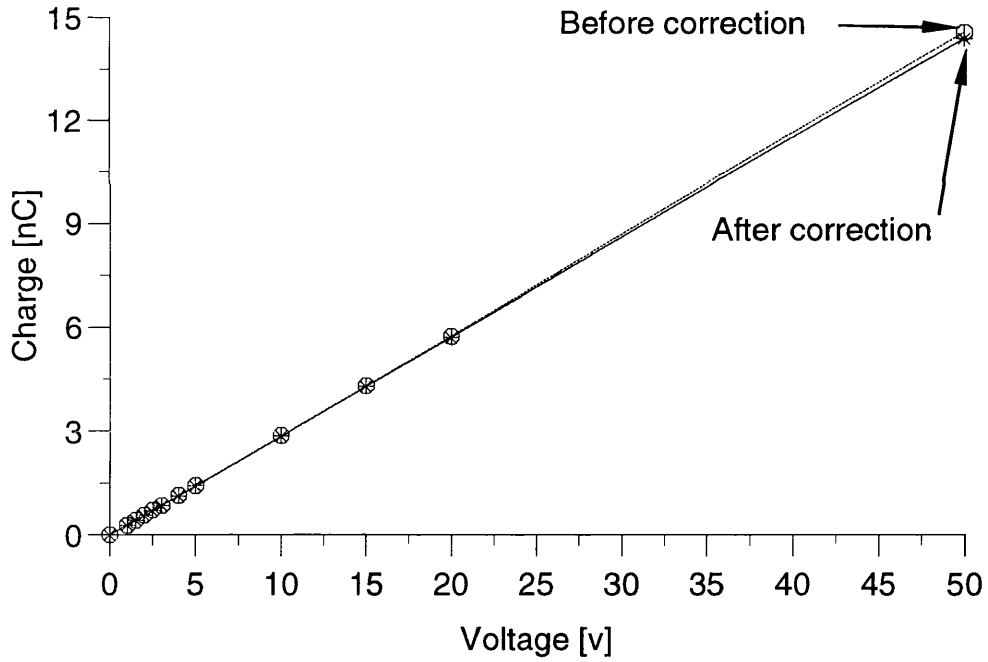

Figure 36 The Q -V curve plotted by using the calculated data sets as shown inTable 3. Solid line plus asterisk markers corresponds to the case with charge corrected by the way as discussed in the section 6.2.3 and dash line plus octagon markers to that without charge corrected.

exactly the same to two decimal places as those obtained by directly applying formula (143) as shown in the column 3; (3) that because the linearity is preserved in the calculated results, δV does not need to be small. Indeed, larger values should be

preferred to avoid computational errors; (4) that results associated with charge correction tend to give less deviation to the exact linear Q-V relation than those without any charge correction when the testing voltage takes high values of, say, 20 volts or 50 volts; and (5) that the deviation to the exact constant capacitance value is very small and hence negligible as they only differ at the third decimal place for voltage values of 15 volts or higher.

Therefore, the conclusion is that the model indeed satisfies the assumption made and the perturbation technique can be used to calculate the capacitance matrix.

Finally it should be mentioned that although theoretically there is no particular restriction to choose the magnitude of the δV as concluded above, our experience shows that if the δV is too small, especially when V itself is small too, large numerical errors occur. Similarly, if δV is too big, a deviation to the linear relation will occur as seen above, especially when V itself is very big. In this work, a value of δV from 2 times to 10 times the value of V is normally used.

6.3.2. Implementation of perturbation technique

Suppose that at time t, we have full information about the director field distribution $\{\mathbf{n}(\mathbf{r}, t)\}$ and potential field distribution $\{\varphi(\mathbf{r},t)\}$, the pixel voltages $V_p(t)$ and bus voltages $V_b(t)$ as well as the pixel charge(s) $Q_p(kT_p/2+t_c<t)$ which are assumed constant(s) since the voltage was last connected, and bus charges $Q_b(t)\big|_{old}$ which are varying with time (not constants). Both sets of charges are calculated in the way detailed in section 6.2. Now, the remaining task is to find the pixel (floating) voltage $V_p(t+\Delta t)$ for next time step at $t+\Delta t$. For this, the knowledge of at least part of the capacitance matrix C is required according to Eq (105) or (106).

Let us fix the director profile $\{\mathbf{n}(\mathbf{r}, t)\}$ and hence the permittivity (dielectric tensor) $\bar{\bar{\varepsilon}}$ (which is equivalent to keeping the physical character of the cell as an ordinary capacitor unchanged) and change the value of (pixel i or bus i) voltage from $V(i,t)$ to $V(i,t)+\delta V(i)$, while leaving *all other voltages unchanged.* Then a new potential profile $\{\varphi(\mathbf{r},t)_{\text{new}}\}$ can be found by using the standard procedure described in Section 5.2.2. This in turn allows us to calculate a new set of charges $Q_p(t)\big|_{new}$ and $Q_b(t)\big|_{new}$ by the method developed in section 6.2. Comparing $Q_p(t)\big|_{new}$ and $Q_b(t)\big|_{new}$ with

$\boldsymbol{Q}_p(kT_p/2+t_c<t)$ and $\boldsymbol{Q}_b(t)\big|_{old}$ give $\delta\boldsymbol{Q}_p(t)$, and $\delta\boldsymbol{Q}_b(t)$. By using Eq. (144) each element of the $\boldsymbol{C}$ matrix can be therefore calculated.

6.3.3. Calculation of *C*-matrix

Now let us apply the above logic to Eq. (102b) by performing the perturbation sequentially on the pixel voltages 1, 2, ..., and then bus voltages 1, 2, ... First, by increasing the $V_p(1)$ to $V_p(1)+\delta V_p(1)$ while keeping all other voltages and director configuration $\{n(r,t)\}$ fixed, the new potential profile $\{\varphi(\mathbf{r},t)_{new}\}$ and hence, the new set of charges $Q(t)+\delta Q(t)$ can be calculated. Using the relation (102b) itself, this generates the following matrix equation:

$$\begin{bmatrix} C_{pp}(1,1) & C_{pp}(1,2) & \cdot & C_{pb}(1,1) & C_{pb}(1,2) & \cdot \\ C_{pp}(2,1) & C_{pp}(2,2) & \cdot & C_{pb}(2,1) & C_{pb}(2,2) & \cdot \\ \cdot & \cdot & \cdot & \cdot & \cdot & \cdot \\ C_{bp}(1,1) & C_{bp}(1,2) & \cdot & C_{bb}(1,1) & C_{bb}(1,2) & \cdot \\ C_{bp}(2,1) & C_{bp}(2,2) & \cdot & C_{bb}(2,1) & C_{bb}(2,2) & \cdot \\ \cdot & \cdot & \cdot & \cdot & \cdot & \cdot \end{bmatrix} \begin{bmatrix} \delta V_p(1) \\ 0 \\ \cdot \\ 0 \\ 0 \\ \cdot \end{bmatrix} = \begin{bmatrix} \delta Q_p(1) \\ \delta Q_p(2) \\ \cdot \\ \delta Q_b(1) \\ \delta Q_b(2) \\ \cdot \end{bmatrix} \tag{145}$$

from which it is quite straightforward to get the following elements of $\boldsymbol{C}$

$$C_{pp}(1,1)\big|_t = \left.\frac{\delta Q_p(1)}{\delta V_p(1)}\right|_{\substack{V_p(2),V_b=fixed \\ \{n(\mathbf{r},t)\}=fixed}} \tag{146}$$

$$C_{pp}(2,1)\big|_t = \left.\frac{\delta Q_p(2)}{\delta V_p(1)}\right|_{\substack{V_p(2),V_b=fixed \\ \{n(\mathbf{r},t)\}=fixed}} \tag{147}$$

$$C_{bp}(1,1)\big|_t = \left.\frac{\delta Q_b(1)}{\delta V_p(1)}\right|_{\substack{V_p(2),V_b=fixed \\ \{n(\mathbf{r},t)\}=fixed}} \tag{148}$$

$$C_{bp}(2,1)\big|_t = \left.\frac{\delta Q_b(2)}{\delta V_p(1)}\right|_{\substack{V_p(2),V_b=fixed \\ \{n(\mathbf{r},t)\}=fixed}} \tag{149}$$

Similarly, by increasing $V_p(2)$ to $V_p(2)+\delta V_p(2)$, $V_b(1)$ to $V_b(1)+\delta V_b(1)$, and $V_b(2)$ to $V_b(2)+\delta V_b(2)$ in turn, while fixing relevant variables, and calculating the corresponding new potential field $\{\varphi(\mathbf{r},t)_{new}\}$ and increments in charges $\delta\boldsymbol{Q}(t)$, the rest of C elements can be easily obtained as follow:

$$C_{pp}(1,2)\Big|_t = \frac{\delta Q_p(1)}{\delta V_p(2)}\Big|_{\substack{V_p(1),V_b=fixed \\ \{\mathbf{n}(\mathbf{r},t)\}=fixed}} \tag{150}$$

$$C_{pp}(2,2)\Big|_t = \frac{\delta Q_p(2)}{\delta V_p(2)}\Big|_{\substack{V_p(1),V_b=fixed \\ \{\mathbf{n}(\mathbf{r},t)\}=fixed}} \tag{151}$$

$$C_{bp}(1,2)\Big|_t = \frac{\delta Q_b(1)}{\delta V_p(2)}\Big|_{\substack{V_p(1),V_b=fixed \\ \{\mathbf{n}(\mathbf{r},t)\}=fixed}} \tag{152}$$

$$C_{bp}(2,2)\Big|_t = \frac{\delta Q_p(2)}{\delta V_p(2)}\Big|_{\substack{V_p(1),V_b=fixed \\ \{\mathbf{n}(\mathbf{r},t)\}=fixed}} \tag{153}$$

and

$$C_{pb}(1,1)\Big|_t = \frac{\delta Q_p(1)}{\delta V_b(1)}\Big|_{\substack{V_p,V_b(2)=fixed \\ \{\mathbf{n}(\mathbf{r},t)\}=fixed}} \tag{154}$$

$$C_{pb}(2,1)\Big|_t = \frac{\delta Q_p(2)}{\delta V_b(1)}\Big|_{\substack{V_p,V_b(2)=fixed \\ \{\mathbf{n}(\mathbf{r},t)\}=fixed}} \tag{155}$$

$$C_{bb}(1,1)\Big|_t = \frac{\delta Q_b(1)}{\delta V_b(1)}\Big|_{\substack{V_p,V_b(2)=fixed \\ \{\mathbf{n}(\mathbf{r},t)\}=fixed}} \tag{156}$$

$$C_{bb}(2,1)\Big|_t = \frac{\delta Q_b(2)}{\delta V_b(1)}\Big|_{\substack{V_p,V_b(2)=fixed \\ \{\mathbf{n}(\mathbf{r},t)\}=fixed}} \tag{157}$$

as well as

$$C_{pb}(1,2)\Big|_t = \frac{\delta Q_p(1)}{\delta V_b(2)}\Big|_{\substack{V_p,V_b(1)=fixed \\ \{\mathbf{n}(\mathbf{r},t)\}=fixed}} \tag{158}$$

$$C_{pb}(2,2)\Big|_t = \frac{\delta Q_p(2)}{\delta V_b(2)}\Big|_{\substack{V_p,V_b(1)=fixed \\ \{\mathbf{n}(\mathbf{r},t)\}=fixe}} \tag{159}$$

$$C_{bb}(1,2)\Big|_t = \frac{\delta Q_b(1)}{\delta V_b(2)}\Big|_{\substack{V_p,V_b(1)=fixed \\ \{\mathbf{n}(\mathbf{r},t)\}=fixe}} \tag{160}$$

$$C_{bb}(2,2)\Big|_t = \frac{\delta Q_b(2)}{\delta V_b(2)}\Big|_{\substack{V_p,V_b(1)=fixed \\ \{\mathbf{n}(\mathbf{r},t)\}=fixe}} \tag{161}$$

The expressions (146) - (161) give all elements of $\boldsymbol{C}$. However not all of them are needed as discussed before because only Eq. (103) or (105) is used to calculate the pixel floating voltage. That means that expressions (148), (149), (152), (153), (156), (157), (160), and (161), i.e., sub-matrices $\boldsymbol{C}_{bp}$ and $\boldsymbol{C}_{bb}$ are not used. These elements appear in Eq. (104) which, as discussed earlier, is not used (Eq. (103) is preferred instead) because there exist inevitable numerical errors in calculating $\boldsymbol{Q}_b$ and $\delta\boldsymbol{Q}_b$ due to the small physical dimension of the bus electrode(s).

6.3.4. Regarding the symmetry of the *C*-matrix

It should be mentioned that theoretically, $\boldsymbol{C}$-matrix should be symmetric, i.e., for example, the sub-matrix $\boldsymbol{C}_{pb}$ should be equal to $\boldsymbol{C}_{bp}^{T}$, $C_{bb}(1,2)\equiv C_{bb}(2,1)$, and $C_{pp}(1,2)\equiv C_{pp}(2,1)$. However, the numerical results show a small disparity. This is because for one calculation, say, $C_{pb}(1,2)$, δQ_{pixel} is needed [see Eq. (158)] and for the other, say, $C_{bp}(2,1)$, δQ_{bus} is needed [see Eq. (152)]. The errors in both δQ_{pixel} and δQ_{bus} are very different because the pixel electrode is much bigger than the bus electrode. Also, this disparity may be further worsened by the asymmetric mesh of triangles which are used to represent the structure and the difficulty in calculating accurately the charges on the ending nodes of the electrodes, particularly for the small bus electrode.

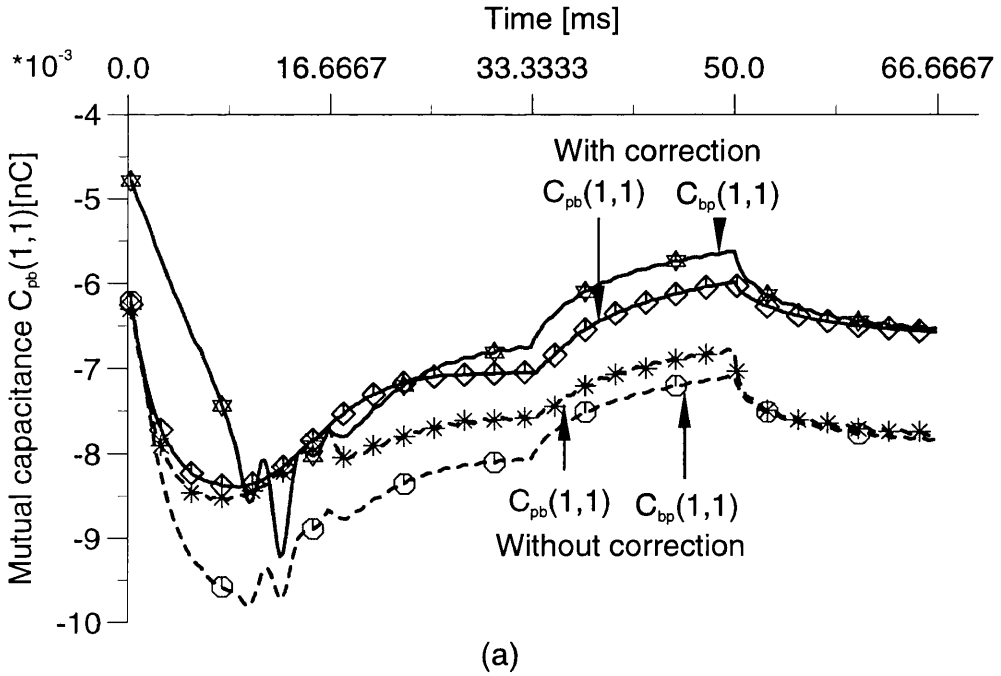

(a)

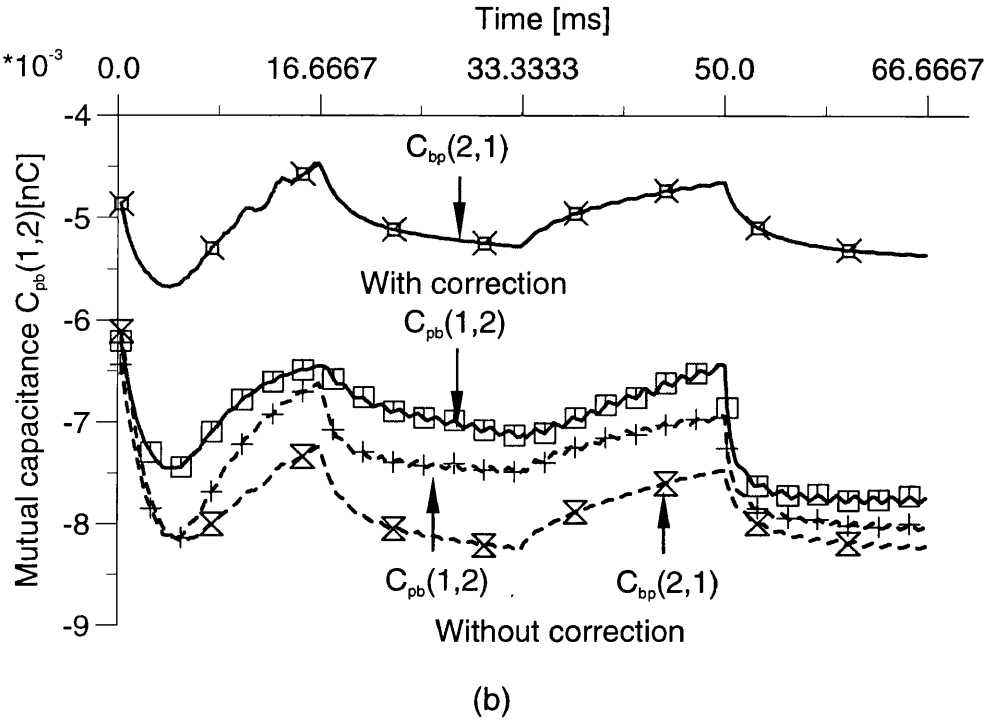

(b)

Figure 37 Mutual capacitances between bus electrode 1 and pixel electrode 1 (a), and between bus electrode 2 and the pixel 1 (b) with a view to examining the symmetry between C_{pb} and C_{bp} in two cases (1) with charge density corrected and (2) without any correction made.

In order to understand this clearly, the mutual capacitance between two bus electrodes and pixel electrode $C_{pb}(1,1)$ and $C_{bp}(1,1)$, $C_{pb}(1,2)$ and $C_{bp}(2,1)$ are calculated under two conditions (1) with charge density corrected and (2) without the density corrected. The whole calculation is done for the LCD system used in section 5.2.3, but with constant charge constraint. $C_{pb}(1,1)$ is calculated as specified by equation (154), i.e., by changing the voltage of bus electrode 1 to get the charge increment of pixel electrode and $C_{bp}(1,1)$ is done by increasing the voltage of the pixel electrode to obtain the charge change in the bus electrode 1 as defined by (148). As discussed previously, big difference between the pixel size and the size of bus electrode causes the two different calculations being of different degree of accuracy. The calculations of $C_{pb}(1,2)$ and $C_{bp}(2,1)$ are done in similar way following Eqs. (158) and (149). Figure 37(a) shows the discrepancy of the mutual capacitance $C_{pb}(1,1)$ from $C_{bp}(1,1)$ between bus electrode 1 and pixel electrode 1 during the whole evolution time and (b) is showing the results for $C_{pb}(1,2)$ and $C_{bp}(2,1)$ between bus line 2 and the pixel electrode 1.

6.3.5. Equivalent circuit

The formalism of Eqs. (103) and (104) have resemblance to the mesh equation for the two-port network that relates two-current variables to two-voltage variables as in network analysis theory [95]. As an example, let us consider a π-circuit, as that shown in Figure 38. There, I_X is current, V_X is voltage, and Y_{XY} could be a resistor R, a capacitor C or an inductor L. According to network theory, the corresponding node equations are as follow

$$I_A = (Y_{AA} + Y_{AB})V_A - Y_{AB}V_B \tag{162}$$

$$I_B = -Y_{AB}V_A + (Y_{BB} + Y_{AB})V_B \tag{163}$$

If Y_{XY} represent capacitors, then

$$Y_{AA} = sC_{AA},\ Y_{BB} = sC_{BB},\ Y_{AB} = sC_{AB} \tag{164}$$

Here C_{AA}, C_{AB}, and C_{BB} are capacitances and s is the Laplace variable. Inserting Eq. (164) into the Eq. (163) gives

$$I_A = s(C_{AA} + C_{AB})V_A - sC_{AB}V_B \tag{165}$$

$$I_B = -sC_{AB}V_A + s(C_{BB} + C_{AB})V_B \tag{166}$$

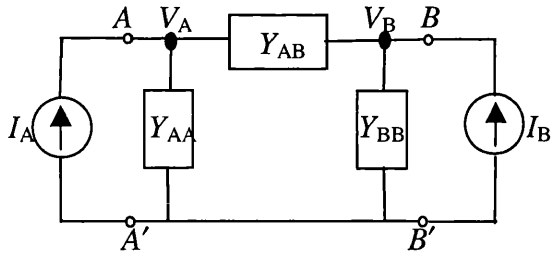

Figure 38 A two-port network π-circuit. Y_{xy} could be R, C, or L

The equations (165) and (166) define the admittance (capacitance) parameters as

$$y_{AA} = s(C_{AA} + C_{AB}) \equiv \left.\frac{\delta I_A}{\delta V_A}\right|_{\delta V_B = 0} \tag{167}$$

$$y_{AB} = -sC_{AB} \equiv \left.\frac{\delta I_A}{\delta V_B}\right|_{\delta V_A = 0} \tag{168}$$

$$y_{BA} = -sC_{AB} \equiv \left.\frac{\delta I_B}{\delta V_A}\right|_{\delta V_B = 0} \tag{169}$$

$$y_{BB} = s(C_{BB} + C_{AB}) \equiv \left.\frac{\delta I_B}{\delta V_B}\right|_{\delta V_A=0} \tag{170}$$

Let $I/s = \tilde{Q}$, as it has the dimension of charge. Equations (165) and (166) can be re-written as

$$\tilde{Q}_A = \tilde{y}_{AA}V_A + \tilde{y}_{AB}V_B \equiv (C_{AA} + C_{AB})V_A - C_{AB}V_B \tag{171}$$

$$\tilde{Q}_B = \tilde{y}_{BA}V_A + \tilde{y}_{BB}V_B \equiv -C_{AB}V_A + (C_{BB} + C_{AB})V_B \tag{172}$$

where

$$\tilde{y}_{AA} = (C_{AA} + C_{AB}) \equiv \left.\frac{\delta \tilde{Q}_A}{\delta V_A}\right|_{\delta V_B=0} \tag{173}$$

$$\tilde{y}_{AB} = -C_{AB} \equiv \left.\frac{\delta \tilde{Q}_A}{\delta V_B}\right|_{\delta V_A=0} \tag{174}$$

$$\tilde{y}_{BA} = -C_{AB} \equiv \left.\frac{\delta \tilde{Q}_B}{\delta V_A}\right|_{\delta V_B=0} \tag{175}$$

$$\tilde{y}_{BB} = (C_{BB} + C_{BB}) \equiv \left.\frac{\delta \tilde{Q}_B}{\delta V_B}\right|_{\delta V_A=0} \tag{176}$$

Comparing the above equations (173) – (176) with expressions (146), (154), (148), and (156) reveals close similarity. Most importantly, comparing expressions (171) and (172) and the equations (103) and (104) immediately reveals the relation:

$$C_{pb} = -C_{AB} = C_{bp} \text{ or } C_{AB} = -C_{pb} = -C_{bp} \tag{177}$$

$$C_{pp} = C_{AA} + C_{AB} \equiv C_{AA} - C_{pb} \text{ or } C_{AA} = C_{pp} + C_{pb} \tag{178}$$

$$C_{bb} = C_{BB} + C_{AB} \equiv C_{BB} - C_{pb} \text{ or } C_{BB} = C_{bb} + C_{pb} \tag{179}$$

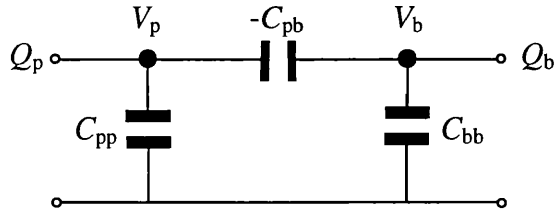

Figure 39 An analogue Pi-circuit to Figure 38 for exploring the physical interpretation of the conceptual capacitances in the current model

The relation (177) explained why the mutual capacitances C_{pb} (C_{bp}) between pixel and bus are always negative since the physical capacitor C_{AB} in the equivalent circuit must

be positive. The close similarity between expressions (171) and (172) and the equations (103) and (104) enables us to draw an analogue two-port network π-circuit for C_{pp}, C_{bb}, and C_{pb} as above (Figure 39)

6.4. The logic of numerical implementation

Compared with constant voltage model, the implementation of the numerical procedure for the constant charge model becomes rather complicated due to the constant charge condition. The general logic would be as follows: within a Crank-Nicolson time-stepping procedure, a consistent director and potential distribution is found by iterations, using finite elements for the potential distribution and finite differences for the director using the voltages at the electrodes as boundary conditions. The evolution in time of the potential and director distribution is controlled by the boundary conditions imposed by the (time varying) voltages applied at the electrodes. When a voltage is applied to the pixel electrodes, the method works as in the constant voltage model. The total charge in the electrodes can then be calculated by integrating the charge density. When the voltage in the pixel electrodes is left floating, the charges calculated previously are assumed to remain constant and are used with the generalised capacitance matrix, to calculate the actual voltages in the pixel electrodes. The capacitance matrix is calculated at each time step (since it is varying as the liquid crystal switches) using a perturbation analysis as described above. The inclusion of external capacitors connected to the pixel electrodes follows simply by adding a fixed capacitance to the time varying pixel self capacitances. The total pixel charges which are assumed to be constant will then be distributed between the pixels and the storage capacitors.

Briefly speaking, the whole procedure of the numerical calculation can be divided in two parts:

Before floating process starts, the model is treated exactly the same as the constant voltage model and therefore the calculation procedure followed is the same as described in 5.2.

Once the floating process begins, the constant charge condition takes effect, generalised capacitance matrix C needs to be evaluated by voltage perturbation technique developed as above under a fixed director profile in order to predict the

floating voltage of the pixel for next time step. The self-consistent potential and director fields are calculated under the newly obtained floating voltage and then the corresponding charge on the pixel electrode is calculated again to see if it remains a constant. If it does not, then the ***C***-matrix is re-calculated and the rest of the above procedure is repeated. This iterative process will not cease until a "satisfactory" floating voltage is found that gives rise to a self-consistent potential and director profile which yields a constant charge.

To be specific, the detailed procedures are implemented in the computer program as follows:

1) Reading in input data (**READING**)
2) Set up initial distributions for directors and the potential throughout the mesh (**INIVAL**)
3) Identify and store boundary nodes (pixel electrodes, bus electrodes, and ground electrode, periodic and Neumann), and nodes on the top layer and bottom layer to which the fixed pretilt angle value can be assigned (anchored) (**BOUNDID**)
4) Identify and store the sparsity pattern (**SPARS**)
5) Start the time stepping
6) Check if pixel voltage is still fixed (constant voltage mode) or floating (constant charge mode). If it is still fixed then go to (9). Otherwise execute (7)
7) Conduct perturbation technique to calculate capacitance matrix ***C*** [**VOLTSET**, **POTFIND** (**MATV**, **BOUNDV**, **MA48AD**, **MA48BD**, **MA48CD**, **NEWV**), **GETQ1**, **GETQ2**, **GETCAP1**, **GETCAP2**]
8) Calculate floating voltage (**GETNEWV**)
9) Apply the (fixed or floating) voltage to the pixel electrode (**VOLTSET**)
10) Calculate potential field $\{\varphi\}$ with fixed directors distribution using the procedure described in 4.3.5 [**POTFIND** (**MATV**, **BOUNDV**, **MA48AD**, **MA48BD**, **MA48CD**, **NEWV**)]
11) Calculate director field $\{\mathbf{n}\}$ with fixed potential obtained in (10) using the procedure given in 4.3.6 (**TIMENXNYNZ**)
12) Check if the fields: $\{\mathbf{n}\}$ and $\{\varphi\}$ are convergent to the given tolerance. If yes, go to next procedure (13). If no, go back to (10) to repeat until a self-consistent solution is found for $\{\mathbf{n}\}$ and $\{\varphi\}$(**NORMNXYZ**)

13) Is it the last time step for the constant voltage mode over the current half frame? If yes, calculate the charge $\boldsymbol{Q}_0(kT_p/2+t_c)$ and then go to (16) and if no, then execute next process (14)

14) Is it in floating mode? If yes, then calculate the charge $\boldsymbol{Q}(t)$ and go to (15). If no, go to (16)

15) Compare $\boldsymbol{Q}(t)$ and $\boldsymbol{Q}_0(kT_p/2+t_c)$ to see if they are equal within a given accuracy. If yes, go to next procedure (16), if no, go to (7). Repeat the above relevant processes until the constant charge condition is satisfied.

16) Snapshot request. If a snapshot is needed then go to process (17) to outputs the intermediate results, if not, then do next time step, i.e., repeat the processes (5) to (15).

17) Output intermediate/final results. If it is not the final time step, then do next time step, i.e., go back and repeat (5) to (15) until the final time step is reached and finally, result is stored.

6.5. Flowchart

Flowchart

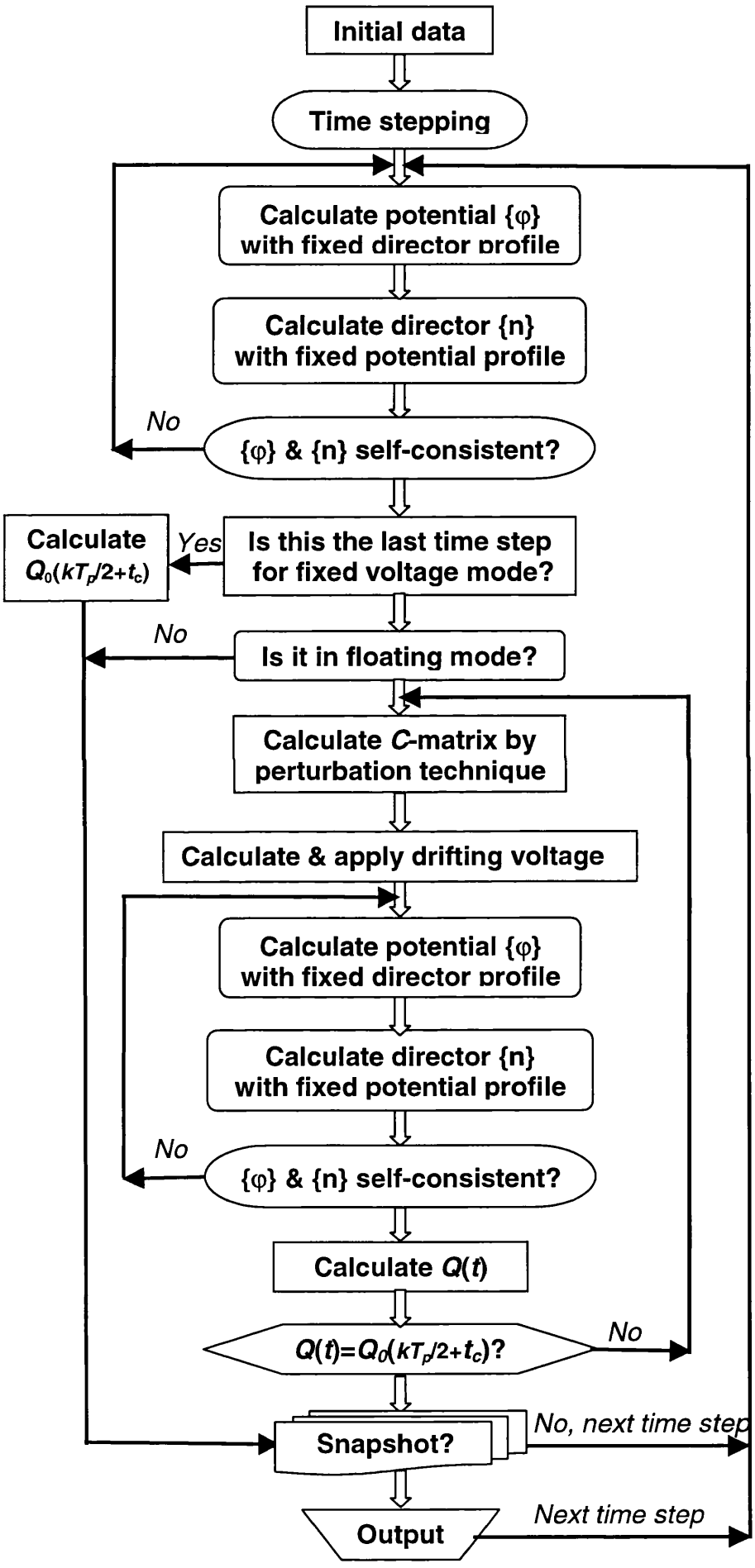
Initial data
Time stepping
Calculate potential {φ} with fixed director profile
Calculate director {n} with fixed potential profile
No
{φ} & {n} self-consistent?
Calculate $Q_0(kT_p/2+t_c)$
Yes
Is this the last time step for fixed voltage mode?
No
Is it in floating mode?
Calculate C-matrix by perturbation technique
Calculate & apply drifting voltage
Calculate potential {φ} with fixed director profile
Calculate director {n} with fixed potential profile
No
{φ} & {n} self-consistent?
Calculate Q(t)
$Q(t)=Q_0(kT_p/2+t_c)$?
No
Snapshot?
No, next time step
Output
Next time step

6.6. Study of a large sample

A large sample, fabricated especially by Philips Research Laboratories (Redhill) (PRL) was experimentally tested by author and analysed using the described computer model.

The sample (see Figure 40), consists of a rectangular pixel of 28mm×33mm and the

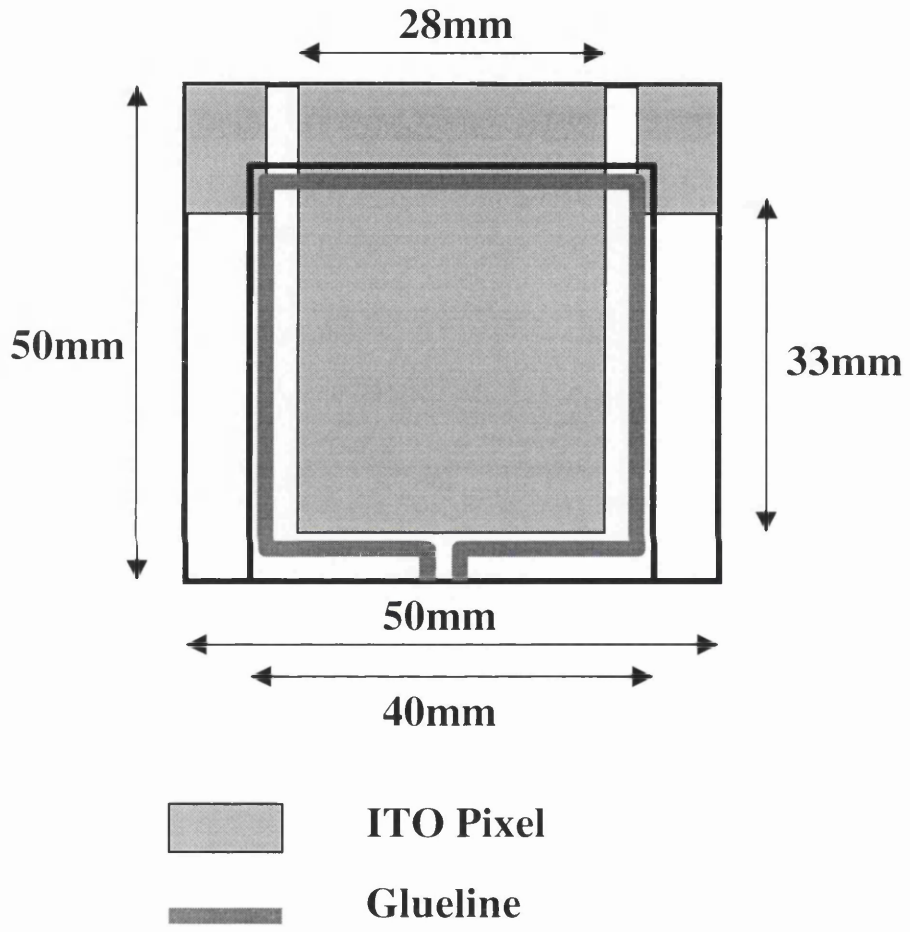

Figure 40 The geometry of the test cell in PRL (Redhill) for which the optical property has been measured by the author in January, 1999.

cell thickness is only of 4.8μm. This gives an x-z aspect ratio of the order of 1000:1. Using the same discretization as in the previous examples (of cells of 90 μm), that is, with Δx=1.5μm and Δz=0.25μm, the mesh for this sample would have a prohibitively large number of nodes. To avoid this, the following Cut and Paste approach was adopted.

6.6.1. Cut and paste approach

For the normal sized model cell as that shown in Figure 21, it can been seen that the director and potential distributions are almost uniform in the central part of the cell. It can be inferred, therefore, that for the large sample or test cell as shown in Figure 40 which is of a very big width, the director and potential distributions would exhibit the same pattern, i.e., invariant in space in the large portion of the cell around the centre. In this way, this part of cell can be cut off so that only a normal sized model cell needs to be modelled with considerable savings in modelling time without loss of any important detail.

In calculating the total charge, the contribution from this part which is cut off will be added to that corresponding to the actual modelled cell. The charge on this part of the pixel electrode should obviously equal the charge density in the middle of the pixel electrode times the length that has been cut off. Following this approach to calculating the total charge for the whole cell, the information on the generalised capacitance matrix $\boldsymbol{C}$ can be obtained by the perturbation technique that was developed earlier. A physically correct drifting voltage therefore can be finally determined which will guarantee the correct director and potential profiles. Based on this director profile, the average transmittance can be calculated by only sampling a representative narrow strip of the sample in the centre around the cell-gap (z) direction (which is quite sufficient due to the uniform director distribution in space within the bulk area of the cell in the centre). The transmittance obtained in this way can be therefore compared with the corresponding measurements which are conducted against the whole sample.

6.6.2. Example - Apply to the test cell

Let us apply the above technique to the test cell as shown in Figure 40. Consider the modelling of a cell with a total length of 66μm (from -33μm to 33μm) from which the pixel electrode takes 51μm. Therefore the dropped (cut off) piece of pixel electrode is of Δl_{cut} =27949μm, making the total length of 28mm. As before, the spatial steps Δx and Δz are, respectively, chosen to be 1.5μm and 0.25μm. The middle point is not exactly located at a pixel node in this case, rather, it is between node 17 and node 18. Therefore, the arithmetic mean of the charge densities of those two nodes is used as a density for the middle point. This density times the dropped length Δl_{cut}=27949μm

gives the charge for the cut-off part of the pixel electrode. This charge is then added to the total charges of the pixel of 51μm to get total charges for the whole test cell. Then, capacitance matrix $\boldsymbol{C}$ is calculated by perturbation method. Finally, the pixel drifting voltage is calculated and applied to get the required director and potential distributions. With this director distribution, the average normal transmittance is calculated by sampling only a very narrow area ranging from $x = -1.5\mu m$ to $x = 1.5\mu m$ along z-direction. The results will be presented in Section 6.14.

6.7. Case study (I) – without external capacitor

In this section, the results for the following electrode configurations are presented: (1) special case 1 - one pixel electrode without any bus electrodes considered as in the case of the test cell; (2) special case 2 - one pixel electrode with two bus electrodes whose voltage polarity is fixed; (3) realistic case: the configuration is the same as for Case 2, but the polarity of the bus voltages is not fixed. In all above cases, no external capacitor is included.

6.7.1. One pixel electrode without buses

This is the simplest, a special electrode configuration as there are no bus electrodes considered. The modelling parameters are the same as given in Table 2 (page 65). The results of dynamic behaviour of pixel voltage, mid-plane tilt angle, LC cell capacitance, charge on pixel electrode, and average normal transmittance are plotted in Figure 41 to Figure 45. The source voltage of 4 volts is applied to the pixel electrode for only 20μs within each half frame time (16.6667μm), then left to drift until the next half frame. It can been seen from Figure 41 that the voltage is drifting down until the next half-frame where it is reset again. During the first two half-frame times, it drifts down more than in later frame. This behaviour is consistent with that observed experimentally. It can be physically interpreted as follows:

When LC cell switches, the tilt angle of a director which is initially pre-set as 4° increases with time as shown in Figure 42, therefore the LC cell capacitance as a function of permittivity (directors) increases accordingly as shown in Figure 43, while

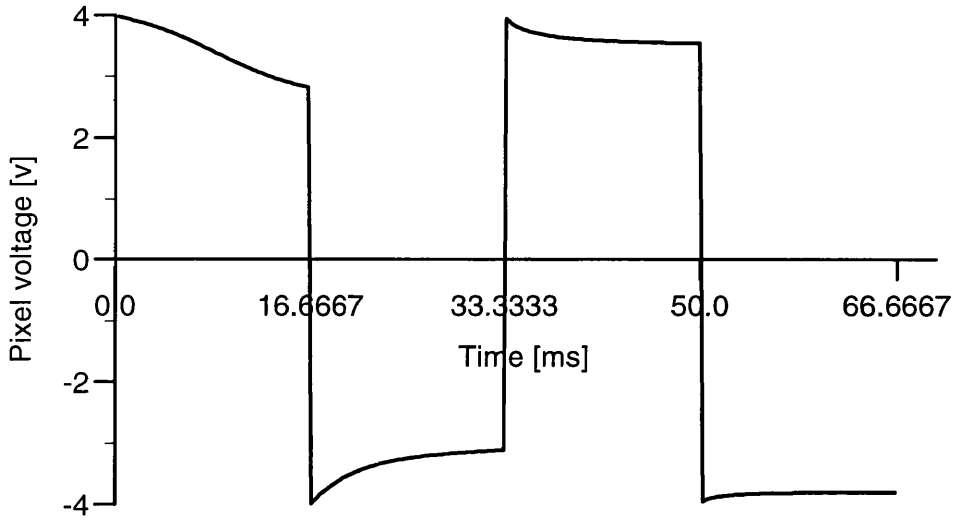

Figure 41 The evolution of drifting pixel voltage with time (connection time t_c only lasts 20μs within each half frame)

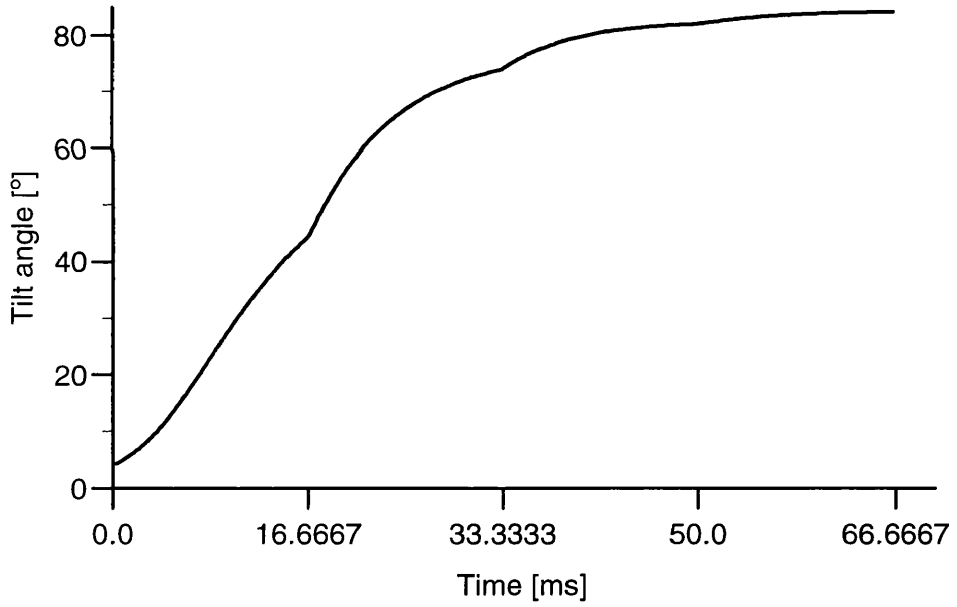

Figure 42 Switching behaviour of pretilt angle for a director located at the centre of the LC cell [co-ordinate: (0.0, 0.0)] with an initial pretilt angle 4°.

the range at which the tilt angle and hence the capacitance increases during the first two half-frame time is bigger than at later time. Since the charge must be maintained as

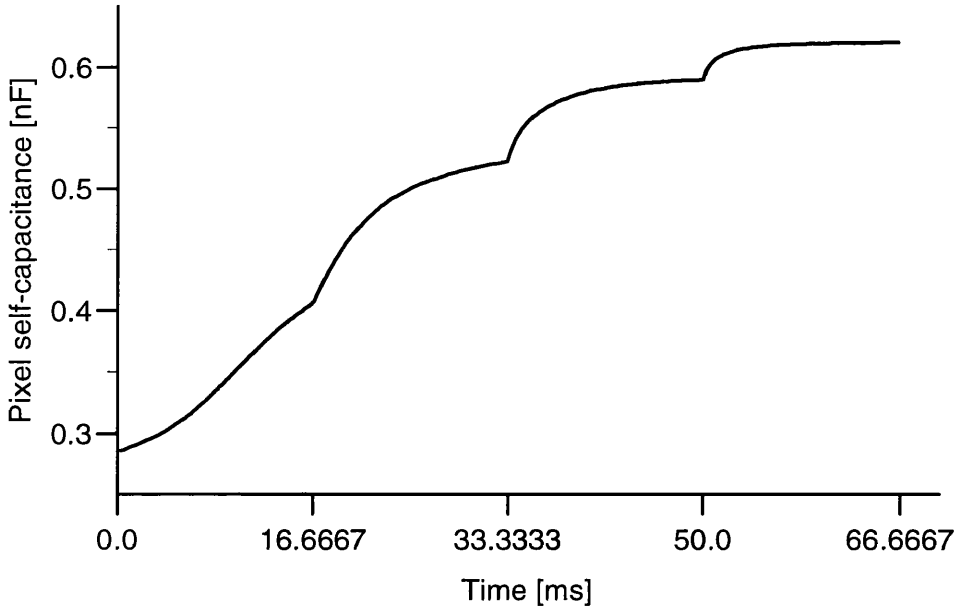

Figure 43 LC cell capacitance changing with time

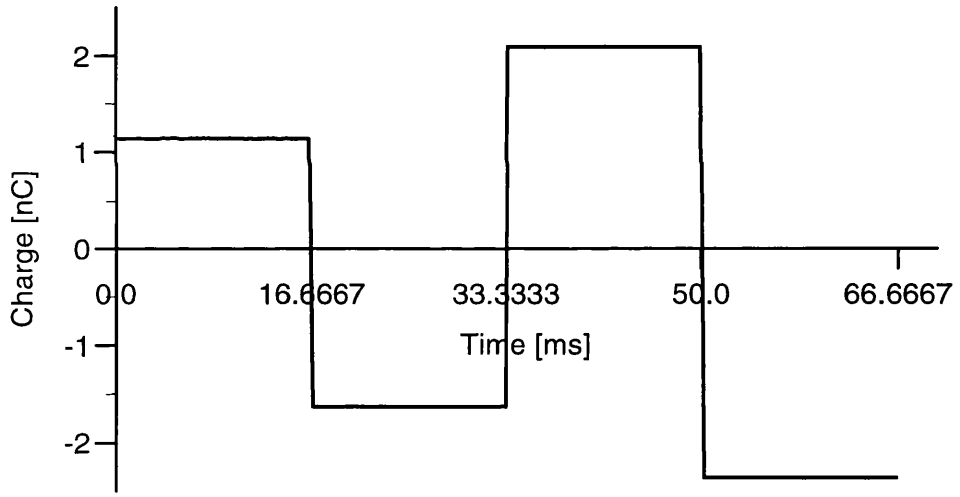

Figure 44 Pixel electrode charge against time

a constant as shown in Figure 44 during each half-frame, by relation $V=Q/C$, when the capacitance C increases, the voltage V must decrease.

The increase in the level of the constant charge from half frame to half frame as shown in Figure 44 is due to the rise in the level of the capacitance at the beginning of the concerned half-frame time, say, the third and so on as shown in Figure 43, while the lower values of the capacitance at the beginning of the first and the second half-frame times (see Figure 43) are responsible for the correspondingly low levels of the

constant charges as illustrated in Figure 44. In short, the charge depends on the capacitance.

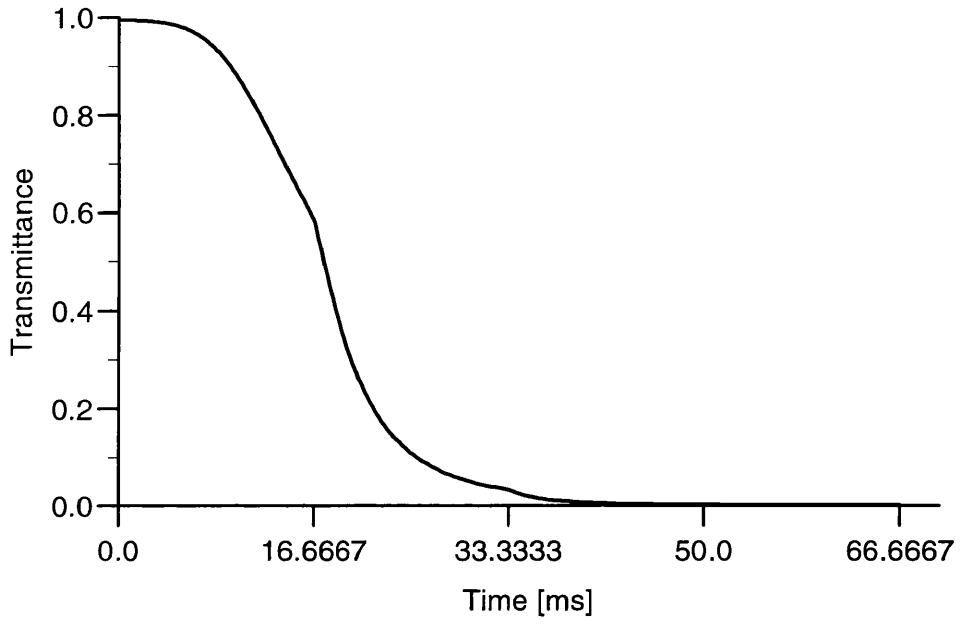

Figure 45 Normal transmittance varying with time (crossed polarizers pair)

Figure 45 shows how the LC cell changes from bright state to the dark state and how long it takes for such a change (about one and a quarter of a period).

6.7.2. One pixel electrode, two bus lines with fixed voltage polarity

This is a simplified case, but with realistic electrode configuration, i.e., one data (column) electrode and two select (row) electrodes, while the select voltage is fixed at +5 volts without polarity change allowed during the whole modelling time span. The purpose of studying this case is to see what kind of difference will occur between case 1 which has been studied as above without any bus electrode and the case when a polarity-fixed bus line is used.

Figure 46-Figure 49 show the differences of floating voltages, tilt angles of a director in the cell centre, capacitances, and transmittances between the current case and the case discussed in the above section 6.7.1. Figure 46 gives a comparison of pixel floating voltages between two different cases. As we can see from this figure, the pixel voltage in the case of no bus electrode (dashed line) decreases slower than that (solid line) in the case of having bus electrodes with fixed polarity for the first 29.5ms

and then the tendency is reversed. However, the same reverse tendency for the capacitance (Figure 48) does not occur until 42ms due to the delay in the response of the director to the change in the voltage (relaxation).

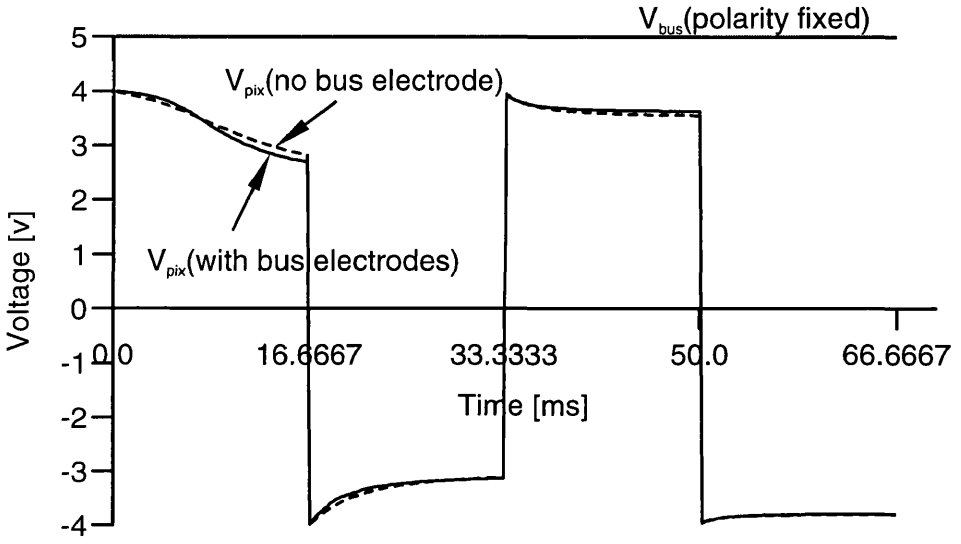

Figure 46 A comparison of pixel floating voltages between the case of no bus electrode and the case with bus electrodes but with fixed polarity.

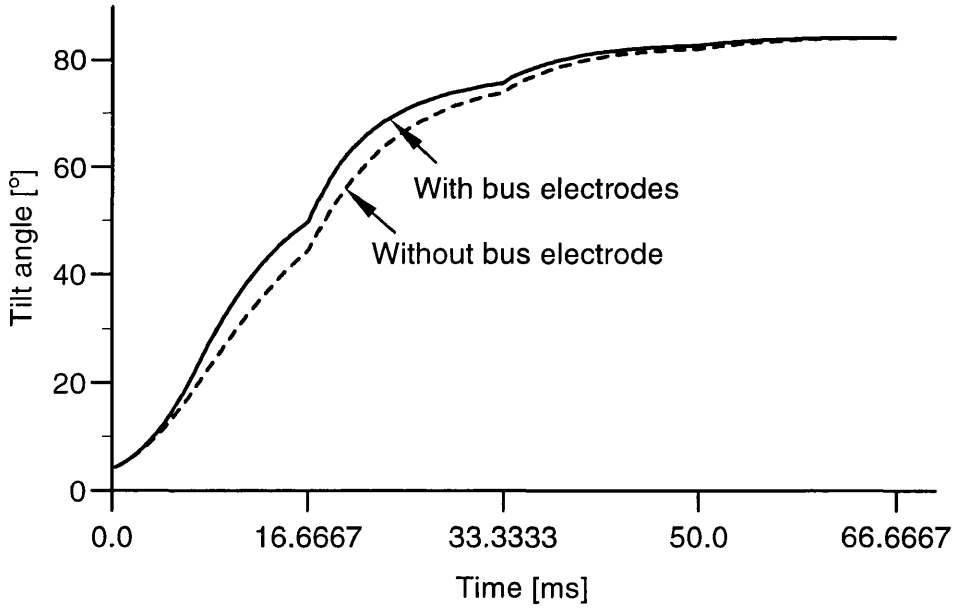

Figure 47 Switching behaviour corresponding to voltages in Figure 46

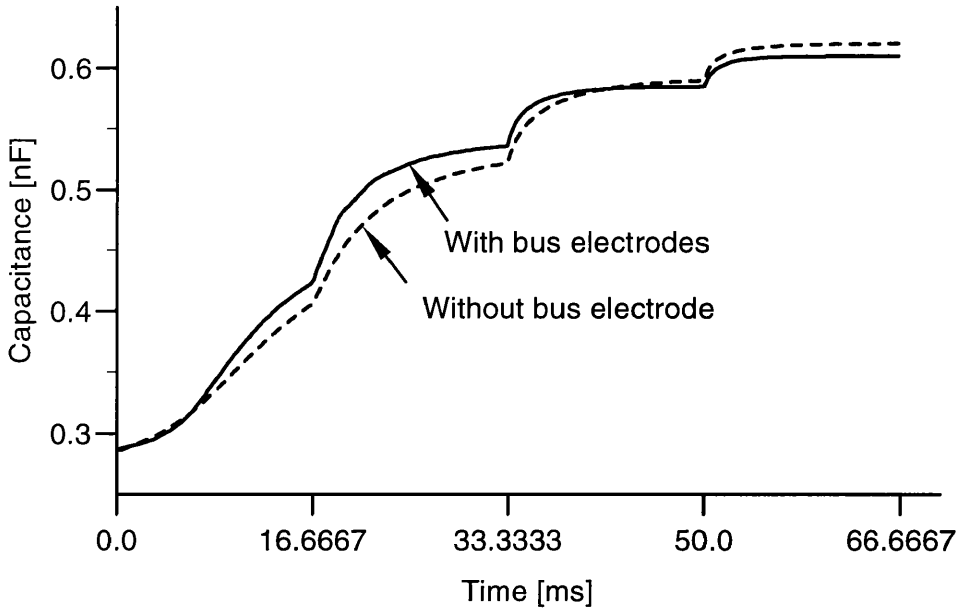

Figure 48 Capacitance versus time

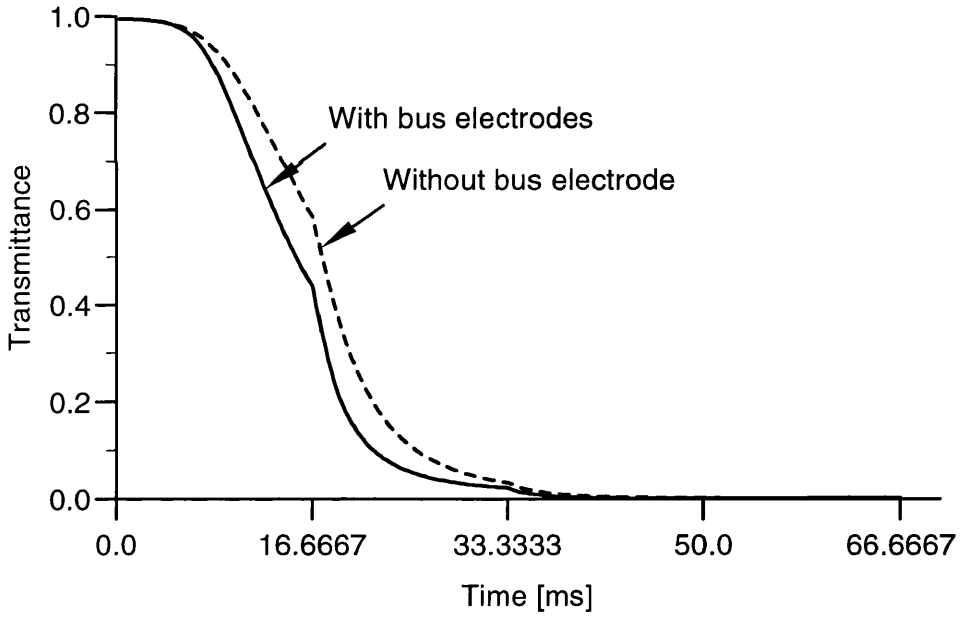

Figure 49 Optical transmittance

Examining all these figures, we can conclude that the presence of bus electrodes does have influence on the dynamic behaviour of LC device - it speeds up the switching process in general. This is because a positive (single polarity) 5 volts of bus voltage is used which strengthens the effect of the pixel voltage.

6.7.3. One pixel electrode and two bus lines with changing polarity

In this case, the voltage of the bus lines is allowed to change polarity every 30 μs. Figure 50 - Figure 54 show the dynamic behaviour (solid line) of the pixel voltage, tilt angle of the director in the cell centre, pixel self-capacitance, transmittance, and the pixel charge as well as those corresponding to the constant voltage model (dash line). From them, five observations can be obtained:

The pixel voltage drops most during the first half-frame time because the directors are switched (become tilted) rapidly as shown in Figure 51 and hence the cell capacitance increases dramatically (see Figure 52). The drop slows down during the second-half frame time, and after that (one frame time), the voltage tends to remain constant when the tilt angle and hence the capacitance approaches a stable value.

There is a periodical fluctuation pattern superposed onto the average pixel voltage curve. This is purely due to the rapid change in the polarity (every 30μs) of bus voltage coupled to the pixel voltage through the mutual capacitance between pixel and bus electrodes. This does not occur at all in the case of no bus electrodes (Figure 41) or having bus electrodes but with a polarity-fixed voltage applied (Figure 46) or with a zero volt bus voltage. However, this fluctuation behaviour can be reduced if a proper external capacitor is used as discussed in the following section.

The abrupt changes appearing in each curve for tilt angle (Figure 51), capacitance (Figure 52), and transmittance (Figure 53), occurring at half-frame intervals are due to the voltage resetting at the beginning of each half-frame time.

Due to voltage floating, it takes longer time for the system to reach the stable state because the gradual voltage dropping during each half-frame time slows down the switching process of the system compared with no voltage dropping as in the case of constant voltage model. However as one can see from Figure 51 to Figure 53 that for the first 12.6ms, the system is switched faster in the case of constant charge model than in the case of constant voltage model. This is because the floating voltage in the first case had a 50% time on average to reach a value which is above the constant voltage of 4.0v during the period of first 4.5ms time span due to the coupling from the bus lines as shown in Figure 50.

The constant charge condition is satisfied as shown in Figure 54.

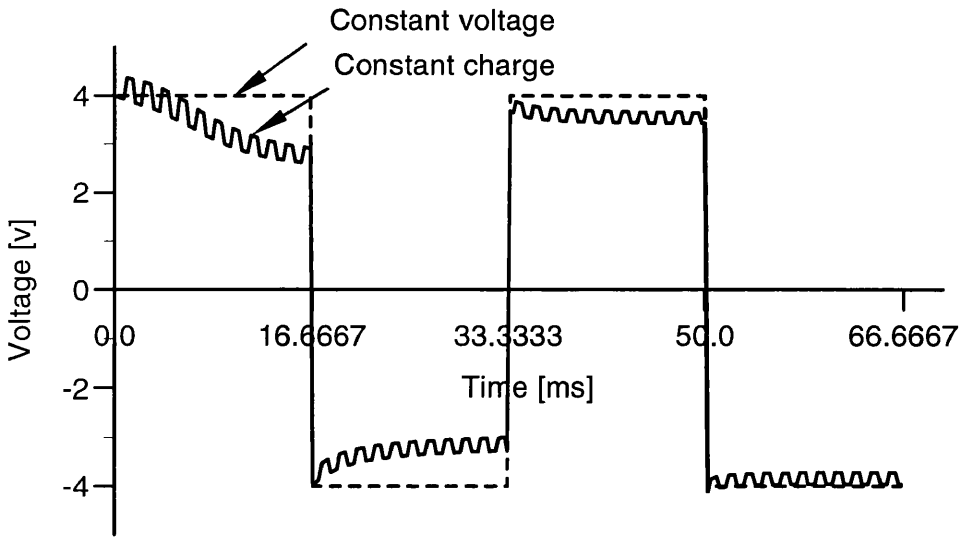

Figure 50 Floating pixel voltage versus time

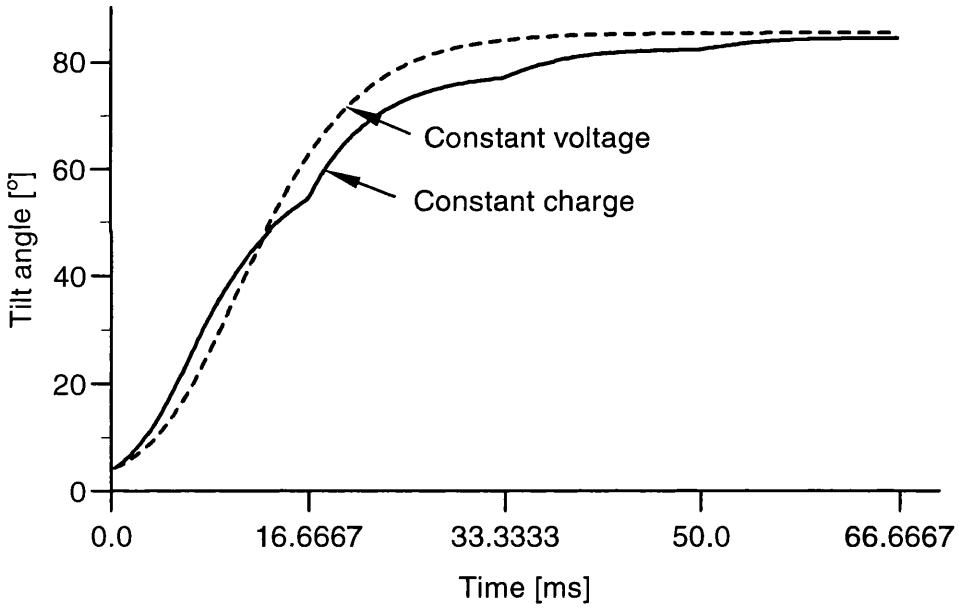

Figure 51 The dynamic behaviour of switching of the director in the cell centre

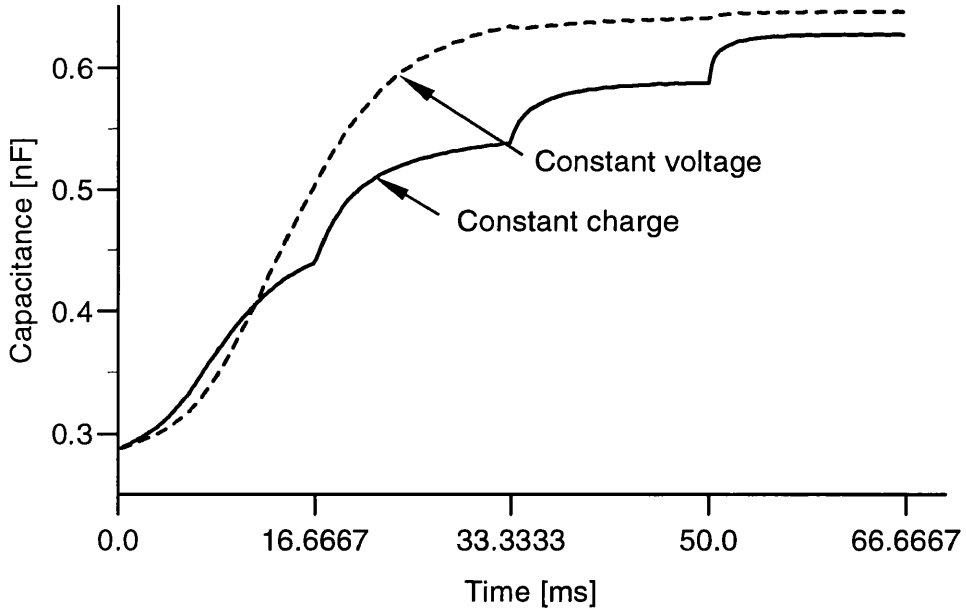

Figure 52 Pixel self-capacitance vs. time

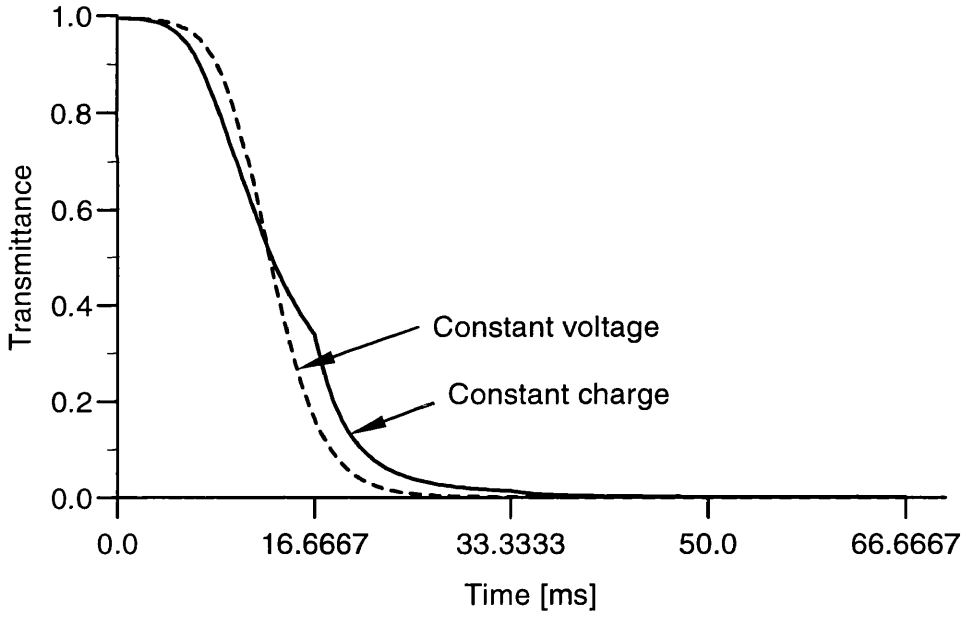

Figure 53 Transmittance vs. time

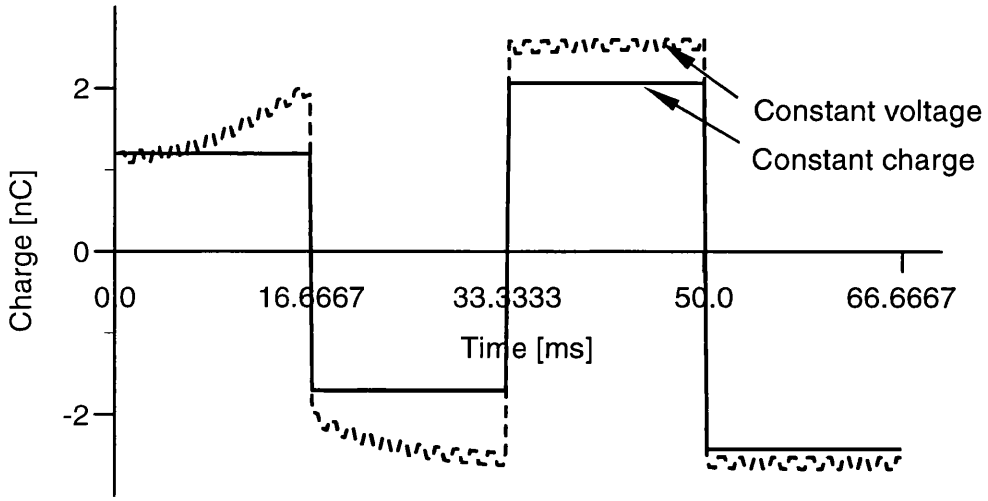

Figure 54 Charge vs. time, showing the constant charge condition is satisfied

6.8. Case study (II) – with external capacitor

As pointed out above, the rapid change in the polarity of the bus line voltages causes a corresponding fluctuation in the floating pixel voltage and the voltage resetting leads to abrupt change in dynamic behaviour of LC cell at the beginning of each half-frame time. However, these unwanted effects can be suppressed by introducing an external capacitor of certain amount as shown in Figure 55 - Figure 58 below. The effects of 4 different values of the storage capacitor C_{ext} are shown (C_{ext}=0.5nF, 5nF, 10nF, and 1000nF). In order to make an intuitive comparison, included also are the previously discussed two other cases: the constant voltage model ($\equiv C_{ext}=\infty$) and constant charge model *without* storage capacitor, i.e., C_{ext}=0. From this set of figures, the following observations can be obtained:

With an increase in the value of external capacitor, the oscillation behaviour gradually disappears, so the abrupt changes in the dynamic behaviour of the system occurring at half frame intervals. Even a value of 0.5nF (which is roughly equal to the pixel self-capacitance) can curb the oscillation dramatically as shown in Figure 55;

The dynamic behaviour of the cell for an external capacitor of 5nF is nearly the same as for one of 10nF;

When the value of C_{ext} is increased to1000nF, the system behaviour is actually the same as that for constant voltage model;

When the external capacitance is 0.5nF, the LC cell switching is slower than when a value of 5nF or 10nF or 1000nF is used;

Another interesting phenomenon is that an external capacitor of 5nF gives rise to a faster switching than one of a 1000nF or a constant voltage ($C_{ext}=\infty$). 5nF, that is about 8 times of pixel self-capacitance, appears to be the optimal value for this cell as this is sufficient to eliminate the oscillations and higher values slow down the switching. This non-linear relationship between response speed and value of the external capacitor is proved in the next section to be related to the application of the bus voltage;

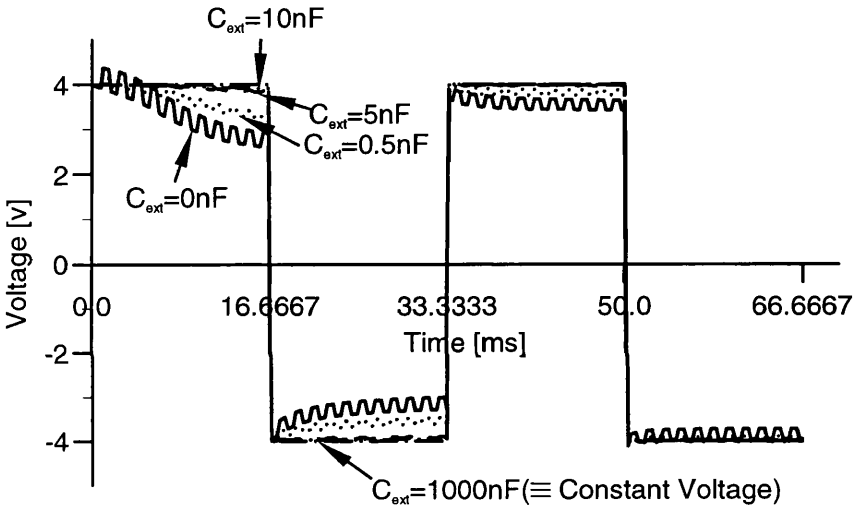

Figure 55 Voltage versus time under various external capacitance C_{ext}

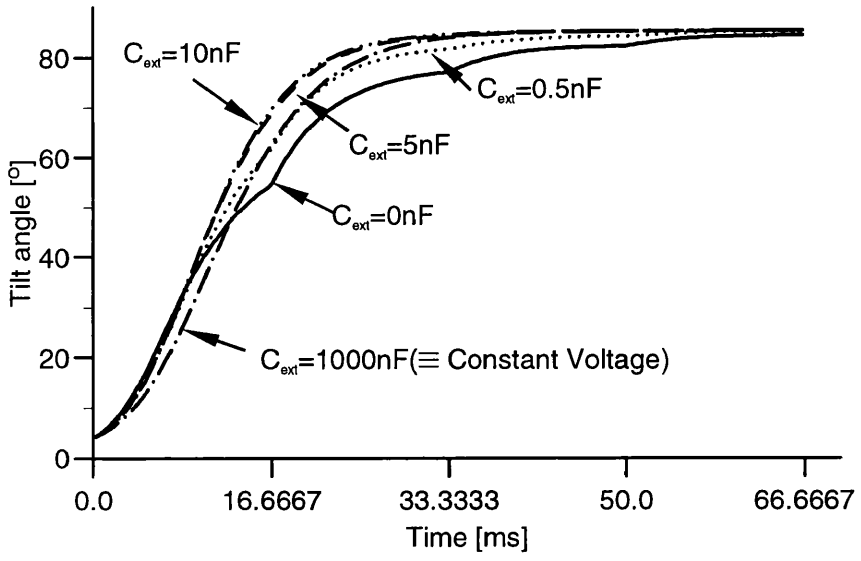

Figure 56 Dynamic behaviour of tilt angle of the director at the cell centre under various storage capacitance C_{ext}

As discussed in the above section, because the pixel voltage stays above the constant voltage level of 4.0v for a 50% of time on average within the first 4.5ms in the cases of the external capacitance of 0.5nF (due to the bus voltage coupling effect), the system responds faster during the first 15.6ms than for the case of a constant voltage.

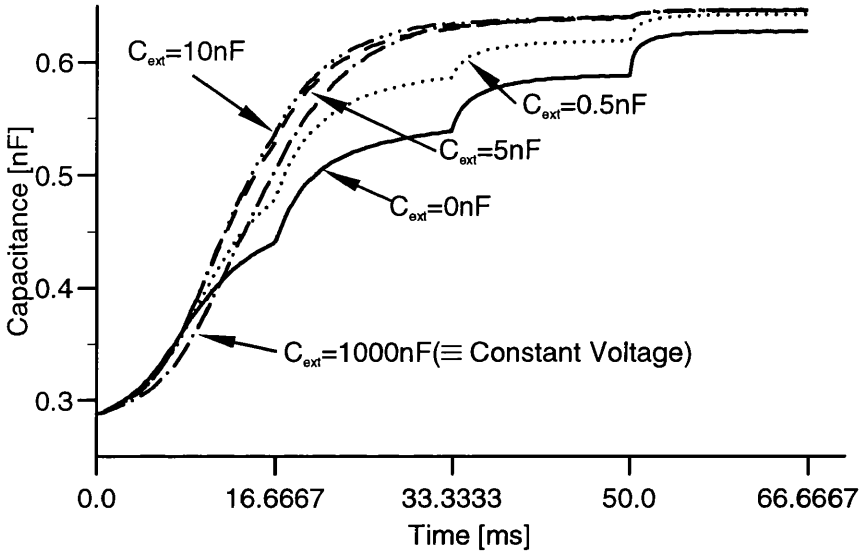

Figure 57 Variation of pixel self-capacitance with time under different external capacitance C_{ext}

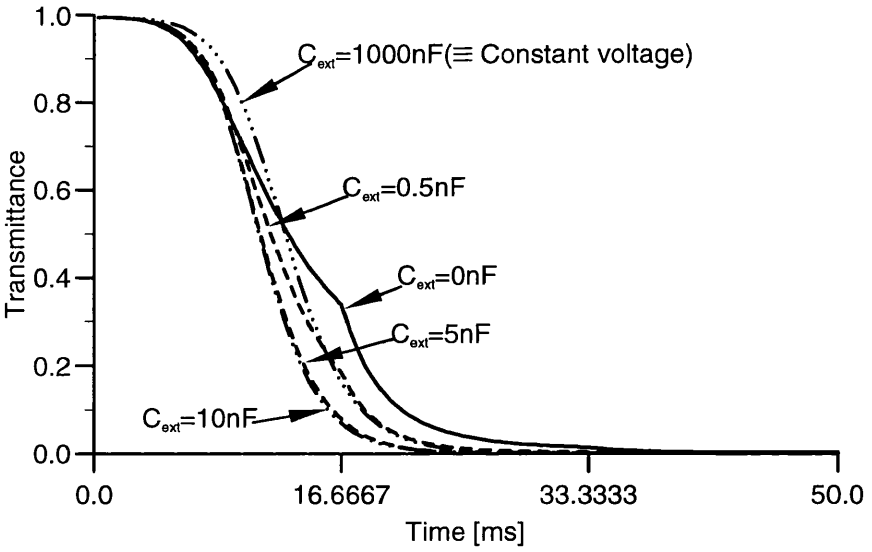

Figure 58 Transmittance versus time for different external capacitance C_{ext}

6.9. The effect of bus voltage on the dynamic behaviour of LCD

As mentioned before, the bus voltage does have influence on the dynamic behaviour. Therefore, this section is dedicated to address this issue.

6.9.1. No visible influence under constant voltage mode

First, let us look at Figure 59 that shows the dynamic behaviour of the transmittance under 3 different bus voltage conditions:

No bus electrodes involved at all or a zero volt bus voltage applied if bus electrodes are involved;

A symmetric bus voltage varying from +5v to –5v used;

An asymmetric bus voltage varying from +6v to –4v used.

As one can see that under constant voltage mode, the difference among them is negligible and this also holds true for the capacitance and mid-plane tilt angle of the director. That means that in the case of a constant voltage, no matter if the bus voltage is zero, or symmetric or asymmetric, or even there is no any bus electrodes involved at all, there is no visible influence upon the pixel switching behaviour.

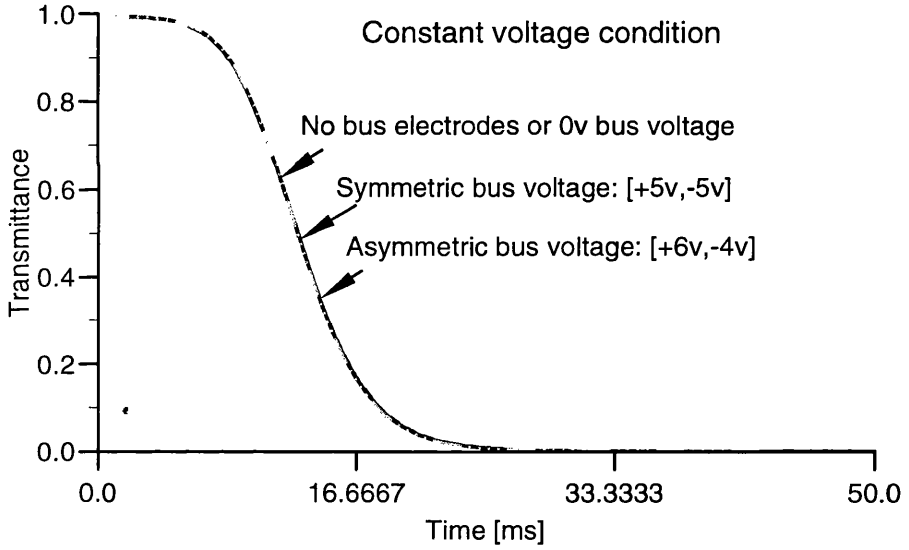

Figure 59 Transmittance versus time under different bus voltages for constant voltage model

6.9.2. Appreciable influence from the buses under floating voltage mode

Next, let us move to Figure 60 that shows the transmittance curves versus time under three different bus voltage conditions as mentioned above, but with a 5nF external capacitor connected in each case. The conclusions we can draw here are that:

Application of bus voltage (symmetric or asymmetric) has an appreciable effect on the dynamic behaviour of system compared with the case of no bus electrodes involved. The actual effect is to make the switching progress speed up as shown in this figure;

The results for both symmetric and asymmetric bus voltage conditions are indistinguishable. In other words, in terms of transmittance (capacitance and tilt angle at the cell centre) it really does not matter if symmetric or asymmetric bus voltage is applied.

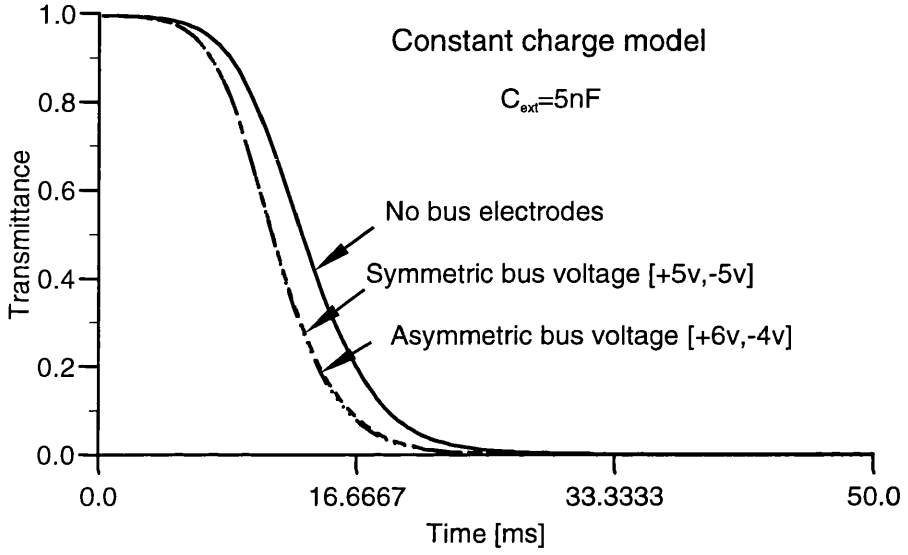

Figure 60 Transmittance versus time under different bus voltage for constant charge model

6.9.3. Other effects

Figure 61 shows a comparison between transmittance curves without bus electrodes for two values of C_{ext}: 0nF and 5nF and those for bus voltages applied, with C_{ext}=1.5nF and C_{ext}=5nF. The curve for the constant voltage case is also shown – this is equivalent to $C_{ext} = \infty$ (solid line). Two main features can be noticed here:

In the case of no bus electrodes involved, the transmittance curves converge to the curve for the constant voltage from the right-hand side of the latter;

For the case of the application of the bus voltage, the curves for C_{ext}=1.5nF and C_{ext}=2.5nF (not plotted here) deviate from the limit (solid line), until the C_{ext} reaches an optimal value of 5nF (10nF gives nearly the same result, see Figure 58). However, if C_{ext} is further increased, then the curve is no longer moving away from the limit,

rather it converges to the limit from the left-hand side. Particularly, when C_{ext} is increased to 1000nF, it actually coincides with the limit curve.

The conclusion is that the presence of the bus voltage does exert noticeable influence on the switching behaviour of the LC cell under constant charge mode – it speeds up the switching process of the cell in general and cannot be ignored.

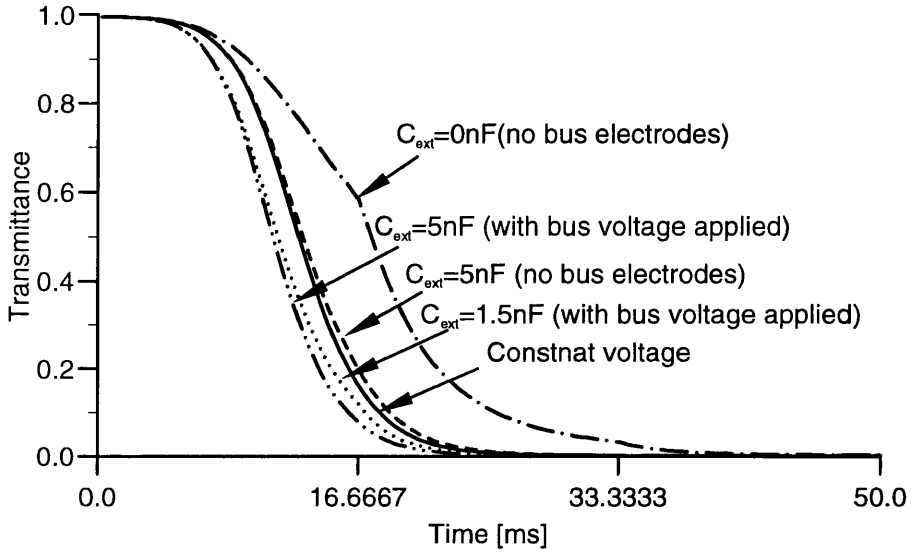

Figure 61 Transmittance versus time under different bus voltage conditions – a comparison

6.10. The effect of different elastic constant *K* and viscosity γ

Different values of the elastic constant *K* have different effects on the LC cell optical response, so do the rotational viscosity γ's. Physically speaking under a given source voltage, the bigger value of *K* will slow down the response of the LC system than a smaller value because bigger *K* means bigger deformation to the system, and hence, higher energy state for which the system will take longer time to reach stable state. This conclusion applies to the viscosity as well. The bigger the γ, the slower the system will respond because bigger value of γ will obviously prevent directors from quick response to the applied field. Our modelling results for a source voltage of 4v as shown in Figure 62 confirm the above analysis. As one can see that a viscosity of 0.5 makes the response of system dramatically slower than a value of 0.123.

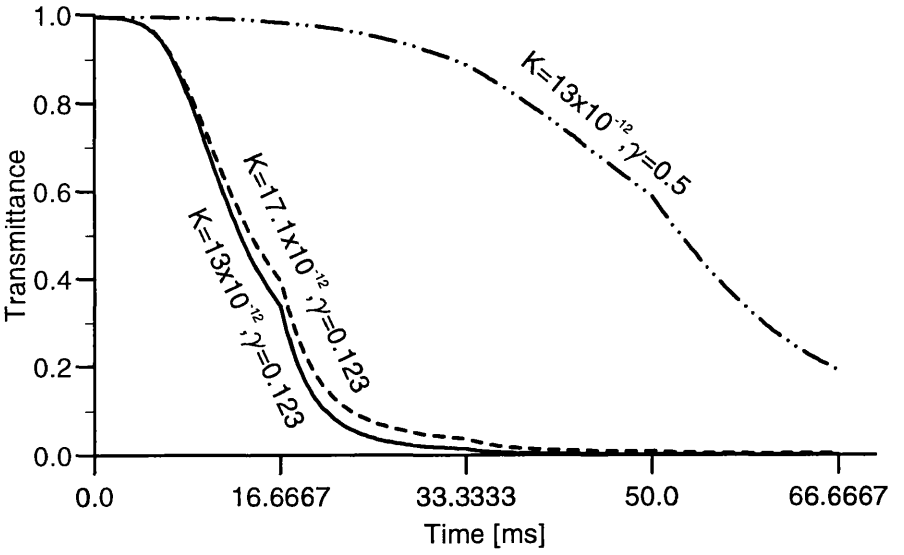

Figure 62 Optical response to different elastic constant *K*'s and rotational viscosity γ's

6.11. The effect of different levels of the source voltage

Figure 63 shows the effect of 7 different levels of the applied voltages on the optical response of the system. It can be seen that different levels of the voltages give different grey levels. It appears that the mid-grey level lies between 2v and 2.5v. All other parameters used are the same as given in Table 2.

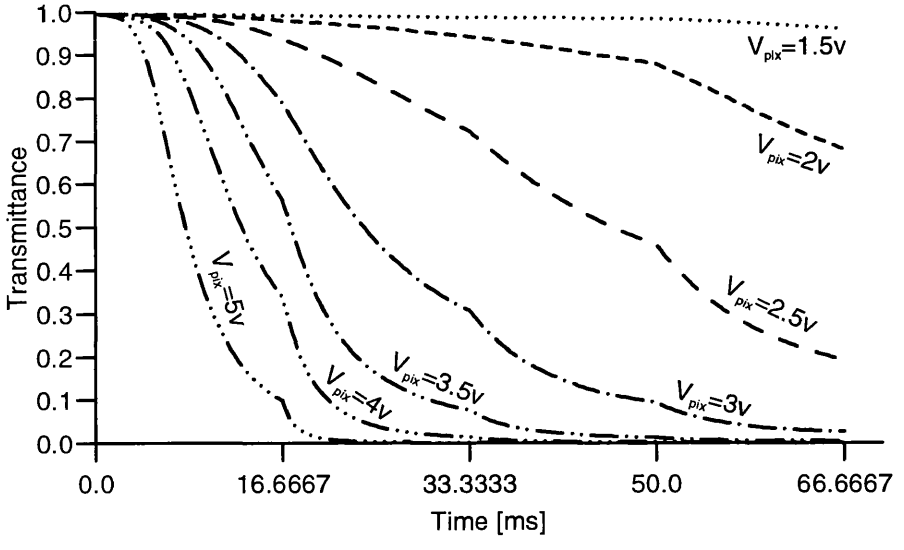

Figure 63 Optical response to various voltage levels

6.12. Further case study (I) – flicker

Flicker is another experimentally observed dynamic behaviour of LC displays. It is generally known that discharging effects cause flicker [25]. However, Onozawa *et al*'s work [25] demonstrated that flicker arises from imbalanced pixel voltage, or DC bias/component that exists in actual operation of the LCD device due to the alternating polarities of the pixel voltage. Discharging effects amplify the flicker arising from voltage imbalance. Vetter's *et al*'s study [26] also demonstrated how a small DC bias could cause flicker. In our 2D model, resistive discharging through cell conductance is not considered at all. Here, we investigate into the effects of voltage imbalance. We superpose 3 different DC components: 0.3v, 0.5v, and 1.0v to the base voltage of 3 volts to make the pixel voltage imbalanced as shown in Figure 64 and examine the flicker effect. The parameters used for the modelling are the same as given in Table 2, but the period of the source voltage is chosen as 30ms, rather than 33.33ms. As one can see from Figure 65 the flicker behaviour is reproduced here with 30ms sub-harmonics. The bigger the DC component, the more striking is the harmonic pattern. Figure 66 and Figure 67 show the corresponding behaviour of the mid-plane tilt angle and the cell capacitance. Therefore, our modelling supports Onozawa *et al*'s conclusion.

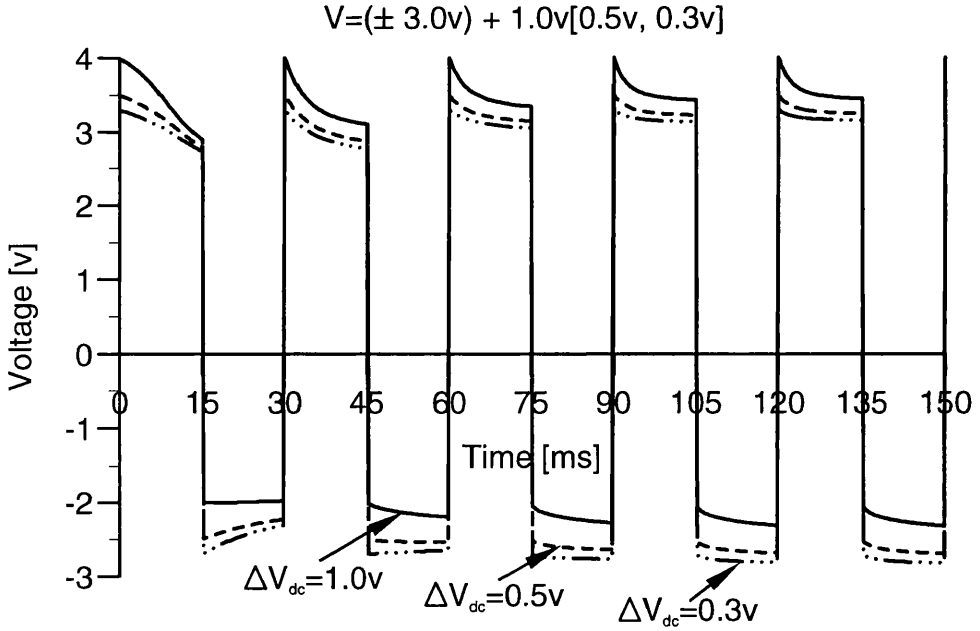

Figure 64 3 DC bias voltages: 0.3v, 0.5v, and 1.0v superposed to the base voltage 3v.

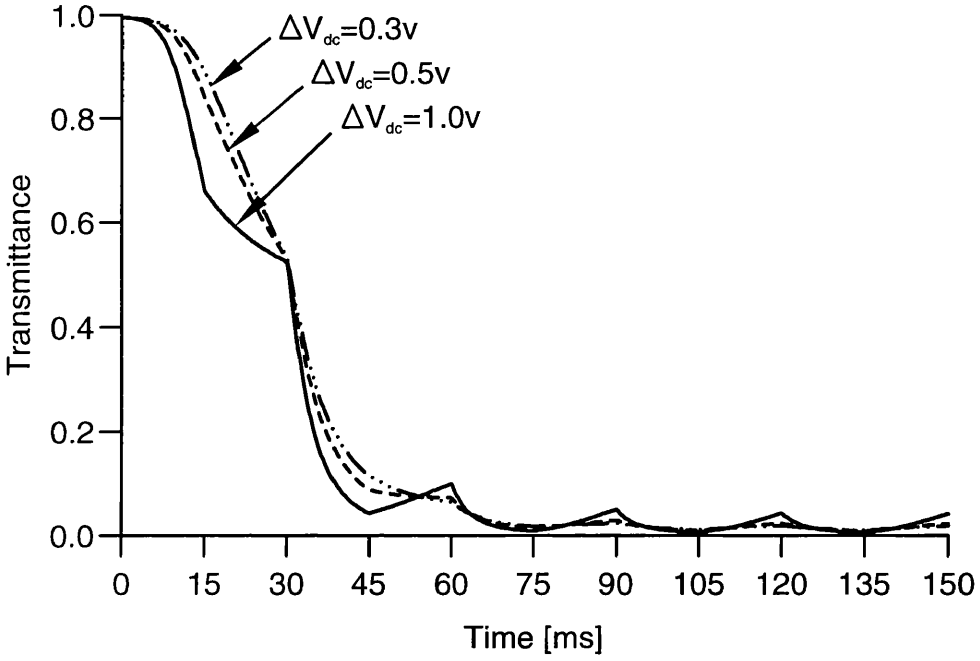

Figure 65 Transmittance curves showing the flicker for 3 DC components: 0.3v, 0.5v and 1.0v

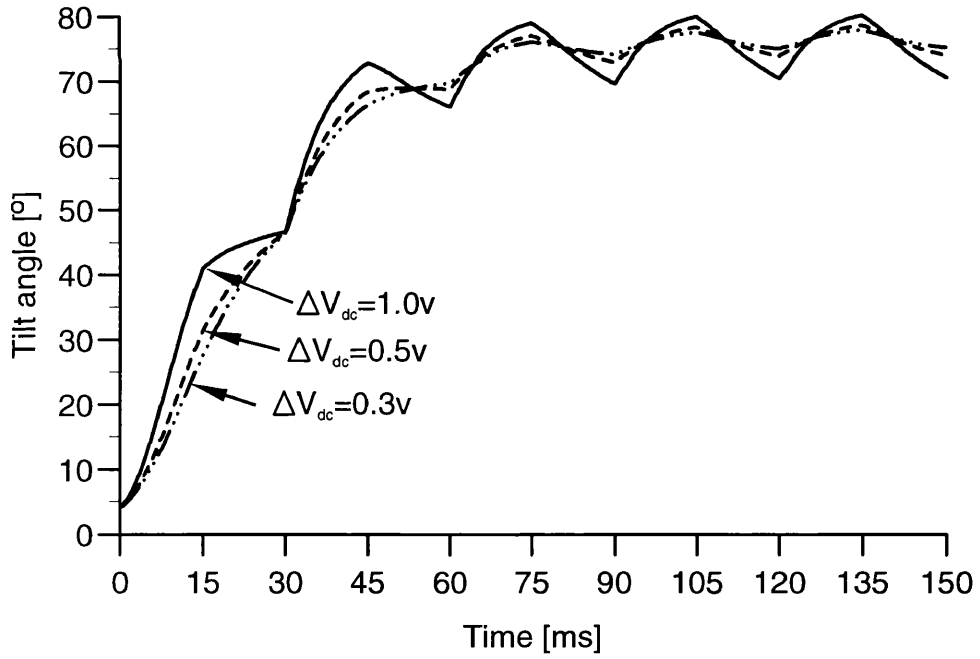

Figure 66 Behaviour of tilt angle of director at cell centre in the case of 3 DC components

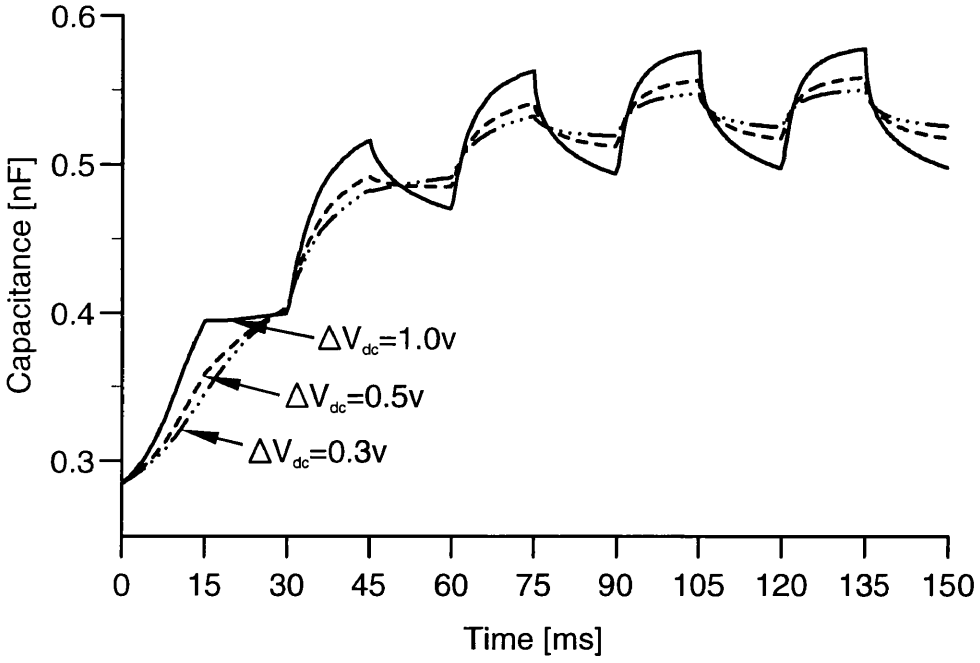

Figure 67 Behaviour of capacitance for 3 cases of DC bias

It is worthwhile to point out that there also exists flicker in TFT devices even the source voltage is balanced (no offset) due to the influence of bus lines of non-zero volts on the floating voltage of the pixel as shown in Figure 68. It can be seen that with no bus lines or zero-volt bus lines, there is no flicker predicted, and symmetric

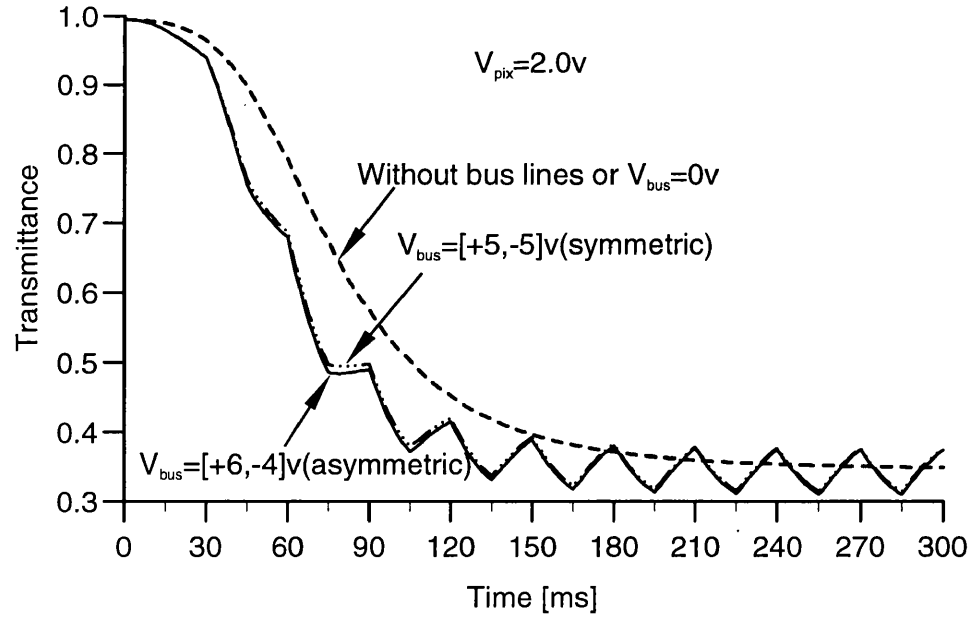

Figure 68 Flicker that is caused by non-zero bus voltage (no matter whose pattern is symmetric or non-symmetric) even the source voltage is balanced (no offset) from 2v to -2v.

and non-symmetric bus voltages make little difference in the flicker caused. The underlying reason for the flicker formed in this case is essentially the same as the above discussed case, i.e., existence of DC component. But, here this imbalance in pixel voltage is caused by the bus voltage as discussed in Section 6.7.3 and shown in Figure 50.

6.13. Further case study (II) - two pixel electrodes and one bus line

Unlike all previous oversimplified 1D models [25-27], Our 2D model not only allows us to consider the cell geometry with 1 pixel and 2 bus electrodes, but also the one with 2 pixel and 1 bus electrodes as depicted in Figure 28 in sub-section 6.1.1(v). This geometry occurs when dealing with a very big pixel which cannot be directly handled computationally. In this case we have to cut the width of each pixel on both sides and use a Neumann boundary condition, i.e., assume that directors and the potential profiles are the same in the central area under each pixel. Also, the voltage applied to the pixels are different. Therefore, a 4v source is set for pixel 1 and 3v for pixel 2. The transmittance, capacitance, and tilt angle can be calculated separately. The cell geometry is shown in Figure 70(a) which depicts the snapshot of the profiles of the directors and the potential. All other parameters used in the modelling are the same as those given in the Table 2, but the period of the source voltage is set as 30ms here. Figure 69 shows floating voltages of two pixels. Figure 70 (a) and Figure 71 (a) are two snapshots of the directors and potential profiles which are taken at half-frame time (t=15ms) and two complete frame times (t=60ms). Figure 70 (b) and Figure 71 (b) are the corresponding transmittance profiles. From those, the defect formation, structure, and evolution can be discerned as well.

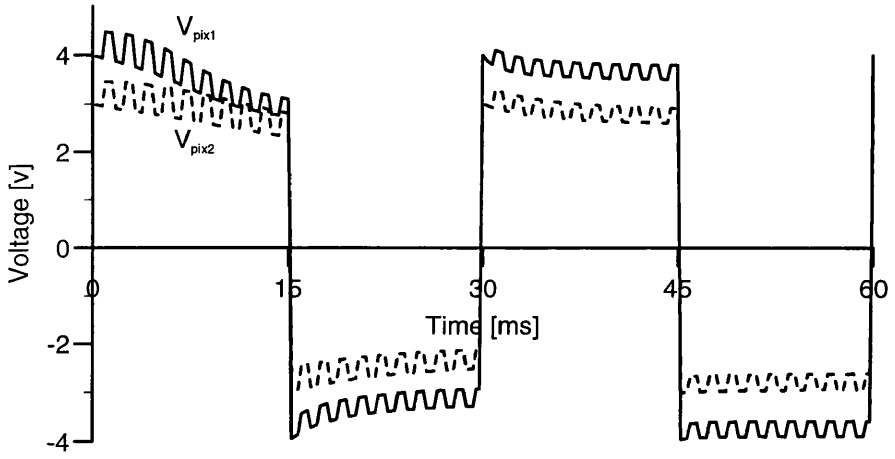

Figure 69 Floating voltages of pixel 1 and pixel 2. 4v source for pixel 1 and 3v for pixel 2

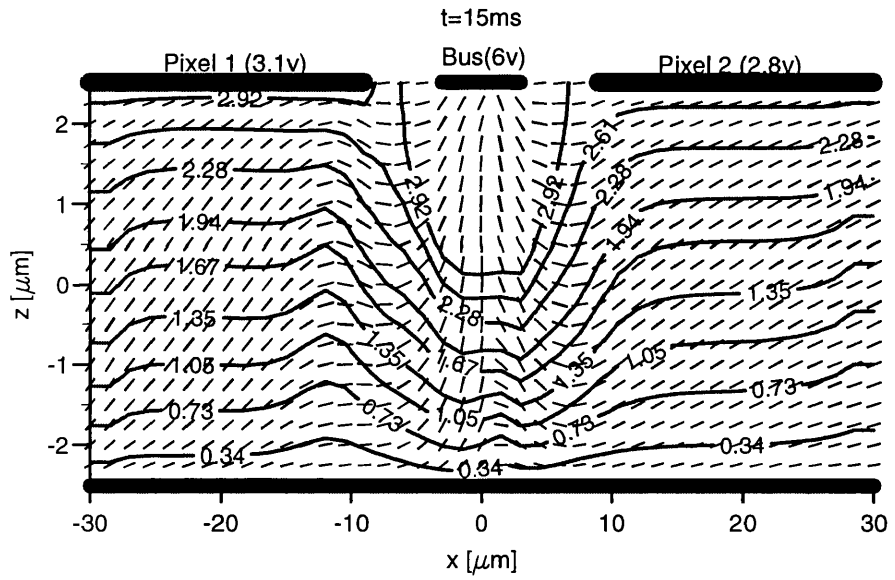

(a)

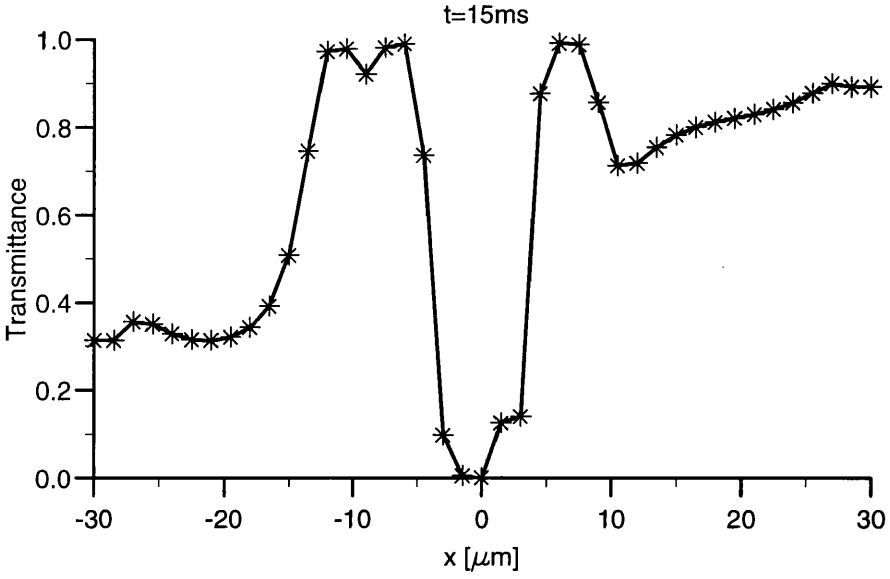

(b)

Figure 70 (a) A snapshot of profiles of director and potential at *t*=15ms. (b) Corresponding transmittance profile

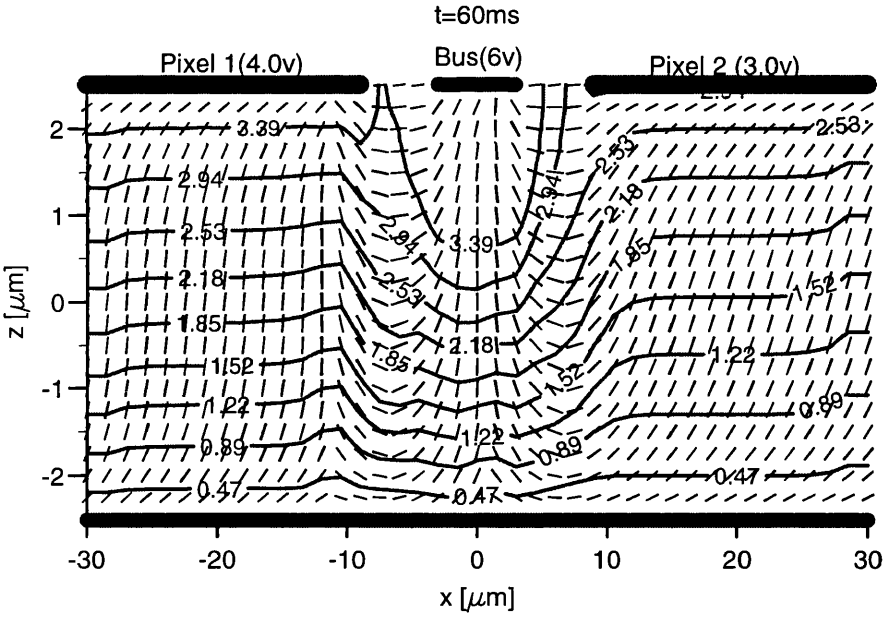

(a)

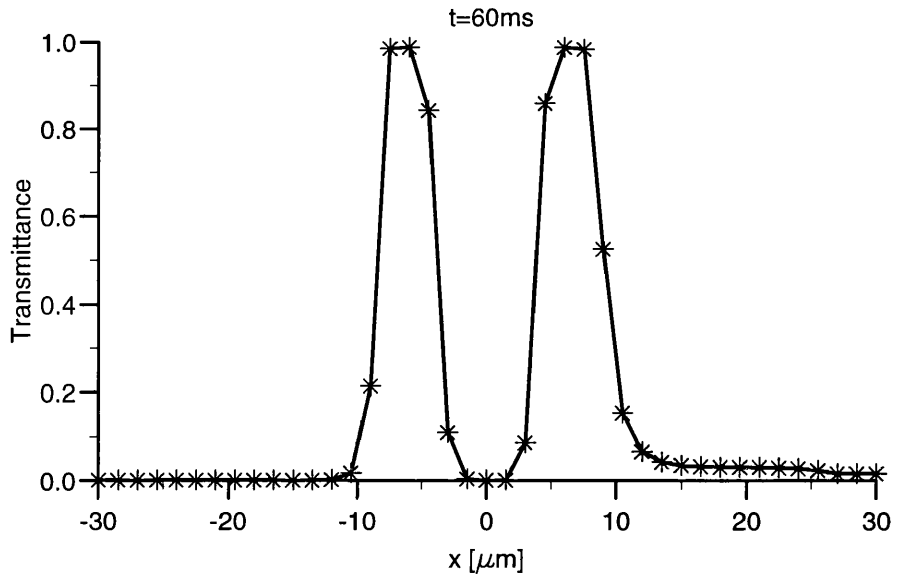

(b)

Figure 71 (a) The second snapshot of profiles of director and potential at *t*=60ms. (b) The corresponding transmittance profile

Figure 72 gives the tilt angle versus time of three directors picked from location (-19.5, 0.0) μm under the pixel electrode 1, cell centre (0.0,0.0) under the bus electrode, and (19.5,0.0)μm under the pixel electrode 2. It can be seen that the director under the bus electrode gets switched fast and the switching largest in magnitude.

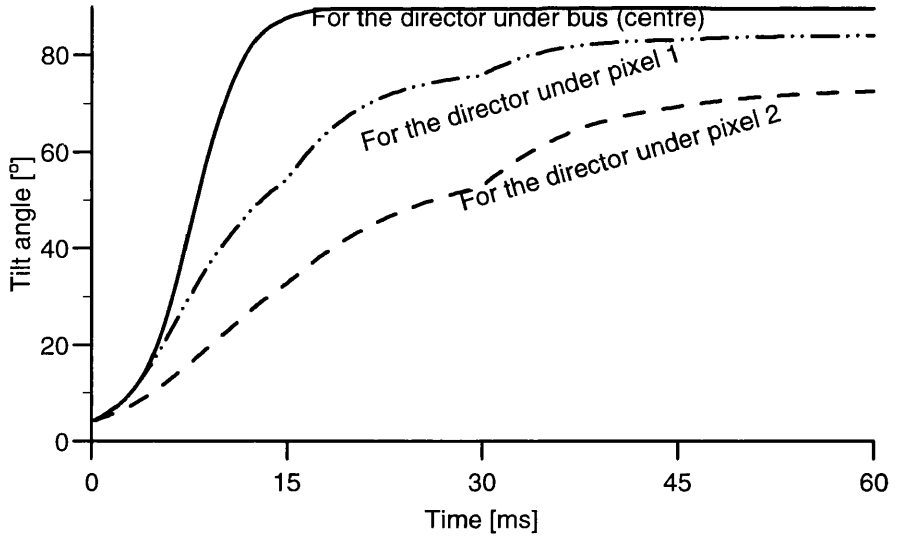

Figure 72 Switching behaviour of the director (a) at the location (-19.5, 0.0) under pixel electrode 1, (b) at the cell centre (0.0,0.0) under bus electrode, and (c) at (19.5,0.0) under pixel electrode 2

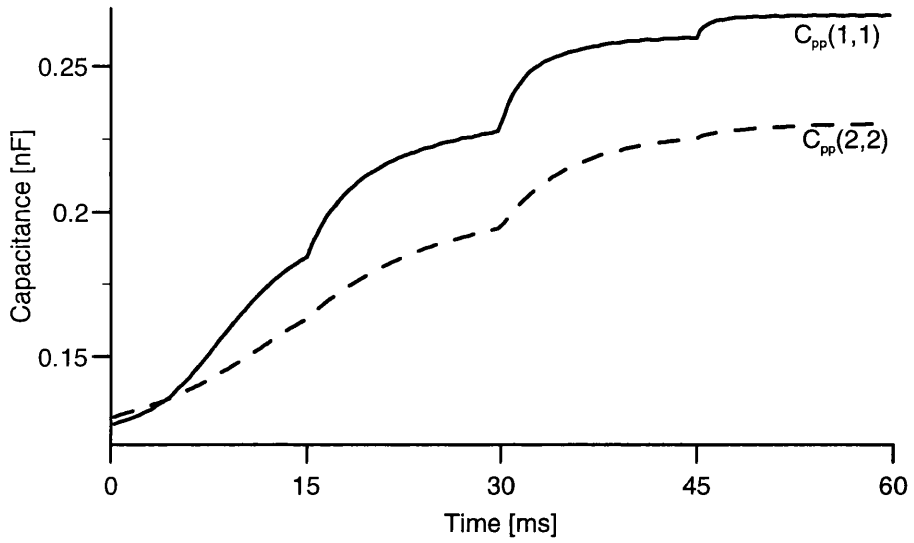

Figure 73 Self-capacitance of pixel 1 and pixel 2 versus time

The self-capacitance of pixels 1 and 2 are shown in Figure 73 and the transmittance through those two pixels is given in Figure 74. From them it can be seen that the general dynamic behaviour for this geometry under constant charge condition is similar to that for the previously discussed case of one pixel and two buses.

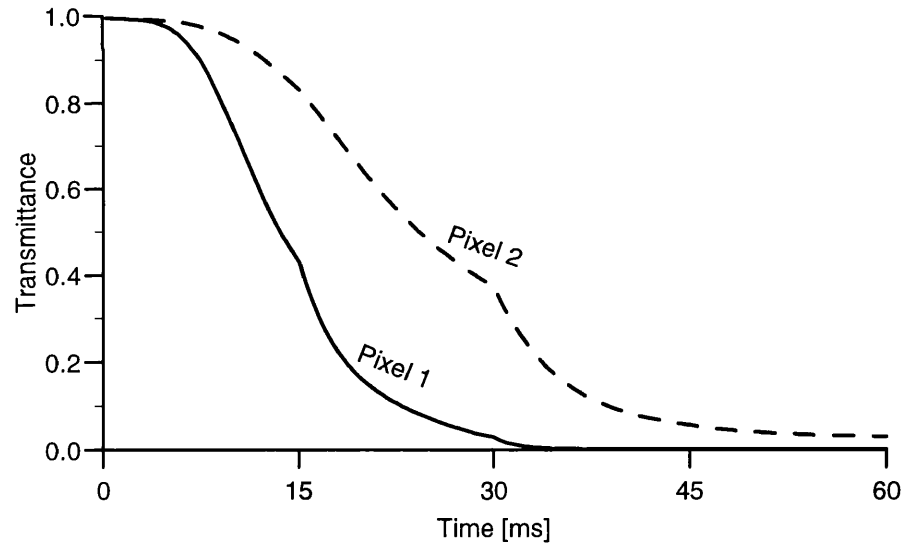

Figure 74 Evolution with time of transmittance passing through pixel electrodes 1 and 2

6.14. Comparison between modelled results and the measurement

This section attempts to give a comparison of transmittance between measurement and modelling.

6.14.1. Measurements

The measurements were made by the author at Philips Research Laboratories (Redhill) in January 1999 on a sample cell like that pictured in Figure 40. The transmittance was measured at various voltage levels. A frequency of 30Hz is used for the driving voltage. The duration of the gate pulse is 16.667μs. The temperature was maintained at around 23°C. Only a single pixel electrode is involved. There was no bus line.

6.14.2. Modelling

The modelling is done for the geometry of the above cell using the 'cut and paste' technique described in Section 6.6. Two different cases are modelled which correspond to two different values of the rotational viscosity: γ=0.1, and 0.123 for white-black (Figure 75) and black-white transitions (Figure 76). According to the measurements, a driving voltage of 0.5v gives a white state while 5v leads to a black state. Pre-tilt is 4° and the twist is 90° from 45° at the bottom to –45° at the top. $\varepsilon_{\perp}$=3.1 and $\Delta\varepsilon$=5.2. The elastic constant $K=13\times10^{-12}$. The voltage was set to 0.5v in the case of white-black transition and 5v in the case of black-white transition for sufficient time before switching in order to match the initial conditions which were used in the measurements.

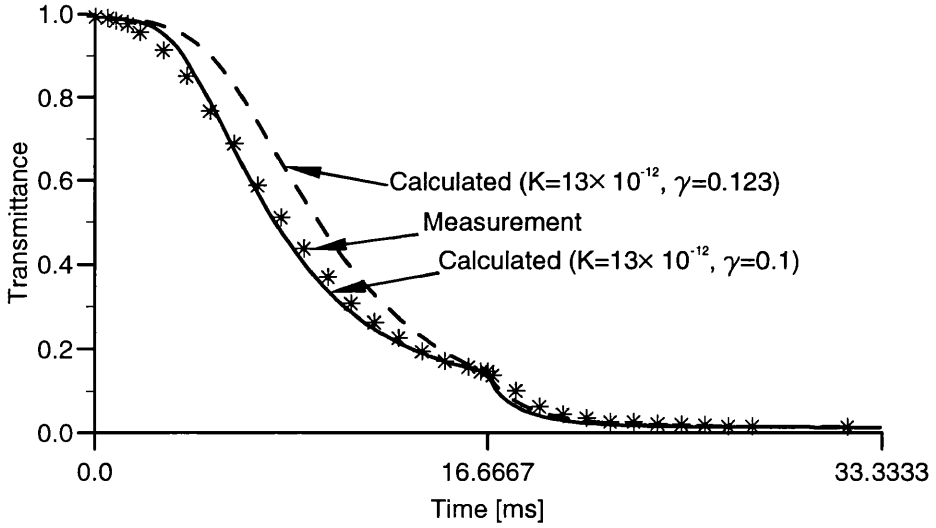

Figure 75 A comparison of transmittance between measurement made on sample cell in Philips and modelling (from white (0.5v) to black (5v))

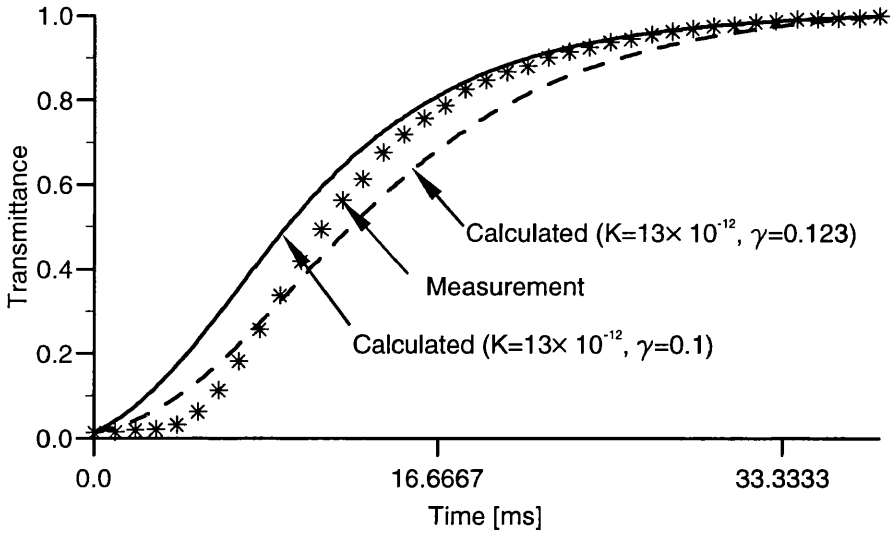

Figure 76 A comparison of transmittance between measurement made on sample cell in Philips and modelling (from black (5v) to white (0.5))

6.14.3. Comparison

Figure 75 shows the measurement (marked asterisks) and the modelled results from white to black transitions. As one can see that the calculated result for γ=0.1 gives a very good fit to the measurement and the one for γ=0.123 decays slightly slower than the measurement before half frame time and after that the agreement actually is very good. The results are very sensitive to the viscosity whose precise value for the measured cell is not known. In the case of the black-white transition as shown in Figure 76, the curve for γ=0.1 gives a very good agreement with the measurement after 19 ms. Before 9 ms, both rise faster than the measurement which may be due to the different initial condition (in the measurement the cell was exposed to 5 volts for such a long time duration, say, minutes, that it reached a complete dark state) and after that the one with higher viscosity rises slower. Further calculations show that a value of K=13×10^{-12} seems the best choice for the single elastic constant model. It is worthwhile to point out that the modelling only takes single elastic constant into account while the measurement was made for the physical test cell which contains all deformation effects. Therefore, it is anticipated that certain difference will exist. It is expected that if a three elastic constant model is used, the agreement would be better during all time span.

The agreement between the measurement and the calculations are very good.

6.15. Validation of the capacitance calculation

Figure 77 shows a comparison between the modelled capacitance and the theoretical one. The isotropic medium (i.e., $\Delta\varepsilon=0$) is used for the modelling under 4 different values of ε_r. The capacitance is calculated using perturbation technique as described in Section 6.3. The theoretical calculation is based on the formula: $C=\varepsilon_0\varepsilon_r w/d$ (unit depth), where w=48μm, the width of the LC cell; d=4μm, the thickness of the cell.

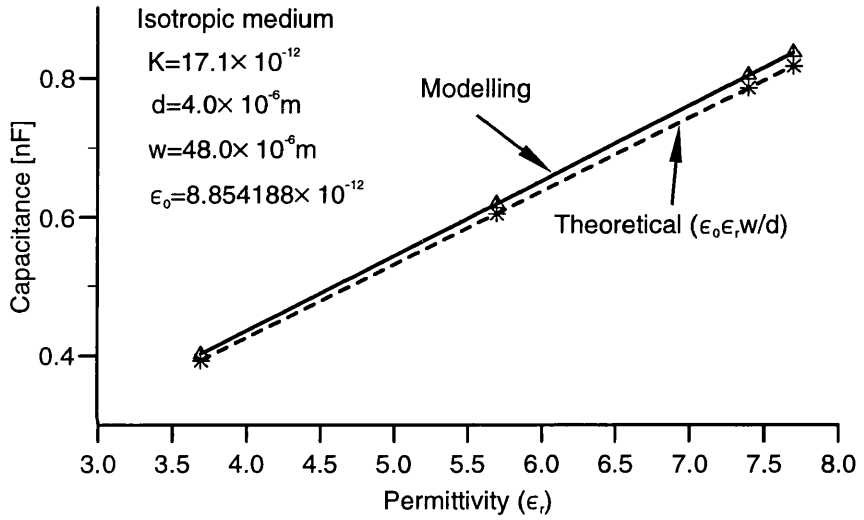

Figure 77 A comparison of the modelled capacitance for the isotropic medium and the theoretical one

It can be seen that the agreement between the modelling and the theory is very good.

6.16. Examination of effects of different spatial and temporal discretisation step lengths

In all above calculations, the Δx is chosen to be 1.5μm and Δy 0.25μm (which gives as aspect ratio of r=6. Note that throughout this section, Δy should be understood as Δz), and the time step Δt is 5μs. Although this choice gives us accurate enough numerical results, it would be, however, quite interesting to try different temporal and spatial step lengths Δx, Δy and Δt to see what influence they will have on the actual numerical results. In this section, a full examination of this is conducted. 4 typical cases are studied:

The time step Δt is varying under fixed Δx and Δy, i.e., fixed ratio;

Δx is changing and Δy is fixed under fixed time step Δt;

Δx is kept fixed and Δy is chosen differently;

Δx and Δy are both changing, but the ratio r of $\Delta x/\Delta y$ is kept equal to 1.

6.16.1. Varying Δt , fixed ratio $r=\Delta x/\Delta y=1.5\mu m/0.25\mu m=6$

In this case, the ratio r is fixed as 6 as before while the time step Δt is chosen to be: 5μs, 10μs, and 15μs respectively. The main purpose to examine this case is to see which time step gives satisfactory results and at the same time economical (fast) computing. From Figure 78 (a)-(e) which shows the variations in time of transmittance (a), capacitance (b), tilt angle of the director at the cell centre (c), voltage (d), and the charge (e), it can be seen that the results for the time step of 10μs are very close to those for the time step of 5μs. The results for the time step of 15μs are deviating strikingly from those for the 5μs and 10μs during the transient period. Therefore, although the time step of 15μs certainly shortens a lot of CPU, it gives a distorted pictures of the dynamic behaviour of the system. It appears here that 10μs time step length gives satisfactory results and twice faster speed than 5μs does. Therefore, it seems that 10μs time step would be a rational choice as far as system parameters used here (the same as given in Table 2, but the period of the source which is chosen to be 30ms) are concerned.

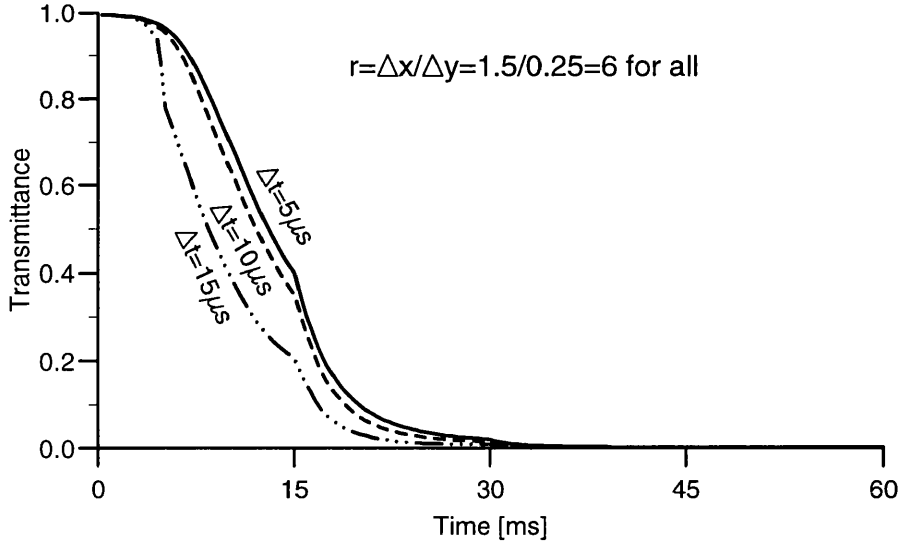

(a)

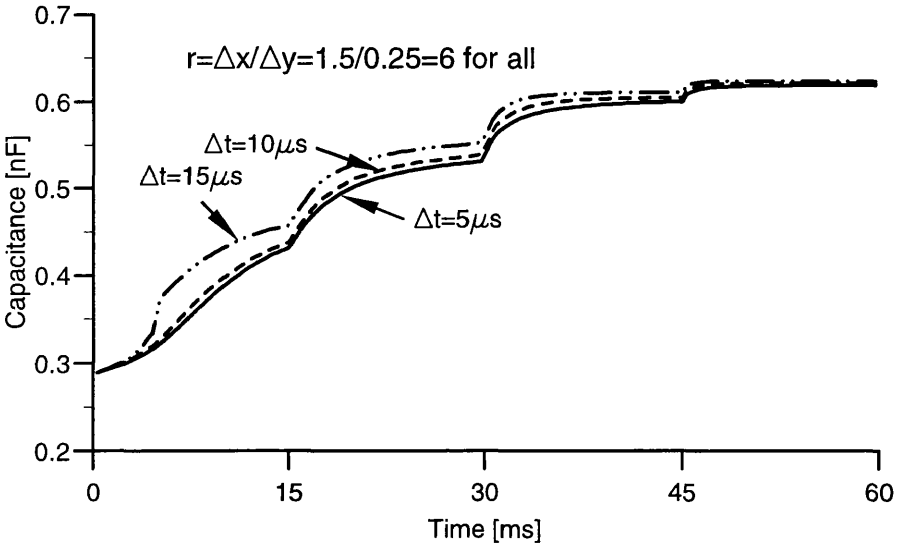
r=Δx/Δy=1.5/0.25=6 for all
Δt=10μs
Δt=15μs
Δt=5μs
Capacitance [nF]
0.7
0.6
0.5
0.4
0.3
0.2
0
15
30
45
60
Time [ms]

(b)

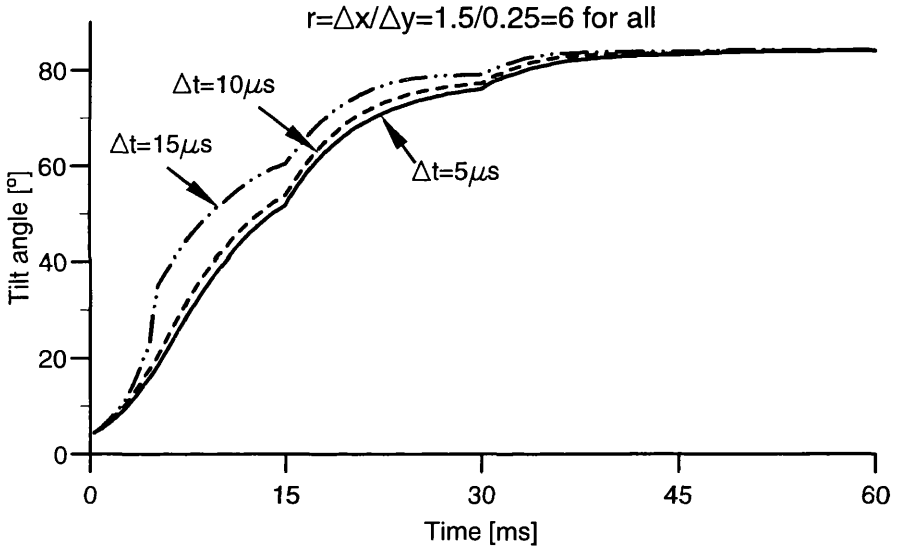
r=Δx/Δy=1.5/0.25=6 for all
Δt=10μs
Δt=15μs
Δt=5μs
Tilt angle [°]
80
60
40
20
0
0
15
30
45
60
Time [ms]

(c)

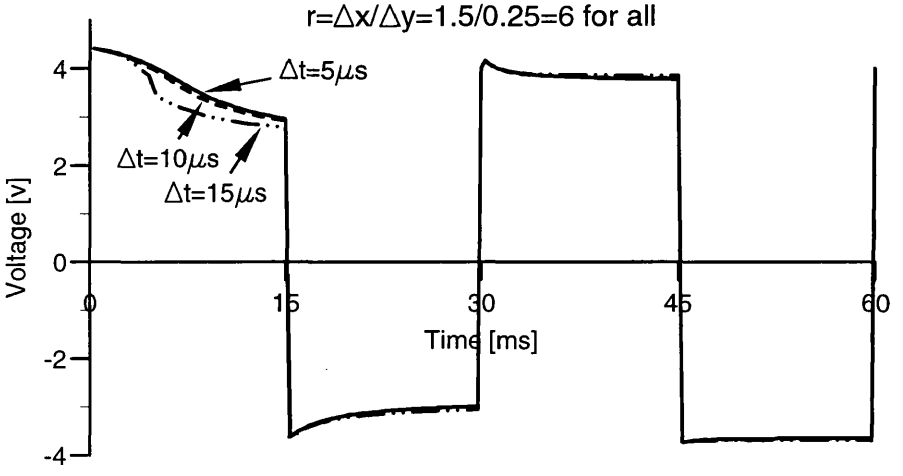
r=Δx/Δy=1.5/0.25=6 for all
Δt=5μs
Δt=10μs
Δt=15μs
Voltage [v]
4
2
0
-2
-4
0
15
30
45
60
Time [ms]

(d)

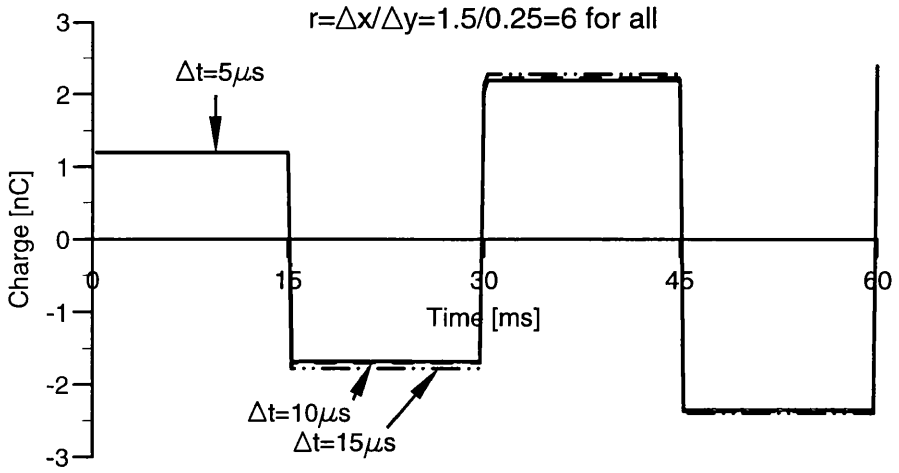

(e)

Figure 78 Effects of different time step Δt[μs] (=5, 10, and 15) on (a) transmittance, (b) capacitance, (c) tilt angle of the director at the cell centre, (d) pixel floating voltage, and (e) Charge deposited on pixel electrode, under fixed ratio $r=\Delta x/\Delta y$=1.5μm/0.25μm=6

6.16.2. Varying Δx , fixed Δy=0.25μm and Δt=5μs

In this case, Δy is fixed to be 0.25μm as has been used so far while the Δx is chosen to be: 0.25μm, 0.5μm, 1.0μm, and 1.5μm respectively. This results in the ratio r= 1, 2, 4, and 6. The aim is to see the difference to the results. Figure 79 (a)-(d) shows the effects of different Δx on the (a) transmittance, (b) voltage, (c) the charge, and (d) the capacitance. It can be seen that the transmittance (Figure 79(a)) and the voltage (Figure 79 (b)) are not sensitive to the spatial discretisation step Δx in the concerned range. However, the variations in Δx do have influence on the charge and hence the capacitance as shown in Figure 79 (c) and Figure 79 (d) respectively. This can be understood as follows: The calculated value of the total charge is very sensitive to the number of the nodes on the pixel electrode. In general, the smaller the Δx, the more nodes the pixel electrode contains, and hence, the more accurate the total charge will be. Therefore, as the pixel capacitance is closely related to the pixel charge, therefore, different levels of accuracy in the charge result in different levels of accuracy in the capacitance. Also, from the charge curves in Figure 79 (c) one can spot that the effect of different Δx is simply to translate the curves – a kind of linear behaviour. This is

demonstrated especially clearly in Figure 79 (d) for the capacitance curve – the smaller the Δx, the bigger and more accurate the value of the capacitance. Because of this, the pixel floating voltage is unaffected due to the linear effects. As the normal transmittance is an average over all nodes along x-direction, it is not sensitive to the magnitude in the step Δx, instead, it is quite sensitive to the number of layers, i.e., Δy as will be shown in the following sub-section. So, the conclusion is that in terms of transmittance and pixel voltage, the magnitude in Δx does not matter too much, however, as far as the charge and the capacitance are concerned, the smaller the Δx , the higher the accuracy. The choice of Δx=1.5 for a fixed Δy=0.25μm gives the worst accuracy in the charge and capacitance (but achieves most efficient computation) because the limited physical dimensions of pixel electrode and especially bus electrodes. However, this problem can be overcome if a locally denser mesh is introduced under pixel and bus electrodes only.

The cell length used in this section and the following two sections is ranged from –10.5μm to 10.5μm, the pixel electrode is from –7.5μm to 7.5μm (no bus electrodes are introduced), and the period of the source is 30ms. All other parameters used are the same as shown in Table 2.

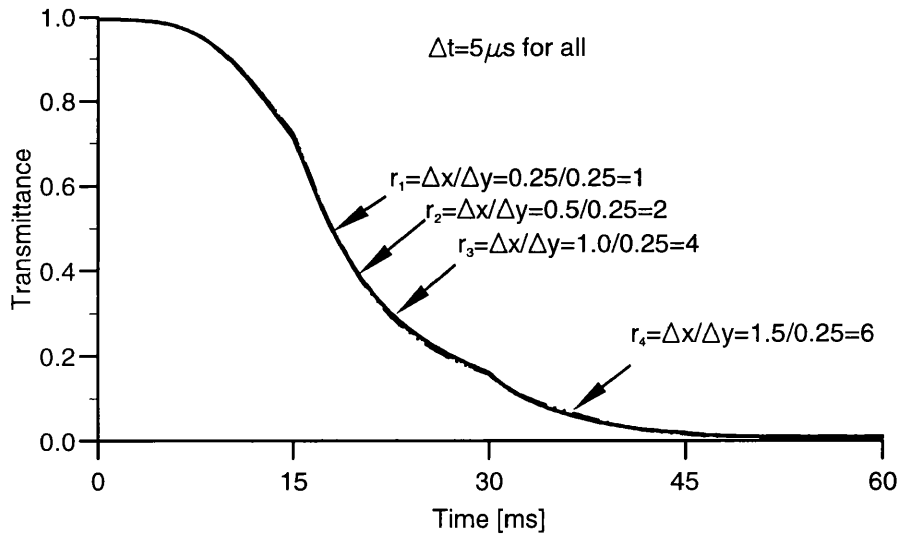

(a)

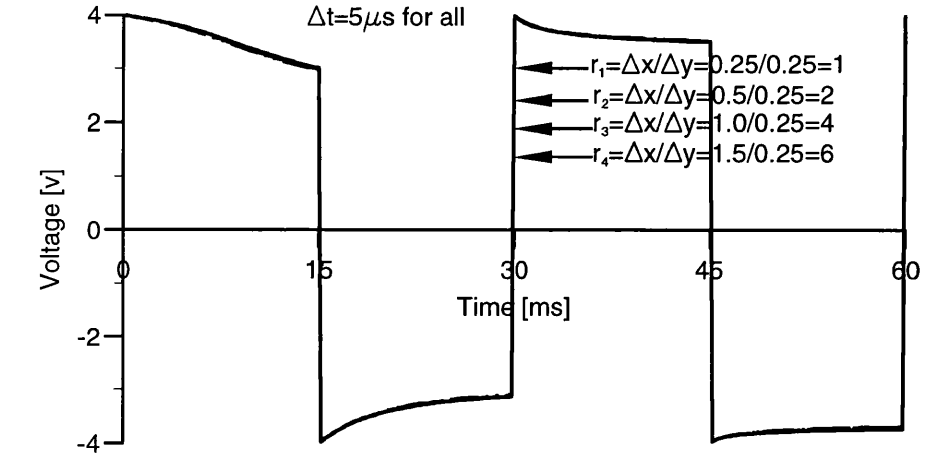

(b)

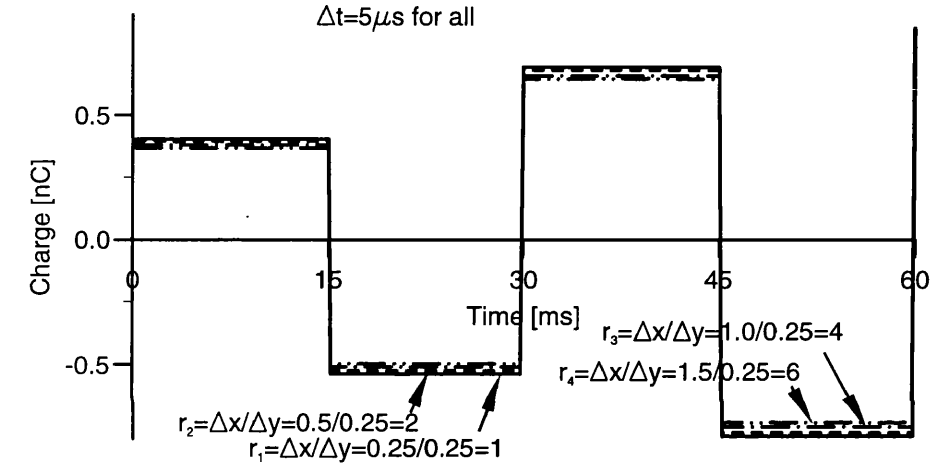

(c)

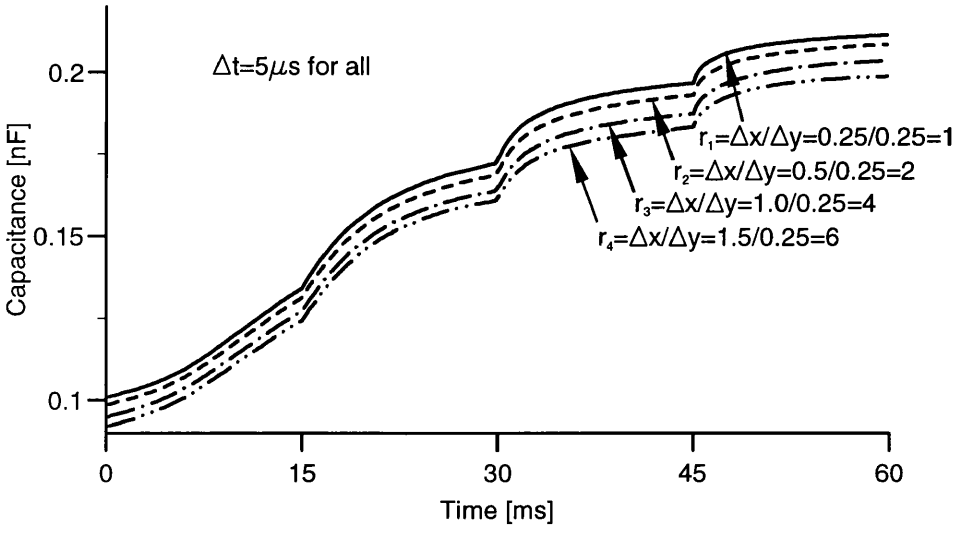

(d)

Figure 79 Effects of varying Δx[μm] (=0.25, 0.5, 1.0, and 1.5) on (a) transmittance, (b) voltage, (c) charge, and (d) capacitance, under fixed Δy=0.25μm and Δt=5μs

6.16.3. Varying Δy , fixed Δx=1.5μm and Δt=5μs

The modelling in this section is done with 3 different Δy: 0.25μm, 0.5μm, and 1.0μm given that Δx=1.5μm and Δt=5μs are fixed. The aim is to study the effects of varying Δy on the numerical results. As we can see from Figure 80 (a)-(d), in all cases the results are sensitive to the variation in Δy. In particular, the ratio of 1.5, i.e., the use of Δy=1.0μm leads to the worst accuracy. The ratio of 6, i.e., choice of Δy=0.25μm gives the best results – this is what we used in all our previous modelling. The results for the ratio 3, i.e., Δy=0.5 are very close to those for the ratio 6, (Δy=0.25μm), except for the capacitance (see Figure 80(b)). The complexity of the influence of different Δy in this case may be related to the fact that smaller divisions Δy represent more layers of the LC cell, that leads to a fine description of physical properties, while the bigger divisions Δy give less layers of LC cell that leads to a coarse average. The conclusion is that for fixed Δx=1.5, Δy=0.25 is the best choice.

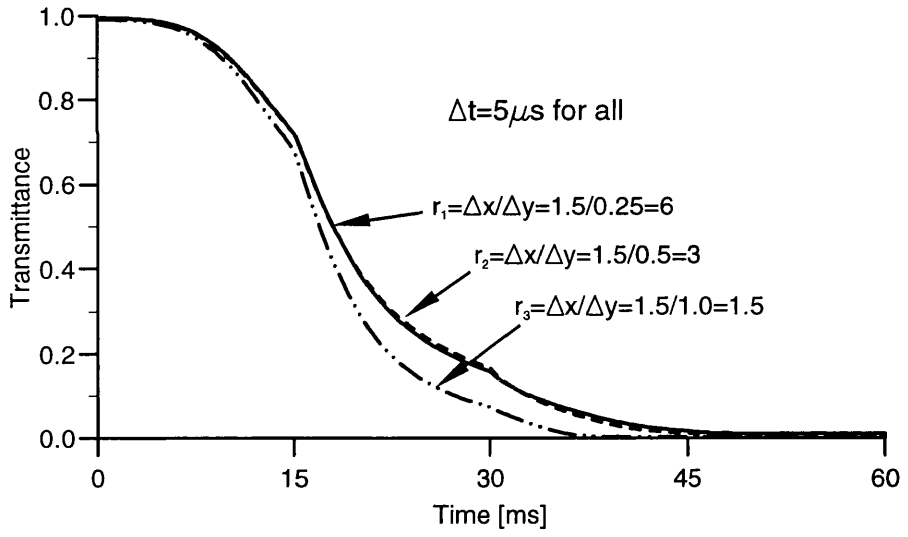

(a)

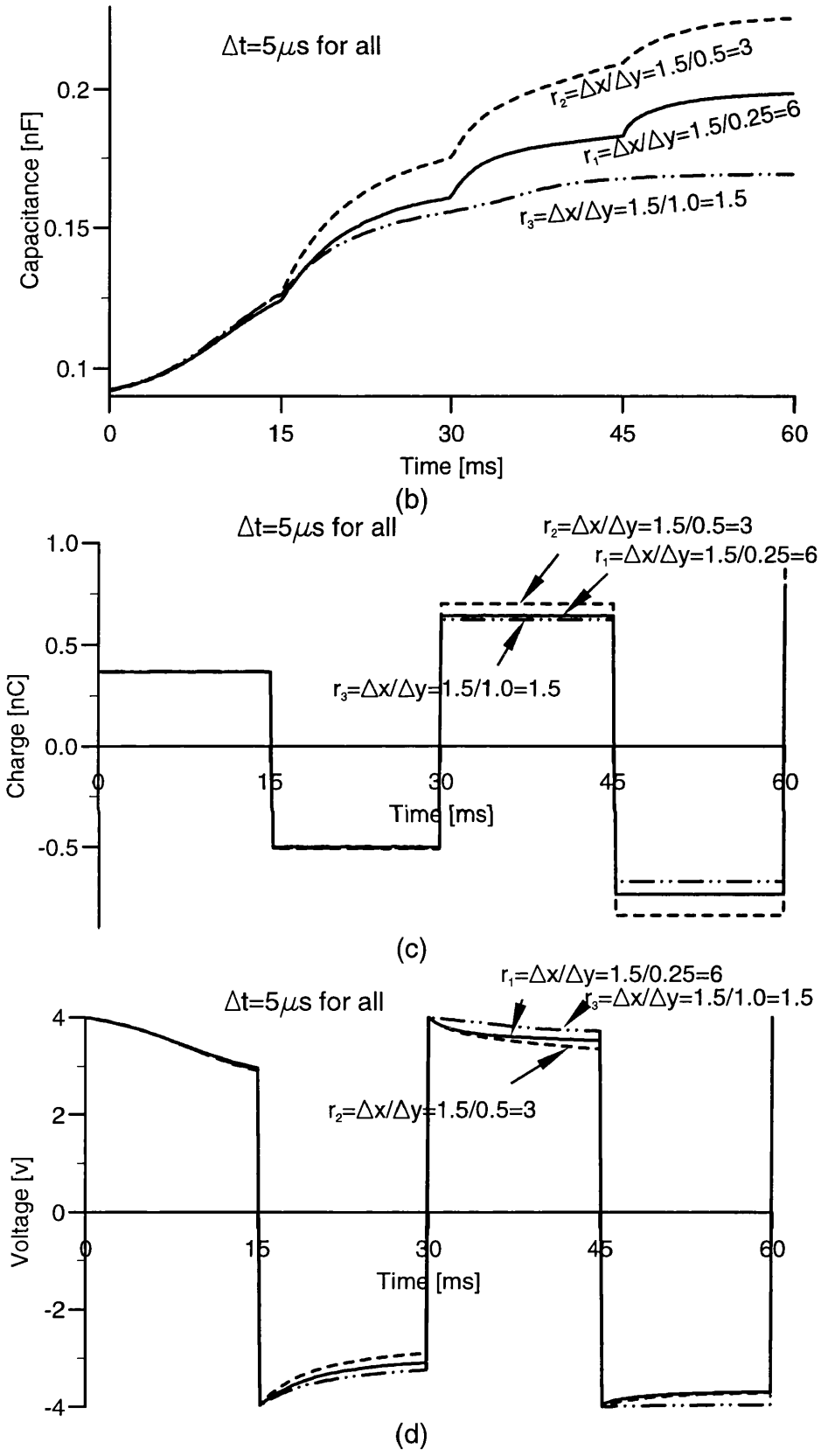

Figure 80 Effects of varying Δy[μm] (=0.25, 0.5, and 1.0) on (a) transmittance, (b) capacitance, (c) charge, and (d) voltage, under fixed Δx=1.5μm and Δt=5μs

6.16.4. Simultaneously varying $\Delta x \equiv \Delta y$, fixed ratio $r=\Delta x/\Delta y=1$ and $\Delta t=5\mu s$

In this section, the problem is looked at from a different angle. Namely, we keep the ratio r=1 while changing the magnitude of Δx and Δy simultaneously to see what kind of results we can get. From Figure 81 which shows dynamic behaviour of (a) transmittance, (b) capacitance, (c) charge, and (d) voltage under 3 different sets of Δx ($\equiv\Delta y$) = 0.25μm, 0.5μm, and 1.0μm, it can be see that in spite of the ratio being equal to 1 in all 3 cases, the effects of different values of Δx and Δy on the results are very similar to the case discussed in the above sub-section 6.16.3. That means it is mainly due to the different step of Δy that the divergent results are obtained, the simultaneously varying Δx only plays a minor role in this case as no notably similar effects of the varying Δx on the results are obtained here as in subsection 6.16.2. The results show an insensitivity to the changes in Δx (although Δx changes here simultaneously with Δy). As far as the transmittance and the voltage are concerned, the results for Δy=0.5 are very close to those for Δy=0.25 which are our benchmark. A Δy=1.0 gives rise to a much divergent effect.

In summary, use of 0.25 of Δy gives the most accurate results and a choice of 0.5 offers satisfactory results irrespective of Δx.

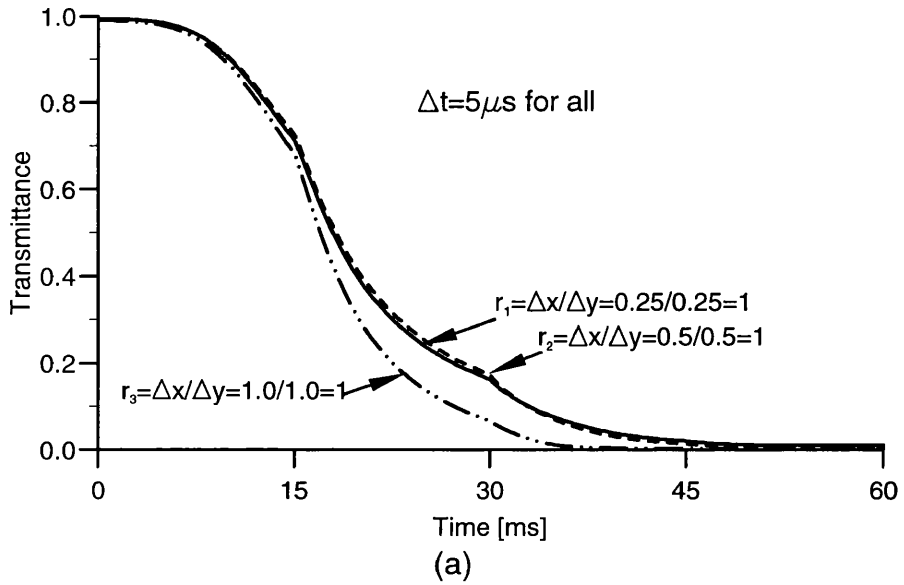

(a)

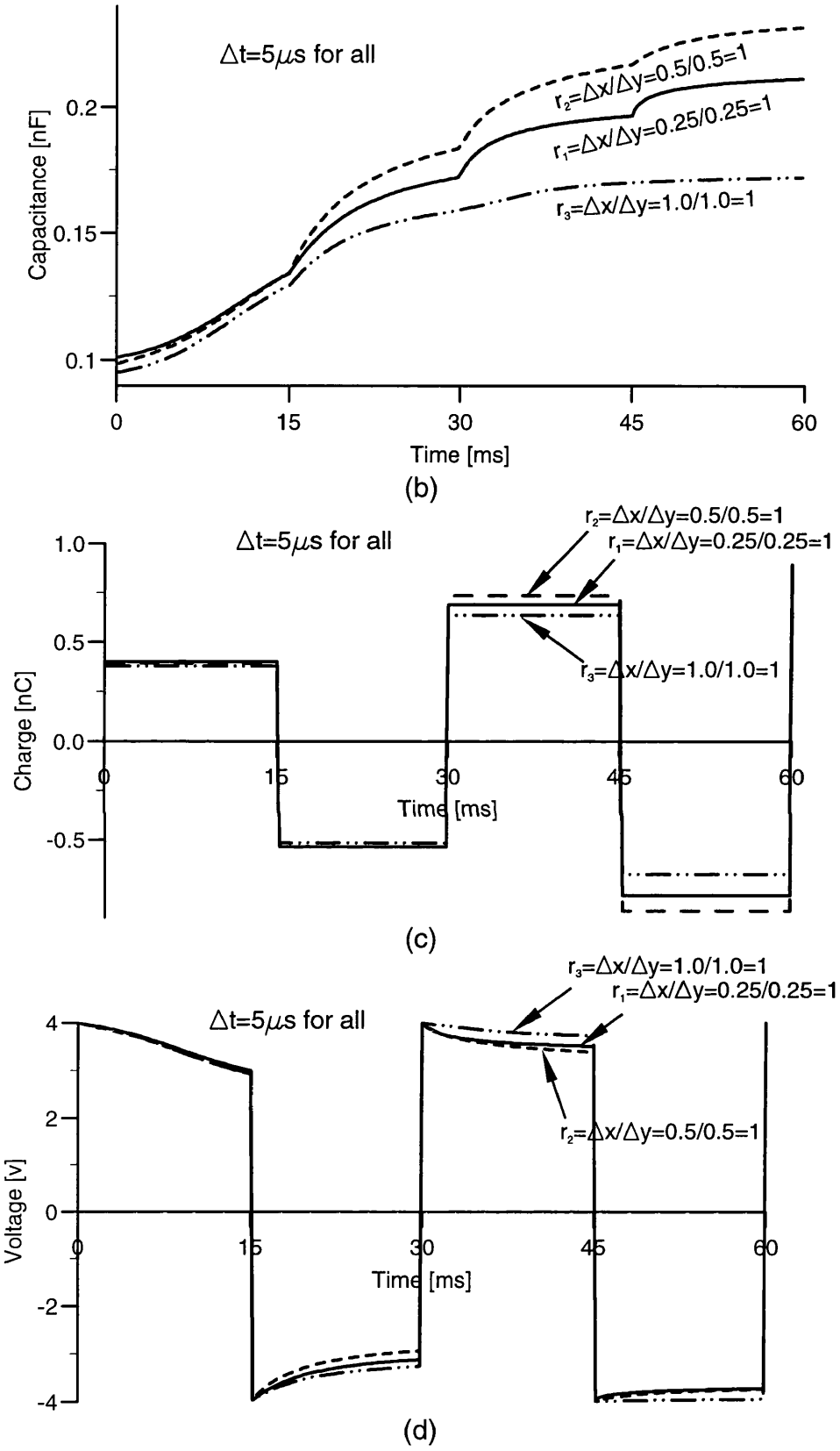

Figure 81 Effects of simultaneous change in Δx and Δy [μm] (=0.25, 0.5, and 1.0) on (a) transmittance, (b) capacitance, (c) charge, and (d) voltage, under fixed ratio $r=\Delta x/\Delta y\equiv 1$ and $\Delta t=5\mu s$

7. Calculation of transmittance of twisted nematic liquid crystal displays (TN-LCDs)

There are a number of papers in the literature dealing with the transmittance against viewing angle. Some of them are based on the 2×2 extended Jones matrix methods [38],[39],[43] which restrain the incident light to a particular plane, say, *x*-*z* plane, others use the 4×4 methods [96-100] which are devised for the normal incident light only. Therefore, none of them calculates the transmittance for arbitrary off-axis incidence, i.e., incidence at any polar angle ϑ_k and azimuthal angle φ_k. The typical assumption made [38],[39],[43] is that the incident beam lies in the *x*-*z* plane, i.e., its *y* component of the incident wave vector **k:** k_y is zero, that means $\varphi_k=0$. Hence it is inconvenient for *direct* examination of the relation between transmittance *T* and both angles: ϑ_k and φ_k. In this chapter, we present a full derivation of a generalised 2×2 formulation to calculate the average optical transmittance of a LC cell as a function of the viewing angles: polar ϑ_k and azimuthal φ_k. The main advantage of calculating *T* as a function of ϑ_k and φ_k is that it makes the representation of transmittance graphically clearer and easier to understand.

7.1. Theory

7.1.1. Eigen-waves

The propagation vector for arbitrary incidence (ϑ_k ,φ_k) can be written as:

$$\mathbf{k} = k_0[\sin(\vartheta_k)\cos(\varphi_k), \sin(\vartheta_k)\sin(\varphi_k), \cos(\vartheta_k)] \qquad (180)$$

Here $k_x = k_0\sin(\vartheta_k)\cos(\varphi_k)$, $k_y = k_0\sin(\vartheta_k)\sin(\varphi_k) \neq 0$, $k_z = k_0\cos(\vartheta_k)$,

$k_0 = \omega/c = 2\pi/\lambda$, λ is the wavelength of the incident light in free space.

The entire LCD system can be considered as divided into N layers. The first layer is assumed to be the entrance polarizer and the last to be the exit polarizer. The second and the $(N-1)^{th}$ layers are glass substrates. A stack of N-4 uniaxial homogeneous layers approximates the LC layer. Each of these layers can be characterised by a dielectric tensor $\bar{\bar{\varepsilon}}$ which is defined in Eq. (20) or Eq. (58). Keeping in mind that

$\varepsilon_{\perp}=n_o^2$ and $\varepsilon_{\parallel}=n_e^2$, where, n_o and n_e are, respectively, the ordinary and extraordinary indices of refraction of the liquid crystal medium or polarizer, Eq. (20) can be expended in explicit form as follows:

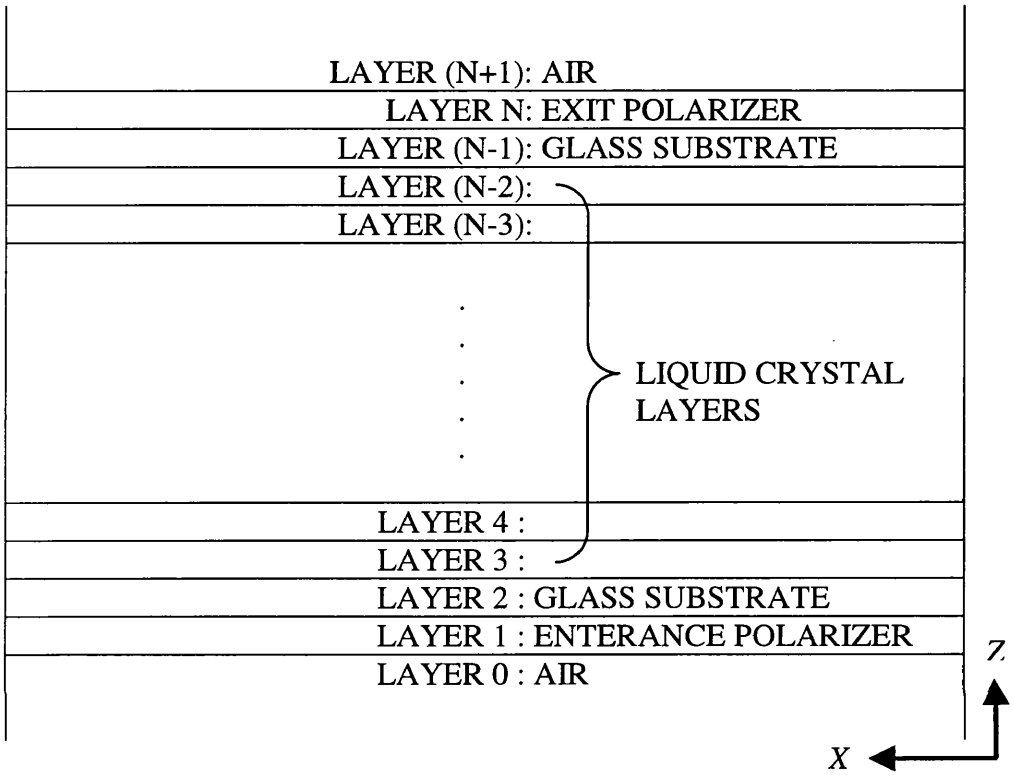

Figure 82 Schematic diagram of a TN-LCD system divided into N layers

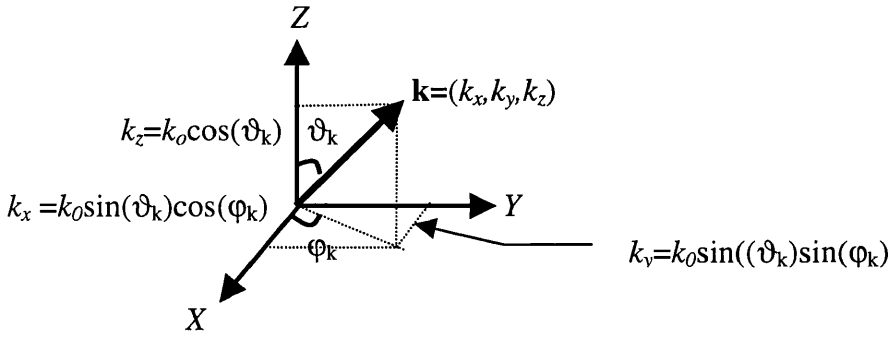

Figure 83 The orientation of the incident wave vector k

$$\begin{cases} \varepsilon_{xx} = n_o^2 + (n_e^2 - n_o^2)\cos^2\theta\cos^2\phi \\ \varepsilon_{xy} = \varepsilon_{yx} = (n_e^2 - n_o^2)\cos^2\theta\sin\phi\cos\phi \\ \varepsilon_{xz} = \varepsilon_{zx} = (n_e^2 - n_o^2)\sin\theta\cos\theta\cos\phi \\ \varepsilon_{yy} = n_o^2 + (n_e^2 - n_o^2)\cos^2\theta\sin^2\phi \\ \varepsilon_{yz} = \varepsilon_{zy} = (n_e^2 - n_o^2)\sin\theta\cos\theta\sin\phi \\ \varepsilon_{zz} = n_o^2 + (n_e^2 - n_o^2)\sin^2\theta \end{cases} \quad (181)$$

It should be emphasised that here, the definition of θ for the director is different from that of ϑ_k for the incident wave vector **k** which is a polar angle (see Figure 83). For liquid crystal layers, θ is the tilt angle of the LC director (i.e., the angle between the LC director and the *x-y* plane), and ϕ is the twist angle between the projection of the LC director on the *x-y* plane and the *x*-axis. For polarizer layers, n_o and n_e are complex numbers, θ is the angle between the extraordinary optical axis (absorption axis) of the polarizer layer and the *x-y* plane, and ϕ is the angle between projection of the extraordinary optical axis of the polarizer layer on the *x-y* plane and the x-axis. For the normal polarizer arrangement, $\theta = 0°$. For glass substrates, $n_e=n_o$ and $\bar{\bar{\varepsilon}}$ reduces to a diagonal matrix.

For each layer, assuming the plane wave

$$\mathbf{E}(\mathbf{r},t) = \mathbf{E}_0 \exp[i(\mathbf{k}\bullet\mathbf{r} - \omega t)] = \mathbf{E}_0 \exp[i(k_x x + k_y y + k_z z - \omega t)] \quad (182)$$

and

$$\mathbf{H}(r,t) = \mathbf{H}_0 \exp[i(\mathbf{k}\bullet\mathbf{r} - \omega t)] = \mathbf{H}_0 \exp[i(k_x x + k_y y + k_z z - \omega t)] \quad (183)$$

is the solution of Maxwell's equations in the non-magnetic medium characterised by a dielectric tensor of equation (181), we obtain

$$\frac{\mathbf{k}}{k_0}\times\left(\frac{\mathbf{k}}{k_0}\times\mathbf{E}_0\right) + \bar{\bar{\varepsilon}}\bullet\mathbf{E}_0 = 0 \quad (184)$$

and

$$\mathbf{H}_0 = \frac{\mathbf{k}}{k_0}\times\mathbf{E}_0 \quad (185)$$

Inserting $\mathbf{k}=(k_x, k_y, k_z)$ and $\mathbf{E}_0=(E_{x0},E_{y0},E_{z0})$ in equation (184) and using the shorthand notation: $k_x/k_0 \Rightarrow k_x$, $k_y/k_0 \Rightarrow k_y$, $k_z/k_0 \Rightarrow k_z$, we obtain

$$(-k_y^2 - k_z^2 + \varepsilon_{xx})E_{x0} + (k_x k_y + \varepsilon_{xy})E_{y0} + (k_x k_z + \varepsilon_{xz})E_{z0} = 0 \quad (186a)$$

$$\left(k_x k_y + \varepsilon_{yx}\right)E_{x0} + \left(-k_z^2 - k_x^2 + \varepsilon_{yy}\right)E_{y0} + \left(k_y k_z + \varepsilon_{yz}\right)E_{z0} = 0 \qquad (186b)$$

$$\left(k_x k_z + \varepsilon_{zx}\right)E_{x0} + \left(k_y k_z + \varepsilon_{zy}\right)E_{y0} + \left(-k_x^2 - k_y^2 + \varepsilon_{zz}\right)E_{z0} = 0 \qquad (186c)$$

Here $k_x/k_0=\sin(\vartheta_k)\cos(\varphi_k)$, $k_y/k_0=\sin(\vartheta_k)\sin(\varphi_k)$, $k_z/k_0=\cos(\vartheta_k)$.

The condition for the equations (186) to have a non-trivial solution is that the coefficient determinant must be equal zero, i.e.,

$$\begin{vmatrix} \left(-k_y^2 - k_z^2 + \varepsilon_{xx}\right) & \left(k_x k_y + \varepsilon_{xy}\right) & \left(k_x k_z + \varepsilon_{xz}\right) \\ \left(k_x k_y + \varepsilon_{yx}\right) & \left(-k_z^2 - k_x^2 + \varepsilon_{yy}\right) & \left(k_y k_z + \varepsilon_{yz}\right) \\ \left(k_x k_z + \varepsilon_{zx}\right) & \left(k_y k_z + \varepsilon_{zy}\right) & \left(-k_x^2 - k_y^2 + \varepsilon_{zz}\right) \end{vmatrix} = 0 \qquad (187)$$

Expanding expression (187) gives rise to an eigenvalue equation for k_z – the unknown - to the power of 4, therefore the four following eigenvalues are found to be:

$$\frac{k_{z1}}{k_0} = \sqrt{n_o^2 - \frac{k_x^2}{k_0^2} - \frac{k_y^2}{k_0^2}} \qquad (188)$$

$$\frac{k_{z2}}{k_0} = -\frac{\frac{k_x}{k_0}\varepsilon_{xz} + \frac{k_y}{k_0}\varepsilon_{yz}}{\varepsilon_{zz}} + \left(\frac{n_o^2 n_e^2}{\varepsilon_{zz}} - \frac{\varepsilon_{xx}\varepsilon_{zz} - \varepsilon_{xz}^2}{\varepsilon_{zz}^2}\frac{k_x^2}{k_0^2} - \frac{\varepsilon_{yy}\varepsilon_{zz} - \varepsilon_{yz}^2}{\varepsilon_{zz}^2}\frac{k_y^2}{k_0^2} - \frac{2n_o^2\varepsilon_{xy}}{\varepsilon_{zz}^2}\frac{k_x}{k_0}\frac{k_y}{k_0} \right)^{1/2} \qquad (189)$$

$$\frac{k_{z3}}{k_0} = -\sqrt{n_o^2 - \frac{k_x^2}{k_0^2} - \frac{k_y^2}{k_0^2}} \qquad (190)$$

$$\frac{k_{z4}}{k_0} = -\frac{\frac{k_x}{k_0}\varepsilon_{xz} + \frac{k_y}{k_0}\varepsilon_{yz}}{\varepsilon_{zz}} - \left(\frac{n_o^2 n_e^2}{\varepsilon_{zz}} - \frac{\varepsilon_{xx}\varepsilon_{zz} - \varepsilon_{xz}^2}{\varepsilon_{zz}^2}\frac{k_x^2}{k_0^2} - \frac{\varepsilon_{yy}\varepsilon_{zz} - \varepsilon_{yz}^2}{\varepsilon_{zz}^2}\frac{k_y^2}{k_0^2} - \frac{2n_o^2\varepsilon_{xy}}{\varepsilon_{zz}^2}\frac{k_x}{k_0}\frac{k_y}{k_0} \right)^{1/2} \qquad (191)$$

It is straightforward to verify that if $\varphi_k = 0$, i.e., $k_y = 0$, all the above expressions reduce to those given in Refs. [38] and [39] for simpler model.

It should be noted that two values (k_{z1}, k_{z2}), i.e., equations (188) and (189) of the four eigen-waves correspond to propagation in $+z$ direction, or transmitted waves, while the two others, i.e., equations (190) and (191) correspond to reflected waves going in the $-z$ direction. For each k_{zi} ($i=1,2$) there is a corresponding electric field: $(E_{xi},E_{yi},E_{zi})= (E_{xi0},E_{yi0},E_{zi0})\exp[i(k_x x+k_y y+k_{zi}z-\omega t)]$ ($i=1,2$)

7.1.2. Construction of the extended 2×2 Jones matrix for a single layer

Since reflected waves inside a TN-LCD are usually small, in the following treatment we assume they can be neglected, i.e., we assume that only two transmitted eigen-waves 1 and 2 are propagating in the medium.

For wave 1, we express E_{y1} in terms of E_{x1}. By using equations (186b) and (186c) we obtain

$$E_{y1} = e_{y1}\frac{E_{x1}}{e_{x1}} = e_{y1}M_{x1} \tag{192}$$

Where

$$e_{x1} = \left(\frac{k_x^2}{k_0^2} + \frac{k_{z1}^2}{k_0^2} - \varepsilon_{yy}\right)\left(\frac{k_x^2}{k_0^2} + \frac{k_y^2}{k_0^2} - \varepsilon_{zz}\right) - \left(\frac{k_y}{k_0}\frac{k_{z1}}{k_0} + \varepsilon_{zy}\right)\left(\frac{k_y}{k_0}\frac{k_{z1}}{k_0} + \varepsilon_{yz}\right) \tag{193}$$

$$e_{y1} = \left(\frac{k_x^2}{k_0^2} + \frac{k_y^2}{k_0^2} - \varepsilon_{zz}\right)\left(\frac{k_x}{k_0}\frac{k_y}{k_0} + \varepsilon_{yx}\right) + \left(\frac{k_x}{k_0}\frac{k_{z1}}{k_0} + \varepsilon_{zx}\right)\left(\frac{k_y}{k_0}\frac{k_{z1}}{k_0} + \varepsilon_{yz}\right) \tag{194}$$

and

$$M_{x1} = \frac{E_{x1}}{e_{x1}} = \frac{E_{x10}}{e_{x1}}\exp\left[i\left(k_x x + k_y y + k_{z1} z - \omega t\right)\right] \tag{195}$$

Similarly, for eigen-wave 2, we express E_{x2} in terms of E_{y2}. By using equations (186a) and (186c), we have

$$E_{x2} = e_{x2}\frac{E_{y2}}{e_{y2}} = e_{x2}M_{y2} \tag{196}$$

Where

$$e_{x2} = \left(-\frac{k_x^2}{k_0^2} - \frac{k_y^2}{k_0^2} + \varepsilon_{zz}\right)\left(\frac{k_x}{k_0}\frac{k_y}{k_0} + \varepsilon_{xy}\right) - \left(\frac{k_x}{k_0}\frac{k_{z2}}{k_0} + \varepsilon_{xz}\right)\left(\frac{k_y}{k_0}\frac{k_{z2}}{k_0} + \varepsilon_{zy}\right) \tag{197}$$

$$e_{y2} = \left(-\frac{k_y^2}{k_0^2} - \frac{k_{z2}^2}{k_0^2} + \varepsilon_{xx}\right)\left(\frac{k_x^2}{k_0^2} + \frac{k_y^2}{k_0^2} - \varepsilon_{zz}\right) - \left(\frac{k_x}{k_0}\frac{k_{z2}}{k_0} + \varepsilon_{xz}\right)\left(\frac{k_x}{k_0}\frac{k_{z2}}{k_0} + \varepsilon_{zx}\right) \tag{198}$$

and

$$M_{y2} = \frac{E_{y2}}{e_{y2}} = \frac{E_{y20}}{e_{y2}}\exp\left[i\left(k_x x + k_y y + k_{z2} z - \omega t\right)\right] \tag{199}$$

It could be noted that equations (193)-(195) and (197)-(199) above are the extensions of the corresponding ones in Refs. [38] and [39] to include the k_y component of incident wave **k**.

Having defined all those expressions as above, we are now in position to specify **E**-vector by the mode vector

$$\begin{bmatrix} M_{x1} \\ M_{y2} \end{bmatrix}$$

as

$$\begin{bmatrix} E_x \\ E_y \end{bmatrix} = \begin{bmatrix} E_{x1} \\ E_{y1} \end{bmatrix} + \begin{bmatrix} E_{x2} \\ E_{y2} \end{bmatrix} = \boldsymbol{S} \begin{bmatrix} M_{x1} \\ M_{y2} \end{bmatrix} \tag{200}$$

Where

$$\boldsymbol{S} = \begin{bmatrix} e_{x1} & e_{x2} \\ e_{y1} & e_{y2} \end{bmatrix} \tag{201}$$

From equations (195) and (199), the mode vector propagates from the bottom [denoted by subscript 0] of n^{th} layer to the top [denoted by the subscript d_n – the thickness of the layer] of n^{th} layer by

$$\begin{bmatrix} M_{x1} \\ M_{y2} \end{bmatrix}_{n,d_n} = \boldsymbol{G}_n \begin{bmatrix} M_{x1} \\ M_{y2} \end{bmatrix}_{n,0} \tag{202}$$

where

$$\boldsymbol{G}_n = \begin{bmatrix} \exp(ik_{z1}d_n)) & 0 \\ 0 & \exp(ik_{z2}d_n) \end{bmatrix} \tag{203}$$

and d_n is the thickness of the n^{th} layer.

Using equations (200) and (202), the **E**-vector at the bottom of the n^{th} layer is related to the **E**-vector at the top of the n^{th} layer by

$$\begin{bmatrix} E_x \\ E_y \end{bmatrix}_{n,d_n} = \boldsymbol{J}_n \begin{bmatrix} E_x \\ E_y \end{bmatrix}_{n,0} \tag{204}$$

where

$$\boldsymbol{J}_n = \boldsymbol{S}_n \boldsymbol{G}_n \boldsymbol{S}_n^{-1} \tag{205}$$

Using the boundary condition that tangential components of the E-field are continuous at each layer interface, i.e.,

$$\begin{bmatrix} E_x \\ E_y \end{bmatrix}_{n+1,0} = \begin{bmatrix} E_x \\ E_y \end{bmatrix}_{n,d_n} \tag{206}$$

we obtain

$$\begin{bmatrix} E_x \\ E_y \end{bmatrix}_{n+1} = \boldsymbol{J}_n \begin{bmatrix} E_x \\ E_y \end{bmatrix}_n \tag{207}$$

Here, simplified notations

$$\begin{bmatrix} E_x \\ E_y \end{bmatrix}_n = \begin{bmatrix} E_x \\ E_y \end{bmatrix}_{n,0} \tag{208}$$

and

$$\begin{bmatrix} E_x \\ E_y \end{bmatrix}_{n+1} = \begin{bmatrix} E_x \\ E_y \end{bmatrix}_{n+1,0} \tag{209}$$

are used.

Equation (205) is what we are looking for and corresponds to the extended Jones matrix representation at an off-axis incidence, ie, at any angles ϑ_k, φ_k for the n^{th} layer.

7.1.3. Physical implication of equations (205) and (207)

Equations (205) and (207) can be understood as follows. $\boldsymbol{S}_n^{-1}$ transforms the **E**-vector at the bottom of the n^{th} layer into the mode vector. $\boldsymbol{G}_n$ then propagates the mode vector from the bottom of the n^{th} layer to the top of the n^{th} layer. Finally $\boldsymbol{S}_n$ transforms the mode vector at the top of the n^{th} layer back into the **E**-vector at the top of the n^{th} layer, which is equal to the **E**-vector at the bottom of the $(n+1)^{th}$ layer (from the boundary condition).

7.1.4. Extended Jones matrix representation for the whole LCD system

Applying equation (207) to every layer including the two polarizer layers, we then have the transmitted **E**-vector that is related to the incident **E**-vector by the matrix $\boldsymbol{J}$:

$$\begin{bmatrix} E_x \\ E_y \end{bmatrix}_{n+1} = \boldsymbol{J} \begin{bmatrix} E_x \\ E_y \end{bmatrix}_0 \tag{210}$$

where

$$\boldsymbol{J} = \boldsymbol{J}_n \boldsymbol{J}_{n-1} \boldsymbol{J}_{n-2} \cdots \boldsymbol{J}_3 \boldsymbol{J}_2 \boldsymbol{J}_1 \tag{211}$$

is the extended Jones matrix representation for the entire LCD system at incident angles ϑ_k, φ_k.

7.1.5. Theoretical formulation for total optical transmittance calculation

The general definition of the transmittance is, in the wave frame, given by

$$T = \left\| \boldsymbol{E}^{out} \right\|^2 \Big/ \left\| \boldsymbol{E}^{in} \right\|^2 \tag{212}$$

The previous analysis has been based on the x-y-z Cartesian co-ordinate system. It is, however, more convenient to calculate the transmittance in the wave frame. Therefore we need to transform equations (205) and (207) to those in the wave frame. Let E_s and E_p be, respectively, the s-component and p-component of incident beam in the wave form, then their respective projections $\left(E_x^{(1)}, E_y^{(1)}\right)$ and $\left(E_x^{(2)}, E_y^{(2)}\right)$ in the Cartesian system are as follows

$$\begin{aligned} E_x^{(1)} &= E_s \cos\vartheta_k \cos\varphi_k, & E_x^{(2)} &= -E_p \sin\varphi_k \\ E_y^{(1)} &= E_s \cos\vartheta_k \sin\varphi_k & E_y^{(2)} &= E_p \cos\varphi_k \end{aligned} \tag{213}$$

Adding them together, we then have the total (E_x, E_y)

$$\begin{aligned} E_x &= \cos\vartheta_k \cos\varphi_k E_s - \sin\varphi_k E_p \\ E_y &= \cos\vartheta_k \sin\varphi_k E_s + \cos\varphi_k E_p \end{aligned} \tag{214}$$

Hence, the transformation relation between Cartesian system and wave frame is found to be

$$\begin{bmatrix} E_x \\ E_y \end{bmatrix} = \boldsymbol{R} \begin{bmatrix} E_s \\ E_p \end{bmatrix} \tag{215}$$

Here the transformation matrix R is of form

$$\boldsymbol{R} = \begin{bmatrix} \cos(\vartheta_k)\cos(\varphi_k) & -\sin(\varphi_k) \\ \cos(\vartheta_k)\sin(\varphi_k) & \cos(\varphi_k) \end{bmatrix} \tag{216}$$

Inserting Equation (215) in Equation (210), we then have an expression for the **E**-vector in the wave frame as below

$$\begin{bmatrix} E_s \\ E_p \end{bmatrix}_{n+1} = \boldsymbol{W} \begin{bmatrix} E_s \\ E_p \end{bmatrix}_0 \tag{217}$$

where

$$\boldsymbol{W} = \boldsymbol{R}^{-1}\, \boldsymbol{J}\, \boldsymbol{R} = \boldsymbol{R}^{-1}\boldsymbol{J}_n \boldsymbol{J}_{n-1} \boldsymbol{J}_{n-2} \cdots \boldsymbol{J}_3 \boldsymbol{J}_2 \boldsymbol{J}_1 \boldsymbol{R} \tag{218}$$

We can rewrite expression (218) as below

$$\begin{aligned} \boldsymbol{W} = \boldsymbol{R}^{-1}\, \boldsymbol{J}\, \boldsymbol{R} &= \boldsymbol{R}^{-1}\boldsymbol{J}_n \boldsymbol{R}\, \boldsymbol{R}^{-1}\boldsymbol{J}_{n-1}\boldsymbol{R}\, \boldsymbol{R}^{-1}\boldsymbol{J}_{n-2}\boldsymbol{R} \cdots \boldsymbol{R}^{-1}\boldsymbol{J}_3 \boldsymbol{R}\, \boldsymbol{R}^{-1}\boldsymbol{J}_2 \boldsymbol{R}\, \boldsymbol{R}^{-1}\boldsymbol{J}_1 \boldsymbol{R} \\ &= \boldsymbol{J}_n^w \boldsymbol{J}_{n-1}^w \boldsymbol{J}_{n-2}^w \cdots \boldsymbol{J}_3^w \boldsymbol{J}_2^w \boldsymbol{J}_1^w \end{aligned} \tag{219}$$

Here $\boldsymbol{J}_m^w = \boldsymbol{R}^{-1}\boldsymbol{J}_m\boldsymbol{R}$ $(m=n,n\text{-}1,n\text{-}2,\ \ldots,\ 3,2,1)$ is the representation for the extended Jones matrix for each layer *in the wave frame*. We can see that the co-ordinate system transformation from Cartesian to wave frame is mathematically equivalent to undertaking a rotational transform for each extended Jones matrix $\boldsymbol{J}$ of each layer. The rotational matrix is $\boldsymbol{R}$.

The fraction of energy transmitted through all layers is

$$T = \frac{\left|E_{s,n+1}\right|^2 + \left|E_{p,n+1}\right|^2}{\left|E_{s,0}\right|^2 + \left|E_{p,0}\right|^2} \tag{220}$$

which depends on the matrix elements W_{ij} as well as on the polarization state of the incident beam ($E_{s,0}$, $E_{p,0}$). For an unpolarized incident beam, the Jones vector of the incident beam can be written as

$$\begin{bmatrix} E_{s,0} \\ E_{p,0} \end{bmatrix} = \frac{E_0}{\sqrt{2}} \begin{bmatrix} e^{i\alpha_1} \\ e^{i\alpha_2} \end{bmatrix} \tag{221}$$

where α_1 and α_2 are two random variables such that the time-average quantities $\langle\cos(\alpha_1\text{-}\alpha_2)\rangle$ and $\langle\sin(\alpha_1\text{-}\alpha_2)\rangle$ vanish simultaneously. Let us verify this. Inserting equations (217) and (221) in equation (220), and after re-arrangement, we have

$$\begin{aligned} T(\alpha_1,\alpha_2) = \frac{1}{2}\Big(&\left|W_{11}\right|^2 + \left|W_{12}\right|^{12} + \left|W_{21}\right|^2 + \left|W_{22}\right|^2\Big) \\ &+ \left(W_{11}W_{12}^* + W_{21}W_{22}^*\right)e^{i(\alpha_1-\alpha_2)} + \left(W_{11}^*W_{12} + W_{21}^*W_{22}\right)e^{-i(\alpha_1-\alpha_2)} \end{aligned} \tag{222}$$

Now $T(\alpha_1, \alpha_2)$ is the function of α_1, α_2. Taking assemble average, ie, performing a integral over α_1, α_2 from 0 to 2π, we arrive at

$$T = \frac{1}{(2\pi)^2}\int_0^{2\pi}\int_0^{2\pi} T(\alpha_1,\alpha_2)d\alpha_1 d\alpha_2 = 1/2\left(|W_{11}|^2 + |W_{12}|^2 + |W_{21}|^2 + |W_{22}|^2\right) \quad (223)$$

Because the integrals of exponential terms obviously vanish, i.e., cross-interference terms make no contribution to the transmittance.

The biggest advantage of working in the wave frame lies in that one can keep the intensity of the incident beam $I_0 = |E_{x,0}|^2 + |E_{y,0}|^2 = E_0^2$ a constant, totally independent of the incident angles: ϑ_k and φ_k. This in return guarantees that the transmittance at normal incidence, i.e., $\vartheta_k = 0^\circ$ takes on the same values no matter what kind of value φ_k takes, i.e., it is independent of φ_k.

7.1.6. Loss corrections

When an incident beam enters through the polarizer layer or the LC layer from the air or vice versa, there are usually significant transmission losses at the entrance and exit surfaces due to reflections.

One of the methods to take them into account is to modify the expression for the extended Jones matrix representation (211) by including the appropriate reflection and transmission coefficients. In this case

$$\boldsymbol{J}^{lc} = \boldsymbol{J}^{out}\,\boldsymbol{J}\,\boldsymbol{J}^{in} \quad (224)$$

Where

$$\boldsymbol{J}^{in} = \boldsymbol{D}\boldsymbol{J}^{ent}\boldsymbol{D}^{-1} = \quad (225)$$

$$\begin{bmatrix} \dfrac{2n_a\cos^2\varphi_k\cos\vartheta_p}{n_a\cos\vartheta_p + n_p\cos\vartheta_k} + \dfrac{2n_a\sin^2\varphi_k\cos\vartheta_k}{n_a\cos\vartheta_k + n_p\cos\vartheta_p} & \dfrac{n_a\sin(2\varphi_k)\cos\vartheta_p}{n_a\cos\vartheta_p + n_p\cos\vartheta_k} - \dfrac{n_a\sin(2\varphi_k)\cos\vartheta_k}{n_a\cos\vartheta_k + n_p\cos\vartheta_p} \\ \dfrac{n_a\sin(2\varphi_k)\cos\vartheta_p}{n_a\cos\vartheta_p + n_p\cos\vartheta_k} - \dfrac{n_a\sin(2\varphi_k)\cos\vartheta_k}{n_a\cos\vartheta_k + n_p\cos\vartheta_p} & \dfrac{2n_a\sin^2\varphi_k\cos\vartheta_p}{n_a\cos\vartheta_p + n_p\cos\vartheta_k} + \dfrac{2n_a\cos^2\varphi_k\cos\vartheta_k}{n_a\cos\vartheta_k + n_p\cos\vartheta_p} \end{bmatrix}$$

And

$$\boldsymbol{J}^{out} = \boldsymbol{D}\boldsymbol{J}^{ext}\boldsymbol{D}^{-1} = \quad (226)$$

$$\begin{bmatrix} \frac{2n_p\cos^2\varphi_k\cos\vartheta_k}{n_a\cos\vartheta_p+n_p\cos\vartheta_k}+\frac{2n_p\sin^2\varphi_k\cos\vartheta_p}{n_a\cos\vartheta_k+n_p\cos\vartheta_p} & \frac{n_p\sin(2\varphi_k)\cos\vartheta_k}{n_a\cos\vartheta_p+n_p\cos\vartheta_k}-\frac{n_p\sin(2\varphi_k)\cos\vartheta_p}{n_a\cos\vartheta_k+n_p\cos\vartheta_p} \\ \frac{n_p\sin(2\varphi_k)\cos\vartheta_k}{n_a\cos\vartheta_p+n_p\cos\vartheta_k}-\frac{n_p\sin(2\varphi_k)\cos\vartheta_p}{n_a\cos\vartheta_k+n_p\cos\vartheta_p} & \frac{2n_p\sin^2\varphi_k\cos\vartheta_k}{n_a\cos\vartheta_p+n_p\cos\vartheta_k}+\frac{2n_p\cos^2\varphi_k\cos\vartheta_p}{n_a\cos\vartheta_k+n_p\cos\vartheta_p} \end{bmatrix}$$

Here $\boldsymbol{D}$ is a 2-dimentional rotational transform and $\boldsymbol{D}^{-1}$ is its inverse

$$\boldsymbol{D}=\begin{bmatrix}\cos(\varphi_k) & -\sin(\varphi_k)\\ \sin(\varphi_k) & \cos(\varphi_k)\end{bmatrix} \tag{227}$$

And [101]

$$\boldsymbol{J}^{ent} = \begin{bmatrix} \frac{2n_a\cos\vartheta_p}{n_a\cos\vartheta_p+n_p\cos\vartheta_k} & 0 \\ 0 & \frac{2n_a\cos\vartheta_k}{n_a\cos\vartheta_k+n_p\cos\vartheta_p} \end{bmatrix} \tag{228}$$

and

$$\boldsymbol{J}^{ext} = \begin{bmatrix} \frac{2n_p\cos\vartheta_k}{n_a\cos\vartheta_p+n_p\cos\vartheta_k} & 0 \\ 0 & \frac{2n_p\cos\vartheta_p}{n_a\cos\vartheta_k+n_p\cos\vartheta_p} \end{bmatrix} \tag{229}$$

where n_a is the refractive index of light in the incident medium (usually air for which $n_a\cong1$) and ϑ_p is defined by

$$\vartheta_p=\sin^{-1}\left[\sin(\vartheta_k)/\mathrm{Re}(n_p)\right] \tag{230}$$

in which $\mathrm{Re}(n_p)$ stands for the average of the real parts of the two indices of refraction: n_e and n_o of the polarizer.

So far, we have established the whole theoretical framework for the calculation of the optical properties at any off-axis incident angles: ϑ_k and φ_k.

7.1.7. Transmittance after loss corrections

After introducing the correction of transmission losses in the air-LCD interfaces, equations (224)-(226), the matrix $\boldsymbol{W}$ becomes

$$W^{lc} = R^{-1} J^{lc} R = R^{-1} J^{out} J J^{in} R = R^{-1} J^{out} J_n J_{n-1} J_{n-2} \cdots J_3 J_2 J_1 J^{in} R \tag{231}$$

It is easy to verify that

$$R^{-1} J^{out(in)} R = R^{-1} D J^{ent(ext)} D^{-1} R = J^{ent(ext)} \tag{232}$$

Therefore W^{lc} can be rewritten as

$$W^{lc} = J^{ext} R^{-1} J R J^{ent} = J^{ext} W J^{ent} \tag{233}$$

Accordingly, expression (223) for calculation of transmittance becomes

$$T^{lc} = 1/2\left(\left|W_{11}^{lc}\right|^2 + \left|W_{12}^{lc}\right|^2 + \left|W_{21}^{lc}\right|^2 + \left|W_{22}^{lc}\right|^2 \right) \tag{234}$$

At this point, we have completed the construction of the theoretical framework.

7.2. Computational implementation

A robust computer code has been written in Fortran 90, implemented, and tested in Sun workstation. There are several options available for the user to choose: (1) whether a pair of polarizers is applied or not; (2) whether the loss corrections are considered or not; (3) whether the contribution from the magnetic effect is included or not, and (4) whether glass layers are introduced or not and so on. Also there are several formats of outputs available for the purpose of the graphic representation. One of them is specially designed for Matlab to draw the polar diagram, the others are for general graphic packages, e.g., Unigraph. Furthermore, the user can choose to output only the data sets for the pure polarizers alone or a complete set of data for the whole LC cells. Particularly, the output for the relation between the transmittance $\boldsymbol{T}$ and x or y or (x,y) co-ordinates for a given pair of incident angles (φ_k, ϑ_k) is also available, which is useful to analyse the spatial structure of the transmittance at a given viewing angle. For any fixed azimuthal angle φ_k, the polar angle ϑ_k varies from 0° to 90°, then φ_k can be changed from 0° to 360°.

7.2.1. Calculation of T as a function of positions x and/or y

On occasions, it is very useful to examine the spatial distribution pattern of transmittance T at any incident angles. In this case, we fix incident angles and then calculate T for all (x,y) points on the x-y plane. For a two-dimensional geometry, only the calculation for all x or y co-ordinates is required. The graphic representation for

the output in this case is T versus x or y or (x,y) for given values of the incident angles: ϑ_k and φ_k.

7.2.2. Calculation of a spatial average of $\overline{T}$ as function of incident angles (ϑ_k, φ_k)

For a two-dimensional model, first, we calculate T as a function of x or y for all values of incident angles (ϑ_k, φ_k), then sum up T over all sampling points of x or y, and finally, normalise the total T by the sampling "length", i.e., total number of the points sampled in the x or y direction, which gives a length average of transmittance $\overline{T}$ as a function of (ϑ_k, φ_k),

For a 3-D LCD model, the summation of T over all sampling area, i.e., all points sampled in x-y plane must be done and then an area average of transmittance of $\overline{T}$ can be obtained normalising T by the "area", i.e., points sampled on x-y plane. In this way, a polar diagram of $\overline{T}$ vs. oblique incidence angles (ϑ_k, φ_k) can be drawn, giving a clear graphical representation of the viewing angle effect in a LC display device.

7.3. Application of theory to the TN-LCD system

The theory developed above and corresponding program has been used to calculate the transmittance for the following the two cases:

a pair of crossed, nearly ideal polarizers without any LC layers or substrate layers - a classic example;

a 90° twisted nematic LC cell with a pre-tilt of 2° and a crossed polarizers pair (from –45° to 45°). The cell width is 118.5μm which is the length of the pixel electrode as well. A pixel voltage of 5V is used. V_{bus}= ±5V with a period of 30μs. K=11.34 pN, γ=0.1 Pa•s. All other related parameters are the same as in Table 2 (page 65)

7.3.1. Crossed nearly ideal polarizers

Figure 84 is a polar diagram of T vs. (ϑ_k,φ_k) for only two polarizer layers whose thicknesses are both chosen to be 5.15×10^{-4}m. Their optical refractive indices are, respectively, n_o^p =(1.5+j0.0), and n_e^p =(1.5+j1.5×10^{-2}). They are positioned at -45° and 45° respectively.

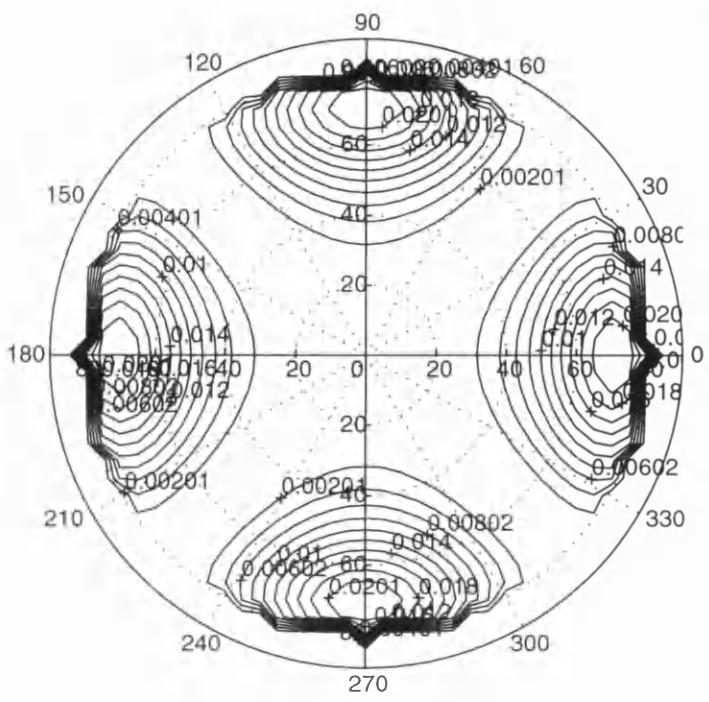

Figure 84 Transmittance of crossed nearly ideal polarizers as function of polar and azimuthal angles (ϑ_k ,φ_k)

It can be seen from Figure 84 that the polarizers divide the contours of transmittance into four visible regions that are symmetrically located and each sub-region has its own symmetric axis.

7.3.2. TN-LC cell

In this case, a driving voltage of 5V is used as shown in Figure 85. The cell is first exposed to zero volt for half a period and, then a voltage of 5V is applied to it for one period. From this point, the voltage is withdrawn and the cell is let to relax for three periods. Two particular time points are considered with a view to analysing the system's relaxation states at different time. The first one is at t=50.01ms when the voltage is just switched off. The second is at t=150.03ms when the voltage has been switched for three periods. The polarizers' parameters are the same as those given in subsection 7.3.1 and the rubbing directions are the same as the polarizers' orientations.

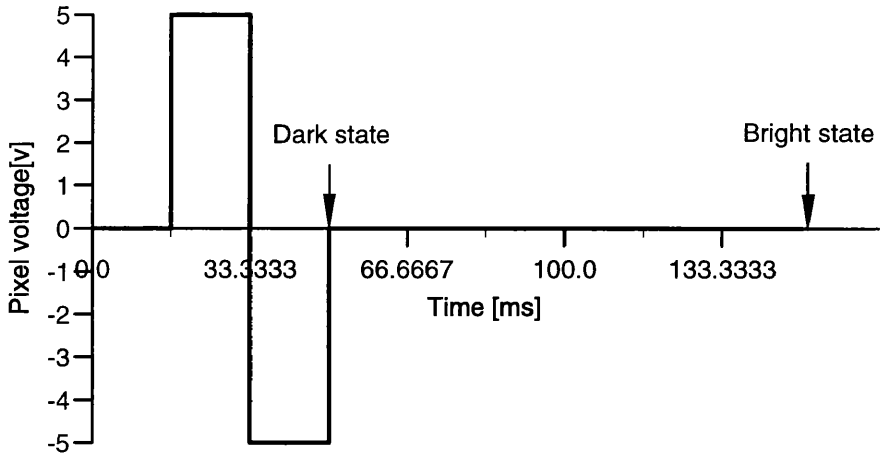

Figure 85 The pixel voltage pattern

Figure 86 shows the transmittance polar diagram at t=50.01ms. Figure 87 is the corresponding director profile. Figure 88 and Figure 89 are another set of the transmittance polar diagram and the corresponding director profile at t=150.03ms Figure 90 shows the contrast ratio of transmittance of the *bright state* (Figure 88) to *dark state* (Figure 86), which is defined as $CR = T_{bright}/T_{dark}$. Only the values of less than or equal to 50.0 are plotted.

It can be seen from those figures that

when t=50.01ms, i.e., when the driving voltage is just switched off or in the dark state, the directors are nearly vertically tilted everywhere [see Figure 87], far from the initial state. This prevents the twist from playing any active role in guiding the light through the LC layers. Therefore, the spatial structure of the transmittance is very similar to the one for the crossed polarizers pair [see Figure 84], but no longer symmetric in space about horizontal axis because of non-zero pretilt;

when t=150.03ms, the pixel voltage has been completely off for three periods, the system has completely relaxed to the bright state. The director field has restored to the initial configuration [see Figure 89]. The tilt has relaxed to the same level as the initial setting. The brightest area becomes larger. The spatial structure of the contrast ratio of this state to the dark state tends to become completely symmetric about the vertical axis as shown in the Figure 90.

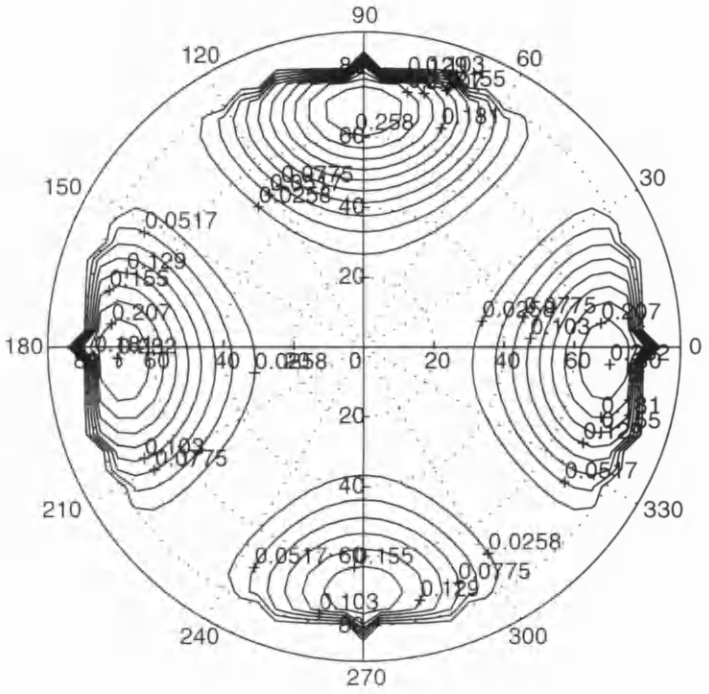

Figure 86 Transmittance vs. viewing angles (ϑ_k, φ_k) at t=50.01ms when the pixel voltage is just switched off or *dark state* since directors are fully switched at this time as shown in Figure 87

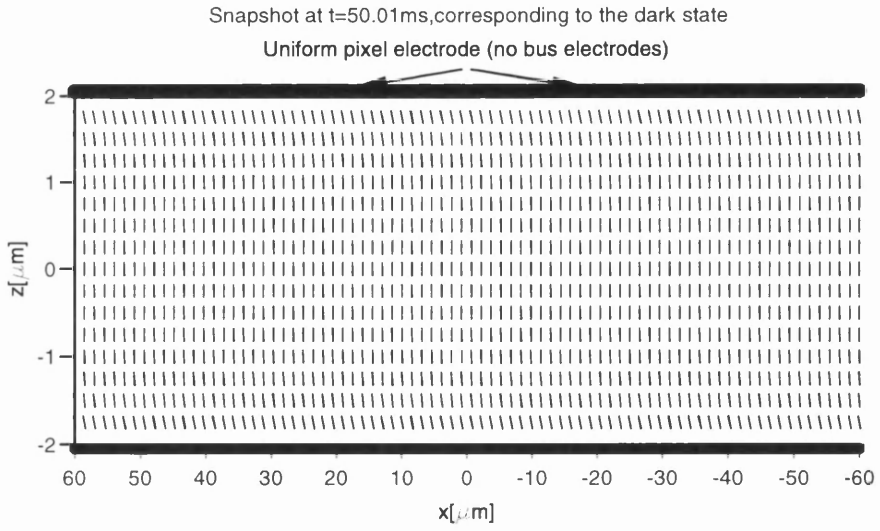

Figure 87 A snapshot of director profile at t=50.01ms when the driving voltage is just switched off.

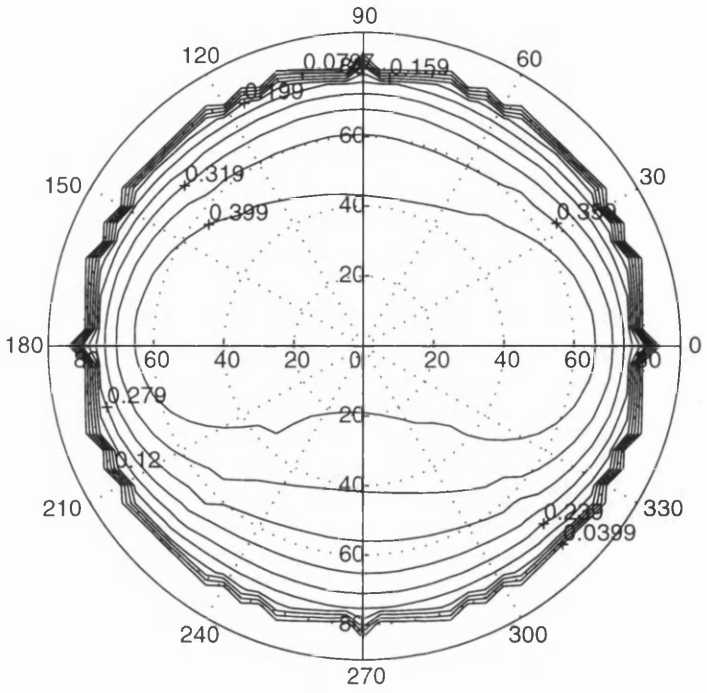

Figure 88 Transmittance vs. viewing angles (ϑ_k, φ_k) at t=150.03ms when the voltage is withdrawn for three periods or *bright state* since the directors have relaxed to nearly their initial states as shown in Figure 89

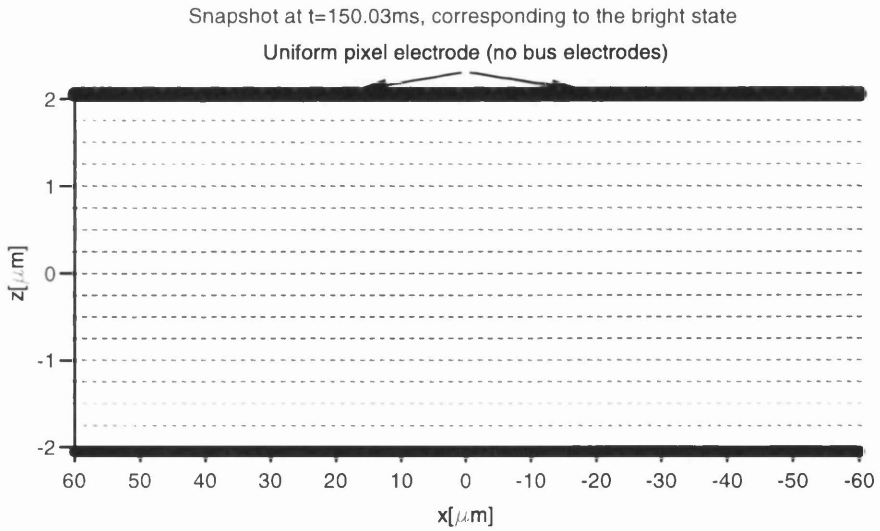

Figure 89 Director profile at t=150.03ms when the voltage has been switched off for 3 periods. The system has relaxed to nearly its initial state

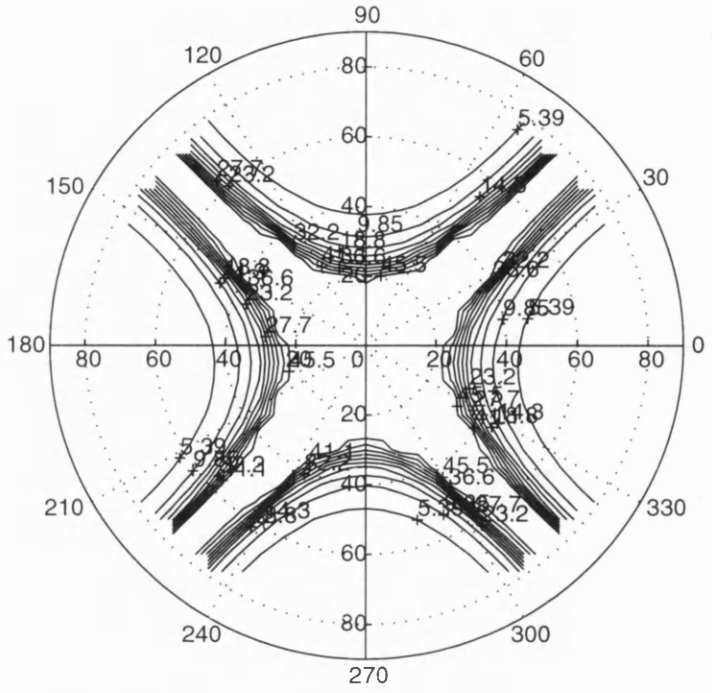

Figure 90 Contrast ratio defined as T_{bright}/T_{dark}. T_{bright} is shown in Figure 88 and T_{dark} as shown in Figure 86. Only ratio values of less than or equal to 50.0 are plotted.

7.4. A comparison with experimental data (from Philips)

In order to validate the theory presented in this chapter, we compare our theoretical prediction for a TN system in IPS mode [19], with the corresponding experimental data from Philips Research Laboratories, a good agreement has indeed been found for both transmittance and contrast. The full details are given in the published paper [102] that is appended to this thesis.

8. Conclusions

A two-dimensional dynamic model developed for the TFT driven display devices has been demonstrated based on the constant charge assumption that means the voltages are applied to the pixel electrodes for only a line time duration t_c, typically between 15μs and 30μs. After that, the pixel voltages are left floating for the rest of half-frame time while the charges that are deposited on the pixel electrodes during the connection time t_c remain constant. A crucial aspect is how to predict the floating voltages of the pixel electrodes for the next time step. To this end, the charges on the pixel electrodes are calculated using a formulation specifically developed for this case. The capacitance matrix (self- and mutual capacitances of all electrodes) for the whole LC cell is obtained by using a perturbation technique which is based on the linear relationship between the voltage and the charge for a given dielectric configuration, i.e., temporally and spatially fixed director distribution, and taking physical sizes of electrodes and their edge effects into account. Once the floating pixel voltages are found, the corresponding spatial patterns of the director and potential are calculated through the iterations by finite differences and finite elements methods. Based on the detailed information about the temporal and spatial distributions of the director and potential, the dynamic behaviour of the systems: floating pixel voltages, mid-plane tilt angles, charges, self- and mutual capacitances, transmittance, and flicker are analysed systematically. The modelled results obtained exhibit notable agreement with the experimentally observed dynamic behaviour, and they are more accurate and realistic than those of the constant voltage model and any 1D charge driving related models [25-27].

External capacitors used in TFT LCDs can be easily incorporated into the model and their effect is fully examined. The ripple phenomenon of the floating pixel voltage due to the coupling with the rapid change in the polarity of bus voltages can be suppressed by increasing the values of the storage capacitor. The same can be done for the flicker. A larger value of the storage capacitance gives rise to a more stable behaviour of the system. A very large value is shown to be equivalent to the constant voltage operation.

Several different electrode configurations are modelled here to show the capability of the model.

Comparisons have been made between the numerical calculations and the measurements for the average transmittance at normal incidence and good agreement has been found.

The effect of the temporal and spatial discretisation steps on the numerical accuracy has also been examined in detail. It has been found that in cases studied, the results are very sensitive to the spatial step Δz, but not sensitive to the spatial discretization size Δx, except the charges and the capacitances as they are very sensitive to the number of nodes used to represent the electrodes. A combination of Δx=1.5 and Δz=0.25, used in all calculations throughout the thesis, gives the best accuracy, while a value of Δz=0.5 gives reasonable results. Though a time step of Δt=5μs used throughout the research gives the best accuracy, a step of 10μs is seen to offer good results as well. A step of 15μs is shown too big.

It has been found that bus lines of non-zero voltages do have influence upon the dynamic behaviours of the systems. Two obvious examples are the ripple effects observed from the floating pixel voltage temporal pattern in the case of the constant charge model or from the charge curve (Figure 26) in the case of the constant voltage model, as well as the flicker generation in the case of symmetric source voltage. In general, it speeds up the director switching process in the constant charge mode.

A three-elastic constant tensorial dynamic formulation developed here, which is supposed to offer an even better modelling capability, is now being implemented outside this project.

A new extended 2×2 Jones matrix representation is derived to enable us to directly analyse the optical properties of LCD cell at any viewing angle with ease and to make a comparison between theoretical prediction and experimental data. A good agreement has been found for a TN cell in IPS mode analysed as an example.

Through this research, it can been seen that computer modelling not only enables us to gain a deep insight into the switching mechanism of LC devices, but also provide us with the following obvious advantages:

1) save money and time on undertaking expensive and time consuming experiments;

2) help identify the optimal material parameters and geometry to guide device design and achieve the best performance by suppressing defects, improving viewing angle characteristics, and increasing the values of the storage capacitors etc.;

3) allow a quick test of any new idea.

Finally, it is worthwhile to point out that the achievements in this project have led to the success in attracting further funds from the EU to support the related project: *Predictive 3D micro-model simulation for Monitor LCDs*, under the Framework 5 programme, in a consortium which apart from our group includes Philips (Eindhoven and PRL, UK), autronics-MELCHERS Gmbh (Germany), the University of Ghent, and the Politecnico di Torino.

References

[1] K. Kanzaki, "Trends in TFT", in Proceedings of the 19th International Display Research Conference – Euro Display'99, Berlin, 6-9 September 1999, p17.

[2] K. R. Schleupen, F. R. Libsch. P. M. Alt, "Status and trends of AMLCD addressing", in Proceedings of the 19th International Display Research Conference – Euro Display'99, Berlin, 6-9 September 1999, pp43-44.

1D static:

[3] H. J. Deuling, "Deformation of nematic liquid crystals in an electric field", Mol. Cryst. Liq. Cryst., **19**, 123-131(1972)

1D static + dynamic:

[4] D. W. Berreman, "Numerical modelling of twisted nematic devices", Phil. Trans. R. Soc. Lond., A, **309**, 203-216(1983).

[5] H. Wöhler, M. Fritsch, G. Haas, and D. A. Mlynski, "A modified Ritz method for the calculation of deformation profiles in chiral nematic liquid crystal cells". In The 9th International Display Research Conference, 16-18 October 1989, Japan, 376-379(1989).

1D dynamic:

[6] D. W. Berreman, "Dynamics of liquid-crystal twist cells", J. Appl. Phys., **25**, 12-15(1974)

[7] C. Z. Doorn, "Dynamic behaviour of twisted nematic liquid-crystal layers in switched fields", J. Appl. Phys., **46**, 3738-3745(1975)

1D dynamic (Leslie-Erickson hydrodynamic equation): optical bounce

[8] D. W. Berreman, "Liquid crystal twist cell dynamics with backflow", J. Appl. Phys., **46**, 3746-3751(1975).

1D static + dynamic new mothed:

[9] M. E. Becker, "A new for computing director profiles", In proceedings of 1994 International Display Research Conference, Monterey, California, pp503-506.

2D static

[10] G. Hass, H. Wohler, M. W. Fritsch, and D. A. Mlyski, "Simulation of two-dimensional nematic director structures in inhomogeneous electric fields", Mol. Cryst. Liq. Cryst., **198**, 15-28(1991).

[11] F. Di Pasquale, F.A. Fernandez, S.E. Day, and J. B. Davies, "Two-dimensional finite-element modelling of nematic liquid crystal devices for optical communications and displays", IEEE J. of selected Topics in Quantum Electronics, **2**, 128-134(1996).

[12] J. B. Davies, S. E. Day, F. Di Pasquale, and F. A. Fernandez, "Finite-element modelling in 2-D of nematic liquid crystal structures", Electron. Lett., **32**, 582-583(1996).

2D static + dynamic tensorial:

[13] A. Kilian and S. Hess, "On the simulation of the director field of a nematic liquid crystal", Liquid Crystals, **8**, 465- 472(1990).

[14] F. Di Pasquale, F. A. Fernandez, J. B. Davies, S. E. Day, "Analysis of twisted nematic liquid crystal display cells using the finite element method", SID, Euro Display 96, In proceedings of the 16th Int. Display Research Conference, October 1-3, 1996, Birmingham, UK.

2D dynamic tensorial:

[15] A. Kilian and S. Hess, "Derivation and Application of an algorithm for the numerical calculation of the local orientation of nematic liquid crystals", Z. Naturforsch, **44a**, 693-703(1989).

[16] A. Kilian and S. Hess, "Computer simulations of the π-cell", Mol. Cryst. Liq. Cryst., **204**, 155-160 (1991).

2D dynamic tensorial (IPS)

[17] F. Di Pasquale, F.A. Fernandez, S.E. Day, J.B. Davies, "Time domain modelling of liquid crystal display cells in two- and three-dimensions, pp47-48, COMPUMAG, The 11th Intl. Conference On the Computation of Electromagnetic Fields, November 3-6, 1997, Rio, Brazil.

[18] F. Di Pasquale, H. F. Deng, F. A. Fernandez, *et al*, "Theoretical and experimental study of Nematic liquid crystal display cells using the In-Plane-Switching mode", IEEE Trans. on electron devices, **46**, 661-668(1999).

2D & 3D dynamic tensorial (IPS):

[19] F. Di Pasquale, F.A. Fernandez, S.E. Day, and J.B. Davies, "Two-dimensional modelling of nematic liquid crystal display cells using the In-Plane Switching mode", SID'97, Int. Symposium, Seminar and Exhibition, Boston, Massachusetts, May 11-16, 1997.

2D dynamic (n not = –n)

[20] M. Kitamura, "Computer simulation of director profile in two dimensional electric field", in SID '93 Dig., 350-353(1993).

[21] K. Sumiyoshi, K. Takatori, N. Takahashi, and Y. Hirai, "A two-dimensional liquid crystal simulation for thin film transistor liquid crystal displays", Liquid Cryst., **14**, 1199-1208(1993).

2D static simple lattice model – matrix method:

[22] T. Kimura and D.G. Gray, "A matrix method for modelling liquid-crystal textures", Liq. Cryst., **13**, 23-30(1993).

3D dynamic tensorial:

[23] A. Lien, "Simulation of three-dimensional director structures in twisted nematic liquid crystal displays", Appl. Phys. Lett., **62**, 1079-1081(1993)

3D static tensorial Monte Carlo:

[24] T. Gruhn and S. Hess, "Monte Carlo simulation of the director field of a nematic liquid crystal with three elastic coefficients", Z. Naturforsch., **51a**, 1-9 (1996)

1D constant charge modelling:

[25] T. Onozawa, T. Ueno, and H. Katoh, "Dynamic electro-optical characteristics in an active-matrix-addressed TN-LCD", In Proceedings of the SID, **31**, 95-100(1990).

[26] P. Vetter B Maximus and H. Pauwels, "Dynamical response in an AM addressed TN-LCD with anisotropic resistivity", J. Phys. D: Appl. Phys. **25**, 481-486(1992).

[27] M. E. Becker, J. Neumeier, and H. Wöhler, "Numerical Modeling of AMLCDs", In Proceedings of the SID, May 19-21, 1992, Boston, M.A., pp15-18.

2D constant charge model:

[28] H. F. Deng, F. A. Fernandez, S. E. Day, and J. B. Davies, "A constant charge based modelling of Liquid Crystal Displays", in Proceedings of the 19th International Display Research Conference – Euro Display'99, Berlin, 6-9 September 1999, pp319-322.

On-Off states of TFT-LCD:

[29] Y. Miyata, T. Ogawa, and T. Chikamura, "Dynamic characteristics of a-Si TFT-addressed LCDs", Proc. SID, **29**, 289-294(1988)

TFT-equivalent circuit to predict flicker:

[30] Y. Numano, M. Hayama, and T. Yamazaki, "Analysis of the optical response characteristics of the TFT-LCD". In Conference on Solid State Device and Materials, 22-24 August 1990, Sendai, Japan, 987-990(1990)

Oseen-Franck equation:

[31] C. W. Oseen, "The theory of liquid crystal", Trans. Faraday Soc., **29**, 883-898(1933)

[32] F.C. Frank, "On the theory of liquid crystal". Discuss. Faraday Soc., **25**, 19-28(1958)

Leslie-Erickson equations:

[33] F. M. Leslie, "Some constitutive equations for liquid crystals", Arch. Ration. Mech. Anal., **28**, 265-283(1968).

[34] J. L. Ericksen, "Conservation laws for liquid crystals", Trans, Soc. Rheol., **5**, 23-34(1961).

[35] H. J. Plach, B. Rieger, E. Poetsch, and V. Reifenrath, "Stability studies on new liquid crystals for active matrix displays", SID Int. Disp. Conf. 136-141(1990)

[36] F. Moia and M. Schadt, "New generation of nematic mixtures for high information content liquid crystal displays, such as OMI-, STN- and TFT-LCDs", SID, Int. Disp. Conf. 132-135(1990).

[37] P. Vetter, B. Maximus, and H. Pauwels, "Influence of fabrication process on LC resistivity in TFT displays", SID Int. Displ. Conf., 320-323(1990).

[38] A Lien, "A detailed derivation of extended Jones matrix representation for twisted nematic liquid crystal displays", Liquid Crystals, **22**, 171-175(1997).

[39] A Lien and C-J Chen, "A new 2×2 matrix representation for twited nematic liquid crystal displays at oblique incidence", Jpn. J. Appl. Phys., **35**, **L**1200-**L**1203(1996).

[40] R. Clark Jones, "A new calculus for the treatment of optical systems – I. Description and discussion of the calculus", J. Opt. Soc. Am. **31**, 488-493(1941).

[41] A. Lien, "Extended Jones matrix representaion for the twisted nematic liquid-crystal display at oblique incidence", Appl. Phys. Lett., **57**, 2767-2769(1990).

[42] A. Lien, "Application of the extended Jones matrix method to LCDs at the oblique incidence", SID 91 Digest, 586-589(1991).

[43] Pochi Yeh, "Extended Jones matrix method", J. Opt. Soc. Am., **72**, 507-513(1982).

[44] H. F. Deng, "*Computer Modelling of Liquid Crystal Displays*", MPhil. Report, 1998.

[45] A. Mosley, "Liquid crystal displays – An overview", Displays, **14**(2), 67-73(1993).

[46] C. H. Hayn, "Liquid Crystal Display", The physics Teacher, **17**(4), 256-257(91981)

[47] A. D. Schelling, "Liquid crystal displays", Electronic Components and Applications, **5**(4), 233-241(1983)

[48] *Electro-optical Displays*, Ed. M A. Karim, Marcel Dekker, Inc., New York, 1992.

[49] S. E. Day, Applications of Liquid Crystals in *Electronic Materials*. Ed. B. Mullin, and S. Miller, published by Plenum, 1991

[50] P. G. de Gennes, The Physics of Liquid Crystals, Clarendon Press, Oxford, 1974.

[51] M. J. Stephen and J. P. Straley, "Physics of liquid crystals", Rev. Mod. Phys., **46**, 617-704(1974).

[52] T. C. Lubensky, "Molecular description of nematic liquid crystal", Phys. Rev. A, **2**, 2497-2514, (1970).

[53] G. H. Brown and W. G. Shaw, "The mesomorphic state - liquid crystals", Chem. Rev., **57**, 1049 -1157(1957).

[54] G. H. Brown and W. G. Shaw, "The mesomorphic state - liquid crystals", Chem. Rev., **57,** 1049 -1157(1957).

[55] P. Pieranski, F. Brochard, and E. Guyon, "Static and dynamic behaviour of a nematic liquid crystal in a magnetic field, Part II: dynamics", J. Phys., **34**, 35-48 (1973).

[56] H. van Sprang, H.G.Koopman, "Experimental and calculated results for the dynamics of oriented nematic with twist angles from 210 to 270, J. Appl. Phys, **64**, 4873-4883(1988).

[57] L. D. Landau , "Zur theorie der pasenumwandlunge 1", Phys. Z. Sowjetunion, **11**, 26-47(1937)

[58] L. D. Landou and E. M. Lifshitz, Statistical Physics, Addison-Wesley, Reading, 1958

[59] W. Maier and A. Saupe, "Eine einfache molekular-statistische theorie der nematischen kristallinflüssigen zustandes", Z. Naturforsch, **13a**, 564-556(1958).

[60] W. Maier and A. Saupe, "Eine einfache molekular-statistische theorie der nematischen kristallinflüssigen phase. Teil I", Z. Naturforsch, **14a**, 882-889(1959).

[61] W. Maier and A. Saupe, "Eine einfache molekular-statistische theorie der nematischen kristallinflüssigen phase, Teil II" , Z. Naturforsch, **15a**, 287-292(1960).

[62] J. R. McColl, "Effect of pressure on order in the nematic liquid crystal – p-azoxyanisole", Phys. Lett., **A38**, 55-57(1972)

[63] J. R. McColl and C. S. Shih, "Temperature dependence of orientational order in a nematic liquid crystal at constant molar volume", Phys. Rev. Lett., **29**, 85-87(1972)

[64] L. Onsager, "The effect of shape on the interaction of colloidal particles", Ann. NY Acad. Sci., **51**, 627-659(1949)

[65] J. E. Mayer, "Theory of Real Gases" in *Handbuch der Physik*, Ed. S. Flugge, Springer, Berlin, **12**, 73-204(1958)

[66] H. Zocher, "The effect of a magnetic field on the nematic state", Trans. Faraday Soc., **29**, 945-957(1933)

[67] J. L. Ericksen, "Nilpotent energies in liquid crystal theory", Arch. Ration. Mech. Anal., **10**, 189-196(1962)

[68] G. Vertogen, S.D.P. Flapper, and C. Dullemond, "Elastic constants of nematic and cholesteric liquid crystals and tensor fields", J. Chem. Phys. **76**, 616-618(1982).

[69] G. Vertogen and W. H. de Jeu, *Thermotropic liquid Crystals, Fundamentals*, Verlag Chemie, Weinheim, 1980.

[70] S. Hess S and I. Pardowitz, "On the unified theory for non-equilibrium phenomena in the isotropic and nematic phases of a liquid crystal; spatially inhomogeneous alignment" , Z. Naturforsch., **36a**, 554-558 (1981).

[71] G. Vertogen and W. H. de Jeu, Thermotropic Liquid Crystals, Verlag Chemie, Weinheim, 1980.

[72] P. G. de Gennes, "Short range order effects in the isotropic phase of nematics and cholesterics", Mol. Cryst. Liq. Cryst., **12**, 193- 214(1971).

[73] S. Hess, "Irreversible thermodynamics of non-equilibrium alignment phenomena in molecular liquids and in liquid crystals - I. Derivation of non-linear constitutive laws, relaxation of the alignment, phase transition ", Z. Naturforsch., **30a**, 728-738(1975);

[74] S. Hess, "Irreversible thermodynamics of non-equilibrium alignment phenomena in molecular liquids and in liquid crystals – II. Viscous flow and flow alignment in the isotropic (stable and metastable) and nematic phases", Z. Naturforsch., **30a**,1224-1232(1975).

[75] S. Hess, Vektor- and Tensor-Rechnung, Palm und Enke, Erlangen, 1980.

[76] S. Hess und W. Kohler, Formeln zur Tensorrechnung, Palm und Enke, Erlangen, 1980.

[77] I. Pardowitz and S. Hess, "Elasticity coefficients of nematic liquid crystals", J. Chem. Phys., **76**, 1485-1489(1982).

[78] I. Pardowitz and S. Hess, "On the theory of irreversible processes in molecular liquids and liquid crystals, non-equilibrium phenomena associated with the second and fourth rank alignment tensors", Physica A **100**, 540-562(1980).

[79] S. Hess, "Pre- and Post—transitional behaviour of the flow alignment and flow-induced phase transition liquid crystals", Z. Naturforsch., **31a**, 1507-1513(1976).

[80] S. Hess, "Transport phenomena in anisotropic fluids and liquid crystals", J. Non-Equilib. Thermodyn. **11**, 175-193(1986).

[81] S. Hess, "Fokker-Planck-equation approach to flow alignment", Z. Naturforsch., **31a**, 1034-1037(1976).

[82] F. Leenhouts and A. J. Dekker, "Elastic constants of nematic liquid crystalline Schiff's bases", J. Chem. Phys., **74**, 1956-1965(1981).

[83] H. Gruler, "Elastic constants of nematic liquid crystals", Z. Naturforsch., **28a**, 474-483(1973).

[84] K. Schiele and S. Trimper, "On the elastic constants of a nematic liquid crystal", Phys. Status Solidi, **B 118**, 267-274(1983).

[85] D. W. Berreman and S. Meiboom, "Tensor representation of Oseen-Frank strain energy in uniaxial cholesterics", Phys. Rev. A, **30**, 1955-1959(1984).

[86] S. Dickmann, J. Eschler J, O. Cossalter, and D. A. Mlynski, "P-53: Simulation of LCDs including elastic anisotropy and inhomogeneous field", SID 93 DIGEST, 638-641(1993).

[87] P.P Silvester and R.L. Ferrai, *Finite Elements for Electrical Engineers*, 2nd Ed. Cambridge University Press, 1990.

[88] O.C. Zienkiewicz and K. Morgan, *Finite Elements and Approximation,* John Wiley & Sons, Inc., 1983.

[89] O.C. Zienkiewicz, and R.L. Taylor, *The Finite Element Method, Volume 1 – Basic Formulation and Linear Problems*, McGraw-Hill Book Company Europe, England (1994).

[90] R. D. Richtmyer and K.W. Morton, *Difference Methods For Initial-value Problems*, Interscience, p189 (1967).

[91] W. L. Wood, *Practical Time-stepping Schemes*, Clarendon Press, Oxford (1990).

[92] J. Crank and P. Nicolson, "A practical method for numerical integration of solutions of partial differential equations of heat conduction type", Proc. Camb. Phil. Soc., **43**, 50-67(1947)

[93] O. C. Zienkiewicz and R. L.Taylor, *The Finite Element Method, Volume 2 – Solid and Fluid Mechanics, Dynamics and Non-linearity*, McGraw-Hill Book Company Europe, England (1991).

[94] G. H. Golub and C. F. Van Loan, *Matrix Computations*, North Oxford Academic, Oxford, 1983, pp119-124.

[95] F. F. Kuo, *Network Analysis and Synthesis*, 2nd Ed., John Wiley & Sons, Inc., New York, 1966.

[96] D. W. Berreman, "Optics in stratified and anisotropic media: 4×4-matrix formulation", J. Opt. Soc. Am., **62**, 502-510(1972).

[97] H. Wöhler, G. Haas, and M. Fritsch, D. A. Mlynski, "Faster 4×4 matrix method for uniaxial inhomogeneous media", J. Opt. Soc. Am. A **5**, 1554-1557(1988).

[98] M. Schadt and W. Helfrich, "Voltage-dependent optical activity of a twisted nematic liquid crystal", Appl. Phys. Lett., **18**, 127-128(1971).

[99] C.-J. Chen, A. Lien, and M. I. Nathan, "4×4 matrix method for biaxial media and its application to liquid crystal displays", Jpn. J. Appl. Phys., **35**, **L**1204-**L**1207(1996).

[100] P. Yeh, "Optics of anisotropic layered media: a new 4×4 matrix algebra", Surface Science, **96**, 41-53(1980).

[101] M. Born E. Wolf, "*Principles of Optics*", Pergamon, NY, 1980.

[102] F. Di Pasquale, H. F. Deng, F. A. Fernandez, S. E. day, J. B. Davies, M. T. Johnson, A. A. van der Put, J. M. A van de Eerenbeemd, J. A. M. M. van Haaren, and J. A. Chapman, "Theoretical and experiment study of nematic liquid crystal display cells using the In-Plane-Switching mode", IEEE Trans. on Electron Devices, **46**, 661-668(1999).

Appendix

A copy of the paper [102] is included next.

F. Di Pasquale, H. F. Deng, F. A. Fernandez, S. E. day, J. B. Davies, M. T. Johnson, A. A. van der Put, J. M. A van de Eerenbeemd, J. A. M. M. van Haaren, and J. A. Chapman, "Theoretical and experiment study of nematic liquid crystal display cells using the In-Plane-Switching mode", IEEE Trans. on Electron Devices, **46**, 661-668(1999).

Theoretical and Experimental Study of Nematic Liquid Crystal Display Cells Using the In-Plane-Switching Mode

Fabrizio Di Pasquale, *Member, IEEE,* Hui Fang Deng, F. Aníbal Fernández, *Member, IEEE,* Sally E. Day, J. Brian Davies, *Fellow, IEEE,* M. T. Johnson, A. A. van der Put, J. M. A van de Eerenbeemd, J. A. M. M. van Haaren, and Jeff A. Chapman

Abstract— **In this paper a two-dimensional (2-D) dynamic model, based on a tensor formulation and solved numerically by combining finite elements and finite differences, is proposed and used for analyzing nematic liquid crystal (LC) test cells with interdigital electrodes. We compare theoretical and experimental results concerning the switching behavior, response mechanism, and viewing angle characteristics of nematic LC pixel structures which use the in-plane-switching (IPS) mode. The good agreement observed between theory and experiment in terms of electro-optical properties validates our modeling and demonstrates its potential for design optimization. We show that the proposed LC test cells, using the in-plane-switching mode, ensure switching-ON and -OFF response times of 22 and 28 ms, respectively, and excellent viewing angle characteristics.**

Index Terms— **Liquid crystal devices, liquid crystal displays, modeling.**

I. Introduction

LIQUID CRYSTAL DISPLAYS (LCD's) are very widely used for portable applications but the cost and image quality have not allowed them to become a replacement for cathode ray tubes in spite of their reduced weight and depth. Several problems must be resolved in order to allow LCD's to be used in applications requiring large screens. In particular, with the increasing size of liquid crystal (LC) screens for portable computers and for use in offices and video applications, it is important to improve the viewing angle characteristics and response speed, to be able to show high quality moving pictures with a large viewing cone and high contrast ratio without color shift. A number of solutions to the viewing angle problem have been suggested, such as the introduction of compensation layers to eliminate the birefringent effect in twisted-nematic (TN) LC cells [1], multidomain TN LC pixel structures using photo-alignment techniques [2], axially symmetric aligned microcells [3], and the in-plane-switching (IPS) mode [4]–[6]. Owing to its relative simplicity and very wide viewing angles, the IPS mode seems to be an attractive solution for large area monitor displays and merits a detailed analysis. Moreover, several ways of improving the response time of the IPS mode have also been reported [7], [8].

In this paper we compare theoretical and experimental results concerning the switching behavior, response mechanism and viewing angle characteristics of a test cell using the IPS mode, which has been fabricated with appropriate parameters for realizing large viewing angle. A two-dimensional (2-D) model, based on a tensor form, is used for describing the dynamic evolution of the director under the influence of external electric fields [9]. The optical properties of the pixel are then computed from this data, using an extended Jones matrix approach [10], [11] which gives the optical transmittance at normal and oblique light incidence.

Manuscript received December 19, 1997; revised November 13, 1998. The review of this paper was arranged by Editor J. Hynecek. This work was supported by The Royal Society and EPSRC, U.K.

F. Di Pasquale, H. F. Deng, F. A. Fernandez, S. E. Day, and J. B. Davies are with the Department of Electronic and Electrical Engineering, University College London, Torrington Place, London WC1E 7JE, U.K.

M. T. Johnson, A. A. van der Put, J. M. A. van de Eerenbeemd, and J. A. M. M. van Haaren are with Philips Research Laboratories, Eindhoven, The Netherlands.

J. A. Chapman is with Philips Research Laboratories, Redhill, Surrey RH1 5HA, U.K.

Publisher Item Identifier S 0018-9383(99)02382-5.

II. Dynamic Model and Electro-Optical Characteristics

This section describes the theoretical model we use for analyzing the dynamic behavior of 2-D nematic LC structures. The electrode configuration can be arbitrary and realistic voltage waveforms are applied to different electrodes as a function of time. The overall display performance is evaluated in term of electro-optical characteristics, considering an average pixel transmittance and its variation as a function of the applied voltage, time and viewing angle. First, the analysis of the electric and elastic properties of the LC material, provides the dynamic evolution of the director $\overline{n}$ and electric field $\overline{E}$, under the effect of external voltages applied to the electrodes.

Neglecting the flow and describing the elastic properties of nematic LC materials with a one-constant approximation, the dynamic model can be based on a tensor formulation which preserves the correct symmetry properties of the material ($\overline{n}$ and $-\overline{n}$ are equivalent in terms of energy) [9]. The equation of motion of the director rotation can be written as

$$n_\nu \left[\gamma \frac{\partial}{\partial t}(n_\nu n_\mu) - k\nabla^2(n_\nu n_\mu) - \epsilon_0 \Delta\epsilon E_\nu E_\mu \right] = 0 \qquad (1)$$

where γ is the viscosity coefficient, k the elastic constant, ϵ_0 is the vacuum permittivity, $\Delta\epsilon = \epsilon_h - \epsilon_l$ the dielectric anisotropy,

where ϵ_h and ϵ_l are, respectively, the permittivities parallel and perpendicular to $\overline{n}$; n_ν, n_μ, and E_ν, E_μ are the Cartesian components of the director and electric field, respectively (ν, $\mu = x, y, z$).

Solving numerically (1) gives the dynamic evolution of the director field $\overline{n}$ and allows one to compute the optical properties of the LC pixel. This is done here by applying a Jones matrix method [10], [11], further generalized by us to be able to calculate the transmission throughout the LC and dielectric layers at any incident angle (azimuth and co-latitude). An average pixel transmittance can also be computed for each viewing angle, applied voltage, and time by averaging over the pixel area and taking into account that some parts of the pixel can be masked.

Note that as the tensor form (1) preserves the symmetry property of the material, it allows one to handle solutions with disclination lines in the director orientation due to fringing fields at the edges of the electrodes [12]. This feature is important for the design of LC pixel structures in which such defects are to be avoided or, at least, controlled [13].

III. Numerical Solution

As the problem described in (1) is highly nonlinear due to the coupling between director and electric fields, its solution can only be obtained numerically by following an iterative procedure. Although (1) can be projected on the three axes of a Cartesian system (x, y, z) and reduced to three partial differential equations (Euler–Lagrange equations) [14], it is important to perform the numerical calculation starting directly from the tensor form [9]. This ensures the correct nematic symmetry property which is essential for a proper analysis of nematic LC structures in which disclinations may occur.

To solve (1), we use an iterative process separated in two parts. Time stepping is performed using the Crank–Nicolson (CN) method, while finite elements and finite differences are both used for the spatial discretization. Within each time step, the solution for the electric field (or potential V) is obtained variationally, assuming a fixed director field and using node-based finite elements. The solution for the director is then performed using CN and finite differences while assuming a fixed potential distribution. These two steps are repeated within each time step to ensure consistency between electric and elastic properties.

Assuming strong anchoring, the director $\overline{n}$ is considered fixed and specified by pre-tilt and twist angles on the surfaces of the LC layer. The potential is instead prescribed on the electrodes and can vary as a function of time, as dictated by the driving scheme. Also periodic boundary conditions are used for $\overline{n}$ and V to represent the periodicity of the display structure.

IV. In-Plane-Switching Mode

In the IPS mode, voltages are applied between electrodes on the same substrate of the pixel structure (Fig. 1). In the OFF-state, where no voltages are applied, the LC molecules are untwisted and homogeneously aligned between the substrates, according to the rubbing directions which are parallel to each other. Placing the cell between crossed polarizers then provides

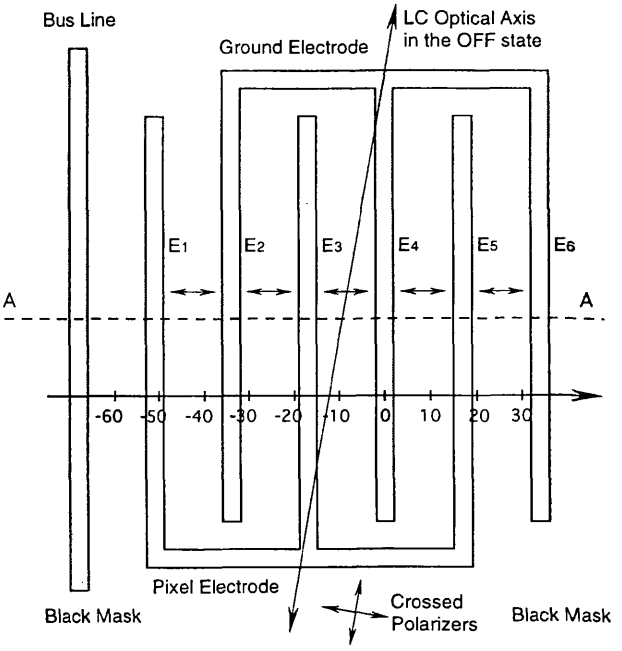

Fig. 1. Schematic diagram of the pixel structure. The small arrows between electrodes indicate the average orientation of directors in the ON-state, in the middle of the cell.

excellent light blocking. Applying an electric field between two electrodes should ideally twist the LC molecules in the same plane of the substrates, gradually increasing the optical transmittance with extremely wide viewing angles. However, fringing fields near the electrodes cause a more complex behavior, with both twist and tilt deformations, and with the possible formation of inversion walls in the structure. As these features affect the overall pixel performance it is important to model these devices at least in two dimensions, taking into account nonuniform electric fields.

Nematic LC test cells using the IPS mode have been fabricated, and then characterized both experimentally and theoretically.

A. Experiment

Fig. 1 shows a schematic diagram of the pixel structure (top view); opaque interdigital electrodes and the bus line have been patterned on the bottom surface of the cell. A black mask is also introduced to avoid the crosstalk from the bus line into the pixel region. The geometrical and material parameters are shown in Table I; ZLI 4792 liquid crystal (Merck, Ltd.) has been used, with a positive dielectric anisotropy. Alignment layers have been introduced on both surfaces of the LC layer with a 10° pretwist from the long side of the electrodes and a pretilt of 1° from the surface. The polarizer and analyzer were set, respectively, parallel and perpendicular to the rubbing direction, which defines the LC optical axis in the OFF-state. The cell gap, the electrode width and separation have been chosen considering the viewing angle and threshold voltage.

The average pixel transmittance for normal light incidence, $\overline{T}$, and the LC response time τ_{LC}, have been measured by gradually increasing the voltage V_p, applied between subpixel and ground electrodes, from 4 to 12 V (see Figs. 2 and

TABLE I
LC PARAMETERS

k_3/k_1	1.39
k_3/k_2	2.8
ϵ_1	3.1
$\Delta\epsilon$	5.2
$\gamma\ [Pa \cdot s]$	0.123
n_o (589 nm)	1.4794
n_e (589 nm)	1.5763
Electrode Width (μm)	4.
Electrode Distance (μm)	13.
Cell Thickness (μm)	4.
Pre-Tilt Angle	1°
Angle to line $A-A$	80°

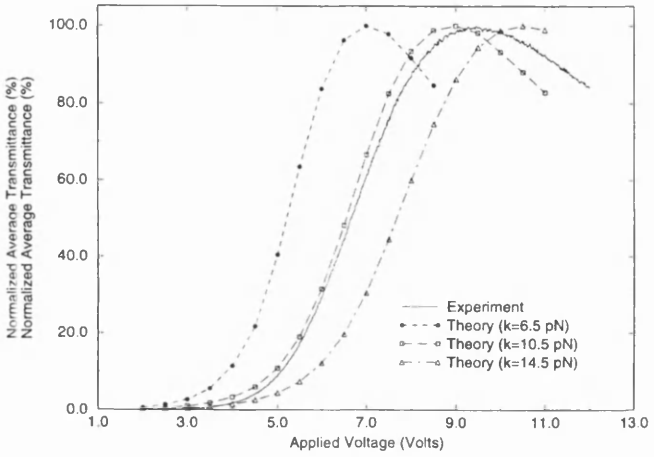

Fig. 2. Normalized average transmittance versus applied voltage.

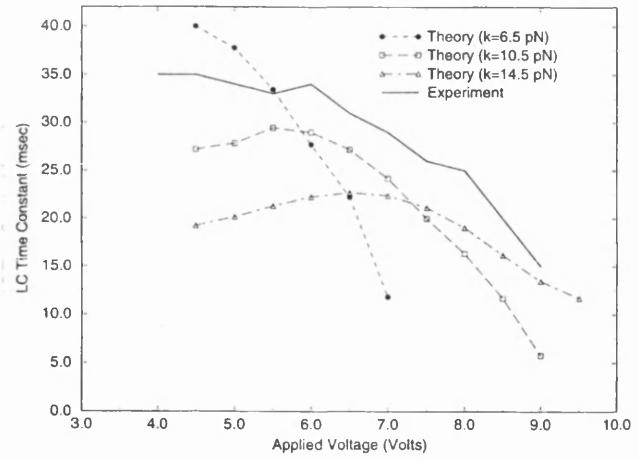

Fig. 3. LC time constant versus applied voltage.

3)). The LC response time $\tau_{\rm LC}$, following an increment ΔV in the applied voltage V_p, is defined as the time interval required for the average transmittance to vary from $\overline{T}(V_p)$ to $\overline{T}(V_p) + [\overline{T}(V_p + \Delta V) - \overline{T}(V_p)]/e$. An increment ΔV of 0.5 V has been used for measuring the LC response time for switching between gray levels.

We have also measured the switching-ON and -OFF response times of the cell, $\tau_{\rm on}$ and $\tau_{\rm off}$, defined as the time intervals required for the average pixel transmittance to change from 10% to 90%, and from 90% to 10% of its maximum

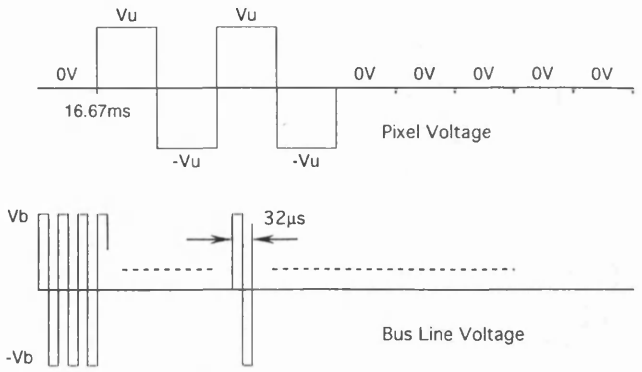

Fig. 4. Voltage waveform applied to the subpixel electrodes and bus line ($V_u = 9.5$ V, $V_b = 12$ V).

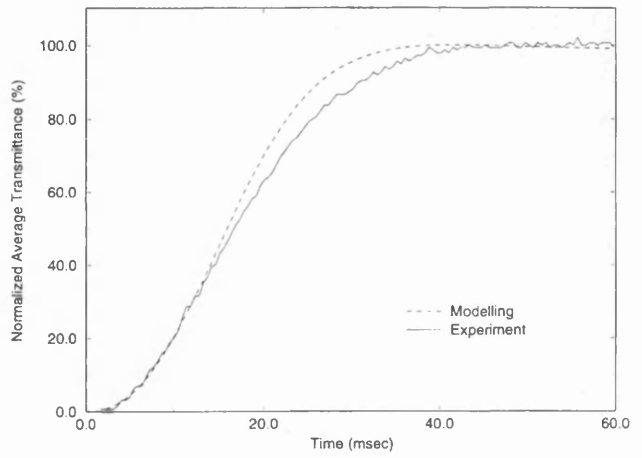

Fig. 5. Normalized average transmittances during the OFF-ON switching process [the time scale starts when the pixel voltage is switched ON (16.67 ms in Fig. 4)].

value, respectively, when voltage waveforms as shown in Fig. 4 are applied to the bus line and subpixel electrodes.

The average pixel transmittance, measured for normal light incidence during the OFF–ON and ON–OFF transitions, is shown in Figs. 5 and 6, respectively. $\tau_{\rm on}$ and $\tau_{\rm off}$, computed from this data according to their definitions, are, respectively, 22 and 28 ms. Note that, for the sake of an easier comparison with the theoretical results which will be described in Section V-B, the average pixel transmittance in Figs. 2, 5, and 6 has been normalized to its maximum value.

Finally, we have investigated the viewing angle characteristics of the test cell by measuring its average transmittance versus viewing directions. Figs. 7 and 8 show the variation of the OFF-state ($V_u = 1.2$ V) and ON-state ($V_u = 9.5$ V) transmittance with viewing direction. Also in this case the transmittance has been normalized to the maximum values in the ON-state. The contrast ratio of the cell versus viewing direction has also been computed as the ratio $\mathrm{CR} = \overline{T}_{\rm ON}/\overline{T}_{\rm OFF}$ and is shown in Fig. 9. A contrast ratio with a minimum value of ten can be obtained over a wide angle of at least 60° in all directions.

B. Modeling

The same pixel structure has been analyzed numerically by considering a 2-D section of the test cell as indicated

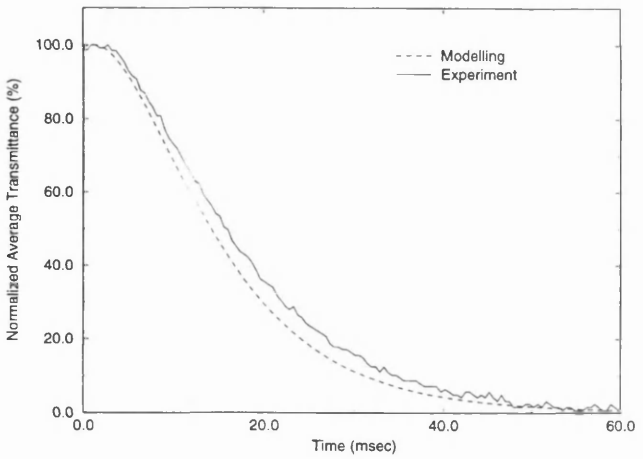

Fig. 6. Normalized average transmittances during the ON–OFF switching process [the time scale starts when the pixel voltage is switched OFF (83.3 ms in Fig. 4)].

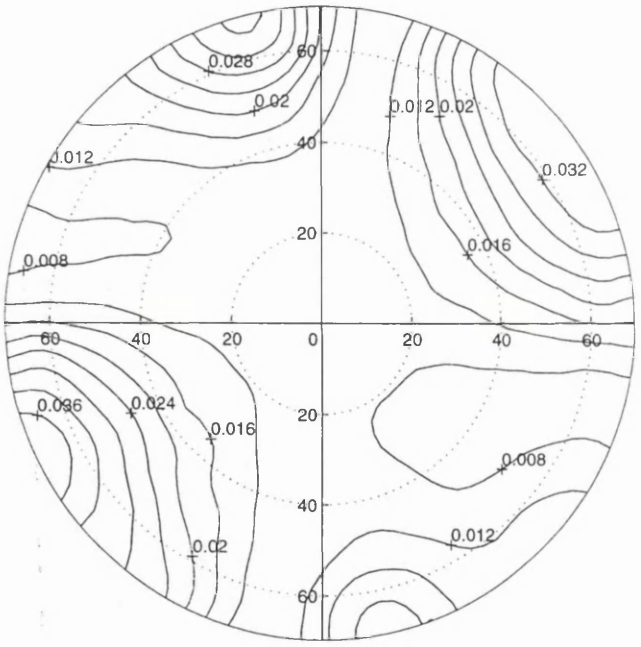

Fig. 7. OFF-state transmittance measured versus viewing direction (V_a = 1.2 V, V_b = 12 V).

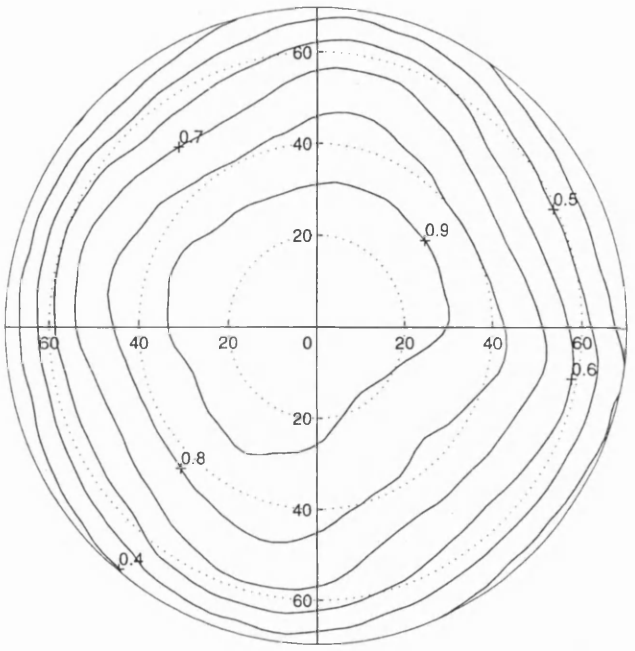

Fig. 8. ON-state transmittance measured versus viewing direction (V_a = 9.5 V, V_b = 12 V).

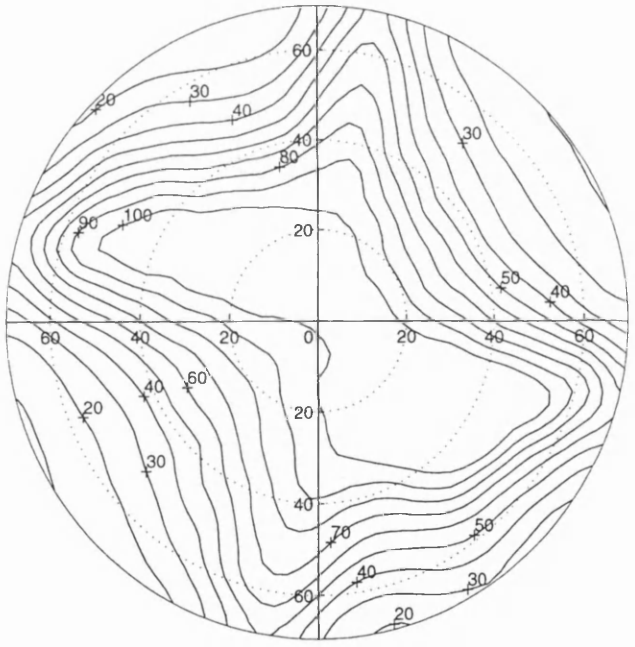

Fig. 9. Variation of the contrast ratio with viewing direction (experiment); isolines below 100.

by the dotted line A-A in Fig. 1. As the elastic properties of the material are described in our model with a one-constant approximation, and due to the fact that all other input parameters of the model are known with good accuracy from measurements and the Merck data sheet, we have studied the test cell by varying the effective elastic constant k in (1). Figs. 2 and 3 show a comparison between theoretical predictions and experimental results concerning the average pixel transmittance and the LC response time versus applied voltage, for three different values of the effective elastic constant.

Since all electrodes in the test cell are opaque and a black mask is introduced to avoid the crosstalk from the bus line, the average pixel transmittance has been computed for normal light incidence by considering only the regions separating the electrodes in the pixel area. Opaque electrodes have been deposited to reduce the detrimental effect due to the tilt deformation and disclination lines forming in the region above the electrodes.

Varying the value of the constant k from 6.5 to 14.5 pN, which almost spans the range of the three k_1, k_2, and k_3 constants, the best agreement between theory and experiment can be found using $k = 10.5$ pN, which is close to the average value of the three elastic constants. The good agreement observed between theoretical predictions and experiment, in

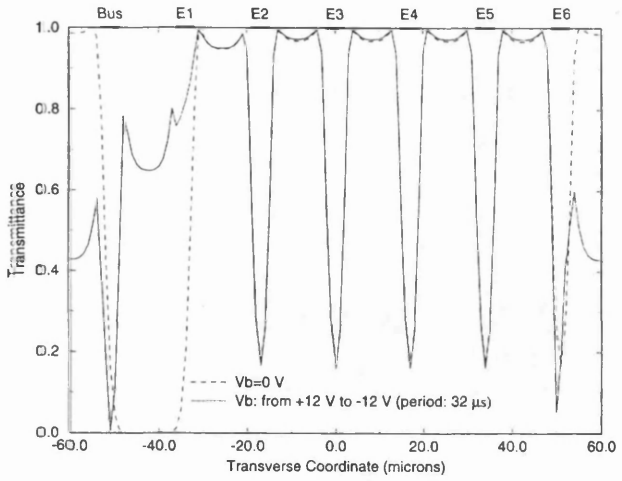

Fig. 10. Transmittance versus transverse coordinate in the ON-state ($V_u = 9.5$ V) with $V_b = 0$ V and V_b varying from +12 to −12 V with a period of 32 μs.

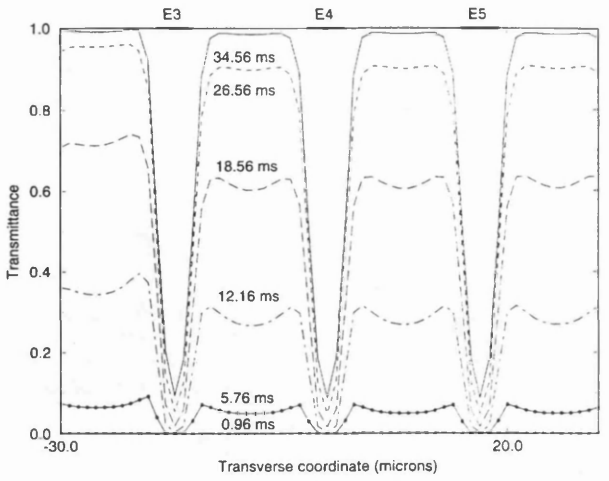

Fig. 12. Transmittance versus transverse coordinate during the OFF-ON switching process (the curves are labeled with time starting after the switching ON of the pixel voltage).

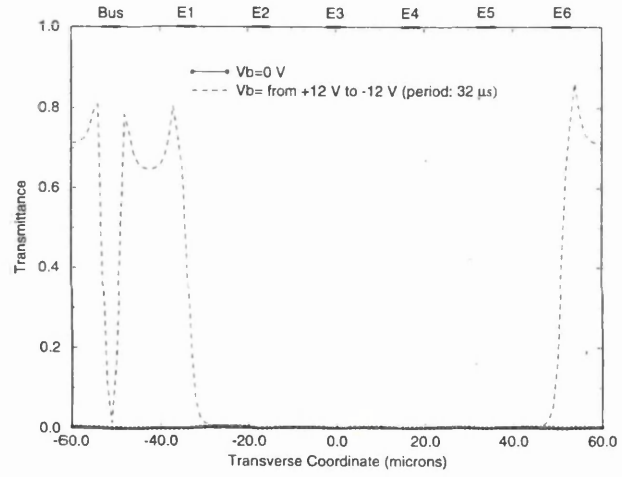

Fig. 11. Transmittance versus transverse coordinate in the OFF-state ($V_u = 1.2$ V) with $V_b = 0$ V and V_b varying from +12 to −12 V with a period of 32 μs.

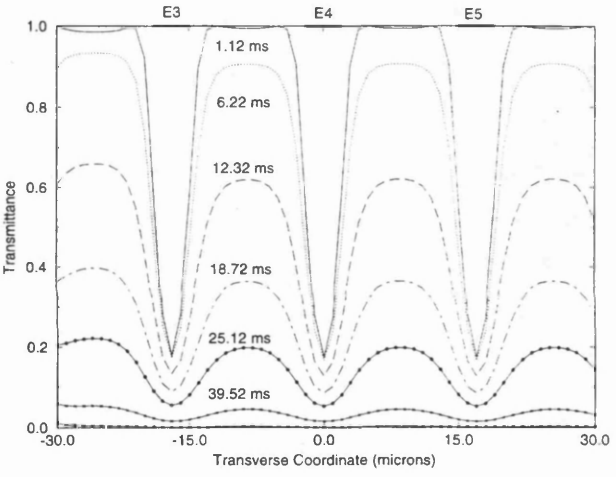

Fig. 13. Transmittance versus transverse coordinate during the ON–OFF switching process (the curves are labeled with time starting after the switching OFF of the pixel voltage).

spite of using a one constant approximation confirms the validity of the model in this application.

Using the effective elastic constant value which gives the best agreement, we then studied theoretically the OFF–ON and ON–OFF switching processes. With voltage waveforms applied to the bus line and subpixel electrodes as used in the previously described experiment and shown in Fig. 4, the switching-ON and -OFF response times of the cell, τ_{on} and τ_{off}, computed from the data shown in Figs. 5 and 6 are, respectively, 19.2 and 25.7 ms and compare well with the measured values, with a difference of about 10%.

Although the voltage applied to the bus line V_b varies from 12 to −12 V with a fast period (32 μs) compared to the LC response time, as the crosstalk from the bus line can affect the optical properties in the pixel area, it is important to take into account this fast field variation, without approximating it with a zero time average [15]. Figs. 10 and 11 show the transmittance for normal incidence versus the transverse coordinate in the ON- and OFF-states, computed with $V_b = 0$ V and V_b varying from 12 to −12 V, respectively. It is clear that the crosstalk from the bus line [16] has a detrimental effect on the optical properties in the pixel area. For this reason the black mask has been introduced, as shown in Fig. 1.

This relatively fast response capability, achieved without requiring any complex driving scheme of the pixel [7], is sufficient for showing moving images. Note that different regions in the pixel area experience different transmittance during the switching. This can be seen in Figs. 12 and 13, where we show the transmittance versus the transverse coordinate in the central part of the pixel, at different times during the OFF–ON and ON–OFF switching processes. The director and potential distributions throughout the same part of the pixel in the ON-state ($T = 83$ ms in Fig. 4) are also shown in Fig. 14. The effect of the tilt deformation above the interdigital electrodes is evident from these figures. Although the electrodes are opaque, the effect of such defects on the switching speed cannot be avoided.

Finally, the viewing angle characteristics of the test cell have been studied theoretically to compare with the experimental results shown in Figs. 7–9. Figs. 15 and 16 show the

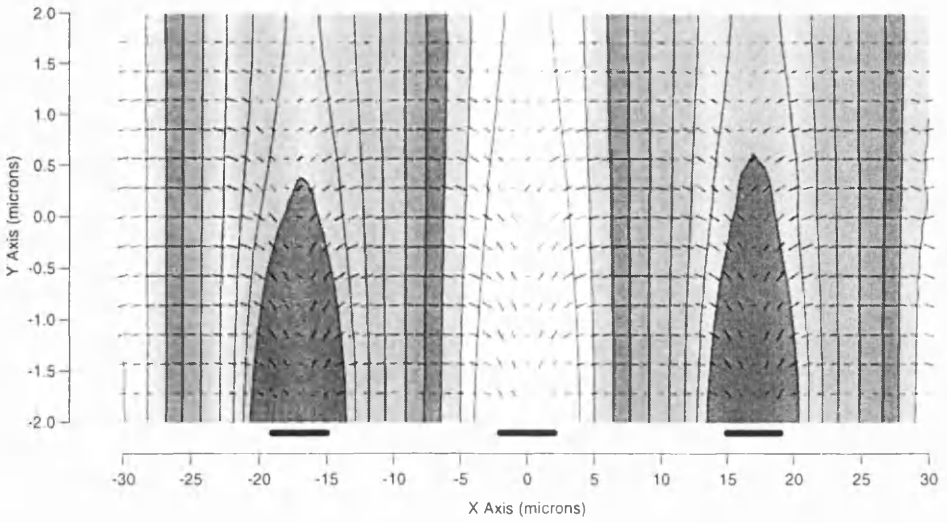

Fig. 14. Director and potential distributions in the ON-state.

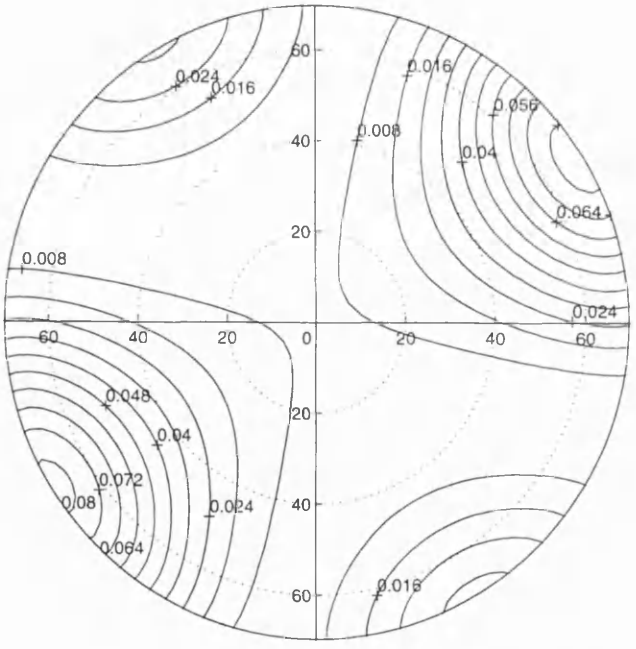

Fig. 15. Variation of the OFF-state transmittance with viewing direction ($V_u = 1.2$ V, $V_b = 12$ V).

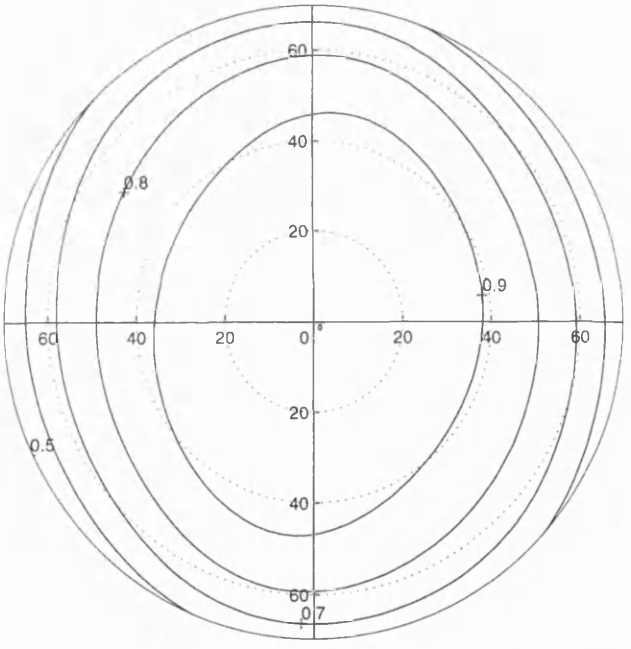

Fig. 16. Variation of the ON-state transmittance with viewing direction ($V_u = 9.5$ V, $V_b = 12$ V).

variation with viewing direction of the OFF-state and ON-state transmittance normalized to the maximum value in the ON-state ($V_u = 9.5$ V), where the modeled transmittance reaches a maximum of about 40% (of the available incident light) for normal incidence and then decreases with oblique incidence. This includes the effects of polarizers, opaque electrodes and and black masks. In the OFF-state ($V_u = 1.2$ V) the average transmittance is always less than 3.7%. Note that the extended Jones matrix method we have used includes losses introduced by the polarizers and the presence of interfaces with air. The contrast ratio of the cell versus viewing direction has also been computed and is shown in Fig. 17.

A good quantitative agreement between theory and experiment can be observed in general. The differences between theory and experiment in the contrast ratio are mainly due to more gradual decrease of the ON-state transmittance with increasing viewing angle in the theoretical prediction, possibly due to the influence of the off-axis behavior of the polarizers. We have also studied the viewing angle characteristic without considering the black mask shown in Fig. 1. The results give a poor contrast ratio and confirm the importance of this black mask to reduce the crosstalk from the bus line.

V. Conclusion

We have presented and compared theoretical and experimental results concerning nematic LC test cells using the IPS mode. The good agreement, observed in terms of electro-optical properties, confirms the validity of our dynamic model

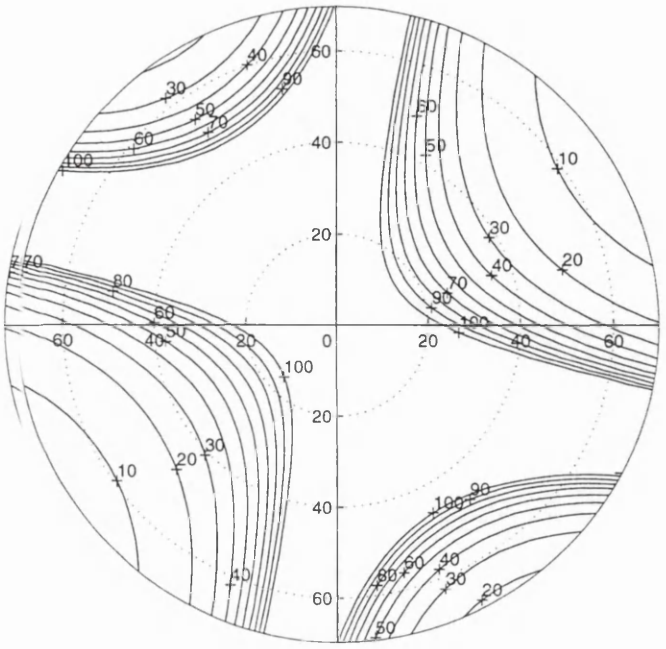

Figg. 17. Variation of the contrast ratio with viewing direction (modeling); isoolines below 100.

annd its potential for design optimization. Differences less thaan about 10% between theoretical and experimental results seeem very reasonable, considering the one elastic constant appproximation and the infinite z-dimension assumptions in our 2-D modeling.

ACKNOWLEDGMENT

The authors would like to thank G. G. H. van de Spijker foor designing and making the IPS test cells.

REFERENCES

[1] H. Hatoh, M. Ishikawa, J. Hirata, Y. Hisatake, and T. Yamamoto, "Improvement of viewing angle characteristics in a twisted-nematic liquid-crystal display by using a cholesteric liquid-crystal compensation layer," *Appl. Phys. Lett.*, vol. 60, no. 1806, pp. 1806–1808, 1992.

[2] H. Murai, M. Suzuki, and S. Kaneko, "Novel high contrast random and controlled 4-domain CTN-LCD's with wide viewing angle," in *Eurodisplay'96*, Birmingham, U.K., Oct. 1–3, 1996, pp. 159–162.

[3] H. S. Soh, J. W. Wu, M. S. Nam, Y. J. Choi, J. Kim, K. J. Kim, J. H. Kim, and S. B. Kwon, "The realization of wide viewing angle TFT-LCD's using photo-alignment method," in *Eurodisplay'96*, Birmingham, U.K., Oct. 1–3, 1996, pp. 579–582.

[4] M. Oh-e and K. Kondo, "Electro-optical characteristics and switching behavior of the in-plane switching mode," *Appl. Phys. Lett.*, vol. 67, no. 26, pp. 3895–3897, 1995.

[5] ——, "Response mechanism of nematic liquid crystal using the in-plane switching mode," *Appl. Phys. Lett.*, vol. 69, no. 5, pp. 623–625, 1996.

[6] T. Suzuki, S. Nishida, M. Suzuki, and S. Kaneko, "Analysis and control of extraordinary domains in wide-viewing-angle in-plane-switching mode TFT-LSD's," in *SID'97*, Boston, MA, May 13–15, 1997, pp. 184–187.

[7] M. Hasegawa, "Response time improvement of the in-plane-switching mode," in *SID'97*, Boston, MA, May 13–15, 1997, pp. 699–702.

[8] S. H. Lee, J. G. You, H. Y. Kim, D. S. Lee, S. K. Kwon, H. S. Park, and C. K. Kim, "Influence of rubbing direction on the electro-optic characteristics of in-plane-switching-mode LCD's," in *SID'97*, Boston, MA, May 13–15, 1997, pp. 711–714.

[9] A. Kilian and S. Hess, "Derivation and application of an algorithm for the numerical calculation of the local orientation of nematic liquid crystals," *Z. Naturforsch.*, vol. 44a, pp. 693–703, 1989.

[10] P. Yeh, "Extended Jones matrix method," *J. Opt. Soc. Amer.*, vol. 72, no. 4, pp. 507–513, Apr. 1982.

[11] A. Lien, "A detailed derivation of extended Jones matrix representation for twisted nematic liquid crystal displays," *Liquid Cryst.*, vol. 22, no. 2, pp. 171–175, 1997.

[12] F. Di Pasquale, F. A. Fernández, J. B. Davies, and S. E. Day, "Analysis of twisted nematic liquid crystal display cells using the finite element method," in *Eurodisplay'96*, Birmingham, U.K., Oct. 1–3, 1996, pp. 305–308.

[13] F. Di Pasquale, F. A. Fernández, S. E. Day, and J. B. Davies, "Two-dimensional finite element modeling of nematic liquid crystal devices for optical communications and displays," *IEEE J. Select. Topics Quantum Electron., Special Issue on "Smart Pixels,"* vol. 2, pp. 128–134, Apr. 1996.

[14] M. Kitamura, "Computer simulation of director profile in two dimensional electric field," in *SID'93 Dig.*, pp. 350–353.

[15] M. E. Becker, H. Wöhler, M. Kamm, and J. Krels, "Numerical modeling of IPS effects: A new approach and more results," in *SID'96 Dig.*

[16] M. Ohta, M. Yoneya, and K. Kondo, "Electric field analysis in TFT-LCD's with in-plane switching mode of nematic LC's," in *Eurodisplay'96*, Birmingham, U.K., Oct. 1–3, 1996, pp. 49–52.